Lawrence Berkeley Laboratory
UNIVERSITY OF CALIFORNIA

Physics Division

The Inclusive Cross Section of Charged Hadrons in 3-Jet Events at $\sqrt{s}$ = 29 GeV

F.R. Rouse
(Ph.D. Thesis)

October 1987

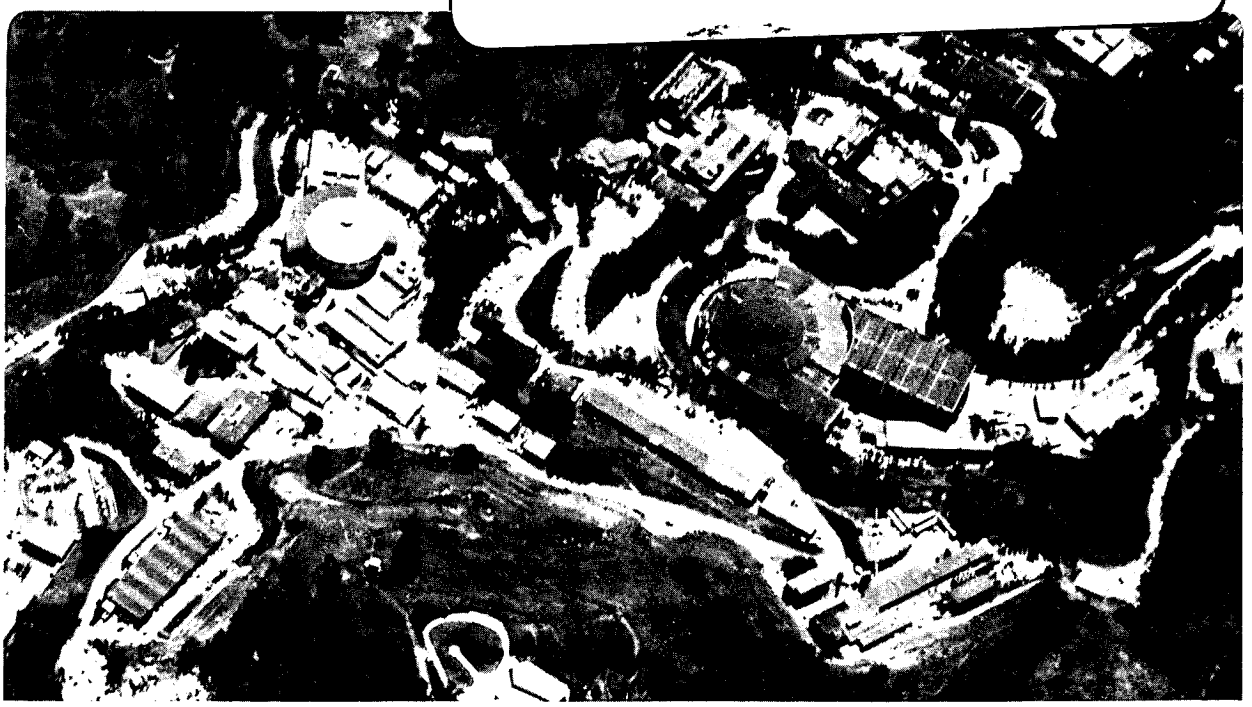

Prepared for the U.S. Department of Energy under Contract DE-AC03-76SF00098

DISCLAIMER

LBL-24729

The Inclusive Cross Section of Charged Hadrons in 3-Jet Events at $\sqrt{s} = 29$ GeV

Forest R. Rouse

Ph.D. Thesis

October 1987

Lawrence Berkeley Laboratory

University of California

Berkeley, CA 94720

This work was supported by the Director, Office of Energy Research, Office of High Energy and Nuclear Physics, Division of High Energy Physics of the U. S. Department of Energy under contract #DE-AC03-76SF00098.

The Inclusive Cross Section of Charged Hadrons in 3–jet events at $\sqrt{s} = 29$ GeV

By

Forest R. Rouse

Ph.D Thesis

October 1, 1987

Lawrence Berkeley Laboratory

University of California

Berkeley, CA 94720

Abstract

We examine the cross section for the production of charged hadrons in 3–jet events produced from e^+e^- annihilation at 29 GeV center of mass energy. The data was taken at the Pep-4/Time Projection Chamber between 1983-1984. In particular we are interested in the production of hadrons by the particle which mediates the strong interaction, the gluon. We find that the number of protons produced by the fragmentation of the gluon is at variance with the LUND model of fragmentation.

This work is supported by the United States Department of Energy under Contract DE-AC03-76SF00098

Contents

Acknowledgements v

1 Introduction 1

2 Phenomenology of Hadronic Interactions 3

2.1 Beginnings: The Emergence of the Quark Model 3

2.1.1 The Parton Model 6

2.2 Towards QCD, the Theory of the Strong Interaction 7

2.2.1 The Need for Color 7

2.2.2 The Gauge Theory, QCD 9

2.2.3 Asymptotic Freedom 13

2.2.4 3–jet events 18

2.3 Fragmentation 23

2.3.1 The Parton Model Revisited 23

2.3.2 Scaling Violations 26

2.3.3 Models of Fragmentation 28

3 The PEP–4 Detector 43

3.1 The PEP–4 Detection System 46

3.2 The TPC 54

3.2.1 TPC Electronics 59

3.2.2 TPC Calibration 65

3.3 Trigger 71

4 Theory of Energy Loss in Materials **79**

4.1 Introduction to Energy Loss 79

4.2 Average Energy Loss 83

4.3 Monte Carlo of Energy Loss in the TPC 87

5 Data Reduction and Event Selection **93**

5.1 Track Reconstruction 94

5.2 Multipass analysis of 1983–1984 97

5.3 TPCLUND: The Simulation of the TPC Detector 120

5.4 3 Jet Event Selection 128

5.4.1 Jet Finding Algorithms 129

6 Unfolding the TPC - The Analysis Method **139**

6.1 The Mathematical formulation of the problem 139

6.2 Testing Unfolding 142

6.2.1 Toy Model for Unfolding the TPC 143

6.2.2 Determining parameters for analytic method 153

6.3 Resolution 157

6.3.1 Energy loss measurement error 157

6.3.2 Multiple Scattering Error 163

6.3.3 Vertex Momentum Measurement Error 171

6.4 Analysis of dE/dx vs $\ln p$ plot 176

6.4.1 Accurate analytic probability calculation 176

6.4.2 Detector considerations 180

6.4.3 Determining Resolution Parameters 188

7 Results and Conclusion **192**

7.1 Testing the method 192
7.2 Inclusive Cross Sections in the Entire Data Sample 197
7.2.1 Systematic Error Determination in Data 207
7.3 3–Jet Events 211
7.3.1 3–Jet Results and Discussion 218
7.4 Conclusions 228

Acknowledgements

Like Rome, large experiments are not built in a day. The Time Projection Chamber (TPC) is no exception. There were well over 100 physicists, engineers and technicians involved directly in the design, fabrication, testing, installation, and running of the detector. In addition, the Stanford Linear Accelerator Center provided the site and yet more manpower to build and run the electron–positron storage ring. I thank them all.

But in particular, I have a large debt of gratitude to many people who directly helped me with this thesis. Werner Hofmann provided the inspiration for the analysis technique presented here. I also wish to thank him for the helpful comments on the jet analysis itself. Similarly, Gerry Lynch and Orin Dahl kindly shared with me their thoughts on data analysis. I am also grateful to Nick Hadley, Bernard Gabioud and Marjorie Shapiro who did the early work on the TPC's resolution. The time I spent with Owen Chamberlain, Ray Fuzesy, Dave Nygren and Peter Robrish is invaluable. They graciously laid a solid foundation for my knowledge of experimental hardware and ionization chambers. I would also like to thank Glen Cowen for the many physics conversations we had.

Additionally, I was one of many fellow students and colleagues who participated in the "battle" of the electronics house. I wish to thank Bill Gary, Kevin Derby, Bill Moses, John Huth, Jon Bakken, Dick Kofler, Nick Hadley and Marjorie Shapiro who because of that time together also became friends.

I do not have the words to express the heartfelt gratitude to my thesis advisor,

Gil Shapiro. Gil was extremely patient and helpful in working out the problems of this analysis. He also provided me with invaluable comments and critiques of this work. In addition, I am also grateful to Harry Bingham and Selig Kaplan, for carefully reading and commenting on this thesis. Jack Eastman, Bill Moses and Rem van Tyen gladly gave of their time to show me how the Macintosh computer can be used to make the dissertation's figures.

One's parents have a large influence on one's life. I am grateful for my parents support and encouragement throughout my graduate studies. I also wish to thank my spouse, Smadar Lavie, for her kindness and for comforting me while sharing the burdens of this project.

Lastly, I should express sincere gratitude to Bob Cahn, Mike Chanowitz, Orin Dahl, Tim Edberg, Michael Gold, Gerson Goldhaber, Dick Kofler, Jay Marx, Carl Pennypacker, Moishe Pripsten, Lynn Stevenson and George Trilling. Special thanks go to Owen Chamberlain, Gerry Lynch, Dave Nygren and Gil Shapiro. All of these dear friends and colleagues showed that they cared for me not only as a scholar, but as a human being. They all wrote letters supporting my plea to be able to conduct my research while not being forced to separate from my spouse, to the California Representatives in Congress. Because of their concern, this thesis was written in Berkeley instead of being dreamed about from the Holy Land.

Chapter 1

Introduction

All particles (and therefore all matter) can be divided into two broad groups: those particles which can undergo the strong interaction (hadrons) and those that do not (leptons). Leptons, as yet, have shown no sign of substructure. Therefore leptons can be viewed as elementary. Hadrons are a different kettle of fish.

Hadrons appear to have substructure. The quark model proposes to build hadrons out of elementary particles (quarks). It should be stated that the quark model has been very successful. From the time it was proposed in the early 1960's until today it can account for every one of the over 100 hadrons which have been discovered in the interim.

The theory of the interaction between the quarks, **Quantum Chromodynamics** (QCD), was proposed in the early 1970's. This theory is the culmination of work which started in the 1930's. Without an attractive potential between nucleons, nuclei would literally fly apart because of the coulomb repulsion between protons. This interaction is called the strong interaction because the force must be strong enough to overcome the coulomb repulsion.

QCD is a field theory analogous to the field theory of electromagnetism, **Quantum Electrodynamics** (QED). In QCD, there is a massless boson which intermediates the strong interaction just as in QED the photon intermediates the

electro–magnetic interaction. The boson in QCD is called the gluon. Therefore, if QCD is a valid theory, we expect to find some evidence for the existence of the gluon.

No quark or gluon has ever been observed directly. Instead all we observe in our detectors is hadrons. The process which an elementary particle (quark or gluon) undergoes in order to reach the observable final state is called **hadronization** or **fragmentation**. In fact we do not expect to see an elementary quark or gluon until fantastically large energies (if then). The strong interaction is so attractive that it may require upwards of 10^{15} GeV in order to break the attraction and observe quarks and gluons as free particles.

We call this phenomenon confinement. There exist no theories of confinement although several approaches like lattice QCD may yield such a theory eventually. The best alternative to the theory of confinement is to model the manner in which confinement expresses itself.

This thesis seeks to probe a phenomenological question: What is the nature of gluon fragmentation?

The thesis is organized as follows: We will first amplify the theoretical framework described in the introduction in chapter 2. Chapter 3 presents a description of the apparatus, chapter 4 then discusses the theory of energy loss by particles in matter. Understanding how particles lose energy as they traverse a gas volume is crucial to understanding the heart of our apparatus. Chapter 5 discusses how events were selected for analysis, chapter 6 our analysis method and finally chapter 7 will present the results.

Chapter 2

Phenomenology of Hadronic Interactions

The 1930's saw the beginning of a long list of particle discoveries. It became apparent there existed a force which overcame the coulomb repulsion between protons within the nucleus of an atom. Otherwise atoms would not be stable. Yukawa predicted that the force was mediated by a particle about 200 times as massive as the electron [1]. The discovery in 1947 of the pion confirmed the prediction and soon physicists were facing a baffling array of particles.

This chapter's brief overview of strong interactions will hardly do the field justice. Nevertheless, we must set a frame for the measurement of inclusive cross sections in 3–jet events. The chapter first will briefly discuss the emergence of the quark model. We will then discuss the parton model which gives strong supporting evidence of the correctness of the quark hypothesis. Afterwards, we will discuss the theory of the strong interaction, QCD, the principle of asymptotic freedom, 3 jet events and finally fragmentation.

2.1 Beginnings: The Emergence of the Quark Model

The situation facing physicists at the beginning of the 1960's was one of confusion. The strongly interacting particles seemed to have an underlying order.

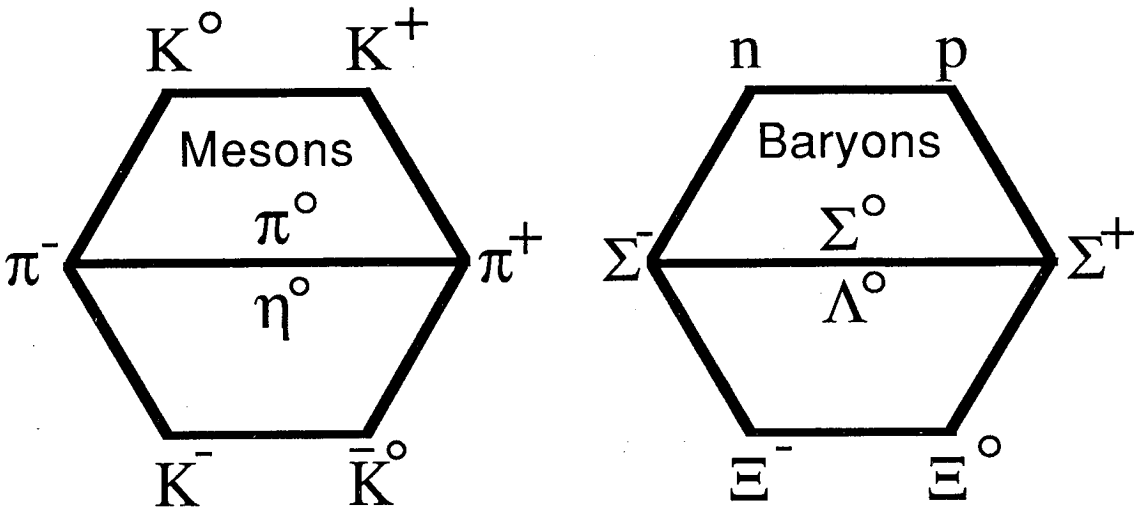

Figure 2.1: The lowest mass multiplets of mesons and baryons. These were the particles which had been discovered at the beginning of the 1960's with the exception of the η^0. Its discovery was one of the first triumphs of the quark model.

Particles with the same spin, parity and distinguished only by differing charge and mass organized themselves into groups (called isospin multiplets)[2,3]. Since the masses of the particles within an isospin multiplet are nearly the same, it was conjectured that a rotation symmetry in charge space of the interaction Lagrangian exists (called isospin symmetry) but the electromagnetic interaction slightly breaks the symmetry.

It was also noticed that there are two sets of particles. One set, the baryons, were of higher mass than the second set, the mesons. Furthermore, a baryon when it decays must net one and only one baryon. But here the mass symmetry was very badly broken. The baryons, for instance, have mass differences up to $30 - 40\%$ within the baryon octet shown in figure 2.1. This is in contrast to the $\sim 0.1\%$ to $\sim 1.0\%$ differences in mass between each of the particles inside an isospin multiplet. Presumably, if there were a symmetry governing the strong

interactions, it was badly broken by the interaction. Several possible global symmetries were advanced during the 1950's and 1960's to explain the observations, but the most successful of the attempts is the quark model.

Murray Gell-Mann and Yuval Ne'eman each advanced separately in 1961 the idea that the underlying symmetry was SU(3)[2]. The baryons and mesons each fell into an irreducible representation of the Lie group SU(3). In 1964 Gell-Mann[4] and Zwieg[5] suggested that all hadrons could be made of more fundamental spin 1/2 particles called quarks[6]. Specifically, quarks correspond to a fundamental multiplet of SU(3) (called a **3** because there are three indices) and all representations of SU(3) could be made out of the quarks. Table 2.1 lists the quarks and the quantum numbers necessary to build all the known hadrons.

Quark	Q/e	I_3	Baryon Number	Strange-ness	Charm	Bottom	Top
u	2/3	1/2	1/3	0	0	0	0
d	-1/3	-1/2	1/3	0	0	0	0
s	-1/3	0	1/3	-1	0	0	0
c	2/3	0	1/3	0	1	0	0
b	-1/3	0	1/3	0	0	-1	0
t	2/3	0	1/3	0	0	0	1

Table 2.1: The quark model. The u, d and s quarks were all that was needed to explain the hadrons discovered until the early 1970's when charm (c) and later in the decade bottom or beauty (b) were observed. Top (t) has not yet been found. Note that anti–quarks have exactly opposite quantum numbers.

Every meson was to be made of a quark and an anti–quark and every baryon was to be made of three quarks. Mathematically, we write the following:

$$\begin{array}{lll} \text{mesons} & q\overline{q} & \mathbf{3}\otimes\overline{\mathbf{3}} \\ \text{baryons} & qqq & \mathbf{3}\otimes\mathbf{3}\otimes\mathbf{3} \end{array}$$

The product space of $\mathbf{3}\otimes\overline{\mathbf{3}}$ can be reduced to a direct sum of two irreducible spaces: an **8** and a **1**. The baryons break into a direct sum of a **10**, two **8**'s

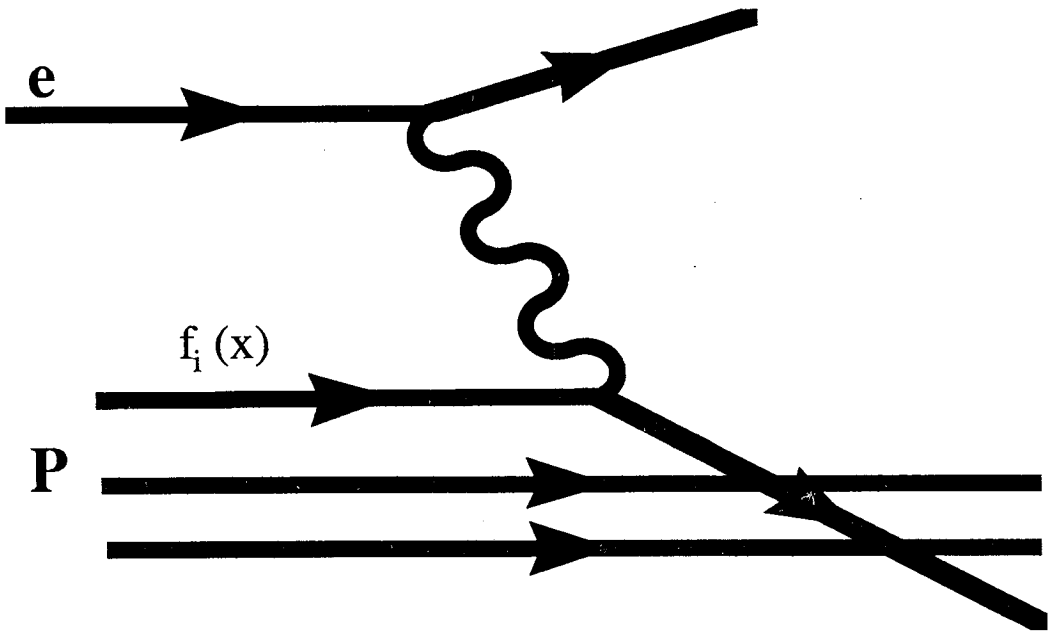

Figure 2.2: The parton model of the proton.

and a 1[6,7]. Successfully predicting that all the hadrons could fall into these categorizations was a major accomplishment of the quark model.

2.1.1 The Parton Model

If the proton were made of point–like objects, it should be possible to do the equivalent of a Rutherford scattering experiment. Just as the point–like constituents of the atom made their presence felt by sometimes scattering α particles through very large angles, so too would the quarks scatter a high energy probe of the proton through large angles. This is the essence of the parton model. Bjorken assumed that the proton could be thought of as a collection of objects, each carrying a portion of the proton's momentum. The strong interaction binds the hadron constituents together. In the limit of using a high energy probe of

a hadron, the interaction will be dominated by the coupling of the probe to the constituents of the hadron and the binding effects will become negligible.

Figure 2.2 is a graphical representation of the proton. The quantity $f_i(x)$ is the probability that the parton i carries a fraction x of the momentum of the proton. Bjorken[8] showed that the scattering cross section for high energy electron–proton (ep) scattering at a given value of Q^2 is dependent only on

$$x = \frac{-q^2}{2M\nu} = \frac{Q^2}{2p \cdot q} \tag{2.1}$$

where q is the 4–momentum transferred from the electron to the proton in the interaction, $-q^2 = Q^2$, M is the mass of the proton, ν is the difference in energy between the initial and final state electron and p is the initial four momentum of the proton. This remarkable result (called Bjorken scaling) was observed at the Stanford Linear Accelerator Center in 1969. The same experiment also observed the expected distribution in angle of the final state electron. Taken together, the two observations indicate that the proton is made of point–like spin 1/2 objects.

2.2 Towards QCD, the Theory of the Strong Interaction

This section describes the basis for the theory of the Strong Interaction, Quantum Chromodynamics, QCD. We shall briefly describe the color symmetry and why it is required. We shall then sketch the gauge field QCD. Basically, QCD is patterned after the very successful theory of the electromagnetic interaction Quantum Electrodynamics, QED. We shall draw on this analogy heavily as QED can be used as a simpler model for its more complicated brother.

2.2.1 The Need for Color

The quark model is an elegant and simple way to bring order to the particle zoo. However, the naive quark model has an immediate problem. The **10** corre-

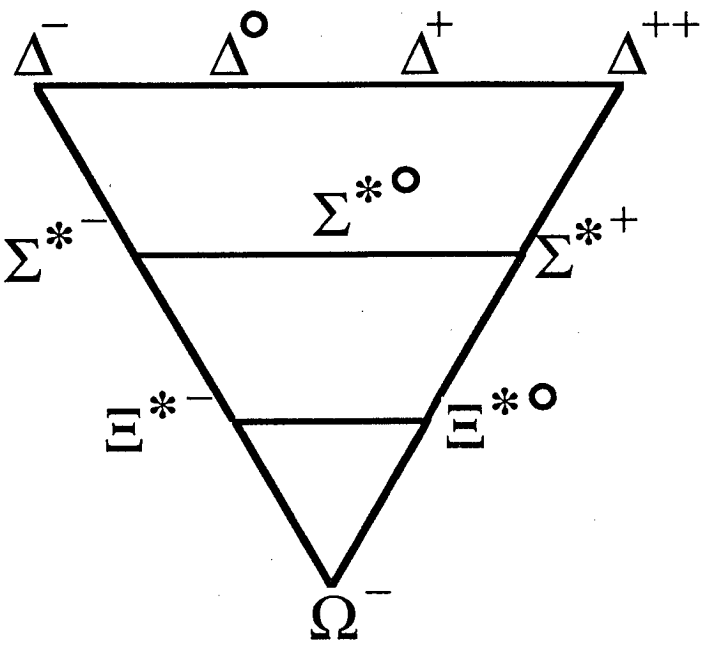

Figure 2.3: The lowest mass baryon **10** in the quark model.

sponding to the spin 3/2 baryons is shown in figure 2.3. The Δ^{++}, for instance, consists of three u quarks. Since the Δ^{++} and the u quark are fermions, the Δ^{++} wave function must be anti–symmetric under the interchange of any two of its constituent u quarks. Yet the Δ^{++} is spin 3/2 and each u quark is spin 1/2. Therefore, the Δ^{++} must be symmetric under the interchange of spin indices. We also suppose the Δ^{++} to be in a relative s wave (orbital angular momentum $L = 0$) because this is the lowest lying **10** of the baryons[3,6,9]. Hence the spacial portion of the wavefunction is also symmetric under $\vec{x} \rightarrow -\vec{x}$. Therefore the wave function of the Δ^{++} is symmetric under the interchange of any two u quarks. Finally, the quarks which make up the Δ^{++} are identical. Hence there must be an internal degree of freedom for quarks which allows the overall symmetry of the Δ^{++} to be anti–symmetric.

The new symmetry is called "color". We have not, as yet, observed individual

quarks. We assume color is the mechanism by which quarks are confined inside of hadrons. Therefore, each hadron must be a color singlet. We need at least three colors in order for a baryon to be a color singlet. We therefore make the minimal assumption that there are three colors.

This hypothesis has some immediate measurable consequences. Consider $e^+e^- \rightarrow q\bar{q}$ and $e^+e^- \rightarrow \mu^+\mu^-$. Since the final states are both of two spin 1/2 fermions, the only difference between the two cross sections is due to the charge of the quark as opposed to that of the muon. Also there are five possible quark species. Hence, the ratio of the hadronic cross section to the muon cross section must be [3,9]

$$\begin{aligned} R &= \frac{d\sigma(e^+e^- \rightarrow \text{Hadrons})}{d\sigma(e^+e^- \rightarrow \mu^+\mu^-)} \\ &= \sum e_q^2 \end{aligned} \tag{2.2}$$

where e_q is the fractional quark charge. Without color the sum over the possible quark species at 29 GeV center of mass energy in the interaction gives 11/9. However we must include the fact that the final state can only be a color singlet and one can use any of the 3 colors. Hence, R is multiplied by 3. Therefore, we expect R to be about 3.7. The result measured at PEP and PETRA is about 3.9[10,11]. The remaining discrepancy will be discussed in section 2.2.4. Finally, a similar argument gives a factor of nine in theoretical estimate of the lifetime of the π^0 and a factor of three to the decay rate of the τ lepton into hadrons. Color is crucial, otherwise the theoretical estimates would not match the measured values of these processes.

2.2.2 The Gauge Theory, QCD

The theory of the strong interactions is patterned after the field theory of the electromagnetic interactions. However, instead of photons mediating the interaction, a massless spin one boson carrying color (called the gluon) mediates the

strong interaction. We present here an overview of the gauge theory of the strong interaction, QCD, based on reference [3]. Let Ψ be the quark wave function. Ψ carries three indices corresponding to the three possible colors (SU(3)):

$$\Psi = \begin{pmatrix} \Psi_r \\ \Psi_g \\ \Psi_b \end{pmatrix} \tag{2.3}$$

where r, g and b refer to the possible colors the quark can carry, red, green and blue.

The interaction Lagrangian is postulated to be invariant under rotations in color space. It can be written as

$$\mathcal{L}_F = -\frac{1}{4} G_k^{\mu\nu} G_{k\mu\nu} + \overline{\Psi}\left(i\gamma_\mu D^\mu - m\right)\Psi \tag{2.4}$$

where

$$\begin{aligned} D^\mu &= \partial^\mu + i g_s \frac{\lambda_k}{2} A_k^\mu \ , \\ G_k^{\mu\nu} &= \partial^\mu A_k^\nu - \partial^\nu A_k^\mu + g_s f_{klm} A_l^\mu A_m^\nu \ , \end{aligned} \tag{2.5}$$

A_k^μ is the gluon radiation field which can take on eight values corresponding to an irreducible representation of SU(3), γ_μ is the Dirac matrix for four-component μ and g_s is the coupling constant of quarks to the gluon radiation field. The eight λ_k matrices are the generators of SU(3) and obey the following commutation rules:

$$[\lambda_k, \lambda_l] = 2i f_{klm} \lambda_m \tag{2.6}$$

where the f_{klm} are the structure constants of the Lie algebra. Table 2.2 gives a list of their values.

We can understand the interaction Lagrangian for QCD by comparing the terms to the more familiar example for electrodynamics. The term

$$\overline{\Psi}\left(i\gamma_\mu(\partial^\mu + i g_s \frac{\lambda_k}{2} A_k^\mu) - m\right)\Psi$$

ijk	f_{ijk}	ijk	f_{ijk}
123	1	345	1/2
147	1/2	367	−1/2
156	−1/2	458	$\sqrt{3}/2$
246	1/2	678	$\sqrt{3}/2$
257	1/2		

Table 2.2: List of structure constants of SU(3). Note that structure constants are symmetric under even and anti–symmetric under odd permutations of the three indices. The structure constant is zero for all combinations of indices not listed or obtainable by permutation.

corresponds to the term

$$\overline{\Psi}\left(i\gamma_\mu(\partial^\mu + ieA_e^\mu) - m\right)\Psi$$

in the Dirac equation[1,12,13]. A_e is the vector potential from electrodynamics. These terms represent the interaction of the particle (quark in the case of QCD, the electron in the case of QED) with the field.

The term

$$-\frac{1}{4}G_k^{\mu\nu}G_{k\mu\nu}$$

is analogous to the term

$$-\frac{1}{4}F^{\mu\nu}F_{\mu\nu} \text{ where } F^{\mu\nu} = \partial^\mu A^\nu - \partial^\nu A^\mu$$

in electrodynamics where F is the electromagnetic stress tensor[14]. These terms correspond to the energy stored in the field.

We see that the only difference between the two Lagrangians comes in the *form* of the terms. We have extra factors, terms and matrices in the case of QCD.

The reason for the differences is that the additional terms are needed to maintain rotational invariance of the interaction Lagrangian in SU(3) *color* space. The terms arise because the matrices which generate SU(3) color do not commute

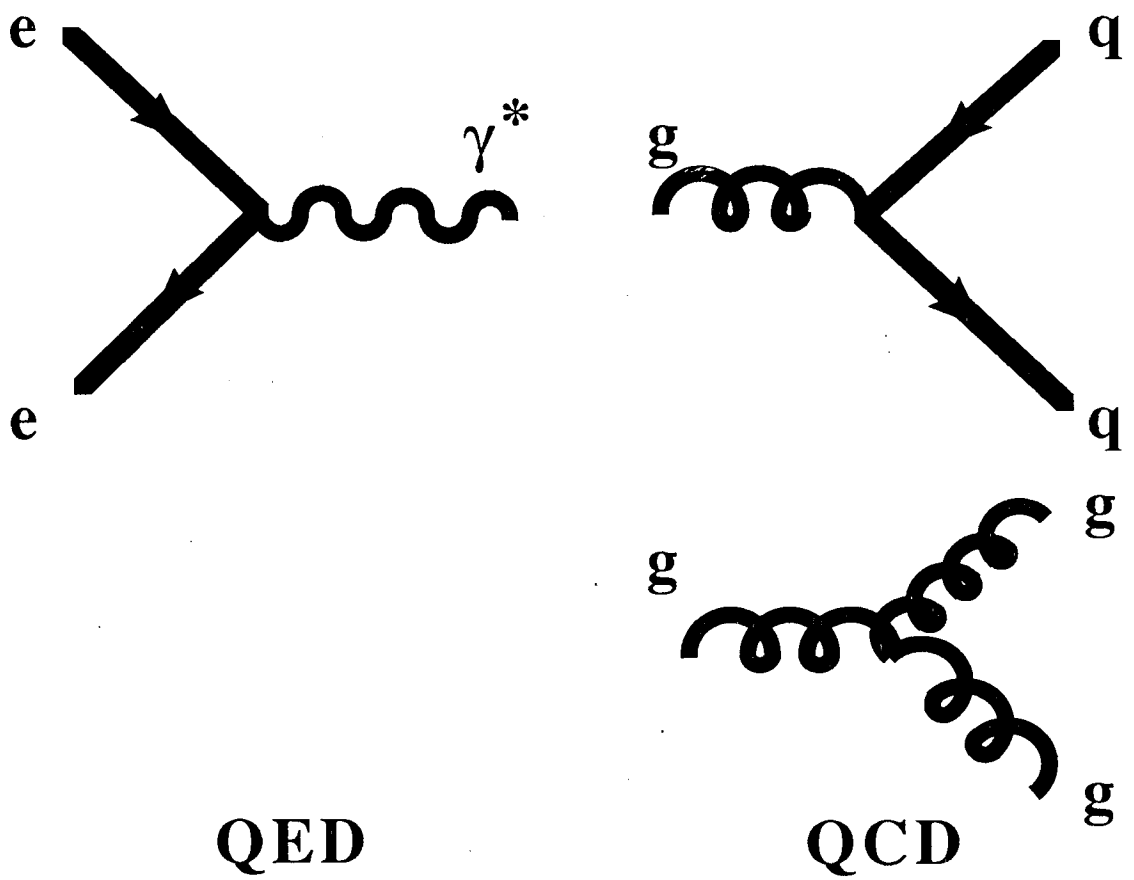

Figure 2.4: Basic Feynman diagrams for QED and QCD.

with each other (SU(3) is a non-abelian group). Charge symmetry in electromagnetism is generated by a unitary one parameter group U(1). Since U(1) is an abelian group we do not need terms which look like

$$g_s f_{klm} A^\mu A^\nu \tag{2.7}$$

in order to maintain gauge invariance in electromagnetism.

The extra terms are a general feature of all non-abelian gauge theories (so called Yang-Mills theories)[15]. However, the only practical difference in using the QCD and QED Lagrangians to calculate amplitudes is the presence of extra interactions which correspond to interactions between the gauge bosons them-

selves. We now have contact interaction terms between the gluons because of the term shown in equation 2.7. Another difference is in the interaction of the quark with the gluon. We must include the generators of SU(3) in the coupling. But the only change over QED is that we increase the strength of the vertex by a constant factor related to

$$\sum_{k=1}^{8} Tr(\lambda^k \lambda^k) \ .$$

Figure 2.4 shows the Feynman diagrams for the basic QED and QCD interactions.

2.2.3 Asymptotic Freedom

Perhaps the most important observational phenomenon that QCD must predict is Asymptotic Freedom. That is in the limit of very high energies, the quarks appear to be free particles. This is an underpinning of the quark–parton model, which, as we saw in section 2.1.1, provides the most consistent picture of the structure of hadrons. But also, QCD must reproduce the low energy behaviour of the strong interaction. As the energy of the interactions drops, the strong interaction can bind quarks together.

This implies that the strong coupling constant can take on two separate behaviors: at low energies the strong coupling constant must be large and at large energies it must be small. We begin the explanation of the phenomenon by considering QED. We will find that QED has similar phenomena, but that the behaviour is exactly opposite to what we need in QCD.

When electrons travel thru space, they can emit virtual photons as shown in figure 2.5a. The virtual photon pairs can themselves form virtual electron–positron pairs as shown in figure 2.5b [9]. The positrons are then pulled closer to the initiating electron by the electrostatic attraction between them and the electrons tend to be pushed to the outside (if a positron initiates the sequence the same phenomenon occurs but the virtual electron and positron exchange

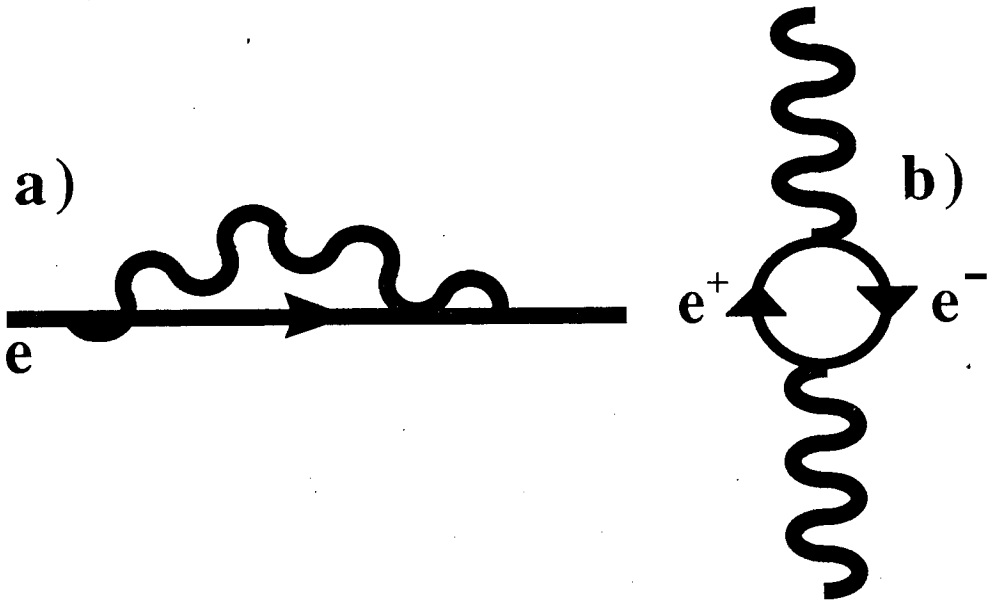

Figure 2.5: Production of virtual electron pairs from the vacuum in QED: a) the emission and absorption of a virtual photon and b) the formation of virtual electron positron pairs.

roles). This happens quite frequently so an electron is surrounded by a cloud of electron–positron pairs. The cloud is neutral and hence it is very hard to see the charge of the initiating particle since there are so many electron–positron pairs.

But as we come closer and closer to the cloud by using higher and higher energy probes, the more we penetrate the layers of virtual pairs surrounding the initiating electron. Therefore we see more and more of the originating electron's charge. This behaviour is called **vacuum polarization** because the virtual electron pairs polarize the vacuum and screen the charge inside the cloud.

The important diagram to calculate is figure 2.5b. If we use the usual Feynman rules to calculate the probability of this process we will find an ugly surprise. The Heisenberg uncertainty principle implies that virtual particles needn't conserve energy because they exist for infinitesimal periods of time. Hence there is

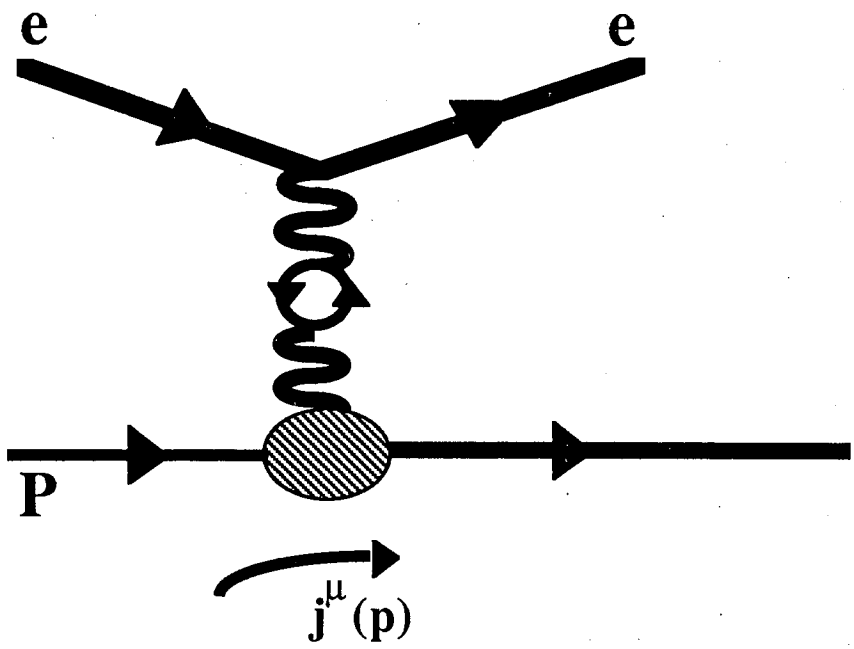

Figure 2.6: Lowest order correction to electron scattering due to presence of fermion loop.

no upper limit on the energy that the particles in the fermion loop can take on. This leads to an infinite probability that the process shown in figure 2.5 occurs. Even more troubling, this is only the first of an infinite number of loop diagrams.

The solution to the dilemma is, to say the least, unsettling. We make the ansatz that the underlying **unmeasurable** charge and mass of the electron are infinite. The infinity due to the loop diagram is then absorbed into the charge to give the finite measured charge of the electron. We cannot measure the bare charge of the electron because it is always surrounded by virtual electron pairs. Hence the electrostatic experiments which measure the force between charged objects do not measure the fundamental charge of the electron. Rather, this sort of experiment measures the *screened* charge of the electron.

We can view the effect of the fermion loop as modifying the photon propaga-

tor. It can be shown[1,9,12] that the photon propagator changes from

$$D_{\mu\nu}(q^2) = -i\frac{g_{\mu\nu}}{q^2} \tag{2.8}$$

to

$$\begin{aligned} D_{\mu\nu} &= -i\frac{g_{\mu\nu}}{q^2} - i\frac{g_{\mu\nu}}{q^2}\left\{\frac{\alpha}{3\pi}\int_{m^2}^{M^2}\frac{dp^2}{p^2} - \right. \\ &\left. \frac{2\alpha}{\pi}\int_0^1 dz z(1-z)\ln\left(1-\frac{q^2 z(1-z)}{m^2}\right)\right\} \end{aligned} \tag{2.9}$$

where $\alpha = e^2/4\pi$, q is the 4–momentum transferred in the process, $g_{\mu\nu}$ is the metric tensor for flat 4–space, m is the mass of the electron and M is the arbitrarily large momentum cut–off for the fermion loop. Using the above photon propagator, the matrix element for $eX \rightarrow eX$ scattering shown in figure 2.6 is

$$-i\mathcal{M} = (ie\overline{u}\gamma_0 u)\left(-\frac{i}{q}\right)\left(1-\frac{\alpha}{3\pi}\ln\frac{M^2}{m^2} - \frac{\alpha}{15\pi}\frac{q^2}{m^2}\right)ej^0 \tag{2.10}$$

where $e\overline{u}\gamma_0 u$ is the electron current and ej^0 is the current to which the electron couples and we take the limit of small momentum transfers q. The important point to take from this equation is not the precise mathematical form (for we have not motivated the mathematical steps leading to it). Rather consider the redefinition of the electric charge to be

$$e_r = e\left(1-\frac{e^2}{12\pi^2}\ln\frac{M^2}{m^2}\right)^{\frac{1}{2}}$$

where e_r is the observed electric charge and we make use of the ansatz that the charge appearing in the Lagrangian should be the infinite but unobservable bare charge e. Then the matrix element will become finite:

$$-i\mathcal{M} = (ie_r\overline{u}\gamma_0 u)\left(-\frac{i}{q^2}\right)\left(1-\frac{e_r^2}{60\pi^2}\frac{q^2}{m^2}\right)e_r j^0\,. \tag{2.11}$$

This effect has been observed in hydrogen and is called the **Lamb shift**.

Renormalization is the procedure by which we include all corrections to photon and electron propagators due to loop diagrams[12]. The Renormalization

procedure must ensure that by including all corrections to all orders that the infinities can all be accounted for by rescaling the charge and mass of the particles in the theory. It also must be true that the final values for the propagators and matrix elements are independent of the upper and lower energy cutoffs used for the loop calculations. If a theory satisfies these requirements, it is considered **renormalizable.**

The independence of propagators and matrix elements from the cutoffs used to calculate the loop diagrams can be stated mathematically. It is called the **Renormalization Group Equation**[9]:

$$\mu \frac{\partial \mathcal{M}}{\partial \mu} = 0 \tag{2.12}$$

where $\mathcal{M}$ is a matrix element and μ is the scale at which the process is occurring. One can then show that in QED, the coupling constant α varies with the renormalization point μ as

$$\alpha(Q^2) = \frac{3\pi\alpha(\mu^2)}{3\pi - \alpha(\mu^2)\ln Q^2/\mu^2} \tag{2.13}$$

where $Q^2 = -q^2$ the 4–momentum transferred squared[9].

We see that this equation is the mathematical explanation of the vacuum polarization. As the Q^2 increases, the denominator goes to zero. Therefore, the coupling constant α grows with increasing Q^2. Physically, the electric charge increases as Q^2 increases. At the point when the denominator becomes zero, α becomes infinite. Using QED as a perturbation theory comes into question at such large Q^2. Nevertheless, the basic phenomenon has been explained.

We need the opposite behavior for the coupling constant in QCD. It should not surprise the reader that the behavior in QCD comes about due to the self–interactions of the gluons. The strong coupling constant $\alpha_s = g_s^2/8\pi$ varies with Q^2 as

$$\alpha_s(Q^2) = \frac{12\pi}{(33 - 2n_f)\ln Q^2/\Lambda^2} \tag{2.14}$$

where we have chosen

$$\Lambda^2 = \mu^2 \exp \frac{-12\pi}{(33 - 2n_f)\alpha_s(\mu^2)}$$

and n_f is the number of quarks. Note that when $Q^2 = \Lambda^2$, $\alpha_s(Q^2) = \infty$. These equations express mathematically the properties required for the strong interaction: At low Q^2, the coupling constant is large. At high Q^2, the coupling constant is small. Notice however if there were enough quarks, the vacuum polarization would overcome the attractive potential caused by the gluons and the coupling constant would not obey the property of asymptotic freedom. There are only five quarks at our current energies so this does not present a problem at the present time.

2.2.4 3–jet events

The previous section showed that the strong coupling constant is small at high Q^2. In electron–positron annihilation the entire center of mass energy is transferred to the final state particles. Hence in electron–positron annihilation at 29 GeV center of mass energy, the quarks and anti–quarks will behave like free particles. When the separation distance between the quarks becomes large enough, confinement forces will begin to dominate the interaction. The confinement forces must become important at distances on the order the size of the proton, about 1 fm(or 10^{-13} cm).

Figure 2.7 shows a graphical view of a strong interaction. There are at least three separate regimes in the interaction:

- The perturbative regime where the quarks are free,
- the pre-confinement/confinement regime where the confinement forces begin to come into play and eventually dominate the reaction and

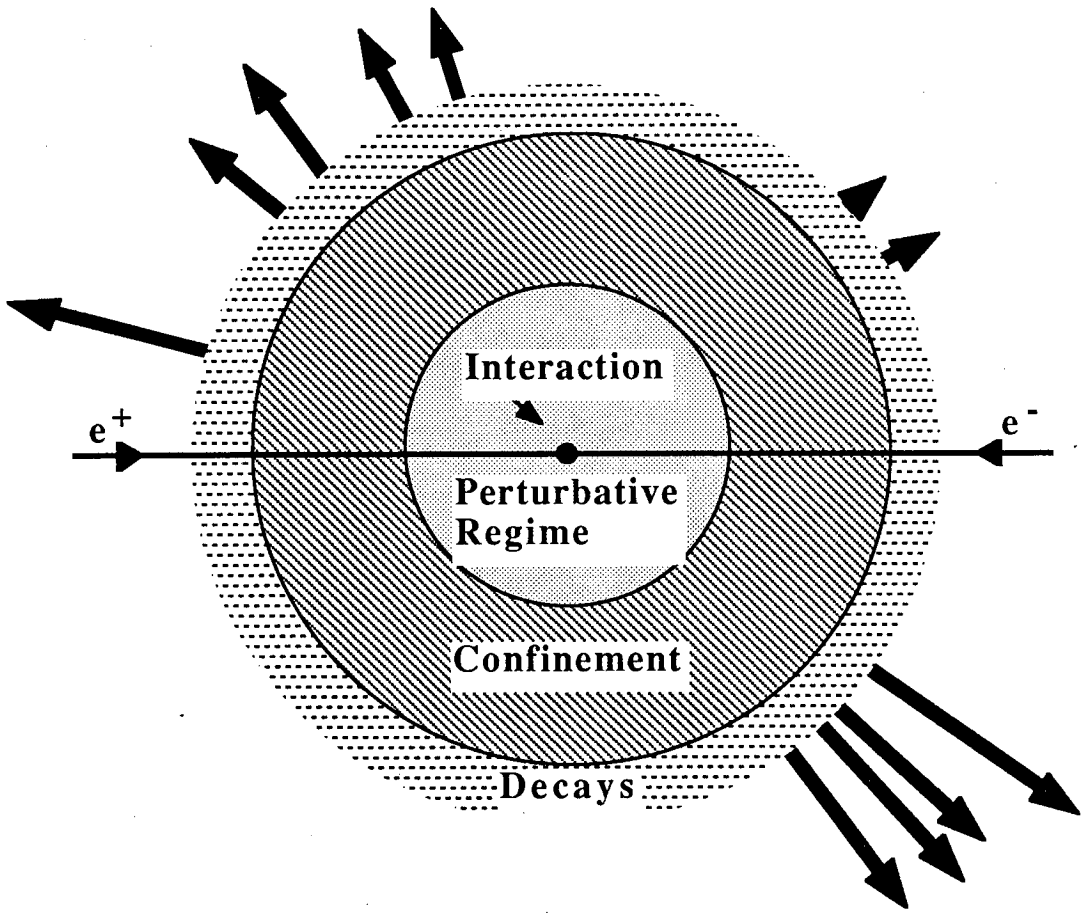

Figure 2.7: The stages of e^+e^- annihilation into hadrons. Not to scale.

- the decay regime where the primary hadrons formed can decay, strongly, electromagnetically, or weakly. We are not concerned with this later phase in particular but the data we are interested in certainly is affected by these processes.

The quark, however, has a finite probability proportional to $\alpha_s(Q^2)$ to emit a gluon. At 29 GeV, the strong coupling constant α_s is in the range of 0.1 to 0.2[16,17,18] and this process has a non–negligible probability of occurring. In

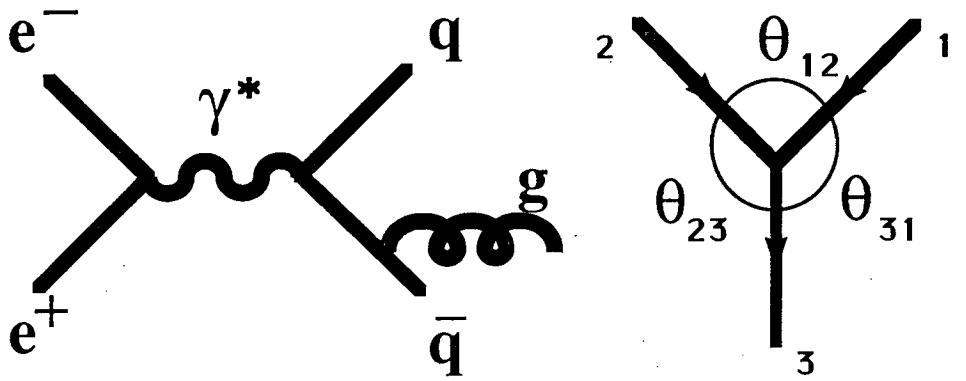

Figure 2.8: a) $e^+e^- \rightarrow q\bar{q}g$. b) The view from Center of Mass frame.

particular, the quark can emit a gluon during the perturbative stage of the interaction. This can lead to a relatively large p_t in the event and gluon hadronization separate and distinct from that of the quark.

We can use Feynman rules to describe and calculate the process shown in figure 2.8, $e^+e^- \rightarrow q\bar{q}g$. If the gluon is a spin one boson, the angular distribution and energies which the three partons will take on in such an interaction are given by the differential cross section

$$\frac{d^2\sigma}{dx_1 dx_2} = \frac{\alpha_s}{3\pi}\sigma_0 \frac{x_1^2 + x_2^2}{(1-x_1)(1-x_2)} \tag{2.15}$$

where $x_i = 2E_i/W$, E_i being the reconstructed energy of the parton and W the center of mass energy of the event and σ_0 is the cross section for the process $e^+e^- \rightarrow q\bar{q}$. We order the energies of the partons according to $E_1 \geq E_2 \geq E_3$ [19,20,21]. This differential cross section expresses the angular distribution of

the partons because

$$x_i = \frac{2 \sin \theta_i}{\sum \sin \theta_i}$$

where θ_1 is the angle between partons one and two, θ_2 is the angle between partons two and three and θ_3 is the angle between partons three and one and we assume all three partons are massless. Requiring conservation of energy and momentum leads to the above equation for x_i. Note that the sum of the three angles is 360° (see figure 2.8b).

We notice that this cross section diverges as x_1 or x_2 goes to 1. If either x_1 or x_2 goes to one, it implies that one of the parton angles goes to 180°. This implies that both x_1 and x_2 go to 1 and x_3 goes to zero by momentum conservation.

This is an example of an "infrared" divergence. We have an infinite probability to radiate zero energy gluons. It is precisely the same process as **bremsstrahlung**[1] or the radiation of low energy photons by electrons in QED. Infrared divergences in both QED and QCD must be renormalized by rescaling the mass of the initiating fermion. Even so, we still have a large probability of radiating low energy gluons in the direction of motion of the quark. Hence most three parton events are indistinguishable from two parton events because there is no way to separate the low mass collinear gluon's hadronization from that of the quark.

There also will be hard gluon radiation where it will be easy to discern the fragmentation of each of the three partons in the event. Such events have been found at PEP and PETRA[22,23] and are widely regarded as confirmation of the existence of a gluon. A vector gluon is favored over a scalar gluon as shown by comparing the angular distribution of the three parton axes with that expected from equation 2.15 [18,24].

Unfortunately, the perturbative picture is not the end of the story. The three parton axes we observe are obscured because we do not observe the primary par-

tons. Rather, the preconfinement and confinement form hadrons into collimated low transverse momentum jets traveling in the general direction of the initiating partons.

The transverse momentum in the jet is due to the Fermi motion of the partons inside of the hadrons into which they are bound. The transverse momentum of the particles relative to the jet axis is well described by a gaussian with a width of about 350 MeV[25,26,27]. The finite value of momentum transverse to the jet means that the hadrons associated with a parton are detected in a cone whose half opening angle with respect to the jet axis is about 10° at 29 GeV. This implies that in a large number of events the hadron jets overlap and we will not easily be able to separate the two partons.

We conclude this section by stating that QCD predicts the existence of events in hadronic interactions which are characterized by three collimated hadronic clusters called jets. Usually, the lowest energy jet will be initiated by a gluon since gluons are emitted by a bremsstrahlung process. However, we expect that some of the events which we characterize as having three jets really were events with two partons or events with multiple hard gluon emission. Multiple gluon events are suppressed by additional factors of α_s for each gluon. Therefore, we expect that the only appreciable contamination of our three jet sample by events whose parton count is not three will be from two ($q\bar{q}$) or four parton events ($q\bar{q}gg$).

Finally, the process shown in figure 2.8 will modify the total hadronic cross section. If we include gluon radiation into the theoretical estimate of R (see equation 2.2), R rises from ≈ 3.7 to ≈ 3.9. The measurements of R congregate around this value with rather large measurement errors[10,11].

2.3 Fragmentation

We have seen from the previous sections that QCD predicts the existence of events in which three collimated hadronic jets will be observed. We know approximately at what rate this process occurs. But we have not yet discussed the rate various particle species will be produced inside of each of the hadronic jets produced in such interactions. In fact, QCD as a perturbation theory cannot tell us much about the low Q^2 reactions because the strong coupling constant is greater than one for reactions with $Q^2 \leq\sim 4$ GeV. This regime is exactly where low mass hadrons are formed.

This is not to say that a theory of hadronization/confinement will not be developed based on QCD. However, we have to use a different approach in the interim. We base this approach on models of hadronization. All of the models of hadronization make some connection with QCD. This connection is generally fairly tenuous and rapidly diverges onto some form or other of assumption which allows us to determine the probability to form various particle types.

We will discuss the parton model and scaling violations as a prelude to our discussion of the various models of hadronization.

2.3.1 The Parton Model Revisited

We shall discuss the parton model in more depth than our quick sketch earlier. We must understand scaling in order to understand the form for the inclusive cross sections we are trying to determine.

The parton model of hadrons is based on the assertion that all hadrons can be constructed out of more elementary constituents. Figure 2.2 is a graphical representation of the parton model. This figure also includes the basic interaction: A high energy photon acts as a probe to the structure of the proton. It couples to one of the constituents of the proton which then scatters. We can use

QED to calculate the probability that this interaction occurs.

Let us consider $ep \rightarrow eX$ scattering. The interaction cross section is equal to

$$\frac{d\sigma}{dE'd\Omega'} = L^e_{\mu\nu} W^{\mu\nu} \tag{2.16}$$

where L is the electron current, W is the hadronic current and the primed coordinates refer to the final state electron[9]. We can write the most general form for the hadronic current based on Lorentz covariance of the strong interaction:

$$W^{\mu\nu} = -W_1 g^{\mu\nu} + \frac{W_2}{M^2} p^\mu p^\nu + \frac{W_4}{M^2} q^\mu q^\nu + \frac{W_5}{M^2}(p^\mu q^\nu + q^\mu p^\nu) \tag{2.17}$$

where p is the initial momentum of the proton, M is the mass of the proton and q, as usual, is the 4–momentum transferred from the electron in the interaction. We now impose the conservation of the electromagnetic current, that is

$$q_\mu W^{\mu\nu} = q_\nu W^{\mu\nu} = 0 \ . \tag{2.18}$$

This requirement determines a relationship between W_1 and W_4, and W_2 and W_5. The most general form for the hadronic current becomes [9]

$$W^{\mu\nu} = W_1(-g^{\mu\nu} + \frac{q^\mu q^\nu}{q^2}) + \frac{W_2}{M^2}(p^\mu - \frac{p\cdot q}{q^2} q^\mu)(p^\nu - \frac{p\cdot q}{q^2} q^\nu) \ . \tag{2.19}$$

We now need a theory of the proton in order to calculate W_1 and W_2. Once one assumes the proton is made of partons, it can be shown that the scaling property of the cross sections occurs. The spin of the partons affects the distribution of the final states in space only. If we assume the partons are quarks, we can use the rules of QED to derive what we expect the structure functions W_1 and W_2 to be.

The scattering cross section for $e\mu \rightarrow e\mu$ is

$$\left(\frac{d\sigma}{dE'd\Omega'}\right) = \left(\cos\frac{\theta}{2}^2 + \frac{Q^2}{2m^2}\sin\frac{\theta}{2}^2\right)\delta\left(\nu - \frac{Q^2}{2m}\right)\frac{4\alpha^2 E'^2}{q^4} \tag{2.20}$$

where m is the mass of the muon, $Q^2 = -q^2$, θ is the scattering angle of the electron in the laboratory frame and $\nu = p\cdot q/M$, M being the mass of the

proton[1,9,12]. If we assume the quark is a spin one half fermion, then the cross section for $eq \rightarrow eq$ scattering, will be the nearly the same as the cross section for $e\mu$ scattering. The only change in the cross section is due to the different charges of the quark and muon. That is, one α in the cross section transforms to αe_q^2 where e_q is the fractional charge of the quark.

One can determine W_1 and W_2 by using equations 2.16 and 2.19 to determine the ep scattering cross section. Using standard methods from QED to determine $L^{\mu\nu}$, one can derive that

$$\left(\frac{d\sigma}{dE'd\Omega'}\right) = \left(W_2 \cos\frac{\theta}{2}^2 + 2W_1 \sin\frac{\theta}{2}^2\right)\frac{4\alpha^2 E'^2}{q^4} \quad . \tag{2.21}$$

One can equate the expressions in equations 2.20 and 2.21. We find that[8]

$$2W_1 = \frac{Q^2}{2m^2}\delta\left(\nu - \frac{Q^2}{2m}\right)$$

and

$$W_2 = \delta\left(\nu - \frac{Q^2}{2m}\right) \quad . \tag{2.22}$$

This derivation of the scattering cross section has considered only one parton in the proton. We must sum over all possible partons in the proton to determine the ep scattering cross section. We define $f_i(x)$ as the probability that parton i carries fraction x of the proton momentum. We identify the high Q^2 behaviour of W_1 and νW_2 with the proton structure functions F_1 and F_2. One must also include the kinematics of the parton model. The energy, longitudinal momentum and mass of the parton is nearly x times the corresponding quantity for the proton. Overall, we find

$$\begin{aligned} F_2(\omega) &= \sum_i \int dx e_i^2 f_i(x) x \delta(1 - \frac{1}{\omega x}) \\ F_1(\omega) &= \frac{\omega}{2} F_2(\omega) \end{aligned} \tag{2.23}$$

where $\omega = 2M\nu/Q^2$. Notice that the integral over the delta function will require that $x = Q^2/2M\nu$. We conclude that the structure functions are independent

of the momentum transferred in the interactions, Q^2, but are only dependent on the fraction of the proton momentum which the parton carries, x.

The property of **scaling** of the differential cross section was derived by Bjorken and Paschos in 1969[8]. It is the basis of proof that the proton is composed of partons. By measuring the structure functions F_1 and F_2, it has been proved the partons are spin 1/2[9]. We now must consider QCD corrections to the parton model.

2.3.2 Scaling Violations

The simple view of the proton is complicated by QCD. Gluons can be emitted by each of the quarks which make up the proton. We must include interaction terms like those shown in figure 2.9.

Gluon–quark interactions which lead to scaling violations can be incorporated into our formalism by calculating the probability of each process shown in figure 2.9. If we only consider the lowest order diagram shown in figure 2.8, the modification to the structure function has been calculated to be

$$\frac{F_2(x,Q^2)}{x} = \sum_q e_q^2 \int_x^1 \frac{dy}{y} q(y) \left(\delta(1-x/y) + \frac{\alpha_s}{2\pi} \mathrm{P}_{qq}(x/y) \ln \frac{Q^2}{\mu^2} \right) \qquad (2.24)$$

where $q(y)$ is the probability of finding the quark with momentum fraction y of the proton momentum before the interaction, x is the fraction of the proton momentum the quark will carry after the interaction[9]. Notice that the first term, $\delta(1-x/y)$, recovers the original parton model calculation. The second term represents the scale violating part of the structure function.

First we notice that the scale violation is only a logarithmic function of Q^2. Next we notice that the strength of the scaling violation is proportional to α_s. This is due to our consideration of only a first order modification to the scattering

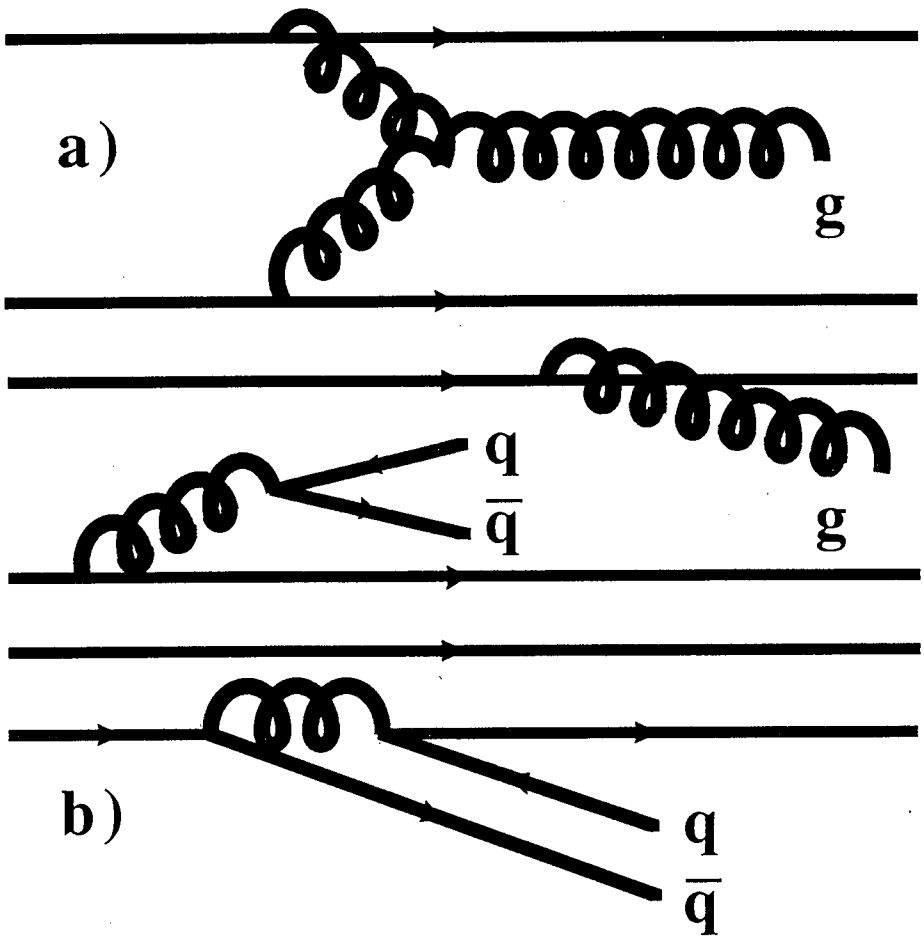

Figure 2.9: Diagrams representing some interactions also present inside the proton.

cross section due to the strong interaction. Finally,

$$P_{qq}(z) = \frac{4}{3}\left(\frac{1+z^2}{1-z}\right)$$

is one of the "Altarelli–Parisi splitting functions"[28] where $z = x/y$. This function represents the interaction of a virtual photon with quark which leads to a quark and a gluon (hence the term "splitting"). The subscript qq refers to the interaction of the photon with a quark density, $q(y)$, which leads to a quark q in the final state.

We can make the interpretation of the second more clear by rewriting equation 2.24:

$$\begin{aligned}\frac{F_2(x,Q^2)}{x} &= \sum_q e_q^2 \int_x^1 \frac{dy}{y}\left(q(y)+\Delta q(y)\right)\delta(1-x/y) \\ &= \sum_q e_q^2 (q(x)+\Delta q(x,Q^2)) \end{aligned} \tag{2.25}$$

where

$$\Delta q(x,Q^2) = \frac{\alpha_s}{2\pi}\ln\frac{Q^2}{\mu^2}\int_x^1 \frac{dy}{y} q(y)\mathrm{P}_{qq}(x/y) \ .$$

This equation expresses mathematically the statement that a quark which carries momentum fraction x could have been generated from a higher momentum quark which has radiated a gluon. We add that this is only one of the possible sources of scaling violations. There are more "Altarelli–Parisi splitting functions" describing the evolution of quark and gluon densities inside of any hadron. For example, P_{qg} represents the probability that an interaction with the initial gluon density leads to a final state quark, P_{gg} represents the probability that an interaction with the initial gluon density leads to a final state gluon and $\mathrm{P}_{qq'}$ represents the probability that an interaction with the initial quark density leads to a different flavor quark in the final state (see figure 2.10).

2.3.3 Models of Fragmentation

We now turn our attention to models of fragmentation. We are interested in how the state $e^+e^- \rightarrow q\overline{q}$ hadronizes. While the discussion in the last two sections has focused on the proton, we should note that the reactions $e^+e^- \rightarrow q\overline{q}$ and $eq \rightarrow eq$ are related. We can use the crossing relation[29]

$$\mathcal{M}_{e^+e^-\rightarrow q\bar{q}}(p_a,p_b,p_c,p_d) = \mathcal{M}_{e^-q\rightarrow e^-q}(p_a,-p_d,p_c,-p_b) \tag{2.26}$$

where $\mathcal{M}$ is the matrix element for the process and p_a, p_b, etc. are the momenta of the particles, to relate the scattering of electrons off of a proton to electron–positron annihilation into hadrons. The only difference is that in the case of the

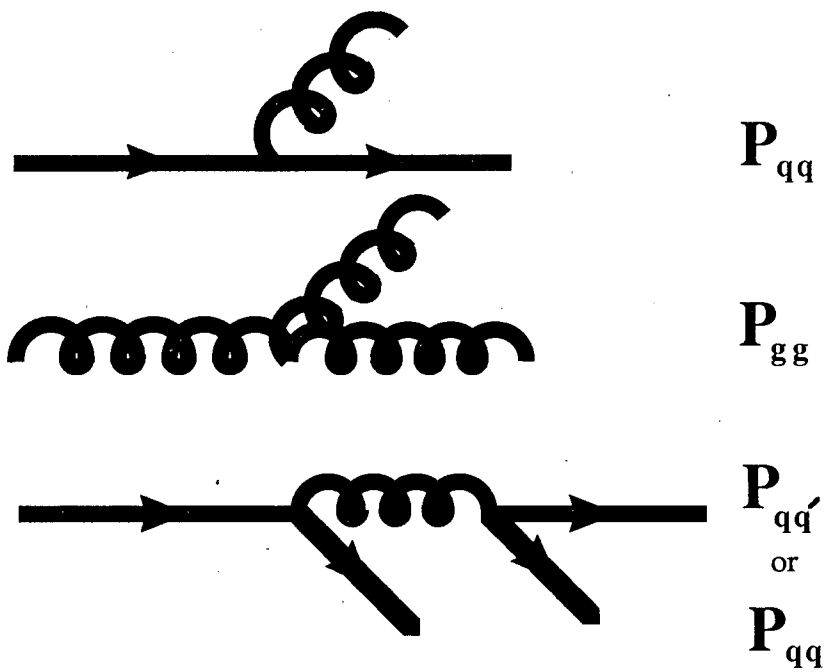

Figure 2.10: Interaction diagrams representing each of the "Altarelli–Parisi splitting functions".

protons there are two other spectator quarks. Even so, scaling of the differential cross section will still be present.

We must introduce a new quantity, $D_q^h(z,Q^2)$, which is the probability that a hadron h contains the debris from quark q and carries the fraction z of its energy. This groups the theoretical uncertainty about fragmentation into one function. In this way the D functions are entirely analogous to the f functions in electron–proton scattering.

The scattering cross section for this process is given by

$$\frac{d\sigma}{dz} \approx \beta\sigma_0 \sum_q D_q^h(z,Q^2) \tag{2.27}$$

where σ_0 is the total cross section of $e^+e^- \rightarrow q\overline{q}$ [30,31,32]. Scaling implies that

$$\frac{1}{\beta\sigma_0}\left(\frac{d\sigma}{dz}\right) = \sum_q D_q^h(z,Q^2)$$

really has no dependence on Q^2. Hence, the fragmentation functions D_q^h are only functions of z.

Energy and probability conservation lead to a constraint on D, [25,33]

$$\sum_{\text{hadrons}} \int_0^1 z D_q^h(z)dz = 1$$

which is analogous to a similar property for the f functions in ep scattering:

$$\sum_i \int_0^1 x f_i(x) = 1 \ .$$

These two equations state that the total fractions of energy (momentum in the case of f) carried away by the resulting particles must total one. The other constraint on both D and f is that scaling holds. This means that D is solely a function of z. The $D_q^h(z)$ functions are often parameterized as

$$D_q^h(z) = A_h \frac{(1-z)^n}{z} \tag{2.28}$$

where n and A_h are parameters. By integrating $zD_q^h(z)$, we find that

$$A_h = < z > (n+1)$$

where $< z >$ is the average z for that particular hadronic species.

Generally, the models of hadronization simply assume the above behaviour of the fragmentation functions. This is an expression of the fact that confinement is incalculable at some level. Therefore, we parameterize the behavior of fragmentation functions according to scaling and leave it at that.

All viable current models of hadronization use Schwinger [34] $\mathbf{1} \oplus \mathbf{1}$ QED as a model for confinement. In $\mathbf{1} \oplus \mathbf{1}$ QED, as a high energy electron–positron pair separate, an induced polarization charge is formed which neutralizes the electric field between the two initial particles. The polarization charge neutralizes the electric field by combining with the initial electron and positron and forming two separate neutral electron–positron bound states. This is exactly analogous to what we believe the process is in QCD. However in QED, it is possible to solve the problem exactly.

Currently, there are three viable models of hadronization. Only one of the models uses QCD in a very direct way by generating parton showers. The other two models are not as closely connected with QCD. We shall now briefly describe each model.

Independent Fragmentation

Feynman and Field in 1977 [25] produced a Monte Carlo model of fragmentation which could explain the jet structure of events observed at SPEAR. They hypothesized that fragmentation can be viewed as a cascade process where $q\overline{q}$ pairs are formed out of the vacuum. Mesons are then formed by the Schwinger mechanism outlined above.

We begin with an initial $\alpha\overline{\alpha}$ pair of quarks where α refers to a specific flavor of quark. As the $\alpha\overline{\alpha}$ pair separate, a color field will arise between them. Presumably, once the energy in the field becomes large enough another pair of quarks, say

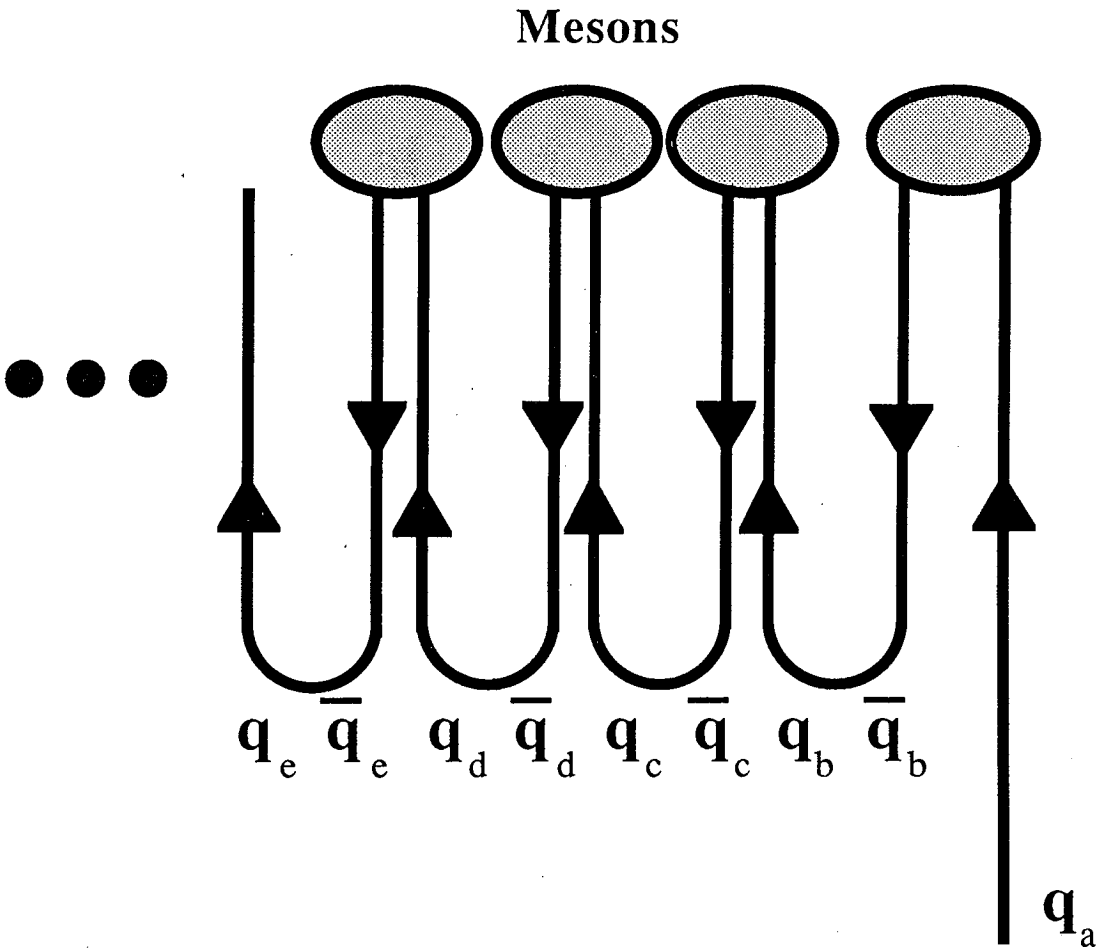

Figure 2.11: Graphical representation of independent fragmentation.

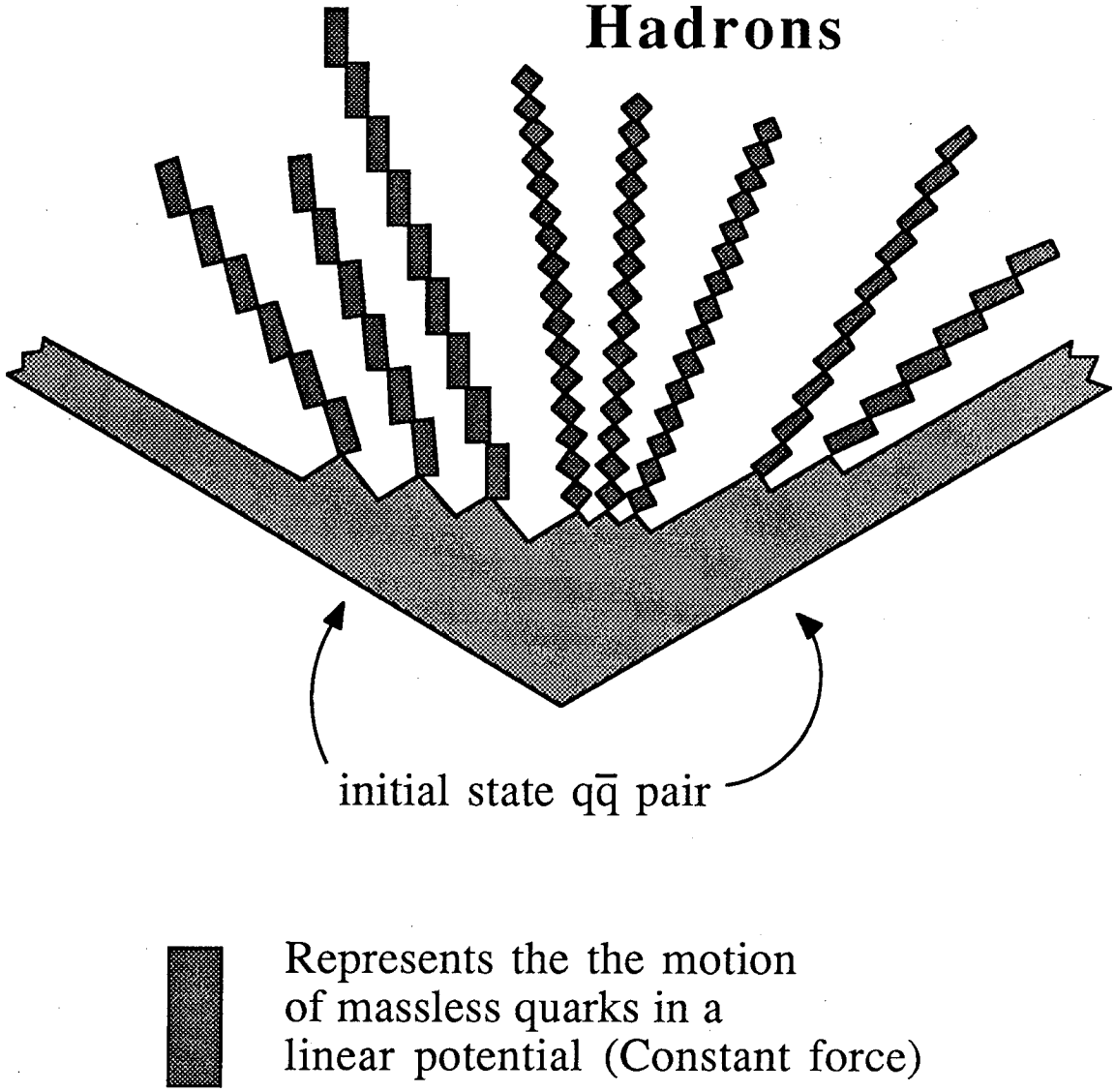

Figure 2.12: Graphical representation of LUND string model.

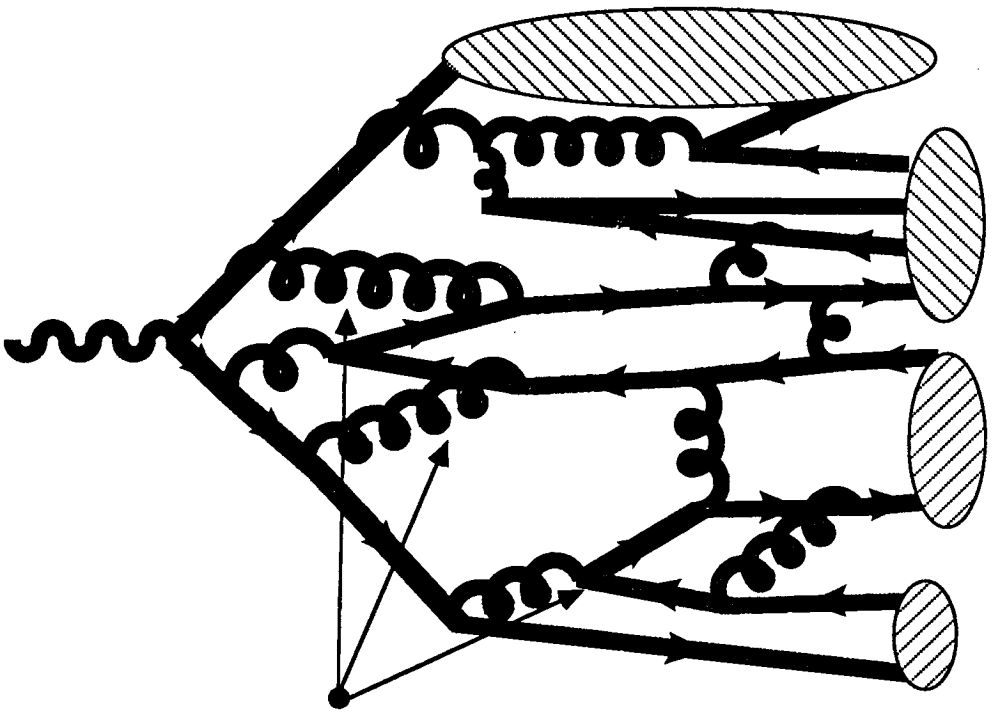

QCD shower forming the
final state.

The formation of Colorless clusters
in the Cluster fragmentation model.
The Clusters subsequently decay to
hadrons.

Figure 2.13: Graphical representation of Cluster fragmentation.

$\beta\overline{\beta}$, can be formed.

The Feynman and Field model starts with the quark and then separately the anti–quark. The $\beta\overline{\beta}$ pair is formed next to the initial quark (or anti–quark as the case may be). A meson is formed by pairing α with $\overline{\beta}$. This meson will get a random fraction, η, of the initial quark energy, W_0. The principal unknown is the probability weight as a function of η. This function is labeled $f(\eta)$. Feynman and Field define this function as

$$f(\eta)d\eta \;=\; \text{The probability that the meson leaves momentum fraction } \eta \text{ to the remaining cascade.} \tag{2.29}$$

The probability function is simply parameterized as

$$f(\eta) = 1 - a + 3a\eta^2$$

where a is a parameter to be fit. Notice that the constant 3 is fixed by the requirement

$$\int_0^1 f(\eta)d\eta = 1$$

and choosing the power of η to be two. The power of η is chosen by consideration of the fragmentation function $F(x_f)$ which equals[25]

$$F(x_f) = f(1 - x_f) + \int_{x_f}^1 f(\eta)F(x_f/\eta)d\eta/\eta \ . \tag{2.30}$$

The quantity $F(x_f)$ is the mathematical statement that a hadron of momentum x_f could have been formed directly from the primary quark (probability that we get a hadron with momentum fraction $1 - x_f$ is $f(1 - x_f)$) or could have been formed after a series of $q\overline{q}$ pairs had been formed before it. The probability that the previous cascades left exactly the correct amount of momentum is given by $F(x_f/\eta)f(\eta)$. Since η could be any number from x_f to 1, we get the rather imposing integral equation shown above. Finally, the function f is a function only of η because of our assumption of scaling.

Transverse energy is now added to each meson. The meson is given p_t according to a gaussian distribution whose width is about 350 MeV.

After the first meson has been formed, the remaining momentum in the system is ηW_0. We then repeat the same process only using this momentum as the starting point and β as the initial quark. This process continues recursively until the momentum given to a meson drops below a minimum threshold. A graphical representation of the scheme is shown in figure 2.11.

We have simplified the explanation of Feynman and Field's model by confining ourselves to one flavor when we determined $F(x_f)$. Actually, we have to consider all possible flavors and the relative probabilities of pulling each of the different flavors out of the vacuum. Also we have neglected the meson spin. Yet including these details will not solve some of the basic problems with the model.

First, momentum and energy are not conserved. In independent fragmentation models these quantities are not conserved even though at each vertex we conserve energy. The problem is that we consider the quark and the anti–quark formed in the interaction $e^+e^- \rightarrow q\overline{q}$ separately. A single massless object (the quark or the anti–quark) materializes into many massive hadrons in Feynman and Field type models. One cannot simultaneously conserve momentum and energy in such a situation.

Moreover, gluon radiation is not included. One has to put gluons in "by hand" by requiring that a certain fraction of the events have gluon radiation. In this case, the gluon is fragmented exactly as the quarks. Finally, there are no baryons in the Feynman and Field model. We might add that these defects were pointed out by the authors themselves. They never meant their model to be a precise statement of nature but rather they wanted it to reflect enough of nature so that experimental measurements could be placed into a framework and normalized.

Hoyer[35] and Ali[36] have implemented fixes to the Feynman and Field model to solve these problems. The precise details of their implementations can be found in their articles. However, independent fragmentation as a model of fragmentation has been ruled out by the observation of the "LUND string effect" which shall be described in the next section.

LUND string model

The LUND group's string model of hadronization takes a slightly different approach to fragmentation. They base their hadronization scheme on manifest Lorentz covariance and putting the quark and anti–quark onto equal footing. They use directly the color field between the quark, anti–quark pair.

We begin by considering fragmentation in two dimensions. We can assume that the quark and anti–quark are traveling in the $+z$ and $-z$ directions respectively. They assume that a potential linear in the separation distance arises as the quark and anti–quark separate. When the distance becomes large enough a $q\overline{q}$ pair will be formed.

So far string fragmentation is exactly the same as Feynman and Field fragmentation. Here is where they diverge. We first note that the color field arising in the separation of a $q\overline{q}$ can be thought of as being linear in the separation distance. Models of Charmonium with a linear potential have done a reasonable job of predicting the spectrum of the $c\overline{c}$ bound states [37,38]. Two massless bosons, traveling at the speed of light inside a constant force field, will oscillate about their center of mass. This is analogous to the motion of a spring.

If one stretches a spring too far, it will break or deform. We know, that if the spring analogy is to work in the strong interactions, a mechanism must be invented to insure that if the spring breaks, color will still be confined. Here the LUND group makes the ansatz that the Schwinger model insures color con-

finement. To wit, when the spring breaks, the $q\overline{q}$ popped from the vacuum, is configured to form to two mesons ($q\overline{q}$ pairs) with the initiating $q\overline{q}$ pair. Hence, the color field between the newly created particles is neutralized thereby confining color to the two *new* springs. These two new springs are then be treated in an equivalent manner as originating spring. LUND calls the springs, "strings". The fragmentation process continues recursively until we no longer have enough energy in the strings to supply the minimum transverse energy required to form the appropriate hadron. We show the graphical representation of the string model in figure 2.12.

This approach has a great appeal (even if it has nothing to do with reality). First, by treating $q\overline{q}$ pairs equivalently, the theory can be made Lorentz covariant. The mechanism is the same as in the Schwinger model. While a single massless object cannot materialize into massive particles, two massless objects can. There are no asymptotic fermion states in Schwinger's model. Furthermore, the spectrum of the only solution contains a single stable neutral boson with mass

$$m = \frac{g}{\sqrt{\pi}}$$

where g is the coupling constant between the electrostatic current and the fermions. What has happened is that the energy contained in the field between the two massless objects is manifested as a "mass". With LUND strings, the constant g becomes the strength of the linear potential between the quark and anti–quark.

Gluon radiation and baryons, are still problems. Gluons are added as kinks on the string. The system is fragmented as two separate strings, each terminated on the kink. This has a measurable consequence. The event center of mass frame (which is the same as the laboratory frame in electron–positron annihilation) and the string rest frame are related by a boost. Because of the boost, particles are observed to be produced closer to the jet axis in the event center of mass frame than would be the case if each jet fragmented separately. This implies that the

string model would produce fewer particles between the jets in the event center of mass frame than independent fragmentation would. A deficit of particles relative to independent fragmentation in fact has been observed in 3–jet events and is called the **LUND string effect**[18,39].

Baryons are added by including the possibility of forming a diquark, anti–diquark pair from the vacuum. The diquark is attracted to the quark side and the anti–diquark is attracted to the anti–quark side of the fragmenting string. This forms a baryon, anti–baryon pair which neutralizes the color field. Fragmentation of the two strings is then continued just as before. This explanation is slightly unsatisfying since stable diquark, anti–diquark pairs could be directly produced in e^+e^- annihilation and hence show up as an increase of R.

Another more promising explanation is due to Casher, Neuberger and Nussinov [26]. They speculate that from time to time $q\overline{q}$ pairs are pulled from the vacuum with the wrong colors to neutralize the color field. States with 4 or more quarks are then formed. Baryons are then the possible result after another $q\overline{q}$ pair is created in the color field. We must conserve baryon number in strong interactions. This is a constraint on any model of baryon production. The scheme of Casher *et. al.* does in fact satisfy this constraint. However the baryon and anti–baryon may not be "adjacent". That is sometimes the color field will be neutralized by the production of mesons between the baryon anti–baryon pair. There is some evidence that this occurs[40].

Baryon production is suppressed because usually the color field is neutralized with the creation of $q\overline{q}$. And even if the color field is not neutralized, it is possible to form mesons and not baryons.

We note that in the same paper the authors derived the suppression of p_t for particles pulled from the vacuum. They derived that if the force field between the quark and anti–quark is linear, the probability of pulling a quark, anti–quark

pair of mass m from the vacuum with transverse momentum p_t to the color force field is proportional to

$$\exp(-c\mathrm{m}_\perp^2) \tag{2.31}$$

where $\mathrm{m}_\perp^2 = p_t^2 + m^2$ is the transverse mass, m is the rest mass of the quark and c is related to the strength of the linear potential arising inside the flux tube. This is the mathematical explanation for why the distribution of the transverse momenta of particles produced in hadronization is a gaussian.

Cluster Model

This model is the most directly connected to QCD of the three. Recall the evolution of quark density that one obtains by considering the lowest order eq scattering. The equation 2.24 hints at the ability to recursively find the quark density inside the proton. Equation 2.24 is much like equation 2.30, the equation which describes the Feynman–Field cascade of quark, anti–quark pairs [41].

Figure 2.13 shows the situation graphically. We begin by considering either quark line. We use the Altarelli-Parisi splitting functions to determine the probability and at what energy gluon emission occurs. When a gluon is emitted it is added to the list of particles to keep track of. We then restart the process with all the new particles we have. Notice that gluons can also couple to other gluons.

The cascade continues until the energy characteristic of the interaction drops below a cut off on the order of 1 GeV. Notice that this is well below the energies at which we think perturbation theory is valid. Partially this problem is alleviated by considering higher order diagrams in the calculation of the Altarelli–Parisi splitting functions than the first order diagram that we used as an example. In particular, the Leading Log Approximation can be used to sum certain classes of diagrams to all orders.

The real problem, however, is the assignment of the results of the shower

calculation into color singlets. Low energy gluons are decayed into light $q\overline{q}$ pairs. Then adjacent quark and anti–quark lines are assigned opposite colors, guarantying that the clusters are colorless[41,42].

Baryons are added by allowing the possibility of producing diquarks. The colorless clusters are decayed by a simple isotropic phase space model. This is perhaps the weakest point of the cluster models as now formulated. Clusters if they produce a baryon, must also produce an anti–baryon. If the cluster contains a baryon and anti–baryon, there is not much energy left over for any other hadrons. Hence, the center of mass of the baryon and anti–baryon is to good approximation the rest frame of the cluster.

The TPC collaboration has measured the angle between the baryon, anti–baryon pair and the jet–axis for that cluster in the baryon, anti–baryon center of mass. If the decay of the cluster were isotropic, one would expect that all angles would be equally populated. Not so, the decay prefers the direction of the jet-axis[40].

Some Concluding Remarks

The preceeding section completes our survey of the strong interaction. The chapter can be summarized as follows:

- All hadrons can be described as being composed of quarks. Quarks are spin 1/2 fermions which carry baryon number 1/3, fractional charge and carry color. Hadrons are colorless objects.

- The Parton Model predicts that the differential cross section, $\frac{1}{\beta\sigma_0}(d\sigma/dz)$, should not be a function of the energy of the interaction. Instead the differential cross section is a function solely the ratio of Q^2 to $2M\nu$.

- QCD is the theory of the strong interaction. It predicts that at low energies we will have very large interactions which lead to confinement. At high energies the interactions between quarks decrease thereby showing that the observation of scaling and QCD are not inconsistent.

- Gluons are the massless mediators of the strong interaction. There are eight different gluons corresponding the **8** representation of SU(3).

- We expect, by scaling, that the fragmentation function D_q^h is a function solely of z in electron–positron annihilation.

- Each hadronization model has its own assumptions and problems. Usually they are dependent on a whole series of parameters which must be fixed by a comparison of the model to the data. For instance the following quantities must be parameterized and optimized by comparison of the Monte Carlo predictions to the data: Ratio of vector to pseudo–scalar mesons, the probability of pulling various quark flavors from the vacuum, the probability for producing a meson at a particular fraction of the initiating quark (or string) energy, the relative probability of diquarks as opposed to quarks etc.

In closing, baryons are the most compelling sector to examine when testing hadronization models. This is because the effects of decay are reduced with the baryons. There is less Q in the reaction baryon $\rightarrow$ proton than in most meson decays to pions or kaons. This implies that more information about the primary process is preserved by protons than by pions or kaons. However, baryon production is suppressed because the higher the mass of the produced hadron, the more its production is suppressed(cf. equation 2.31).

Chapter 3

The PEP–4 Detector

The advent of colliding beam facilities has led to a series of "4π" detectors. The idea of 4π detection is to detect all particles emanating from the reaction. In e^+e^- collisions one possible reaction results in the total annihilation of the initial state particles, leaving energy in the form of a virtual photon which must "turn into" matter. Also the e^+e^- colliding beam is an excellent source of photons, so the interactions between two virtual photons can be studied.

Typically a 4π detector at a colliding beam facility consists of

- An "inner" charged particle detector. This detector is placed as close to the beam as possible and is used to

  1. get as large a lever arm as possible for tracking particles,
  2. provide a fast trigger to read an event,
  3. detect short lived particles and
  4. locate the vertex at which the reaction took place.

  Some 4π detectors use silicon strip detectors or specialized gas proportional chambers for highly precise measurements. However, our inner charged particle detector is a standard drift chamber.

- A central tracking chamber to provide the best tracking of charged particles in the system. This can include standard drift chambers, Cherenkov

imaging detectors or Time Projection Chambers.

- An outer charged particle detector to help with triggering the detector and charged particle tracking. Usually, this detector is a proportional chamber. The electronics can be built to provide Time of Flight information. A Time of Flight system can be used to distinguish between particles up to ~ 2 GeV at modest cost. However, our outer charged particle detector is used only for triggering and tracking of charged particles since the TPC already provides excellent particle identification.

- A magnet to bend the charged particles so the momentum of charged particles produced by the interaction can be measured. We must insure that the detectors inside of the magnet are made of materials which are permeated by a magnetic field (iron is out).

- A calorimeter to detect the neutral energy produced in the interaction. There are two types of calorimeters:

  1. electromagnetic calorimeters to detect photons and electrons and
  2. hadronic calorimeters to detect charged pions, kaons, protons, along with the long lived neutral hadrons, K^0's and neutrons.

  About one third of the energy produced in an e^+e^- annihilation is neutral. Most of the neutral energy is carried away by photons produced in the decay of π^0's. Hence it is most important to have an electromagnetic calorimeter with good photon reconstruction ability. Also, electrons produced in the interaction need to be detected. But if the calorimeter is a good photon detector, it will also be a good electron detector. This is because an electron's interactions with matter are nearly the same as a photon's.

- A muon detector. We detect a muon (μ) by placing many interaction lengths of material before a proportional wire chamber. Since μ leptons only weakly interact with matter, they penetrate the material; while the remaining hadrons, electrons and photons are stripped away by interactions with it.

- End Cap plugs fill out the 4π geometry. These detectors look at small angles and detect forward going particles. They can include calorimetry, muon detection, scintillators, tracking chambers, sodium iodide, lead glass etc.

However, because of cost and space restraints, there is no way to fully instrument all of the solid angle with equal capabilities. This has led to different philosophies on how to make a detector system. Some systems are designed to measure a particular interaction only. Other systems try to detect everything resulting from e^+e^- interaction. Our goal is to have good solid angle coverage augmented by an extremely powerful central detector with the ability to separate different particle types in order to study fragmentation.

Our central detector is called the Time Projection Chamber (TPC). It has the ability to measure energy loss of a particle as it traverses the gas volume of the detector. It simultaneously measures the momentum, thereby determining the mass of the particle.

The TPC is cylindrical in shape. It is 2 m long and 1 m in radius. At each end of the cylinder are six proportional chambers called **sectors** which collect the ionization produced by the particle [43]. A uniform electric field is generated to drift the ionization produced by the track along the z axis of the gas volume to the sectors. A magnetic field is generated to measure the curvature of a charged particle track and hence the momentum of the particle. We must have the electric field and magnetic field *parallel* because of the long length drift geometry of the

TPC. Otherwise the ionization electrons would be pushed by $E \times B$ forces. The more $E \times B$ forces which act on the drift electrons, the more imprecise our position and hence momentum resolution is. If the $E \times B$ forces became too large, we wouldn't even be able to detect the drift electrons with this cylindrical geometry. A by product of making the magnetic field parallel to the electric field is the curling of the drift electrons around the magnetic field lines. Therefore the diffusion perpendicular to the drift direction is reduced.

The next sections will describe each of the detector elements which make up the PEP–4 detector system.

3.1 The PEP–4 Detection System

In the introduction to this chapter, we discussed the basic layout of all e^+e^- colliding beam detection systems. Figure 3.1[44] shows the layout of the PEP–4 detection system.

First, there is an aluminum beam pipe. The pipe has a radius of 8.5 cm and is designed to hold the vacuum of the beam line. We position a pressure wall at 11 cm which holds the 8.5 atm pressure of the TPC. Following the pressure wall is a cylindrical drift chamber. The inner radius of the chamber is 13 cm from the beam and the outer radius is 19 cm from the beam. This chamber is operated with the same gas at the same pressure as the TPC.

Now come the components of the central tracker, the TPC. First, we must create the uniform electric field which is parallel to the beam. This is done by the **inner** and **outer field cages**. The inner field cage is hexagonal in shape and the normal to the plane of any one fin measures 20 cm to the beam. This is followed by the TPC which occupies the space 22 cm to 100 cm from the beam. Outside of the TPC, we place the outer field cage. The final component of the field definition elements is a fine mesh stainless steel screen placed at the mid–

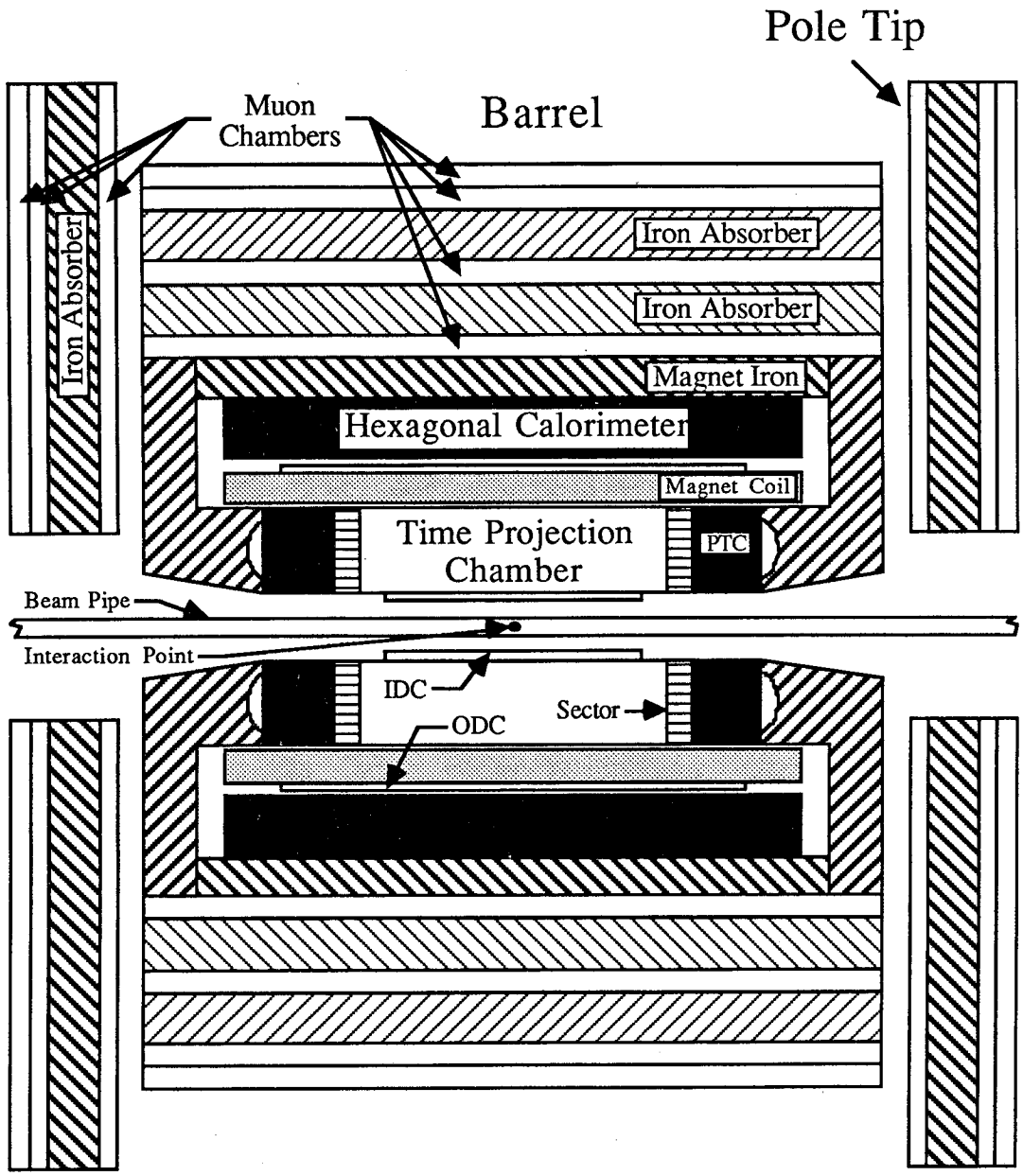

Figure 3.1: The PEP–4 detector.

plane of the TPC. The screen is placed at high voltage. The sectors are grounded. The field cage is a series of precision resistors which divide the voltage to make a uniform electric field inside the drift volume of the TPC.

A solenoidal magnet is used to create the 4 kG magnetic field parallel to the beam. The inner radius of this magnet is 102 cm from the beam. The inner radius of the magnet also has the task of completing the containment of the 8.5 atm TPC gas. The magnet is followed by an outer drift chamber located at 119 cm to 124 cm from the beam.

A set of trapezoidal electromagnetic calorimeters arranged to look like a hexagon looking down the beam axis (the "hex" calorimeter) is located from 125 to 170 cm from the beam.

Finally outside of the hex calorimeters lies an alternating sequence of iron and proportional wire chambers to provide muon detection. The final muon detector is about 310 cm from the beam interaction point. The first layer of iron is placed directly after the hex calorimeters and serves not only as a hadron absorber but also as the magnet return leg. Each iron segment is about 35 cm in length. The last two layers of muon chambers are placed with no iron between them at all. The wires of the last layer of muon chambers are arranged perpendicular to the wires in the previous three layers.

Our endcap plug consists of a "pole tip" calorimeter, which covers from about 11° to 41° in angle from the beam, and a set of muon door detectors which provide forward muon detection. The PEP–9 detection system provides a low angle detection capability and is located forward of the muon "door" detectors. The primary purpose of PEP–9 is to study the interactions of two virtual photons. Since two photon interactions are not the subject of this thesis, the PEP–9 system will not be described further here.

The inner drift chamber (IDC) is a fairly standard proportional wire chamber

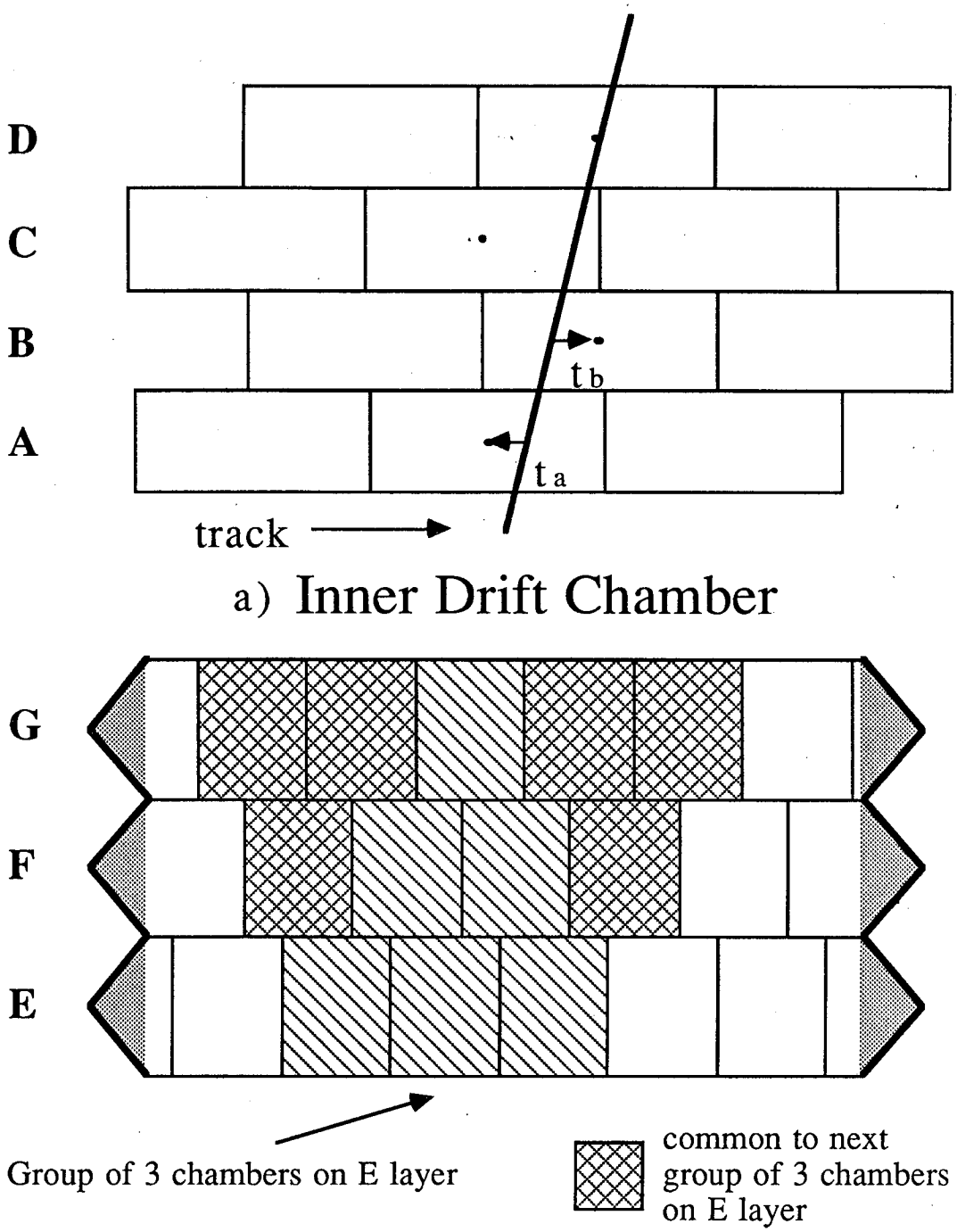

Figure 3.2: Diagram of a) The Inner Drift Chamber and b) the Outer Drift Chamber.

with 60 wires in each of four concentric layers. The layers are labeled A, B, C and D. The wires are strung axially (along the beam direction) and layers A and C are rotated with respect to layers B and D by one half the wire spacing. We do this so that the sum of the time of arrival on the A and B layers is constant for stiff tracks no matter what angle the track comes out with respect to the beam[45]. A diagram of the inner drift chamber is shown in figure 3.2a. The constant sum of the arrival times makes it possible to make a fast trigger on high momentum tracks. We will describe the full trigger system later in this chapter. The detector is designed to be operated with the same gas environment as the TPC. Hence this detector operates with a 8.5 atm mixture of 80% argon and 20% methane gas.

We have been unable, however, to use the detector for tracking purposes for two primary reasons:

1. Early in the data taking cycle, wires began to spark. This necessitated turning off sections of chamber wires. Ultimately the wire voltage was reduced and the electronic gain was increased to compensate for the reduced gas gain. This reduced the position resolution of the IDC.

2. It has been hard to calculate reliably the relative time delay between different wires. Without removing this relative delay, we cannot determine reliably the location inside the drift cell of ionization left by the particle.

The field cages are simply a plastic with high bulk resistivity, G10, with metal strips placed every 4 mm. We placed a precision resistor between each pair of metal strips (see figure 3.3). The sectors are mounted at the ends of the TPC volume and are grounded. We placed a metal screen at the midpoint of the TPC gas volume ($z = 0$). We energize the screen to a potential of -75 kV. The metal strips act as voltage divider where the voltage linearly and uniformly steps from

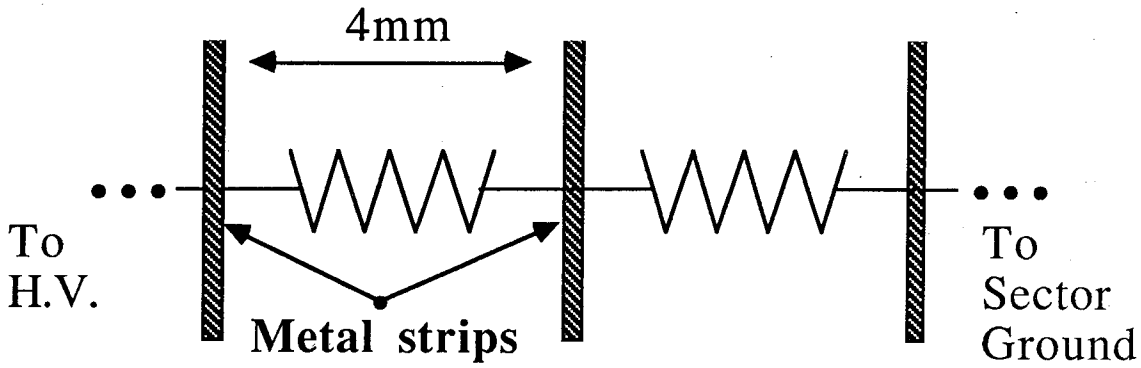

Each metal strip is wound around a hexegonal frame. There are two frames: one is on the inner radius of the TPC (the inner field cage) and the other is on the outer radius of the TPC (the outer field cage).

Figure 3.3: Schematic of a field cage.

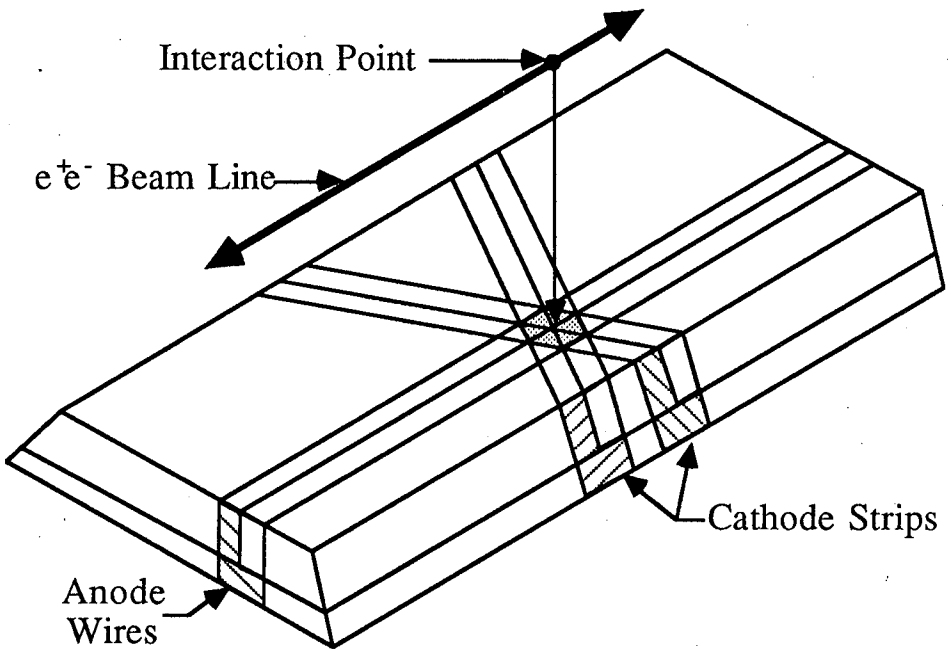

Figure 3.4: HEX calorimeter module. Courtesy Dr. William W. Moses.

-75 kV to zero. Hence the potential on the boundary of the TPC is

$$\phi(\vec{x}) = \frac{-75.\ \text{kV}}{1.\ \text{m}}(100.\ \text{cm} - |\,z\,|)$$

where z is the coordinate along the z axis. The unique electrostatic solution to this boundary value problem is a uniform electric field everywhere inside the volume of the TPC[14]. The electric field is

$$\vec{E} = \begin{cases} E_0\hat{z} & z > 0 \\ -E_0\hat{z} & z < 0 \end{cases} \tag{3.1}$$

where $E_0 = -750.$ V/cm and $\hat{z}$ is the unit vector in the z direction.

The outer drift chamber (ODC), like the IDC, is azimuthally symmetric. However, the ODC has 216 wires strung in each of three separate layers labeled the E, F and G layers. The wires are strung axially and are 304 cm long. Plastic I-beams delimited the drift cells and the grounded cathode surface of the cell is the aluminum sheet which makes up the body of the detector. Figure 3.2b shows the cross section of the ODC perpendicular to the beam direction. Each of the detector layers is rotated with respect to the other layers so that tracks cannot pass through dead areas in all three layers. The ODC is constructed in six segments and is mounted on the magnet coil. Finally, the ODC operates on the exhaust gas of the TPC at atmospheric pressure[45].

The hexagonal calorimeters have 40 layers of 0.25 radiation length thick aluminum–fiberglass laminate alternating with a 6 mm thick gas gap[46]. Sense wires are strung every 5 mm inside the gas volume. The aluminum is cut into slabs and forms the cathode plane. The aluminum slabs are placed at $\pm 60°$ with respect to the wires so a three dimensional picture of the shower could be developed. Nylon wires are strung every 10 mm normal to the sense wires (see figure 3.4). The Nylon wires break the gas volume into 5 mm $\times$ 10 mm geiger cells because of the fact that the nylon wire provides a dead area which ends any shower induced by the passage of a charged particle. The gas volume is filled

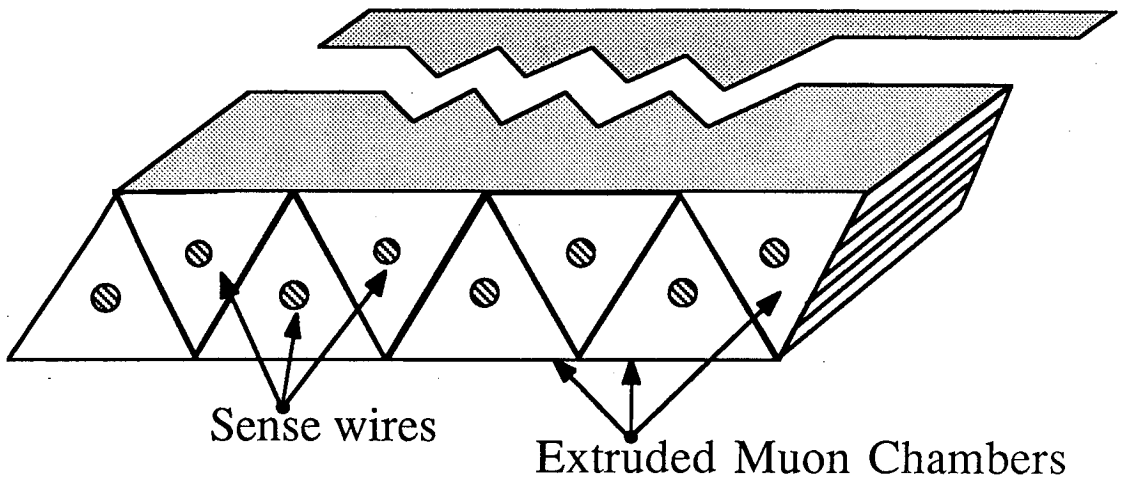

Figure 3.5: Cross section of muon chamber element.

with 80% Argon and 20% Ethyl Bromide mixture. However, we lost two modules during the running due to the formation of Aluminum Bromide.

The muon chambers are proportional chambers whose bodies are made of aluminum. Each of 404 separate muon chambers has seven, eight or eleven triangular tubes extruded from the aluminum. The ends of the chamber form an equilateral triangle. The base of the triangle measures 8.2 cm in length and the chambers range in length from 0.82 m to 7.35 m. We ran the chambers at 2400 V in the proportional mode[47]. The cell efficiency is 99.6% at this voltage in our 80% argon 20% methane gas mixture at one atmosphere pressure (see figure 3.5). The efficiency of the cell dropped off only within 5 mm of the apex of the chamber despite the triangular shape of the cell. We defined the two cell efficiency as the probability that an adjacent muon cell will fire. The two cell efficiency of the chamber is about 65%. Finally, the position resolution of the

muon chamber is $700\mu m$. The excellent position resolution and high efficiency allowed us to track particles independently with the muon chambers[48].

There are four layers of chambers in the barrel region of the detector. The forward region of the detector has 3 layers of muon "door" detectors. The first two muon door detector layers have 35 cm of iron between them. The last two muon door detector layers have no iron between them. However, the wires in the first two layers ran vertically and the wires in the last layer ran horizontally. This is in complete analogy with the muon barrel detectors.

But the heart of the PEP–4 detector system is the Time Projection Chamber.

3.2 The TPC

The idea behind the TPC is simple; measure the momentum of a track and simultaneously make multiple measurements of the energy lost per unit length of gas volume traversed (dE/dx) by that same track. We measure the momentum of a track by measuring the position of the track at several points inside the chamber. Measuring the momentum and the energy loss of the track simultaneously measures the mass of the particle since the energy loss is a function of velocity. Additionally, the TPC has the ability to measure the coordinate along the beam axis. This gives the TPC the ability to determine a three dimensional view of a track, helps reject beam–gas events, and determines a good vertex position. Figure 3.6 is a diagram of the Time Projection Chamber.

We used the concept of a "long length" drift chamber in building the TPC in order to measure each track's parameters. If we built a long traditional drift chamber with many layers of wires strung parallel to the beam, we would have had problems of electrostatic stability and gain uniformity along the wires. We would also have problems measuring the z coordinate. Using a long length drift chamber solves the above problems in an elegant way[49,50].

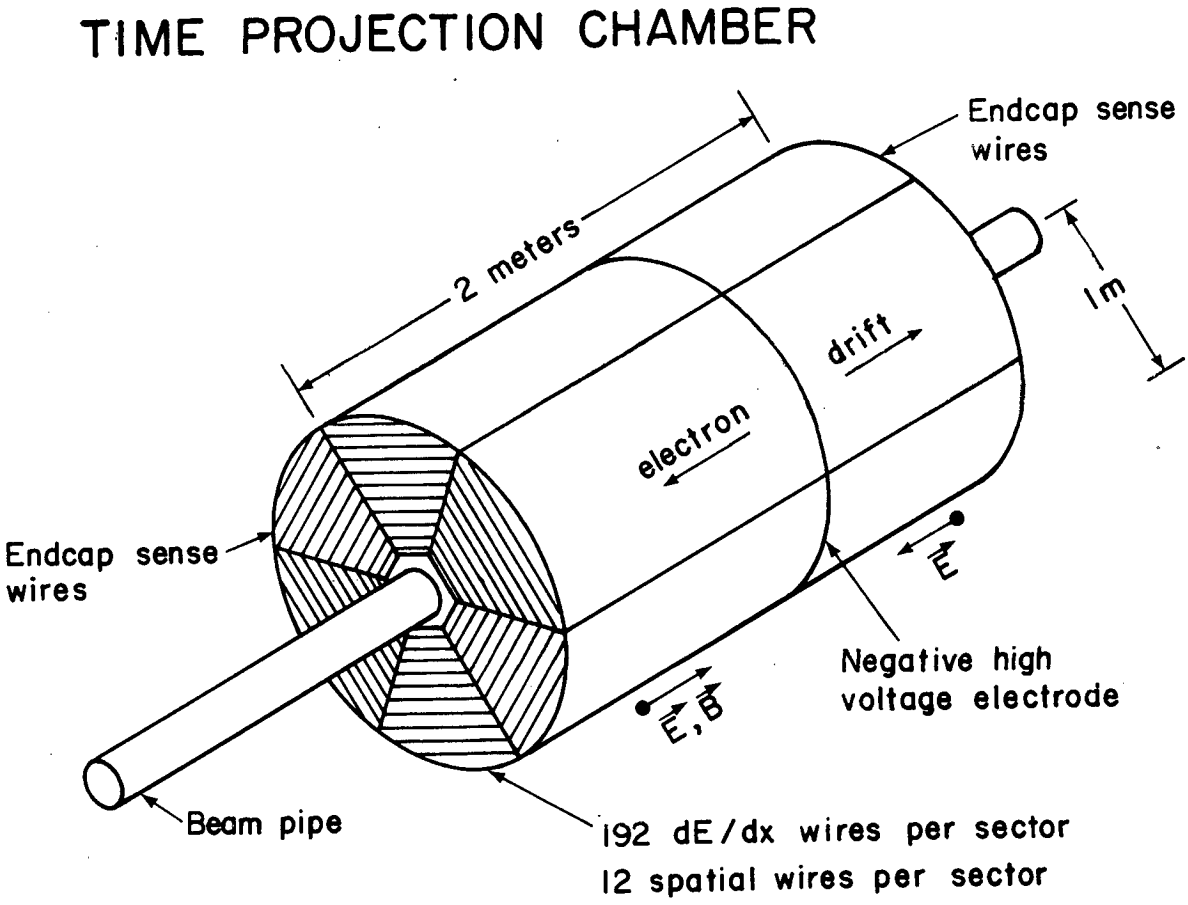

Figure 3.6: The TPC central detector.

We measure the z coordinate by measuring the time it takes for ionization caused by the particle traversing the gas volume to arrive at our detection plane (at the end of the drift in z). Electrostatic problems and gain uniformity problems are reduced because we can divide up the detection plane in a way we choose and hence can reduce the maximum wire length and the average wire length considerably.

But we pay a price for this geometry. We need an electric field to drift the ionization electrons produced by a track. The electric field must be along the z axis. We also need a magnetic field to measure the momentum of the particles. The TPC has drift lengths of up to one meter for the ionization electrons. Therefore the electric and magnetic field must be parallel or else the electrons will be deflected by $E \times B$ forces. The larger the $E \times B$ force, the worse our position and hence momentum resolution will be. A reasonable figure of merit is that the position measurement will off by

$$\Delta x \approx t^2 q \frac{|v_z B_\perp|}{2mc}$$

where t is the drift time, v_z is the drift velocity along the beam direction, $B_\perp$ is the magnetic field perpendicular to the z direction, m is the mass and q the charge of the particle. The above equation shows that the displacement of the measured position from the value it would have in the absence of $E \times B$ forces is dependent on the drift time squared times the magnitude of the magnetic field perpendicular to the z axis.

As the ionization electrons drift thru the gas volume, they scatter off the molecules of the gas. The width of the electron cloud at the end of its drift is widened due to **diffusion**[51]. One must choose a gas where the diffusion will not be so large as to degrade the position resolution that we seek. Argon is a good choice because the scattering cross section is at the Ramsauer minimum for the drift velocities of interest in our case. Additionally, the diffusion is proportional

to the drift time. An ionization electron drifting one meter will have $\sim$ 1 mm diffusion in the TPC.

More seriously, the longer the drift distance the more electrons will be lost due to their interactions with the gas. One must remove all possible sources of electro–negative substances inside the gas volume. All oxygen (particularly in the form of water) must be scrubbed from the incoming gas.

Finally, one must make sure that the gain along the wire of the detecting proportional chambers is uniform. Our design criteria were driven by the desire to measure dE/dx to 3%. This implies our systematic errors should be kept to the 1% level.

We implemented the TPC idea by making two endcaps each of six kite shaped proportional chambers called sectors. Figure 3.7 shows a diagram of one chamber. Every 4 mm we string a sense wire with a field shaping wire strung between each pair of wires. The sense wire plane is 4 mm above the grounded cathode plane of the sector body. A grid of 4 mm pitch is placed 1 mm above the sense wire plane.

The grid, sense and field wires form a drift cell. Drift electrons pass thru the grid and cause an avalanche on sense wires along the path of the track. The field wires help shape the field to reduce the cross talk between adjacent cells. The field wires also improve the electrostatic stability of the chamber. The sense wires are placed at a potential of 3400 volts and the field wires at 700 volts. The gas gain resulting from this electrostatic configuration is 1000.

We placed under every 13^{th} wire a row of 7.5 mm $\times$ 7.5 mm cathode pads. The positive ions liberated by avalanche on a sense wire are attracted to the cathode plane. Hence by measuring the pulse detected by the pads we can localize the avalanche position along the wire. Unfortunately, the cathode pads couple to other sense wires than the wire directly above the pad row. A good

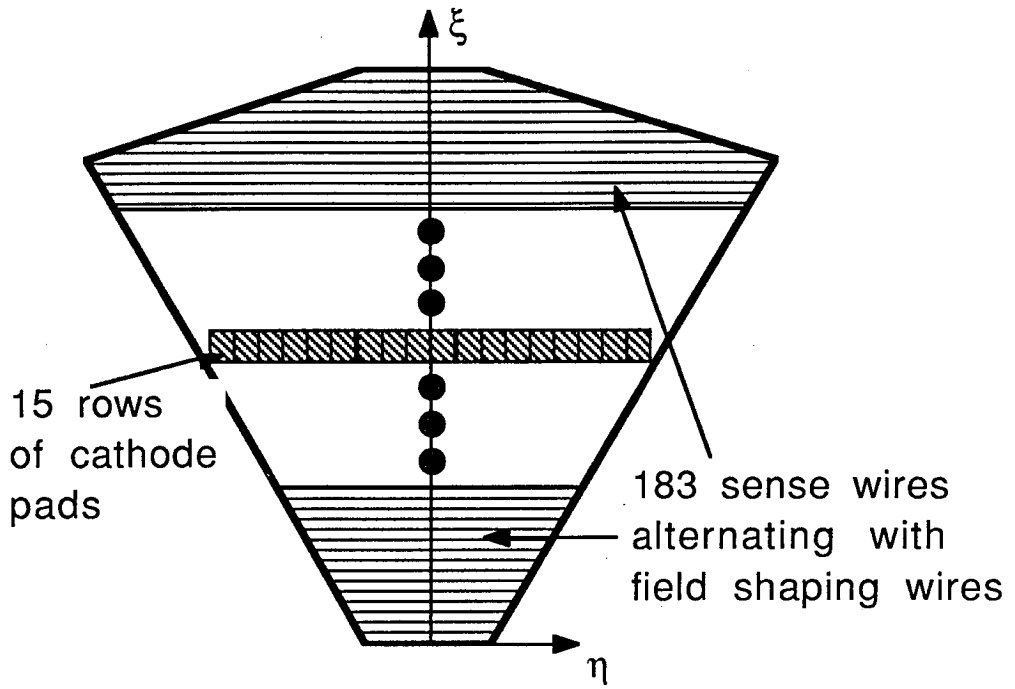

Figure 3.7: Diagram of one sector. The ξ and η coordinates are for each of the 12 separate sectors. ξ is essentially the wire where the hit is measured and η is the distance from the centerline of the sector where the ionization was measured.

approximation to the signal seen by the pads is a sum over the five closest wires to the pad itself[52].

We amplified the signals detected by the sense wires and the cathode pads by a set of preamplifiers located on the sector itself. The preamplifier has a gain on the order of 10^{10} amp/coulomb[1] and it drove a differential signal over a twisted pair of wires. We needed the pre–amplification on the sector because the signals had to travel on the order of 100 feet of wire in order to reach the electronics hut which is located outside of the beam wall. We used a differential signal to reduce the contribution of outside electronic noise sources.

However, locating the preamplifiers on the sector made it necessary to cool the sector too. Gain is extremely sensitive to temperature variations. Hence, if there were systematic variations in temperature we would systematically detect a different signal across the sector. Therefore controlling temperature to $\pm 1°$ C is crucial[53].

The sectors were cooled by circulating water thru aluminum bars. The brass ground plane of several pre–amps is in contact with a brass casing. This brass casing is then placed in contact with the aluminum cooling bars. The arrangement of using metal to metal contacts for the cooling system improves our heat conductivity and allowed us to meet the design goal of less than 1° C variation in temperature across the sector.

3.2.1 TPC Electronics

The energy loss by a particle as it traverses a length of gas is proportional to the number of electrons freed. Hence, by measuring the number of electrons liberated as a track traverses a length of gas, we can determine the energy lost by the track as it traversed that length of gas. Therefore, we need a linear (or at least we need to be able to calibrate any nonlinearities) stable electronic system

[1] pad preamplifiers have about three times the gain of wire preamplifiers.

which can turn the number of electrons detected into a measurable voltage by which we can deduce the energy loss by a particle.

The electronics house is divided into four rows of electronics. Each row has fourteen racks of seven bins. Each bin can hold up to seventeen circuit boards. At most, sixteen separate cards in a bin are used to monitor sixteen electronic channels each. The seventeenth board in a bin is used for master control functions for the rest of the bin. Hence, each bin of electronics can read out up to 256 electronic channels.

A block diagram of the TPC electronics chain is presented in figure 3.8. The electronics chain begins with the preamplifier. The preamplifier is simply an amplifier with a capacitor connected to the input and output stages of the amplifier. This configuration integrates the charge deposited on the input leg of the amplifier. The output stage of the amplifier then drives a differential signal over a twisted pair of wires. The pre–amp has a 200 ns integration time and the capacitor is bled off by using a resistor in parallel to the capacitor. The capacitor discharge circuit has a 5 μsec time constant. We needed to bleed off the capacitor so another avalanche could be seen on the same sense wire or pad.

The next element in the electronics chain is a shaper amplifier. The principal task of this amplifier is to turn the pre–amp signal into a pulse proportional in voltage to the amount of charge detected and to remove the long 5 μsec tail. The shaper accomplished its twin tasks by differentiating the signal and making a "pole–zero" subtraction to remove the long tail. However, the shaper amplifier signal has a slight undershoot which lasts for many micro seconds after the initiating track's signal has been detected in the electronics. This means that signals from tracks subsequent to the initial track must be corrected. Signals from tracks within 3 cm in z are inseparable and hence cannot be used.

The signal from the shaper amplifier is input for a Charge Coupled Device

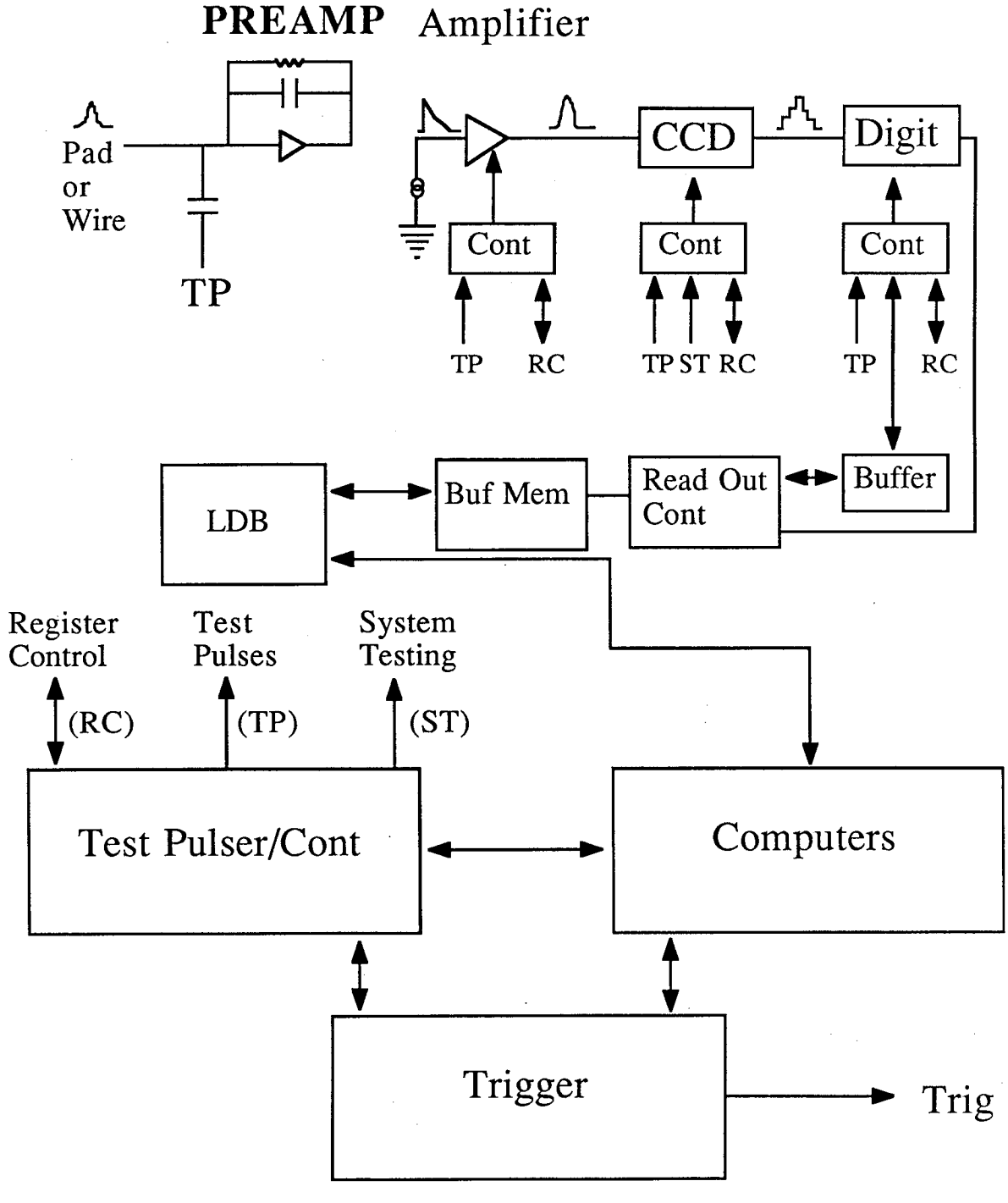

Figure 3.8: The TPC electronics chain.

(CCD). CCDs are semi–conductor devices which have separate charge storage cells called buckets. Our CCDs have 455 buckets. We number the buckets from 0, the output bucket to 455, the bucket where the charge is initially placed. Each bucket holds charge until the device is clocked at which time the charge moves from cell i to cell $i-1$. Thus, the time of arrival of charge Q equals $N \times \tau_{\text{clock}}$ where τ_{clock} is the time between clock pulses and N is the number of clock pulses from time t_0 to the time t at which charge Q was clocked out of the device.

The CCDs were clocked at two separate rates. Ordinarily the CCDs were clocked at 10 Mhz (although they can be run at rates as high as 25 MHz) corresponding to 100 ns per bucket. Usually the information is not digitized. When the drift chamber signaled a possible interesting event (a pre–trigger), the clocking rate was slowed to 50 kHz so the information could be digitized. The TPC only requires 200 buckets to store the entire event at a drift velocity of 5 cm/μsec. We use 300 CCD buckets to be safe.

However, there is a dark current in the CCD which depends on the temperature of the device. Given a particular stable temperature, the dark current adds charge Q_d in time τ_{clock} to charge in each bucket. Hence each bucket has a background of

$$\text{Total Dark Current} = Q_d \times \tau \times N_b \tag{3.2}$$

where N_b is the bucket number inside the device and bucket 1 is the first digitized bucket of the device. The contribution of the dark current must be removed from the signal. Fortunately, equation 3.2 indicates that the contribution of the dark current is linear in the bucket number. We cool the electronics house to 16° C to reduce the effect of the dark current. Typically, four digitizer counts are added to the charge detected after clocking 300 buckets at the slow clock rate for the TPC.

Next, we must digitize and store all relevant information. We record the

channel number, pulse height, and the number of slow CCD clocks elapsed since the pre–trigger time. Digitization of the signal is done by comparing the signal to a ramp run concurrently with the CCD clocks. A separate digitization clock is started when the ramp is at zero. When the ramp passes the value of the signal, the value of the digitization clock is placed into local board memory. If the digitized value of the signal is higher than a preset integer threshold, the channel is flagged as having data present. The threshold is determined channel by channel in the course of calibration. Once the threshold was determined, its value was written onto a board Random Access Memory (RAM). The RAM in which the thresholds are stored is called the "Lower Limit RAM" (LLR).

Any data present on any of the fifteen separate channels on the board will flag the board as having data present and cause the Readout Master Controller to read the data from the board and store it into a Large Data Buffer (LDB) readable by all three online computers. The online computers were an PDP 11/70 which monitored and controlled the electronics of the TPC, and two VAX 11/780 computers. One 11/780 was for PEP–4, the other for PEP9. The LDB stored the event data from each of the detector electronics. Once all the electronics from each of the detectors had been read, all online computers were informed and all other triggers were held off until the computers were finished with the data in the LDB.

The electronics readout is organized into **lists**. Most lists read only one detector's electronics. The trigger, inner and outer drift chambers, the hex calorimeter, the "pole tip"calorimeter, the muon chambers and the results of monitoring voltages, pressures etc. are put into separate lists. The TPC is broken into 30 separate lists[54]. Each endcap of the detector is divided into a set of 15 lists. Each of six wire lists monitors one sector's worth of channels (184 wires) and hence can be placed into one bin of electronics. Pad lists are different. There are

far fewer pad hits in an event. Hence we place up to 1007 pad channels on a pad list. Each pad list may read two separate pad rows. Pad list six, for instance, reads pad rows zero and eight for all sectors. The longer pad rows are read into a single list. Pad list 11 monitors pad row 10 from all sectors, a total of 672 pad channels. All lists, except pad list 10, monitor at most monitor 768 pad channels. Pad list 10 monitors 1007 pad channels. A bin of electronics reads up to 256 electronic channels. Therefore, all pad lists consist of three bins of electronics except for pad list 10's four bins.

The Readout Master Controller reads data at 10 MHz. If more than 200 channels in a particular list have data stored for a particular bucket, we will clock out the next CCD bucket. Hence, if more than 199 channels in a particular list have data, we hold off further CCD clocks until all the data has been stored. One side effect will be to add more dark current to subsequent CCD buckets. We neglect this effect because so few events have this problem and the extra amount of dark current is small in any case.

Finally, the electronic readout is organized to take into account the jet structure of hadronic events. A typical event does not have equal occupancy of hits in each sector. Pads present no special problem since it is unlikely to find two particles with exactly the same momentum in the same event. But wires are a different story. Every charged particle in a jet will in general produce signals detected on the same set of wires. Hence, for a typical ten track, two jet event,

$$5 \text{ tracks/jet} \times 140 \text{ wires} \times 5 \text{ buckets/track} \times 1 \text{ jet}$$

or about 3500 hits on the wires in each of two separate sectors. There will be no hits on any other sector in the event. Worse, we must account for the fact there are events with 20 to 30 tracks. Every list must have enough memory in order to store such events. We would have to have $10K$ words of memory on each list if we simply divided the electronics by sector. We can reduce the electronic storage

requirements and reduce cost and computing load by spreading the storage load of one sector's wires.

This is accomplished by what we call "spiral" readout of the wires of the TPC. Basically, we divide the wire electronics into lists. Each list (0, 1, 2, 3, 4, 5) corresponds to one sector's worth of wires (11 boards $\times$ 16 channels = 192). But, instead of a list of electronics reading one sector, a list monitors wires in every sector. The first board in a list i, detects signals from the first sixteen wires in sector i (wires 0 to 15). Then the next board detects signals from wires 16 to 31 from sector $i+1$ for lists one, three and five and $i-1$ for lists zero, two and four. Wires 32 to 47 for sector $i+2$ are read by the third board in lists one, three and five, $i-2$ for lists zero, two and four. This spiral pattern of readout is maintained until all wires are accounted for[55].

The effect of organizing the readout in this fashion is to spread the load of electronic readout over many lists. Each list has only 32 wires in any one sector that it monitors. Only $4K$ words of memory are needed for each wire list reducing the storage requirements in the LDB by a factor of 2.5 or so. Obviously, this reduces our costs both in purchase of memory and cooling requirements because we use fewer electronic components than otherwise would be the case.

3.2.2 TPC Calibration

We must convert the TPC's electronic digital reading into ionizing electrons in order to realize the power of the TPC. We needed to perform several different calibrations:

- Calibrate the CCD pedestal and dark current contribution to the stored digitized pulse.
- Calibrate the electronic response of the preamplifier and shaper amplifier.
- Absolutely calibrate the response by using a known amount of ionization.

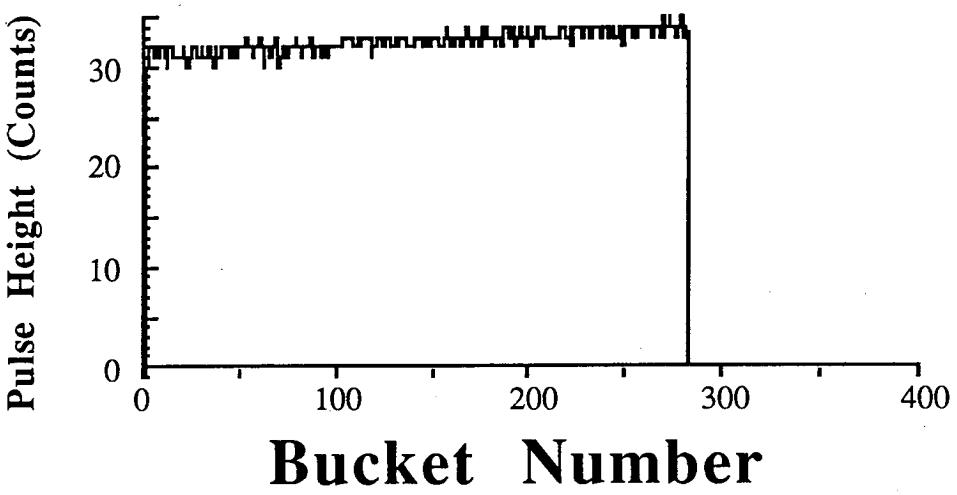

Figure 3.9: Quesient level of a CCD. The curve is Pulse height versus Bucket read. Notice the slight increase in pulse height over the 300 buckets read.

Calibrating the CCD's

We set the threshold lower limit RAM (LLR) value channel by channel to zero in order to determine the pedestal levels and determine the increase of digital counts with time for the channel. Setting the LLR value to zero allowed all the CCD data to be stored in the LDB for analysis. Then we initiated a read out cycle which causes the CCD's to be read out using the slow CCD clock rate. We turned off all sectors to insure that no response to ionization would be measured by the electronics. Figure 3.9 gives an example of the measured pulse height versus bucket number curve. A least squares fit to the data for a line was performed for this curve, i.e.

$$\text{Pulse Height} = AN_b + B \tag{3.3}$$

where N_b is the bucket number, B is the pedestal at zero time and Pulse Height is the digitized pulse height. Determining constants A and B channel by channel establishes the pedestal as a function of bucket number for a particular channel.

A noise value is associated for the channel by determining the RMS deviation of the Data from the fitted line. Only four channels are done at a time because no data is suppressed and Pad Lists have only 2K words of memory in the LDB. The threshold or Lower Limit RAM value for the channel was set to the Pedestal value at bucket 300 plus five times the noise value for the channel. Typically the pedestal at zero time is in the range 20 to 30, the noise value was 2 to 3 counts and the Lower Limit RAM setting was 40 to 50 counts. These numbers should be compared to the 110 digital counts which corresponds to the amount of charge left by a minimum ionizing track in a 4 mm drift cell in the TPC. Channels with excessively high pedestal, noise, Lower Limit RAM or slope were turned off and flagged for repair.

Calibration of Electronic Response

The measured digital pulse height must now be calibrated to an absolute scale of energy loss. We measured the each channel's response in two steps:

1. Determine the response of the channel to a known amount of current as a function of digital pulse height.

2. Determine the response of the channel to a fixed amount of energy loss.

The first step involves placing a known voltage across a capacitor. Pulsing the pre–amplifier as in figure 3.10 has the exact same effect as depositing charge on the wire. Even though we can pulse the pre–amplifiers in this way, we actually pulse the wire grid plane above the sector. The capacitor is then the capacitance between the wires and the grid and the pads and the grid. The digital response of the electronics to charge being placed on the wire is gaussian. The response is fit to a parabola to save time (the description of cluster finding can be found in section 5.1). We use the maximum peak height of the parabola as the electronic

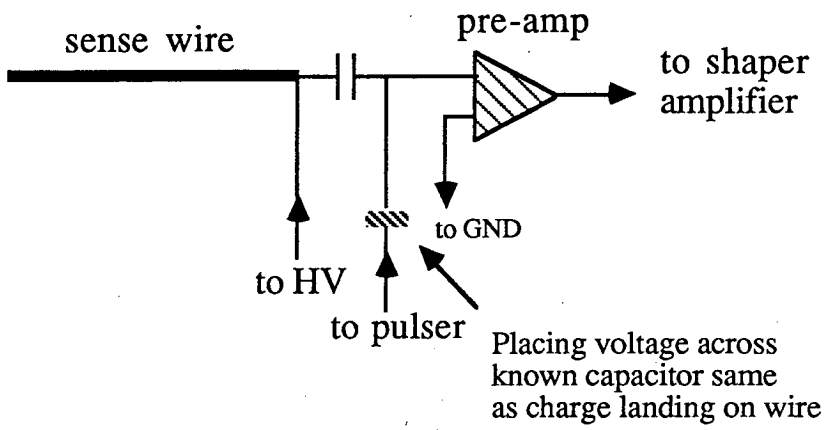

Figure 3.10: Depositing a known amount of charge at the pre-amp input by placing a known voltage across a known capacitance.

response to the pulser voltage. One could also use the area of the fitted parabola as the digital response but the peak height actually produced fewer problems.

A pulser voltage versus digitized electronic response curve can then be made. A typical curve is shown in figure 3.11. The fit is a spline. The digital response is linear between 60 and 400 digital counts. Above 400 counts, the response curve saturates and flattens out. The flattening of the response curve is caused by the saturation of CCD buckets. If the charge that is deposited into a CCD bucket exceeds a maximum amount, the charge spills out of that bucket and shifts it to the next bucket. This affects the fitted electronic response. When the CCD channel saturates, neither a parabola nor a gaussian is a good representation of the CCD response.

A stable, linear pulser is the most important component of the electronic calibration system. Variations in temperature and number of pre–amplifiers pulsed should not change the output of the pulser. The pulser for the TPC is stable to about 0.1 to 0.2 percent to such variations. The pulser is linear to about 0.1%[53].

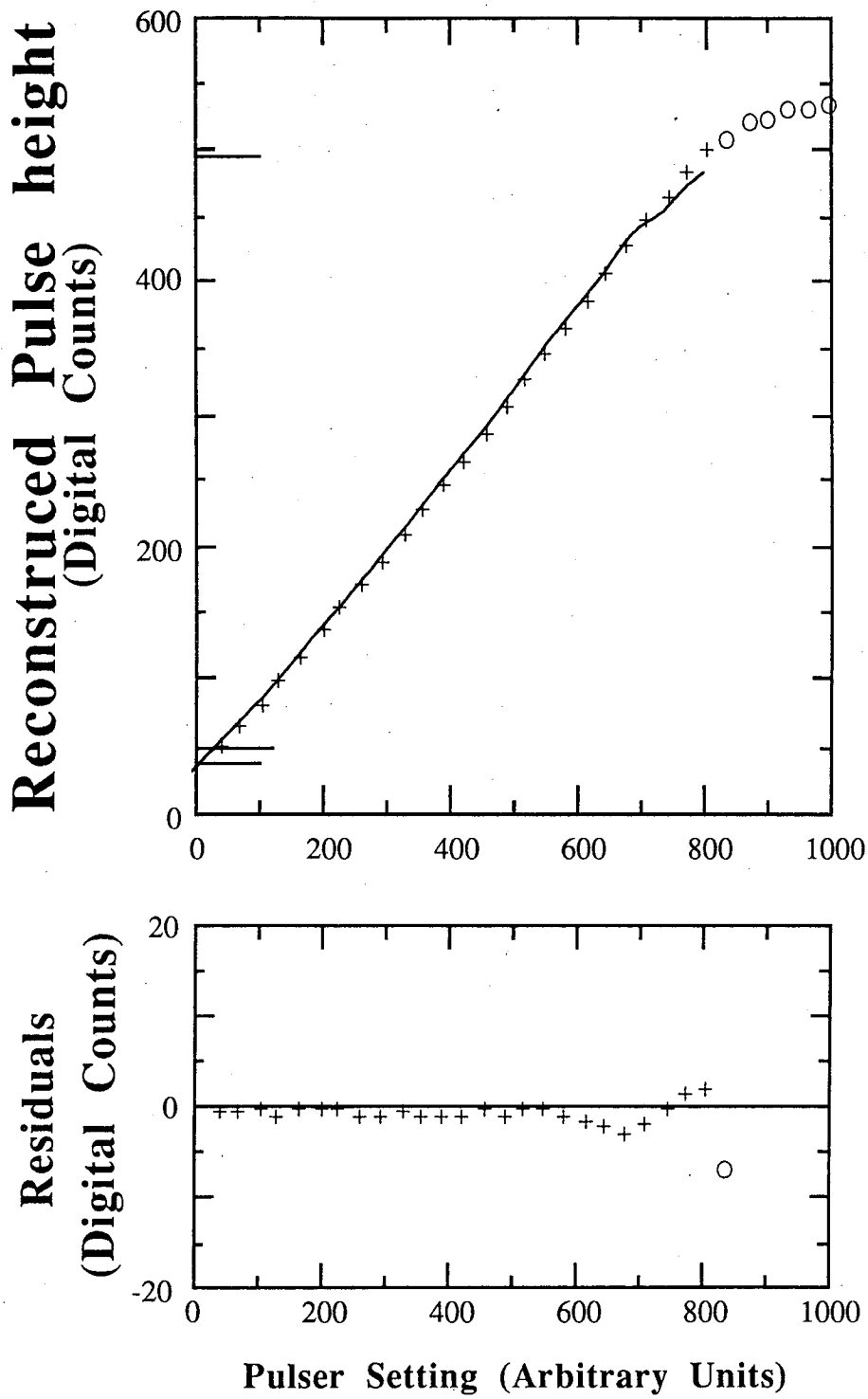

Figure 3.11: Measured pulse height versus pulser voltage curve for a typical TPC electronics channel. In this case a pad channel is shown in the figure.

Electronic calibration was done before and during the running cycle. Whenever the accelerator was off for a day or two, we would do an electronic calibration. We could not calibrate the electronic response of the system if the accelerator was running because track ionization would be confused with the effect of pulsing the grid. Also, we would calibrate the electronics after the running cycle was completed, to check the stability of the calibration. The calibration was stable to the level of 1%.

Fe^{55} Source Calibration

We then calibrate the digital response to an absolute amount of charge deposited on a wire. This is done by use of a Fe^{55} source. The Fe^{55} source releases a 6 keV X-ray. The X-ray converts inside the gas volume depositing about 6 keV onto one wire. The Fe^{55} sources are placed onto little tabs on a metal rod. There is a button source for each wire in a sector on each rod.

A hole along a channel in the sector for the rod is placed in the G-10 face of the sector. Each hole is aligned with each sector wire. A spring is placed at the bottom of the channel for each rod. Ordinarily the spring causes the source rod to be pushed such that the button sources are not in line with the holes in the sector. But, when the channel is placed at 30 pounds higher gas pressure than the TPC, the rod is pushed down so the sources line up with the holes. The holes are lined with a copper alloy and placed at a slight negative potential to reduce the effect of Fe^{55} X-rays which convert inside the hole.

There are three source rods in the sector. They are at positions $-16°$, $0°$ and $30°$ with respect to the center line of the sector. We placed the source rods at different positions to measure gain variations along the wire.

Procedurally, we randomly triggered the TPC, and read out all 455 buckets of the CCD. We ran a source calibration run whenever we had one or two hours of no

beam. Source calibration was once a week in general. Repeating the calibrations helped us monitor the variation of absolute calibrations and to measure the variation of the gain along the length of a wire. Absolute calibrations were stable to about 1%.

3.3 Trigger

The basic philosophy[2] of the TPC trigger was to allow maximal flexibility in designing possible triggers. Thus, coincidence windows can be varied, the number of hits in a chamber which define if there is a "track" can be varied, the total number of "tracks" required by the trigger to cause the electronics to be read and the event stored on tape can be changed etc. We use the tracking ability of the TPC to find tracks. During the running cycle in 1983, the charged particle trigger required two tracks with reasonable vertex positions to be found in the sectors. There are also neutral, muon, cosmic and two photon triggers. Since we are only interested in hadronic events, they will not be described here.

Any trigger decision is constrained by the 2.5μsec time difference between beam crossings. Since it takes about 20μsec to sweep out all the ionization from the TPC, we must break the trigger into two parts. The first stage decision must come fast enough to allow all latches and registers to be reset before the next beam crossing. The first stage decision must also reduce the number of prospective triggers to a minimum. If not, we will miss many "good" physics events because of the time it takes to drift ionization from an event to the sectors. The second stage of the trigger must examine the data in the electronics more carefully and make the decision whether or not to keep the event.

[2]This section is based on references [39,45,56]

Pre–Trigger

The first stage of the trigger is called the pre–trigger. The pre–trigger decision comes within 2μsec of beam crossover, allowing 500 ns to clear all of our electronic registers and latches in preparation for the next beam crossing.

The event must have at least two prospective tracks for there to be a valid pre–trigger. The track is defined by matching hits in the inner drift chamber (IDC) with the outer drift chamber (ODC) or the sector itself. The IDC forms the basis of the decision. It was pointed out in the brief description of the IDC that the layers of the IDC were rotated with respect to one another by one half a drift cell length. This was done so that the sum of arrival times of ionization from a track on layers A and B (C and D) is a constant for high momentum tracks irrespective of angle of that track. A 30 ns time window is placed around the sum of the arrival times on the A and the B (C and the D) layers which rejects tracks with momentum less than 120 MeV. In addition, we require there to be a coincidence between the A and the C layers (or the B and the D layers) to define IDC hits as a prospective track (see figure 3.2a).

We match hits in the IDC and the ODC by designating fixed, overlapping 30° swaths in the two detectors. An ODC track is defined by grouping together ODC drift cells and requiring two hits in different layers of the same group. Layer E of the ODC is divided into 72 non–overlapping groups of three wires apiece. An ODC pre–trigger group consists of one of the groups from layer E, the 4 cells from layer F directly behind layer E and 5 cells from layer G directly behind layer F (see figure 3.2b). The hits on the wires are required to occur within the 300 ns maximum drift time of ionization within an ODC cell. If aligned 30° swaths in the IDC and ODC have hits, a pre–trigger track is defined.

The ODC can only be used for tracks which make an angle greater than 45° with respect to the beam. We must use the sectors for tracks below 45°. In 2μsec,

only $\sim$ 10 cm of ionization in z will have been swept out of the gas volume by the electric field. Hence, the criterion for a track in the sector is relaxed for the purposes of making a pre–trigger.

The sector is divided into 23 groups of eight wires apiece. The signals from these eight wires are grouped together as input to a **majority logic unit**. The signal is taken directly from the output of the shaper amplifier and compared to a trigger discriminator level set for that channel. If more than a certain fraction (usually 3 out of 8) of the eight wires exceed the trigger threshold, the majority logic unit fires.

The drift time is broken into 64 time slices of $\sim 0.4\mu$sec apiece. The TPC midplane occurs at time slice $\sim$ 50. The rest of the time is used for trigger decision. Each time slice corresponds to about 2 cm of drift in the z direction. The majority signal lasts for at least 4 slices. If more ionization drifts in from any of the eight wires during that time, the majority logic unit signal will persist for a longer time.

Majority logic unit signals from neighboring sectors are combined (logical **OR**) into six overlapping **supersectors** (see figure 3.12) in order to reduce edge problems. Two 30° IDC wedges are combined to correspond to any one supersector. If there is a prospective track in either of the two IDC wedges, we enable the corresponding supersector. Subsequently, if a majority logic unit within that supersector fires, a pre–trigger track is defined.

We need at least two pre–trigger tracks within 2μsec of beam crossover in order to have a valid pre–trigger. The pre–trigger rate was between 500 Hz and 1000 Hz compared to the rate of single hits in the IDC of 14 kHz.

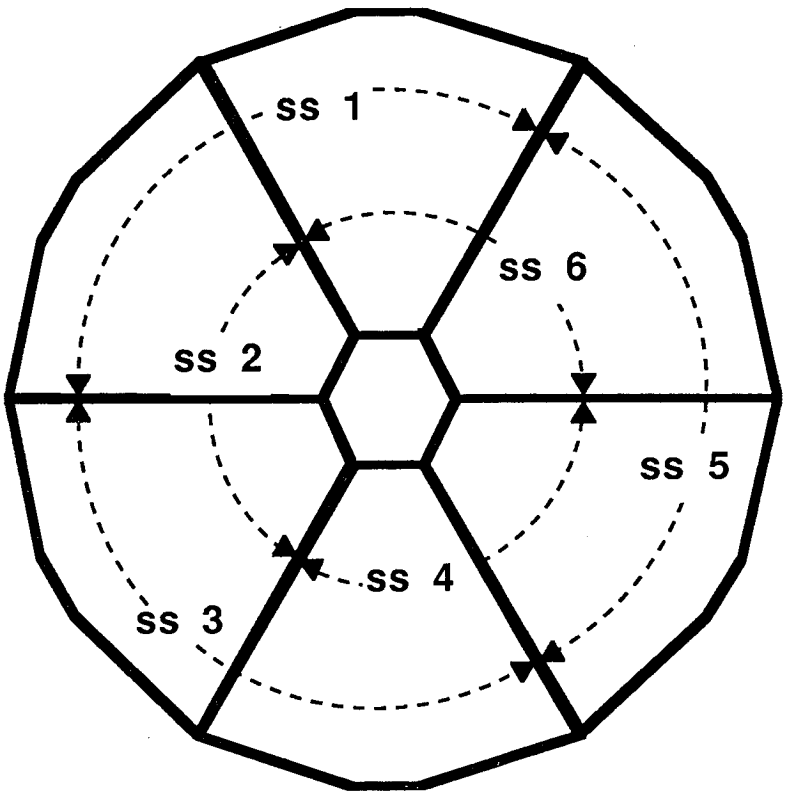

Figure 3.12: The organization of sectors into supersectors.

Ripple and Majority Triggers

Once there is a valid pre–trigger, the trigger system commences a search for tracks using data from the wires. We use the wire data to search for continuous tracks starting at high radius and going inward to lower radius. A time window is made to constrain the vertex of the track to within ~ 25 cm in z. Background from synchrotron radiation is rejected because it is unlikely that hits due to synchrotron radiation will mimic a track. Background from beam–gas interactions is rejected by the vertex cuts.

Any majority logic unit can initiate a ripple trigger within the pre–trigger time of 2μsec. The majority logic unit initiating a ripple trigger enables the next innermost set of three majority logic units. If within 2 to 3μsec one of the set of three logic units fires, the ripple continues to the next innermost set of three logic units. The ripple must continue to the innermost two logic units. A ripple track is defined if the innermost two logic units also have data within a timing window.

The timing window is selected by the pre–trigger. Both timing windows are chosen to require that the track originate from near the origin. This implies we must separate the large angle tracks ($> 45°$) from low angle tracks ($< 45°$). If the pre–trigger was the coincidence of an IDC and ODC wedge ("large" angle pre–trigger), the timing requires that the signal on the inner radius come from within 20 cm of the TPC mid–plane. If the pre–trigger was the coincidence of an IDC wedge and a supersector ("low" angle pre–trigger), the timing requires that the signal on the inner group of wires be within the range 16 to 36 cm in z of the mid–plane.

Finally, the ripple must also be in angular coincidence with pre–triggers from the IDC or the ODC. A ripple track is defined if the supersector in which the ripple occurred has an ODC pre–trigger within 60° of its center for large angle

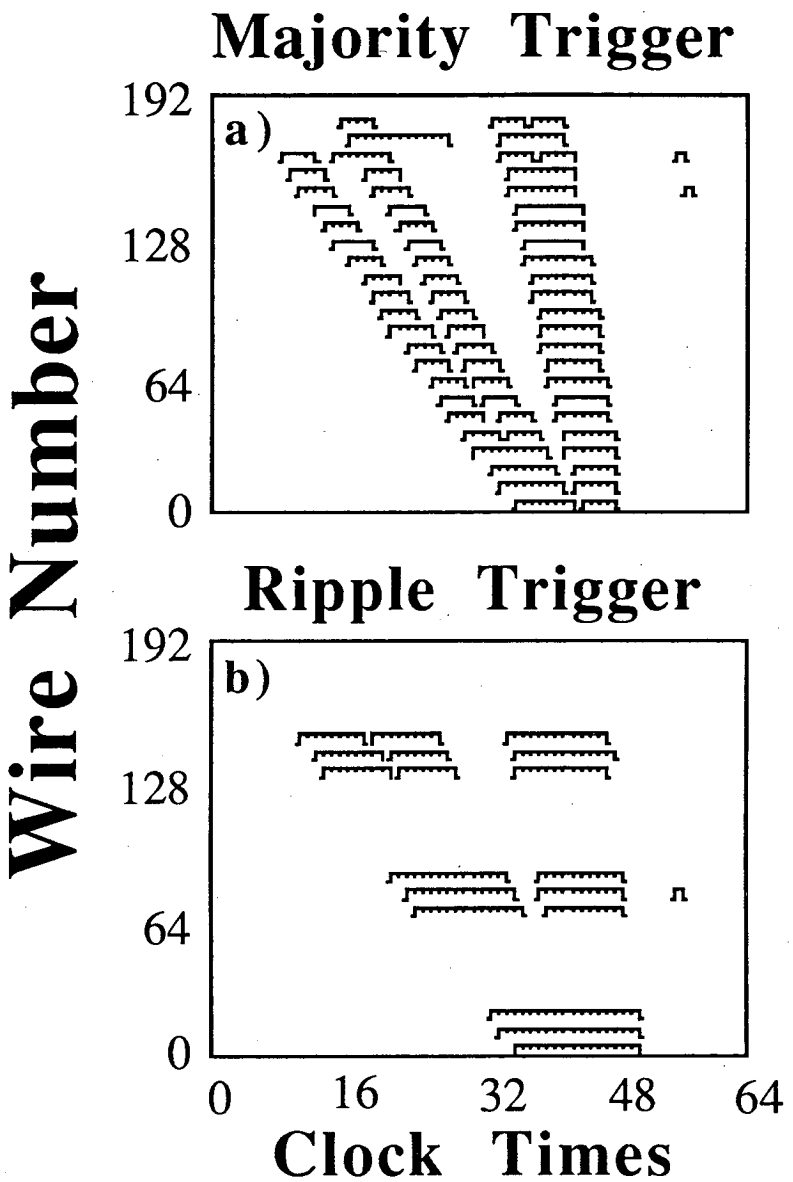

Figure 3.13: Examples of a) a majority trigger and b) a ripple trigger in a $q\overline{q}$ event candidate.

triggers or an IDC pre–trigger in one of the two 30° IDC wedges corresponding to that supersector for low angle triggers. Two such ripple tracks define a ripple trigger. Figure 3.13b gives an example of a ripple trigger in a multi–pronged event.

The ionization from tracks whose angle with respect to the beam is about 90° will arrive on all the wires in the sector nearly simultaneously. Hence, at some point the ripple trigger will cease to function because of signal propagation delays. Tracks whose angles are greater than 84° with respect to the beam will not reliably cause a ripple trigger. For these tracks, a different trigger is used. The majority logic units are segregated into two groups of eight and one group of seven units (a **majority group**). The majority group generates a signal if at least three of the units in the group are on. A majority trigger is generated if

1. all the groups fire in one endcap and at least one majority group in the other endcap fires too,

2. the time of the majority trigger corresponds to positions within 5 cm in z of the TPC midplane,

3. there is a large angle pre–trigger present and

4. at least one ripple signal is generated.

Conditions 1, 2 and 3 impose the requirement that at least two tracks come near the mid–plane whereas condition 4 is imposed to reduce the majority signal rate.

The sum of the rates for ripple and majority triggers is about 0.8 Hz. The overall trigger rate for the experiment was $\sim$ 1.5 Hz. The balance of the triggers are neutral and two photon triggers. This trigger rate allowed us to read, partially analyze and write to tape all events. If the rate were around 4 to 5 Hz, we would begin to have trouble doing these minimum required tasks. The charged particle trigger is greater than 99% efficient for hadronic events with five or more

particles[57,39,53]. The trigger need not be considered further because of this very high efficiency.

Chapter 4

Theory of Energy Loss in Materials

The power of the TPC comes from the ability to measure simultaneously momentum and energy loss per unit length of a particle. The energy loss for particles which carry the same plus or minus charge in a given material is solely a function of $\beta = v/c$ where v is the velocity of the particle and c is the velocity of light[1]. Therefore, the simultaneous measurement of these two quantities gives us a measure of the mass m of the particle. We will describe the basic properties of energy loss and why we went to the TPC design in order to accomplish the goal of good particle identification.

4.1 Introduction to Energy Loss

When a particle traverses a material, it loses energy because of interactions with the atoms which constitute the medium. While one can look at this process quantum mechanically, we present here a semi–classical picture of the interaction.

Most interactions between the particle and the medium occur at large impact parameters. These interactions can be characterized as quasi–elastic scatters where very little energy is transferred from the particle to the atom. These

[1]The only exception to this rule is low momentum electrons. However, the TPC can only measure momenta larger than $\sim$ 100 MeV/c where this should not present a problem.

interactions lead to the excitation of the atom. Most interactions between the particle and the medium are of this type since the volume goes as b^3 where b is the impact parameter.

However, the smaller the impact parameter, the larger the momentum transferred from the particle to the atom. At small impact parameters, electrons scatter directly off of the particle. It is possible to treat the electron as free in this case. Unlike the case of excitation, the energy distribution of the ejected electrons is not a gaussian. The electron energies follow the characteristic $1/E^2$ distribution of Rutherford scattering where E is the energy of the electron. This distribution cuts off at the maximum possible energy that a particle of mass $m \gg m_e$ can impart to an electron

$$E_{max} \approx 2\gamma^2\beta^2 m_e \tag{4.1}$$

where γ and β refer to the incident particle and m_e is the rest mass of the electron.

Herein lies the problem of measuring the energy lost by a particle. Most interactions of an incoming particle with the surrounding medium are well behaved and the energy lost can be described by a gaussian distribution. If we make more measurements by doubling our material and hence doubling our statistics on the number of electrons freed by the particle, we would improve our measurement of the energy loss. This would hold true until the sample thickness became so large that one has to consider the energy lost by the particle itself as it traversed the sample.

But the Rutherford scattering of electrons by the incident particle never allows us to reach this happy state of affairs. There are very few hard scatters in thin samples. But by making our samples too thin, we subject ourselves to excitation fluctuations. We have to make our samples thick enough so that we can measure the energy lost by the particle to the precision we wish. But the number of hard

scatters also increases linearly with sample thickness. Since the energy spectrum of the scattered electrons is so broad (it lasts until $E_{\max}$) and drops off so slowly ($1/E^2$), the average energy lost per unit sample length is very much skewed away from the average excitation energy. Also the width of the distribution is affected by this $1/E^2$ Rutherford scattering tail (called the Landau tail). An ensemble of particles obeying the $1/E^2$ distribution will have ln $E_{\max}$ average energy lost and $E_{\max}$ as its width. The excitation energy is much smaller than $E_{\max}$. Therefore measurements of the average energy lost per unit length of a particle traveling thru a medium will be skewed to much higher values than would be given by just using the excitation interactions. For example, the excitation energy of the K shell in argon is 3.206 kilo electron volts (keV)[58]. The minimum $\gamma\beta$ for a particle accepted in this analysis of TPC data is 0.863. This implies a minimum $E_{\max}$ for the electrons scattered by particles detected in the TPC of 740 keV!

Let us further consider the case of the TPC. Let N_i be the number of electrons freed by excitation of the atom. The width of the excitation peak is 55% FWHM. We wish to determine the width of the peak to about 4% FWHM. This implies we need about

$$N_i = \left(\frac{55\%}{4\%}\right)^2$$

or about 190 electrons freed[53,58]. A sample thickness of 4 mm at 10 atm of Ar-CH_4 will free about 200 electrons. But in this 4 mm sample, we will also have about 18 hard scatters.

The way around this problem is to make many measurements of energy lost in a particular sample thickness. If we do this, we can characterize the energy loss curve including the long Rutherford scattering tail. Then there are several ways of extracting the most probable energy lost for the particle. We chose to throw away what are probably hard scatters and characterize the remaining energy loss measurements. The mean energy loss determined by this procedure is called the

"truncated mean". Typically one throws away between 30 and 40 percent of the measurements and then takes the mean of the remaining 60 to 70 percent to determine the most probable energy loss[59]. In the TPC we use only the lower 65% of the measurements in this determination.

The picture of energy loss we have presented to this point has not included some important secondary processes. First of all, the ground state of an atom does not have only one electron shell occupied (unless we are talking about hydrogen). Hence we must sum over all the occupied energy levels to determine the contribution of excitation to the energy loss. Secondly, it is possible that the atom will already be in an excited energy state before the interaction with the incoming particle. The atom may have been excited by the passage of a previous charged particle, a collision with another atom in the gas, interaction with a photon etc. In any case, the electron emitted might be from a different energy level than the ground state level. Thirdly, there is the possibility of internal conversion of a photon emitted by an atom in an excited energy state which results in an electron being ejected from that atom (Auger electrons). Fourthly, it could be that the deexcitation of an atom results in a photon which converts into visible energy after that photon travels to a different energy loss measurement cell. If this were the case, we would overestimate the energy loss of the track in the cell in which the conversion occurred (if the conversion took place in a measurement cell in which the track in question passed). Conversely, we would certainly measure a lower energy loss in the energy loss measurement cell in which the photon was created. This is one contributor to "cross talk".

We must also consider the interactions of the primary electrons produced by the process of energy loss with the gas as this electron drifts. Secondary electrons can be produced in interactions of the drift electrons with the medium. Finally we must consider the fluctuations in the avalanche at the sense wire. All of these

effects must be taken into account in order to form a complete picture of the measurement of energy loss of a particle as it traverses a medium.

4.2 Average Energy Loss

There are several methods one can use in order to calculate the most probable value of the energy lost by a particle as it traverses a material. We could use a precise quantum mechanical treatment of the problem. However, it turns out that calculating the process semi–classically gives very similar results. We will present a short description of this calculation in this section. It is a summary of the method of Jackson[14] and other authors[50,59,60].

Semi–classically, the interactions which lead to energy loss by a particle traversing a medium are caused by the electric field produced by the particle interacting with the electrons in the medium. The electric field produced by this particle is

$$-\frac{q}{r^2}\hat{r}$$

where q is the particle's charge and r is the distance from the particle to the point of observation in the rest frame of the particle. One must transform this field to that of the medium which is at rest in our, the laboratory, frame. If one sets the impact parameter of the interaction to b, then the electric field seen by an electron due to the passing particle is

$$\vec{\mathbf{E}} = -\frac{q\gamma\ vt}{r^3}\hat{x} + \frac{q\gamma\ b}{r^3}\hat{y} \tag{4.2}$$

where x, y and z form a cartesian coordinate system, $\hat{x}$ is the unit vector of the x axis which is defined as the direction of motion of the particle and $\hat{y}$ is the unit vector along the y axis, $r = \sqrt{b^2 + \gamma^2 v^2 t^2}$, v is the velocity of the particle and t is the time since the electron at the point of observation was at position $b\hat{y}$ in the particle rest frame.

The energy lost by the particle due to the interaction of the electron with the electric field of the particle is simply the kinetic energy taken by the electron from the field

$$\Delta E = \frac{\Delta p^2}{2m_e^2} \tag{4.3}$$

where Δp is the impulse imparted to the electron in the interaction.

$$\begin{aligned} \Delta p &= \left| \int_{-\infty}^{\infty} \vec{\mathbf{F}} dt \right| \\ &= \left| \int_{-\infty}^{\infty} e\vec{\mathbf{E}} dt \right| \\ &= \frac{2e\,q}{bv} \end{aligned} \tag{4.4}$$

Finally, by integrating over all possible impact parameters and summing over all possible electrons in length dx, one gets the energy lost by the particle in length dx. It only remains to determine the limits of the possible impact parameters.

The minimum impact parameter b_{min} is set by the maximum possible energy transferred to the electron. Equation 4.1 and equation 4.4 imply the minimum impact parameter must be

$$\begin{aligned} b_{min} &= \sqrt{\frac{2e^2q^2/m_ev^2}{\Delta E_{max}}} \\ &= \frac{e\,q}{\gamma\, m_e v^2} \end{aligned}$$

where m is the mass of the particle traversing the medium. The average of equation 4.4 over many orbits of the electron around the atom goes to zero. This means once the particle passes at a distances large enough that the electron completes many orbits of the atom during the time of the interaction, no energy will be transferred. This implies that the maximum impact parameter is set by the condition that the time of the interaction can at most be the orbital frequency. We make the ansatz that

$$\frac{1}{\omega} = \frac{b_{max}}{\gamma\, v}$$

where ω is the orbital frequency of the electron. Note that v is the velocity of the passing particle in the rest frame of the electron.

The final result for the energy loss is given by

$$dE/dx = 4\pi NZ\frac{e^2q^2}{m_ev^2}\left[\log B - \frac{v^2}{2c^2}\right] \tag{4.5}$$

where N is the density of the medium in atoms per unit volume, Z is the number of electrons per atom and $B = 1.123\gamma^2 m_e v^3/(\omega e\, q)$. This equation gives us the essentials of the behavior of the energy loss curve. At low momentum, dE/dx falls as $1/\beta^2$. After $\beta\gamma$ passes minimum ionization ($\beta\gamma \sim 3.5$), the energy loss rises logarithmically. It is interesting to compare this result to the precise result derived by Bethe[14]. He derived

$$dE/dx = 4\pi NZ\frac{e^2q^2}{m_ev^2}\left[\log B' - \frac{v^2}{c^2}\right]$$

where $B' = 2\gamma^2 m_e v^2/(\hbar\omega)$. We must reconsider our minimum impact parameter in order to compare the semi–classical result to the quantum mechanical result. If one does this, the only difference between the precise quantum mechanical and the semi–classical formulas for the energy loss is a factor of 2 in the logarithm term and β^2. For small β this is a very small difference and for large β, these terms are swamped by the logarithm of $(\beta\gamma)^2$.

This is not quite the entire story. According to this formulation of the energy loss, as the velocity of the particle increases so should the energy loss. However, the energy loss curve saturates for $\beta\gamma$ of the incident particle about 200. The effect was explained by Fermi in 1940. The plateau in the energy loss curve is called the **Fermi plateau**.

The flattening out of the energy loss curve comes from the break down of one of the principal assumptions at high momentum. It was assumed that the electrons contributed incoherently to the energy loss of a particle traveling through the medium. But b_{max} is about $\beta\gamma\omega$. Take for example the M shell of argon. In

this case $1/\omega$ equals 4.2×10^{-8} cm. The distance between atoms at room temperature in 10 atm of argon is about 5×10^{-8} cm. The number of atoms which a particle traveling thru the medium will "see" at any one particular time is

$$\begin{aligned} N &= \frac{4\pi}{3} b_{max}^3 / \frac{4\pi}{3} r^3 \\ &= (\beta\gamma)^3 \times \left(\frac{b_{max}}{r}\right)^3 \\ &= (\beta\gamma)^3 \times 0.58 \end{aligned} \tag{4.6}$$

where r is the distance between atoms. Hence particles traveling with $\beta\gamma$ on the order of 1 only interact with one atom. But for $\beta\gamma$ on the order of 200, the particle interacts with 4.6 million atoms. One must consider the bulk response properties of the medium when so many atoms are affected.

One can see in equation 4.2 that the electric field of the passing particle as seen by the electrons is proportional to the γ of the particle. If the particle is traveling with the canonical value of $\beta\gamma$ equal to 200, the affected atoms in the medium see a very large electric field. This field will polarize the atoms. This in turn means that our prediction for the number of atoms affected in the medium will be wrong. Polarization of the medium will reduce the interactions of atoms far from the particle by screening the atoms from the electric field produced by the particle. Hence the energy lost by the particle will be reduced.

The effect is called the **Density Effect**, because for denser materials the effect will be enhanced. This can easily be seen from equation 4.6. The closer the packing of atoms, the more atoms which are interacting with the particle at any given time. As a result, in solids polarization effects set in so rapidly that there is hardly any logarithmic rise in the energy loss curve.

It is possible to calculate the change in energy lost by the particles due to the density effect by including the complex index of refraction in our calculation of the electric field produced by the passing particle. The result is that we must

modify the most probable value of the energy lost by the atom to

$$dE/dx = 4\pi NZ\frac{e^2q^2}{m_ev^2}\left[\log B'' - \frac{v^2}{c^2}\right]$$

where B'' equals

$$B'' = \frac{\gamma^2 m_e v^2}{\hbar\omega|1+\beta\gamma^2(1-\epsilon)|}$$

where ϵ is the complex dielectric constant[59,60].

Finally one can include the effect of several atomic shells in an atom. The above expression is summed over several different shells with a weight accounting for the different probabilities for electrons to occupy the shell and the varying probability that a passing particle could interact with an electron in that shell. There is more of a chance that virtual photons emitted by the passing charged particle would interact with weakly bound as opposed to strongly bound electrons to the atom. One can calculate this probability by assuming that the electron is bound harmonically to the atom. Hence the weight is called the **oscillator strength**. One can also include the spectral line shape of the electron in each of its possible atomic levels. One simply multiplies the probability that the electron was in a particular shell by the line shape for that particular shell to determine the oscillator strength.

4.3 Monte Carlo of Energy Loss in the TPC

The ideas on energy loss presented in the previous two sections point toward making multiple energy loss measurements in order to determine the most probable energy loss. A track's velocity is determined by the most probable energy loss because the most probable energy loss for a particular particle is simply a function of the velocity.

Allison and Cobb[59] have reported that the resolution of the most probable

energy loss is

$$R(\%\text{FWHM}) = 96n^{-0.46}(xP)^{-0.32} \tag{4.7}$$

where n is the number of measurements, x is the sample thickness in centimeters and P is the pressure of the gas in atmospheres. The formula indicates that the resolution is inversely proportional to the number of samples raised to a power slightly smaller than 1/2. We would expect the power to be 1/2 if the resolution were strictly a statistical process. However, the slight difference between 0.46 and 0.5 is not significant.

Furthermore, the resolution is also inversely proportional to the cube root of the effective sample length xP. The quantity xP is proportional to the number of electrons the particle encounters in the gas in sample thickness x. If there were no Landau tail, again one would expect the power of the xP term to be 1/2 instead of 1/3. However it is not surprising that the relation is not quite as good as 1/2. There will be more low energy excitation interactions between the particle and the atoms of the medium as we increase xP. If there were no other processes, we would expect the power to be 1/2. But the number of high energy Rutherford scattering interactions also increases as we increase xP. Hence we don't recover all the benefit of increased effective sample length. Additionally, there is no way to totally separate all of the high energy collisions from the low energy excitations. Therefore the reduction of power from 0.5 to 0.32 is not unreasonable.

A simple Monte Carlo program was implemented to check the ideas on energy loss presented in this chapter. The Monte Carlo was based on the ideas of Lapaque and Piuz[61] as expanded by Gerald Lynch and Marjorie Shapiro [53,58]. The basic idea of the Monte Carlo is to generate the number of collisions in the

gas according to the distribution

$$\frac{dN}{dx} = \left(\frac{dN}{dx}\right)_{\text{exc}} + \left(\frac{dN}{dx}\right)_{\text{Rutherford}} \tag{4.8}$$

where exc and Rutherford refer to the excitation and the Rutherford scattering cross sections respectively. An excitation or a hard scatter is chosen and the energy of the electron resulting from the interaction generated according to the appropriate energy distributions for those two types of events.

The excitation term could be a delta function but here it was chosen to follow

$$f_i(E) = \frac{s-1}{E_i}\left(\frac{E}{E_i}\right)^{-s} \tag{4.9}$$

where f_i is the oscillator strength of atomic level i, E_i is the energy of the i^{th} atomic level, E is the energy of the ejected electron and s is a parameter[58,61]. The electron scattering energy is generated to follow the characteristic $1/E^2$ distribution of Rutherford scattering. Figure 4.1 from reference [53] shows a comparison of the results of this Monte Carlo with actual data from the TPC.

We do not use the top 35% of the wire pulse heights in order to measure the most probable energy loss. The resulting truncated mean is the average of the remaining 65% of the pulse heights. The truncated mean is a measure of the most probable energy loss. The function $Tr(\eta)$ represents the value of the most probable energy loss as a function of $\eta = \beta\gamma$ of the particle.

We used TPC data to determine the precise shape of $Tr(\eta)$ for the TPC. We used low energy protons for the $1/\beta^2$ region of the dE/dx versus momentum plot, cosmic ray muons for the minimum ionization and the relativistic rise regions of the curve, conversion electrons from the material in front of the TPC for the end of the relativistic rise and Bhabhas for the Fermi plateau. Figure 4.2 shows the fit to the data and the comparison with the theoretical curve. We see a small difference between the two curves near the Fermi plateau but otherwise there is no measurable difference. The $\sim$ 0.5% difference near the Fermi plateau is

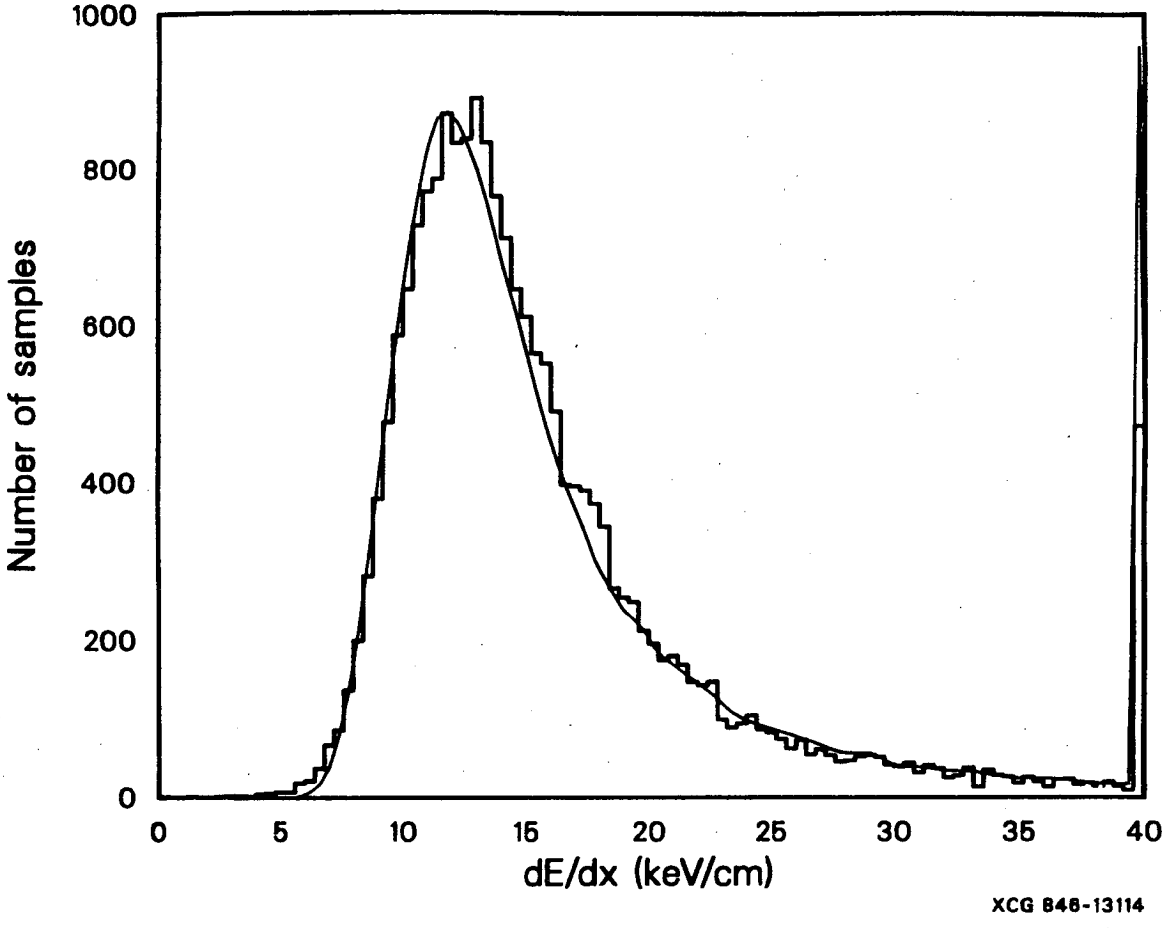

Figure 4.1: Comparison of simple dE/dx Monte Carlo with data taken in 1983. A sample of minimum ionizing pions was used for the comparison.

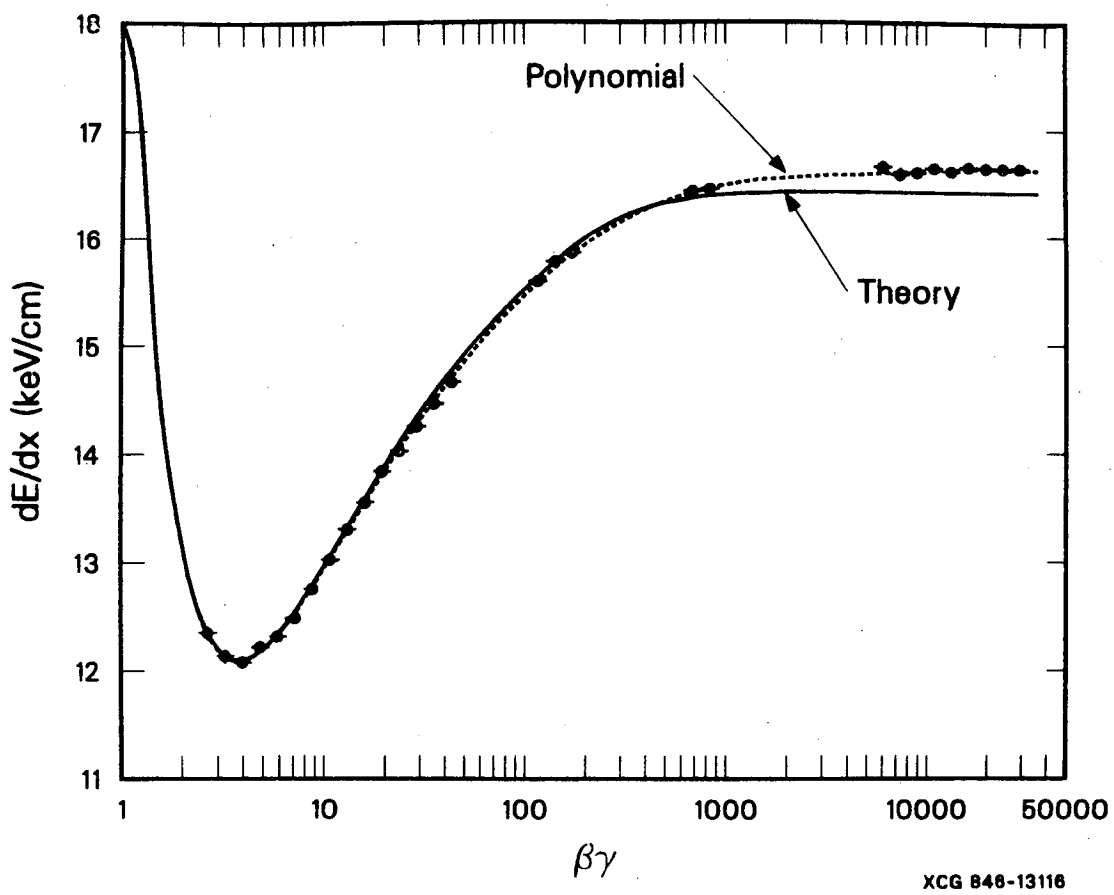

Figure 4.2: Theoretical Energy loss vs $\beta\gamma$ and what we fit using TPC data.

probably because of momentum measurement problems. Measurements of the energy loss curve using a 14 kG magnetic field show that there is no difference between the theoretical curve and the data even at the high momenta[62]. The principal difference between the 4 kG data and the 14 kG data is the improved momentum resolution.

Chapter 5

Data Reduction and Event Selection

This Chapter describes how multi–hadronic events were selected for detailed analysis, corrections applied to this data and finally how events with probable hard gluon radiation (so called *3 jet* events) were selected from the overall set of multi–hadronic events.

We must first find tracks in order to classify the events detected by the TPC. Once we compile the raw data from the TPC detector, we find and associate a momentum and energy loss for each track detected by the TPC. Also we must make corrections dependent on the conditions inside the TPC. In practice we had to approach this problem iteratively as it was impossible to make the corrections without first having a rough idea of what the tracks were. We then used this rough knowledge to improve our space points and to make corrections to these space points. Using the updated set of space points we could then refit the detected tracks.

A multi–pass analysis was implemented in the 1982-1983 data cycle to carry out this analysis. We improved on the iterative process by computing data constants online during the next data cycle in 1984-1985. However I shall only examine the procedures used in 1982-1983 here.

5.1 Track Reconstruction

Let us recall our orthogonal coordinate system definitions from the previous chapter:

- η is the distance from the middle of the sector to the space hit along the pad row,
- ξ is the distance from the base of the sector to the space hit and
- z is the coordinate of the origin of the ionization along the beam axis where $z = 0$ is at the midplane.

The z coordinate is measured by using the charge storage capabilities of CCD's as was mentioned in the electronics section. However, we have not described how to extract these coordinates from the raw space point hit yet.

When a particle traverses any medium, it leaves little bunches of ionization along the path it traversed in that medium (a track). As each of these bunches of ionization drift toward our detection device (in our case a sector), the cloud of ionization diffuses. The clouds of ionization are pushed along the z axis by the electric field and it is therefore convenient to talk about the diffusion along this direction (longitudinal diffusion) separately from the diffusion perpendicular to the direction of motion.

The time it takes for ionization to reach the sector is $(100\ \text{cm} - |d|)/v_z$ where v_z is the drift velocity and d is the z coordinate where the ionization was produced. Hence as long as we are able to measure times on the order of σ_z/v_z by the CCD's we will be able to determine the time of arrival of the ionization at the sector. The diffusion along the drift direction after a one meter drift in Ar-CH_4 is on the order of 3.5 mm. For our conditions, v_z is about 5 cm/μsec. As long as the CCD's can measure times on the order of 50 ns we will be able to determine the

z position of the ionization in the chamber by fitting the number of electrons detected as a function of time.

We define a cluster as three consecutive CCD buckets above the pedestal or quiescent level of an individual electronic channel, and where the middle bucket is a local maximum in pulse height. Recall that in the electronics section we said that the electronics was to first order linear in its response to the number of electrons drifting to a wire. Hence a local maximum in pulse height translates to a local maximum in the number of electrons detected in time. The cluster pulse heights then determine a parabola as a function of time. This gives an expected location of the true maximum in time. By multiplying the expected maximum time by the drift velocity we determine a preliminary z coordinate. This is the procedure used on wire channels.

For the pads, we follow a similar procedure to determine the coordinates in the plane perpendicular to the direction of drift. Due to diffusion perpendicular to the drift direction, the ionization cloud usually extends over at least two adjacent pads. We have to try to associate adjacent pad hits together and form a single space point. We begin by using the same procedure used on wire channels to determine the z coordinate. But if hits on two adjacent pads are within a tolerance in z, we associate the pad hits as originating from the same particle. The hits must be within the larger of two CCD buckets or two CCD buckets times $\tan\lambda$ where $\tan\lambda = z/R$, R being the radial position on the sector of the hit. Two CCD buckets correspond to 1 cm at the drift velocity of 5 cm/μsec. This definition also extends to three pad points. If all three pads have a z coordinate which satisfies the two pad hit criteria, all three pad points are called a single space point. Finally, the z coordinate for the space point is the weighted average of all the z's of each individual pad hit.

The diffusion perpendicular to the direction of drift is equal to

$$\sigma_\perp \propto t \times \frac{1}{P\sigma}\sqrt{\frac{(kT)^3}{m}}$$

where P is the pressure, σ is the elastic cross section for drifting electrons interacting with the gas molecules, T is the temperature of the gas, m is the mass of the electrons and t is the drift time[51]. This width is modified by several effects which will be described later. In total, the pad response width is typically about one half of a cathode pad. The following table gives the percentage of hits which have one, two or three pads[52]:

Number of pads	Percentage of total hits
1	5%
2 pads	55%
3 pads	40%

We can fit a gaussian of the form

$$H_p = H_0 \exp^{(\eta-\eta_0)^2/2\sigma^2}$$

for the pulse heights along the pad row[63]. In this formula H_p is the pulse height on a pad, H_0 is the pulse height of the avalanche, η is the coordinate at the center of the pad and η_0 is the coordinate of the avalanche. If only two adjacent pads are affected by the avalanche, then we need to know the σ in order to determine the gaussian. However if three pads are in a hit, the gaussian is completely determined.

This simple picture of space points then must be corrected for ionization fluctuations and electrostatic distortions before we can make the final track fits. But this is the basis by which we determine the points of ionization left by a track in the plane of the sectors. We now can discuss how track finding and measurement was done step by step.

5.2 Multipass analysis of 1983–1984

Pass 1: Online Data Analysis

During online running, our goal was to make sure to record all "interesting" events and reject obvious "junk" events. "Interesting" events are events that have physics relevance or somebody is willing to analyze. "Junk" events are events which had the signature of cosmic ray, beam-gas or beam-beampipe events. We are constrained to do the classification in 100 ms because our event rate for triggers was 1 to 3 Hz.

We show in Figure 5.1 a typical "interesting" multi–hadron event from an end and side view. Figure 5.2 shows what reconstructed data for the same event looks like in the TPC itself. Notice how free of background the data is. Also notice that we have a three dimensional reconstruction of the data. The combination of low background and having a three dimensional reconstruction allow us to design a very fast and effective filter for rejecting non–interesting events.

We used Digital VAX series 11/780 computers for our online running. We used the same computers for our offline processing so we could use the same programs to run on and off line. There were many benefits we gained by doing this, not the least was that we cut down on redoing the same sort of analysis. But online we gained the ability to select a random subsample of events to analyze completely which were used to monitor the detector systems.

We had an online filter program called **PREANALYSIS** whose function was to reject obvious "junk" events. Basically it searched for the tracks which triggered the Detector. The program used the information from the majority logic trigger units described earlier to define the triggering tracks. The trigger requires that a charged track extrapolate to within 30 cm of the interaction point in z to be considered a "good" track. However we can make tighter cuts on tracks

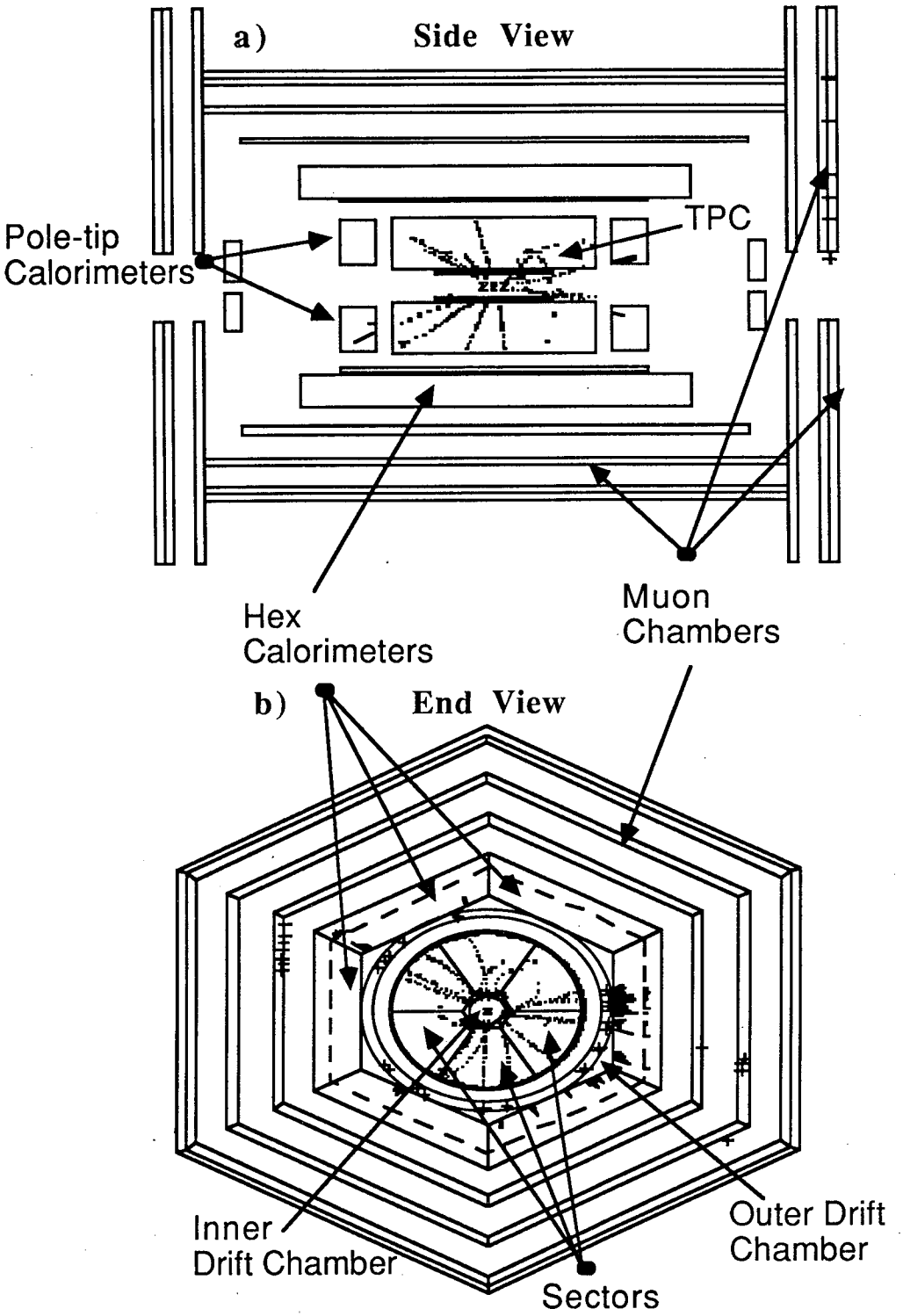

Figure 5.1: Typical multi–hadron event in the PEP–4 detector. a) View from side and b) view from end.

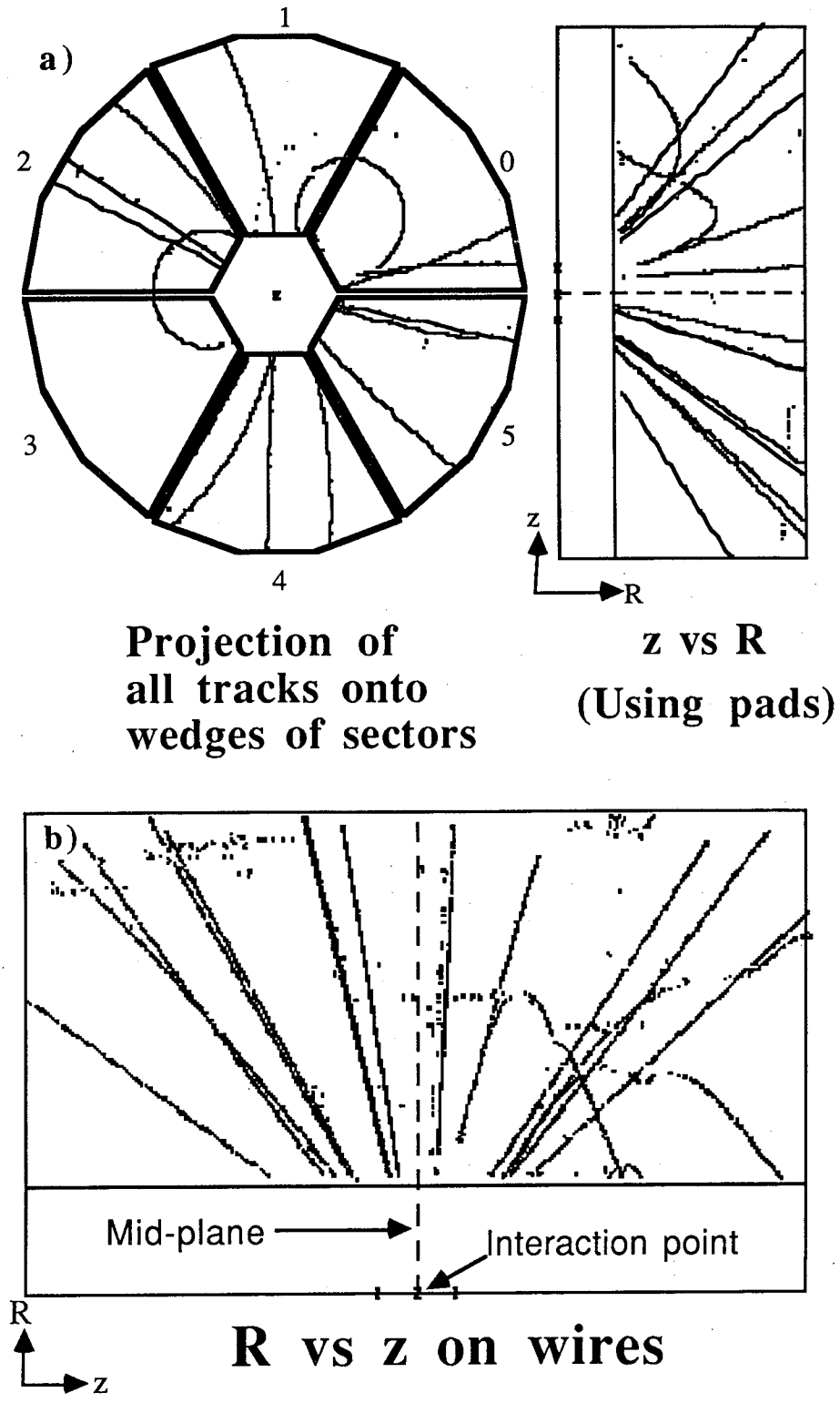

Figure 5.2: Typical multi–hadron event as seen by the sectors. a) Pad data and b) wire data.

with the information from the TPC. Using the digitized data from the sector we can now require that a track be within 14 cm in z and 10 cm in the xy plane of the intersection point. This mostly eliminates beam-gas related background and cosmic ray events from our data sample.

Also if we had a neutral trigger, we required that the shower be consistent with an electron or photon to eliminate false triggers caused by cosmic rays. If a cosmic ray traveled parallel to the cathode plane of a layer, it could deposit enough ionization to exceed the energy threshold of the trigger. Events such as this were eliminated by a simple pattern recognition cut on the shower shape.

Pass 2: Pattern Recognition

Once online filtering has rejected obvious junk events, we can find tracks offline. We find tracks by first forming η clusters described earlier in this chapter. We do the crude job of determining the most probable η position, η_0, of the avalanche along the pad row. We do the simple weighted average of the pulse heights to determine the avalanche position. We then associate a set of η clusters as a track by three different algorithms. They are, three point circle fit, two point circle fit with the third point assumed to be the interaction point, and a histogramming method. The various algorithms are discussed in detail in references [39,57]. I will here present a thumbnail sketch of how they work.

The three point circle fit takes sets of three pad points and tries to fit a helix to them. Since the TPC measures the three dimensional space points, a helix is overdetermined by this set of three pad points. Therefore, we can reject bad tracks extremely quickly. Not all combinations of three pad points are tried. Rather, all possible combinations from particular specified sets of three pad rows are used. The two point circle fit follows a similar scheme except the third point is assumed to be the origin. In both schemes tracks are kept only if the number

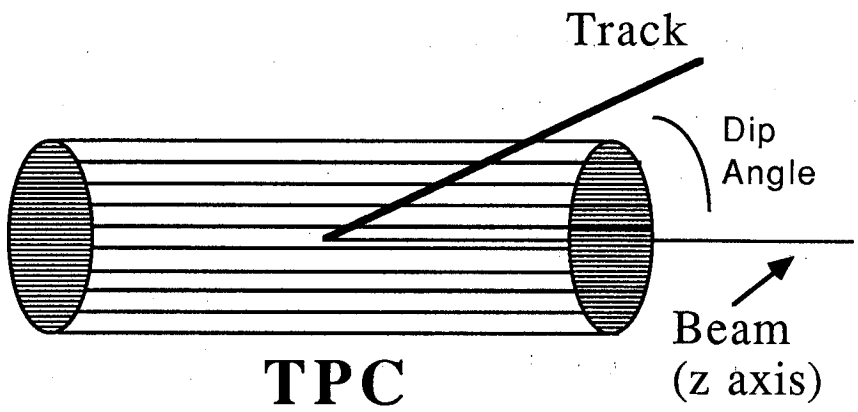

Figure 5.3: Definition of the Dip angle in the TPC.

of good points on them exceeds a certain value. The number of good points ranges from four to seven depending on the track topology (high dip angle tracks require less, and low dip angle tracks require more).

For events with a large number of hits, neither of the above algorithms is used. The amount of time spent checking all possible three (or two) point combinations goes as a high power (≈ 10) of the number of points in that event[57]. We use the histogramming algorithm for large events instead. The idea of the histogramming algorithm is to quickly bin together points which would lie on the same track. It is done by first histogramming pad points into bins of $\sin\lambda$

$$\sin\lambda = z/\sqrt{x^2+y^2+z^2}$$

where λ would be the dip angle of the track (see figure 5.3) if the track originated at the interaction point. A point in a particular $\sin\lambda$ bin is selected. This point is called the privileged point. A circle is then fit to the privileged point, the origin

and another point in the histogram bin. The sagitta for the circle is calculated and histogrammed. For each other point in the histogram, a circle can be formed and for each circle we histogram the sagitta of that circle. The largest sagitta bin is chosen as the orbit road. All points which lie within ± 2 cm of the fitted circle are kept. We repeat the same procedure for all the points which have been rejected by this method. Finally, at the end of the procedure, track segments are merged together if they fit a single orbit, and duplicate tracks are rejected. At the end, we attempt to find tracks with pad points which have not yet been placed on a track using the two point algorithm. Overall the pattern efficiency for finding tracks hitting more than three pad rows was measured to be $95 \pm 5\%$[57]. Pattern is not 100% efficient because of electrostatic distortions which especially effect low angle tracks, dead pad channels and decays of charged hadrons in flight.

We can now make tighter cuts on the events to further reduce our background. For a track to be considered good, it must pass within 10 cm in z and 5 cm in the xy bending plane of the interaction point. We then make a preliminary classification of the event and unless the event falls within some physics category it will be thrown out. For instance, only events consistent with $\tau\overline{\tau}$ would be kept for further τ analysis. The same could be said for hadronic, and two photon analyses.

Pass 3: Monitoring of Constants

We now must begin correcting our space points and dE/dx measurements for detector effects. The first step in this process is to determine detector constants.

In general, we read out many important monitored values event by event. This included voltages for all detector systems, temperatures of the sectors, field cage voltages etc. We then use this data to form best guesses for gain and drift velocity. This still leaves us with run to run variations of the gain and drift

velocity. We then correct these variations by run. The rest of this section will be devoted to describing the way each of the constants was determined.

- The most important constant beside the gain was the drift velocity. The measurement of the z coordinate is the way the TPC gains its ability to determine an event in 3 dimensions. The drift velocity is expected to be a function of the electric field to pressure ratio, which can be approximated by a polynomial[64,65],

$$v = ax + bx^2 + cx^3 \tag{5.1}$$

where $x = E/P$, E the electric field, P the pressure in the TPC and a, b and c are fitted constants. We modified this expression to correct for pressure effects and for variations in the fraction of methane

$$\begin{aligned} x' &= x(\frac{P}{P1})^G \\ x'' &= x'(\frac{0.2}{f})^H \end{aligned} \tag{5.2}$$

where P is the pressure, and we normalize to pressure $P1$ chosen to be 8.5 atm of pressure and f is the measured methane fraction. We use x' to correct for pressure effects and x'' to correct for variations in the fraction of methane (note that 0.2 is the nominal fraction of methane). While these expressions don't have a theoretical basis, we get a good representation of the data by setting H to 0.8 and fitting G to $G = 0.093 \pm 0.008$. Our corrected expression for the drift velocity in the TPC is

$$v = (\frac{f}{0.2})^Q \times (ax'' + bx''^2 + cx''^3)\,. \tag{5.3}$$

Setting Q to 0.3 gives the best representation of our test data from August and November 1980.

This expression is a reasonable estimate of the drift velocity in the TPC. However our knowledge of the methane fraction is limited. Also one worries that the drift velocity depends on experimental conditions since the two measurements of the drift velocity in Ar-CH_4 don't agree with each other and also not with our measurements inside the TPC[66,67,64]. Furthermore, we cannot control things like gas purity, and the temperature inside the TPC changes throughout the day. Hence we took the approach of using the above formula at the beginning of the run to determine the drift velocity and then using the data to measure the drift velocity on a run to run basis.

We can measure the drift velocity in the TPC by selecting cosmic rays which pass thru both the mid–plane and the sector, two track events like bhabha scattering ($e^+e^- \rightarrow e^+e^-$) or $e^+e^- \rightarrow \mu^+\mu^-$ and requiring such events to match in z. Or we can plot the z position for all tracks detected in a particular endcap, requiring that no track be from the opposite side of the mid–plane. We chose the latter method because of the larger amount of statistics available.

- The drift velocity must be corrected for a 1.5°C/m temperature gradient from top to bottom inside the TPC. The drift velocity depends on the pressure and hence the temperature. It manifests itself as a continuous correction from top to bottom in the dip angle because the z position determines the dip angle. It can be expressed as

$$\Delta \tan\lambda = \frac{2\Delta T F}{T}(1 - 1.3\tan\lambda) \tag{5.4}$$

for $y = 0.4$ meters to $y = 0.9$ meters where ΔT is the thermal gradient, F is the slope of the drift velocity vs temperature curve and T is the average temperature[68].

- Another important constant is the beam interaction point. We measure it on a run to run basis. We do this by plotting the vertex position (the common point of all tracks found during pass 2) for all events.

- We lose a certain number of electrons during the drift in long length drift chambers. This is because of capture of electrons by impurities in the gas. For instance 0_2 contamination as low as 0.15 ppm Ar-CH_4 leads to a 1% loss of electrons drifting 1 m in the TPC. Also diffusion affects the rise time of the signal on the wires which changes the electronic response. This effectively does the same thing as electron capture and results in interpreting the reduced pulse height as reduced dE/dx. We must correct for this effect. We do this by plotting pulse height vs z. We can parameterize the electron capture as

$$N = N_0 \exp^{-\alpha L/L_M} \tag{5.5}$$

  where α is the coefficient of electron capture, L is the drift length, L_M is one meter, N_0 is the original amount of ionization and N is the observed ionization[69,70]. This equation also applies to pulse height since pulse height is directly proportional to the number of electrons. Hence the slope of the log pulse height vs z curve gives α. A typical value of α is 0.15 which implies a 15% loss of electrons for electrons drifting one meter.

- We must calibrate the wires. Temperature variations inside the electronics hut will affect the CCD's. The dark current inside these devices depends on the temperature of the device itself and hence the pedestal level will change as a function of time. On average this will change only the overall gain, if we assume each CCD is affected in the same way. The gas purity varies from tank to tank, also affecting the overall gain.

  We correct for gain variations by defining minimum ionizing particles to lose

12.1 KeV/cm in our Ar-CH_4 mixture. We associate wire hits with tracks found in Pass 2 by requiring the origin of the ionization hitting the wire to be within ± 1 cm in z of the presumed track's orbit. If two wire hits on the same wire are within ± 3 cm, we do not use either of the two hits on any track This is because the recovery time of the amplifier makes it difficult to determine the actual pulse height of hits within one half microsecond. If a wire has saturated (where the digitized pulse height vs actual pulse height curve flattens out), we remove that wire's neighbors from the list because we cannot estimate the contribution of cross-talk to the neighboring wire signals.

The 65% truncated mean is then determined. We discard the top 35% of the wire pulse heights and use the average of the remaining pulse heights as an estimator of the average energy lost per 4 mm track segment. We eliminate the tail of the Landau distribution by discarding the top 35% of the wire pulse heights. Sector by sector we require that minimum ionizing pions lose the 12.1 KeV/cm over a run. Recall that electrons are projected to lose about 15 KeV/cm and pions about 12 KeV/cm at 500 MeV/c. Hence in order to reject electrons we do not take all tracks with momentum range corresponding to minimum ionization for pions in Ar-CH_4. Rather we take a wide swath of 2.0 KeV/cm about 12.1 KeV/cm in order to insure that we have only pions.

- Finally run to run constants to calculate electrostatic distortions were calculated. Most of the distortions were caused by positive ions liberated during an avalanche passing back thru the grid and into the drift volume. Additionally the surface of the field cages accumulated charge during the run. We shall discuss distortions in the next section.

Pass 4: Track Reconstruction

We are now able to refine our found space points once we have a preliminary idea of the particle momenta. We can now "hang" wires onto the tracks for dE/dx determination.

Our primary problem is to correct the space points for ionization fluctuations and distortions. We also must make a more accurate determination of the η coordinate. Along the η coordinate the ionization cloud is a gaussian. If three pads are hit, a gaussian which passes through each of the three points is determined. If only two adjacent pads fire, we need to know the sigma of the distribution to determine the gaussian. In either case, using a gaussian form for the pulse heights along the η coordinate is a great improvement over the weighted average method.

Our ability to track particles with the TPC depends on knowledge of σ because one half of the pad hits have one or two pad points. The σ of the gaussian distribution in the η–ξ plane depends principally on the crossing angle of the track to the pad row. The expression for σ of this distribution can be parameterized as the sum of several contributions

$$\sigma^2 = \sigma_0^2 + \sigma_1^2 + \sigma_2^2 \tag{5.6}$$

where σ_0 is the intrinsic width of the pad response due to a point charge at the sense wire including electronic noise[63]. The contribution of diffusion to the width of the pad response distribution is σ_1. The contribution to the broadening due to tracks crossing the sense wires at an oblique angle is estimated by σ_2. We also include in this term the contribution due to the fact that five wires contribute to the signal on a pad row, not just the wire directly above the row, and $E \times B$ effects.

Figure 5.4 shows the situation of a track at angle α to the sense plane. We

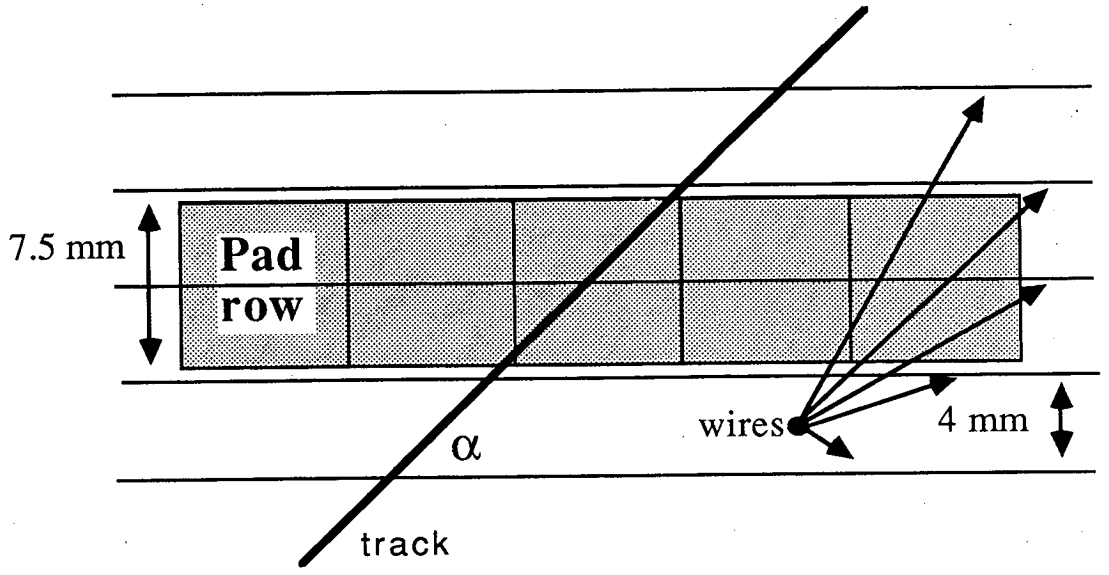

Figure 5.4: Typical oblique track to wires and pads.

can use this picture to determine what the σ_1 and σ_2 terms should be.

$$\sigma_1^2 = \sigma_\perp^2 \frac{L}{L_M}(1 + \tan^2 \alpha) \tag{5.7}$$

and

$$\sigma_2^2 = D^2(\frac{1}{12} + S_2)\tan^2 \alpha \tag{5.8}$$

where L is the drift distance, L_M is the maximum drift distance (one meter inside the TPC), α is the angle the track makes to the normal of the sense wires, $\sigma_\perp$ is the RMS transverse diffusion after drifting one meter, D is the distance between sense wires,

$$S_2 = \sum_{i=-2}^{2} i^2 \frac{w_i}{S_w}$$

$$S_w = \sum_{i=-2}^{2} w_i = 0.5$$

and w_i is the weight of the i^{th} wire. The values of the weights are $w_0 = 0.239$,

$w_1 = 0.117$, $w_2 = 0.0135$, and $w_{-i} = w_i$.

The σ_1 term arises because the RMS diffusion of the electron cloud is proportional to the time the electron cloud has drifted. The $\tan^2 \alpha$ term occurs because, for angled tracks, we must consider the diffusion normal to the wire.

We now must consider the effect of having several wires contribute to the signal on a pad as opposed to the wire above the row. This is the σ_2 term. Consider a track crossing a wire at angle α. Then we would collect ionization along a length of wire $\approx D \tan \alpha$. The primary electrons produced along the length $D \tan \alpha$ now each diffuse. If we assume the electrons are produced with equal probability along $D \tan \alpha$, then this effect contributes

$$\sqrt{\frac{1}{12} D^2 \tan^2 \alpha}$$

to the sigma of the pad response.

We also must consider the effect of having anomalously high ionization on any one of the five wires which contribute most strongly to the pad signal. We assume that the pad response is gaussian. But the actual signal is actually a sum of five displaced gaussians. The term

$$\sqrt{D^2 \tan^2 \alpha \times S_2}$$

estimates the contribution to the sigma of the pad response because of this effect.

We can actually measure the variation of σ with respect to α by using the sigmas determined with three pad points on a track. Reference [52] has further details on the measurement of this variation.

Finally space points must be corrected for distortion effects. Distortions in the TPC are due mainly to positive ion feedback. Positive ions are liberated during avalanches and are attracted to the midplane. Radiation from the beam and real events is preferentially emitted along the beam direction. Hence we expect that most of the positive ions will be produced at low radius. Also the

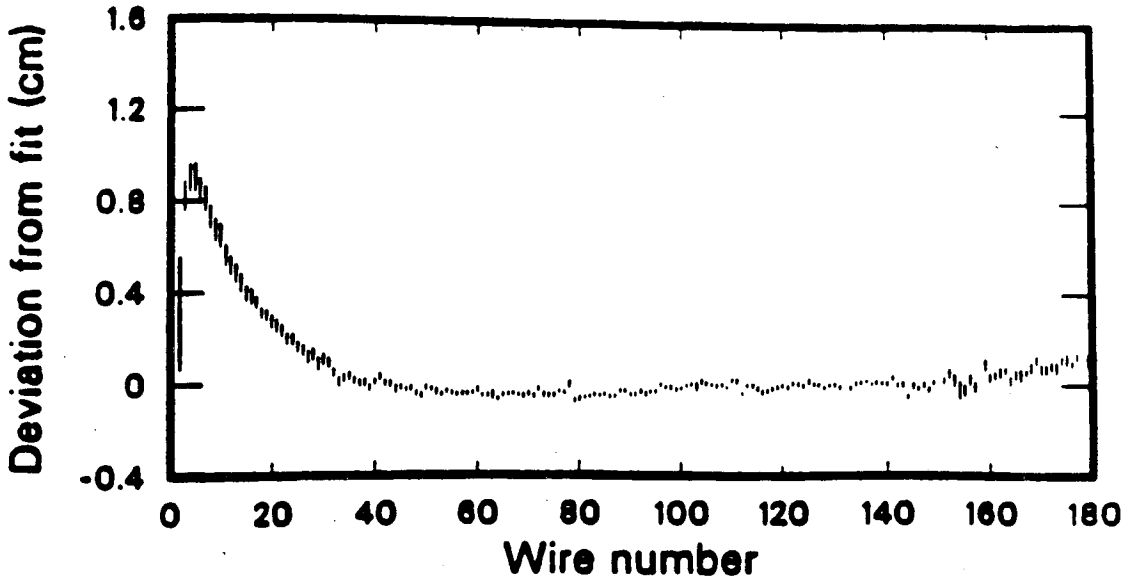

Figure 5.5: Residuals vs wire number. To make this plot we fit radius vs z for the track using only wires between wire number forty to one hundred fifty. This fit is distortion free showing the effect of distortions especially at low radius.

field cages which form the uniform electric field have inhomogeneities in their bulk resistance properties. This means charge builds up on their surfaces. These two facts imply that most of the effects of electrostatic distortions will be at low radius. Figure 5.5 graphically depicts the effect. We plot in this figure the residual in z vs wire number. We fitted r vs z using wires between wire number forty to one hundred fifty. This should be the straight line

$$z = R \tan \lambda \tag{5.9}$$

where λ is the dip angle. We used wires in the middle of the TPC to remove the effect of distortions from the fit. The largest residuals are at low radius although at larger radius there is a much smaller systematic effect.

We can parameterize the charge density which produces these distortions as a gaussian in radius plus a constant. This charge distribution gives rise to a nearly

radial field. It is not perfectly radial because of the hexagonal shape of the inner field cage. Nevertheless, at each sector the field is perpendicular to that wing of the cage. We find the perturbed velocity is given to first order by

$$\begin{aligned} \frac{d\vec{\mathbf{v}}_{\mathbf{p}}(t)}{dt} &= \frac{d^2\vec{\mathbf{x}}_{\mathbf{p}}(t)}{dt^2} \\ &= \frac{e}{m}\vec{\mathbf{E}}_{\mathbf{p}}(\vec{x}(t)) \end{aligned} \tag{5.10}$$

where $\vec{\mathbf{v}}_{\mathbf{p}}$ is the perturbed velocity, $\vec{\mathbf{x}}_{\mathbf{p}}$ is the perturbed position, $\vec{\mathbf{E}}_{\mathbf{p}}$ is the perturbed electric field and $\vec{x}$ is the unperturbed trajectory of the drifting electrons. We can see that particles produced in an e^+e^- interaction are hardly affected by the distortions. This is because the perturbation is integrated over time. A particle produced in an e^+e^- interaction spends a factor of ten thousand less time than the ionization electrons produced along the particle's path inside the TPC. Hence any error in the tracking of a particle is dominated by the effect of the defects on the electrostatic field on the drift electrons.

We must correct the ξ and η coordinates measured by the sectors. The ionization measured by the sector coordinate (ξ, η) really originated at coordinate $(\xi + \Delta\xi, \eta + \Delta\eta)$. Figure 5.6 pictorially shows the effect of the perturbing field on the measured ξ coordinate in the ξ–z plane. The larger the coordinate ξ, the smaller the effect because of the exponentially decreasing perturbing electric field. A distortion map was calculated using equation 5.10. This map related the measured coordinates to the "true" coordinates.

The map gives the shape of the distortion but the magnitude depends on the amount of positive ions inside the TPC at the time of the event. We determine the charge in the chamber by using the fact that at large radius the distortions produce a negligible effect. As figure 5.6 shows, there is an effective z distortion because of the radial distortion field. At measured coordinate (ξ, η), the track should have really passed thru coordinate $(\xi, z + \Delta z)$. If the track was at dip

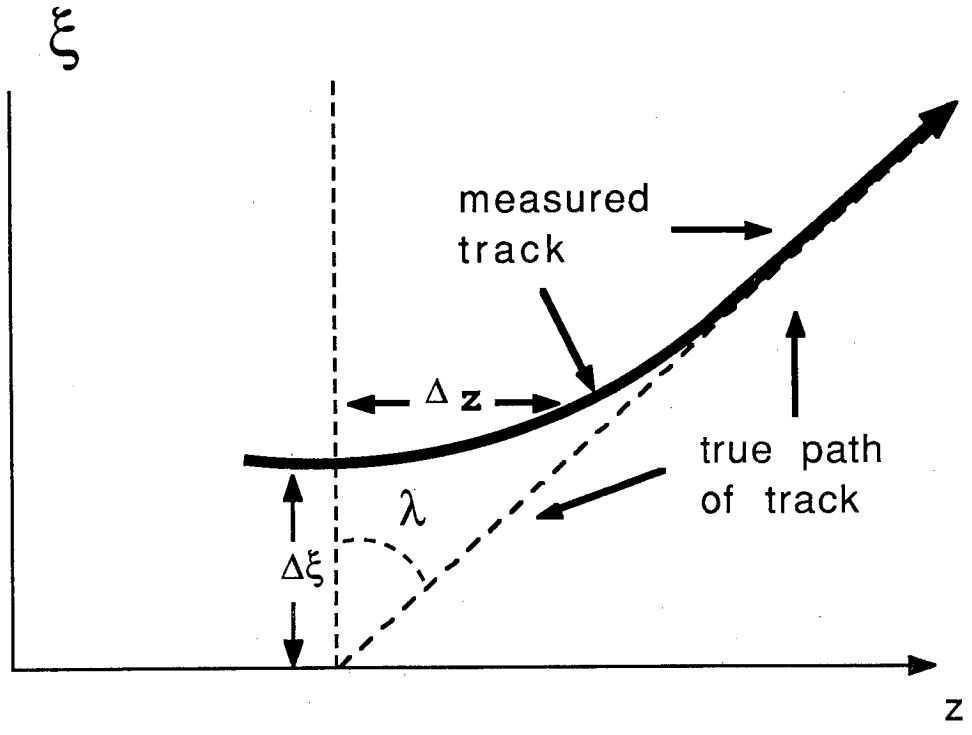

Figure 5.6: Distortion effect on ξ, η and z coordinates measured by the sector.

angle θ, then Δz is related to $\Delta\xi$ by simple geometry:

$$\Delta z \tan\theta = \Delta\xi\,. \tag{5.11}$$

But $\tan\theta$ can be determined in the ξ–z plane by fitting a line to the middle wires (wire numbers 40-150). We average

$$\frac{\Delta\xi^{map}(\xi,\eta,z)}{\Delta z \tan\theta}$$

over all tracks to determine the amplitude factor A for the pad correction. All space points are then corrected by

$$\begin{aligned} \xi &\hookrightarrow \xi + A\Delta\xi^{map}(\xi,\eta,z) \\ \eta &\rightarrow \eta + A\Delta\eta^{map}(\xi,\eta,z) \\ z &\rightarrow z\,. \end{aligned} \tag{5.12}$$

We don't use this procedure for tracks at low dip angle. Here we cannot determine A as above because we cannot easily determine z residuals since z is constant.

Instead we determine an average correction for the entire run in Pass 3 and use this nominal A for the sector coordinate correction for low dip tracks.

We make our final orbits by an iterative process. First we must attach errors to each space point for ionization fluctuations, diffusion, electron capture and distortions. We then minimize the χ^2 for a projected track to refit the momentum and dip of the orbit. We also must correct our dE/dx measurements. Longer sample length per cell because of track dip or distortions must be corrected for.

We can assign a mass using the improved momentum and dE/dx. We now improve our orbit inside the TPC by estimating the energy loss inside the gas for a particle of this mass. We estimate the multiple scattering and energy loss inside the material in front of the TPC and extrapolate the orbit to its closest approach to the e^+e^- beam interaction point. The final step in the process is to require a common origin to all tracks detected in the TPC. This is called the vertex position. If a particular track exceeds a threshold χ^2 when we constrain the origin to the vertex, this track is assumed not to have originated there. We iteratively refit the remaining detected tracks to a new common origin until all tracks constrained in this manner are under the threshold.

Finally we try to find K^0 and Λ^0 vertices using all tracks. This capability was not used in this study.

Pass 5: Hadronic Event Sample

The final step of our data reduction was to isolate a multi–hadronic event sample. It is convenient to consider first the problem of how we determine the most probable species of a particular track. We begin by discussing the particle identification properties of the TPC.

Particle Identification by the TPC

In chapter 4 we discussed the expected energy loss curve for a particular particle. We expect that the most probable energy loss for the particle to be a function of $\eta = p/m$ where p is the momentum and m is the mass of the particle. The TPC, by virtue of its ability to measure energy loss and momentum simultaneously, can determine the mass of a particle. Figure 5.7 shows what the dE/dx versus p curve looks like for the entire hadronic sample. Overplotted onto the data is the fit of the average energy lost per centimeter versus momentum for the different particle species.

There are ambiguous momenta where the mass cannot be determined uniquely because the energy loss for particle species A of mass m_A is the same as for particle species B of mass m_B. We call the points where the dE/dx vs p curves for the two particles intersect, the **cross–over** points. But our detector is also not perfect. We cannot measure energy loss or momentum to infinite precision. The cross–over points are smeared by our detector resolutions to regions of ambiguity(so called cross–over regions). Therefore we must rely on a *statistical* separation of particles.

We begin by taking a slice in momentum of the dE/dx vs p plot. We assume a gaussian distribution of each species of particle in dE/dx. We center this distribution at the expected dE/dx for that species at the momentum corresponding to the center of the momentum slice. We determine a sigma of the gaussian based on our detector resolutions in momentum and energy loss. We sum over all particle species to determine what we expect the data to be for any given number of each species. Finally we fit the number of each species by maximizing the likelihood that for these fitted numbers we would observe our data.

Figure 5.8 shows an example of this fit for two different momentum ranges. We use the more convenient ratio of dE/dx divided by dE/dx expected for a

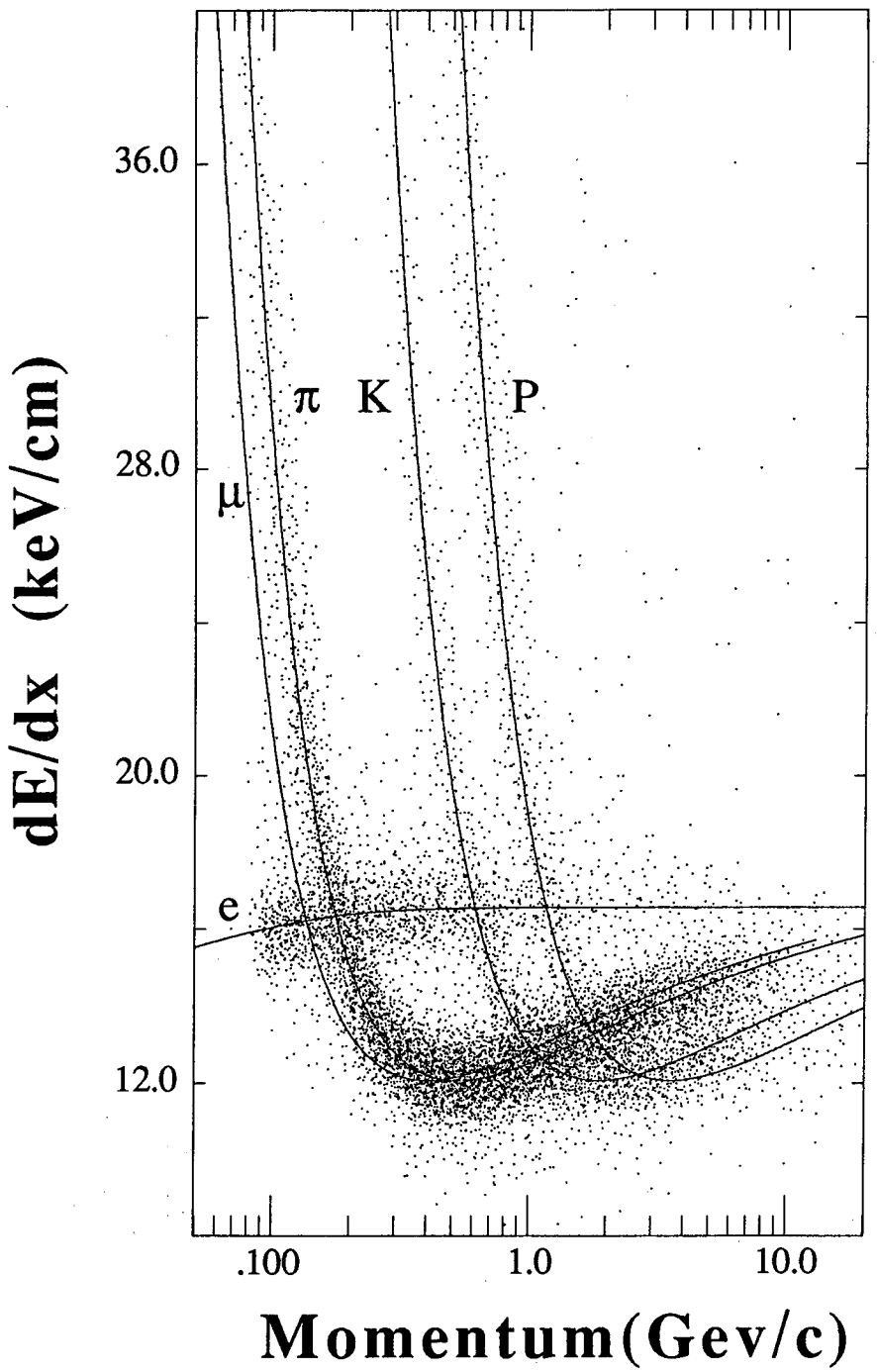

Figure 5.7: dE/dx vs p for the entire data sample under analysis. Overplotted onto the data is our expected average energy loss.

pion of that momentum in the plot. By using this ratio which is denoted

$$\mathcal{R} = (dE/dx)_{measured} \Big/ (dE/dx)^{\pi}_{expected} \tag{5.13}$$

where $(dE/dx)^{\pi}_{expected}$ is the expected energy loss for a pion at our measured momentum, we are able to attain better histogramming resolution and remove most of the variation of the dE/dx curve (most of the particles we observe are pions anyway).

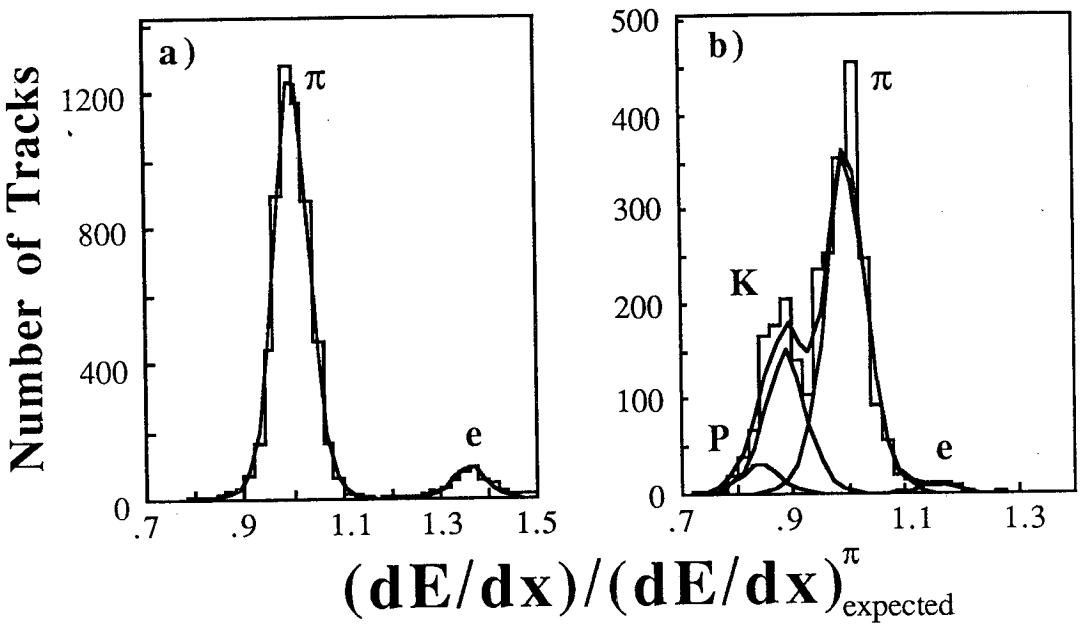

Figure 5.8: Fitting $\mathcal{R}$ for two different momentum slices. Figure a) uses the momentum slice from 450 MeV/c to 550 MeV/c whereas b) uses the slice between 3.7 GeV/c to 5.0 GeV/c. In figure a) pions are well separated from all other particles.

In figure 5.8a, we take the momentum slice 450 MeV/c to 550 MeV/c. Pions in this momentum slice are at minimum ionization in Ar-CH_4, 12.1 KeV/cm. In this slice we see that pions and electrons are well separated but the cross–over region for kaons and electrons has begun. By contrast figure 5.8b shows the momentum range 3.7 GeV/c to 5.0 GeV/c. Here the pions are at best some-

what separated from kaons and protons but kaons and protons are nearly totally confused.

Therefore, the width and center of the distribution of $\mathcal{R}$ for each particle species is vitally important for our statistical separation. We defer until next chapter a discussion of width. We must correct the center of the dE/dx distribution by considering the variation of the number of particles as a function of momentum thru the momentum slice taken. The equation

$$\langle p \rangle = \frac{\int_{p_l}^{p_h} pN_i(p)dp}{\int_{p_l}^{p_h} N_i(p)dp} \tag{5.14}$$

is the average momentum in the momentum slice from p_l to p_h for particle species i where $N_i(p)$ is the spectrum in momentum for this particle species. Using this value for the average momentum gives the average η for any particular particle species and is what should be used in determining the center of the dE/dx distribution. We used the Monte Carlo to estimate the effect of $N_i(p)$ changing over the momentum bin. We also must correct for detector acceptance and average energy loss for each particle type in the material directly in front of the TPC. Further details for the procedure used can be found elsewhere [53,71].

Armed with the numbers of different particles as a function of momentum, we can now make a probability for a particular track being each of the different possible species of charged particle detected in the TPC. We define χ^2 for a track being particle species i as

$$\chi_i^2 = \frac{(\eta_i^{measured} - \eta^{best})^2}{\Delta\eta^2} + \frac{\left((dE/dx)_{measured} - Tr(\eta^{best})\right)^2}{\Delta(dE/dx)^2} \tag{5.15}$$

where $Tr(\eta)$ is the most probable energy loss for a particle at $\eta = p/m$. We minimize this χ^2 to determine η^{best} for each separate charged particle type detected by the TPC. We define the probability of a track being a particular particle

species i as

$$\mathrm{Prob}_i(\chi_i^2) = \frac{N_i(p)}{N_T(p)} \exp^{-\chi_i^2/2} \Big/ \sum_{i=1}^{5} \frac{N_i(p)}{N_T(p)} \exp^{-\chi_i^2/2} \tag{5.16}$$

where $N_T(p) = \sum_{i=1}^{5} N_i(p)$ and the sum over i refers to summing over e, μ, π, K and protons. We parameterize $N_i(p)/N_T(p)$ as a linear function of $\ln p$ for all hadrons, $(0.2/p)^2$ for electrons and zero for muons.

The efficiency of this method to isolate a particular particle type is momentum dependent because of the crossover regions. But our ability to separate electrons from hadrons is quite good over the entire momentum range.

Event Selection

Our goal is to isolate a highly pure sample of $e^+e^- \rightarrow \gamma^* \rightarrow q\overline{q}$. We must eliminate backgrounds from $\tau\overline{\tau}$ events, two photon events and events due to beam interaction with either gas molecules in the beam pipe or with the inner pressure wall of the TPC. We accomplish this goal by first taking a set of well measured tracks and then using that set of tracks to see if the event could be a $q\overline{q}$ event.

A well measured track has:

A Momentum $>$ 120 MeV/c. Particles must traverse a considerable amount of material to be detected by the TPC. Particles of momentum less than 120 MeV/c are most probably secondary interaction remnants (and so did not traverse all the material in front of the TPC) and hence are not related to the primary interaction.

B The extrapolated point of closest approach of the track to the interaction point must be less than 6 cm in the xy plane and 10 cm in z. This gives the best possible cut on tracks not from the primary vertex. We do not

consider V^0's in making the decision to keep the event as a multi–hadronic candidate.

C The polar angle of the track must be greater than 30°. Tracks with a smaller polar angle only cross 1 or 2 pad rows and hence the momentum measurement of these tracks is suspect.

D We require dC to be less than 0.3(GeV/c)$^{-1}$ or dC/C to be less than 0.3 where C is the measured curvature. We throw out badly measured tracks with this cut.

Finally we require

E more good than bad tracks in an event.

If an event passes cut E, we subject our set of good tracks to cuts to eliminate background sources. A track is considered to be **consistent** with an electron if χ^2_e (χ^2 is assigned as described in the previous subsection) for the track is less than 9. If in addition the track's χ^2_e is less than χ^2_i for each other particle hypothesis, the track is considered an electron. If geometrical reconstruction of two tracks yields an invariant mass of less than 15 MeV, we consider the two tracks a conversion pair, and hence the tracks are considered electrons.

We now subject the event to the following cuts:

F The event must have at least five good non electron tracks, i.e., at least five tracks must not have electron as the best particle hypothesis *and* $\chi^2_e < 9$.

G One of the surviving set of tracks must not be *consistent* with an electron, i.e., $\chi^2_e > 9$ for one of the tracks.

H We divide the event into two hemispheres by taking the normal to the sphericity axis thru the interaction point [1] One of the jets on either side of this

[1]Sphericity is a standard measure for how jet–like the event is. See References [22,23] for a definition.

division must have mass greater than 2 GeV/c or have a hadronic jet multiplicity of greater than 3.

I The total energy visible in the event must be greater than 7.25 GeV/c.

J The momentum imbalance along the beam axis

$$\left| \sum_{\text{tracks}} p_z \right| \Big/ \sum_{\text{tracks}} |\vec{p}| \tag{5.17}$$

must be less than 0.40 where p_z is the momentum of a track along z and p is the momentum of a track.

Cuts F, G and H eliminate background from $\tau\overline{\tau}$. Cuts I and J eliminate two photon and beam related background interactions. We are left with about 29,000 multi–hadronic events in experiments 11 and 12 if we apply these cuts. The estimated backgrounds to this sample are listed in the following table[72]:

Source	Background (%)
$\tau\overline{\tau}$	0.4
$\gamma\gamma$	0.8
All Beam related	< 0.1

Table 5.1: Estimates of backgrounds to hadronic event sample.

5.3 TPCLUND: The Simulation of the TPC Detector

The simulation of the TPC detector is not a formal part of the data analysis chain. Nevertheless, simulating the detector is a crucial part of any physics analysis done on TPC data. Simulation of the TPC is crucial for two reasons:

1. We can check our analysis routines by simulating detector data. The simulated data is analyzed by using the same procedure and routines we use when analyzing the experimental data and

2. the simulation of the detector is the only practical way to determine detector acceptances.

We carried out these twin goals by creating two separate Monte Carlo computer programs. One Monte Carlo simulated individual ionizations inside the TPC, tracked these individual packets to each detector element, and simulated the response of the electronics. In particular, this simulated raw data is then used to check raw data analysis routines. We called this Monte Carlo "GLOBAL", because it simulated the event as precisely as we could. Unfortunately, GLOBAL takes about twenty to thirty seconds to simulate the TPC for a typical $q\overline{q}$ event on our VAX 11/780 (which we shall henceforth call VAX). This simulation would simply take too long to produce the number of Monte Carlo events we need to accomplish the second objective of event simulation.

We simplified the problem in order to reduce the time to simulate a $q\overline{q}$ event. We do not produce individual clusters of ionization, rather we rely on the bulk response properties of the materials which make up the detector. Instead of tracking the ions produced along the track to individual detector elements, we rely on parameterizations of both the drift and the electronic response to ionization. Lastly, we approximate the action of our tracking routines instead of producing simulated raw data which then must be reanalysed by our raw data analysis routines. The rest of this section will be devoted to the description of this Monte Carlo.

The simplified event simulation Monte Carlo was called "TPCLUND" or the Fast Monte Carlo (FMC). The time to simulate a typical $q\overline{q}$ event in "TPCLUND" is reduced to about two and half seconds. The simulation program divides the detector into 29 layers. Each layer does not necessarily correspond to individual detector elements. Some layers merely correspond to material inside the detector. Each layer inside the TPC itself only corresponds to one pad row,

not each wire. The seven wires below and 6 wires above and the wire directly adjacent to the pad row are associated with this layer. Hence we have reduced the number of layers required to simulate the TPC from 183 to 15. This is one reason for the increased speed of the Monte Carlo. The simulation ends at the last layer of the outer drift chamber. At this point the track buffer is passed to routines which simulated the calorimeters and the muon chambers.

The track produced by an event generator is tracked through successive layers. We include the possible decays, interactions, etc. for all particles. We include the possibility of bremsstrahlung for electrons. The energy loss is set to

$$\Delta E = \begin{cases} (b + \sqrt{b^2 - 4ac})/2a, & \beta < 0.95 \\ (dE/dx)_{min}\ \Delta x, & \beta \geq 0.95 \end{cases} \tag{5.18}$$

where $(dE/dx)_{min}$ is the energy loss for minimum ionizing particles in the particular material, Δx is the path length in the material and

$$\begin{aligned} a &= E_i \\ b &= E_i^2 + m^2 - E_i\ (dE/dx)_{min}\ \Delta x \\ c &= m^2\ E_i \end{aligned}$$

where E_i is the energy of the particle as it enters the layer. We computed the energy loss for $\beta < 0.95$ by assuming the energy loss equals

$$(dE/dx)_{min}/\beta^2$$

where β refers to the particle. For $\beta \geq 0.95$, we assume there is no relativistic rise and so the energy loss is simply given by the length of the track times the energy loss per unit length for a minimum ionizing particle. The multiple scattering for the particle is determined at the boundary of each layer.

Once the space points are determined, we must then approximate how the electronics would respond. We use equations 5.6, 5.7, and 5.8 to determine the point and its error as measured by the pads. We also add the expected

contribution of distortions to the error. Finally we increase the errors on about 30% of the pads to account for occasional badly measured tracks.

When we track particles through the TPC, we approximate the energy loss to be zero. However, the simulated data must include what the wires would measure as the average energy loss for each particle. So even though we approximate the energy loss as zero for the purposes of tracking particles in the Monte Carlo, we assign energy loss as measured by the wires by using the parameterization of dE/dx as a function of $\beta\gamma$ as detailed in section 4. We do this track by track. Let us call this expected energy loss $(dE/dx)_{exp}$.

After the tracking of the particle has been completed, we determine the number of wires associated with the track. Each pad hit has 13 wires associated with it as described earlier. We now throw out any wire where another track passed within 3 cm in z. We account for delta rays produced by hard scatters as the track passes thru the TPC and saturated wire channels by eliminating a random number of wires along the track. Of course the number of wires eliminated because of delta rays is velocity dependent. We randomly set the energy loss on a wire as a gaussian distribution centered about the average energy loss with width given by

$$\sigma = \sigma_{min}/\sqrt{N} \tag{5.19}$$

where N is the number of wires associated with the track and

$$\sigma_{min} = 3\% \times (dE/dx)_{exp} \times \sqrt{(dE/dx)_m/(dE/dx)_{exp}}$$

where $(dE/dx)_m$ is the energy lost by a minimum ionizing particle in Ar-CH_4.

Tracking is also simplified. Instead of creating simulated raw data that our usual tracking routines use, we consider any track with more than three pad rows hit inside the TPC as found. A helix is fit to the space points to determine the simulated momentum measured. If one space point is shared by two tracks

because of a decay for instance, the point is put on only one track. This is not a bad a approximation to our tracking routines since our measured pattern recognition efficiency is 95% for tracks which have more that three pad points on the track.

We also determine the vertex momentum by a simplified method. We add the expected vertex point for the interaction to each track found. We use the measured vertex position error as the error on this point. A helix fit is then performed on each augmented track separately. Contrast this method with the method used in the Data. We constrain all the tracks found to a single point in the Data.

It took about eight hours to generate 10,000 simulated $q\overline{q}$ events on our VAX. We generated 100,000 events for the purposes of determining acceptances for the $q\overline{q}$ data sample. There were detailed comparisons made between the multi-hadron events and the simulated data. Many of the comparisons can be found elsewhere[53,39]. We will not duplicate all of the comparisons here. However, we will show some comparisons of relevance to the data analysis to be detailed in this thesis. We normalize the Monte Carlo to the Data by scaling the Monte Carlo so that the same number of entries are in both the Data and the Monte Carlo histograms.

Figure 5.9a, b, c shows some overall comparisons of the data with the Monte Carlo. Figure a is the comparison between the overall momentum spectrum measured in the data and the simulation. Figures b and c together show the comparison of the dE/dx spectra.

Figure 5.10a, b and c shows the comparison of the visible energy for jets 1, 2 and 3 in three jet events. We define jet 1 as the most energetic jet in a three jet event and jet 3 as the least energetic jet. A description of how jet energies are assigned can be found in section 5.4.1. Figure 5.11a shows the comparison

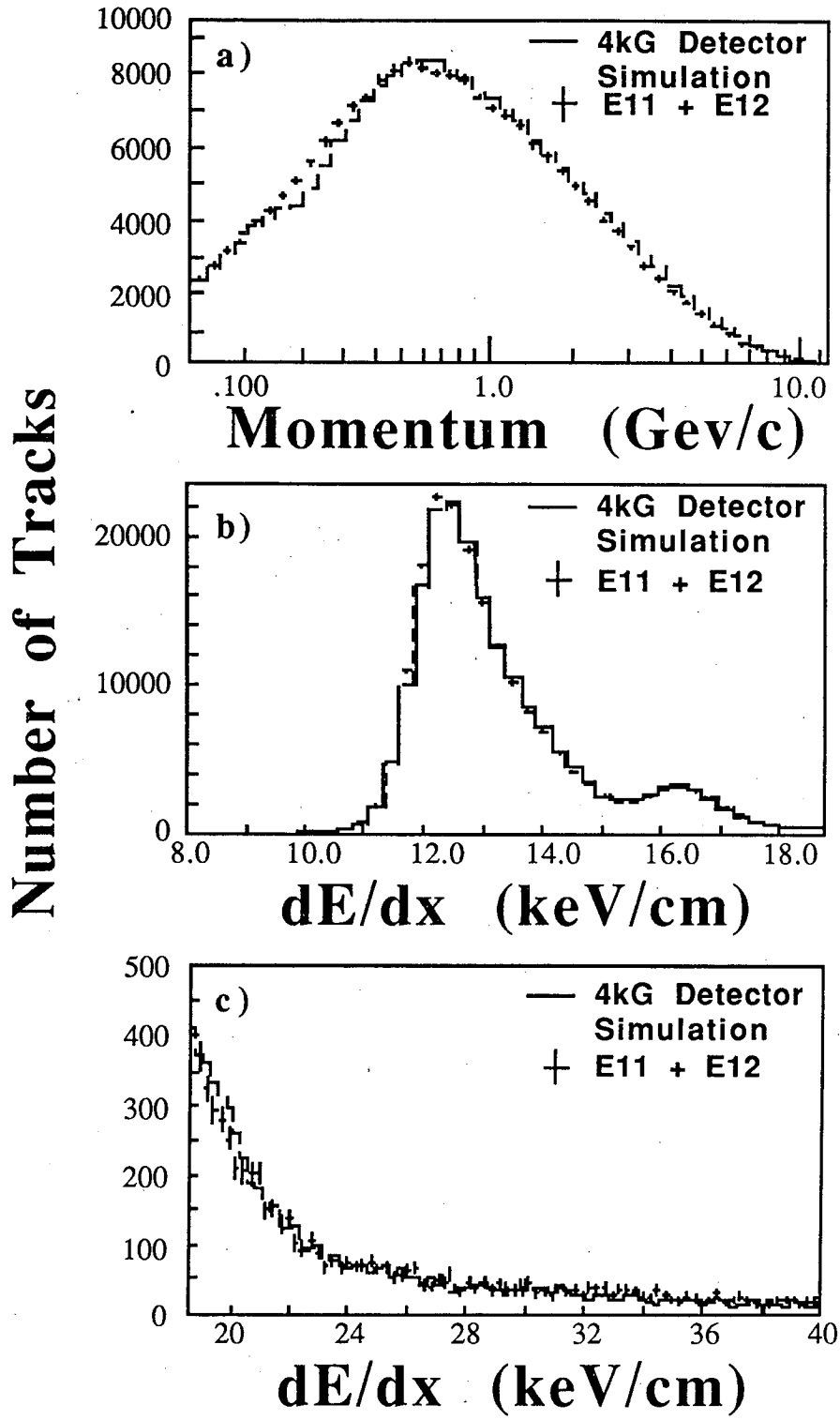

Figure 5.9: Comparisons between the Data and the Monte Carlo. a) are the momentum spectra, b) and c) are two separate dE/dx ranges.

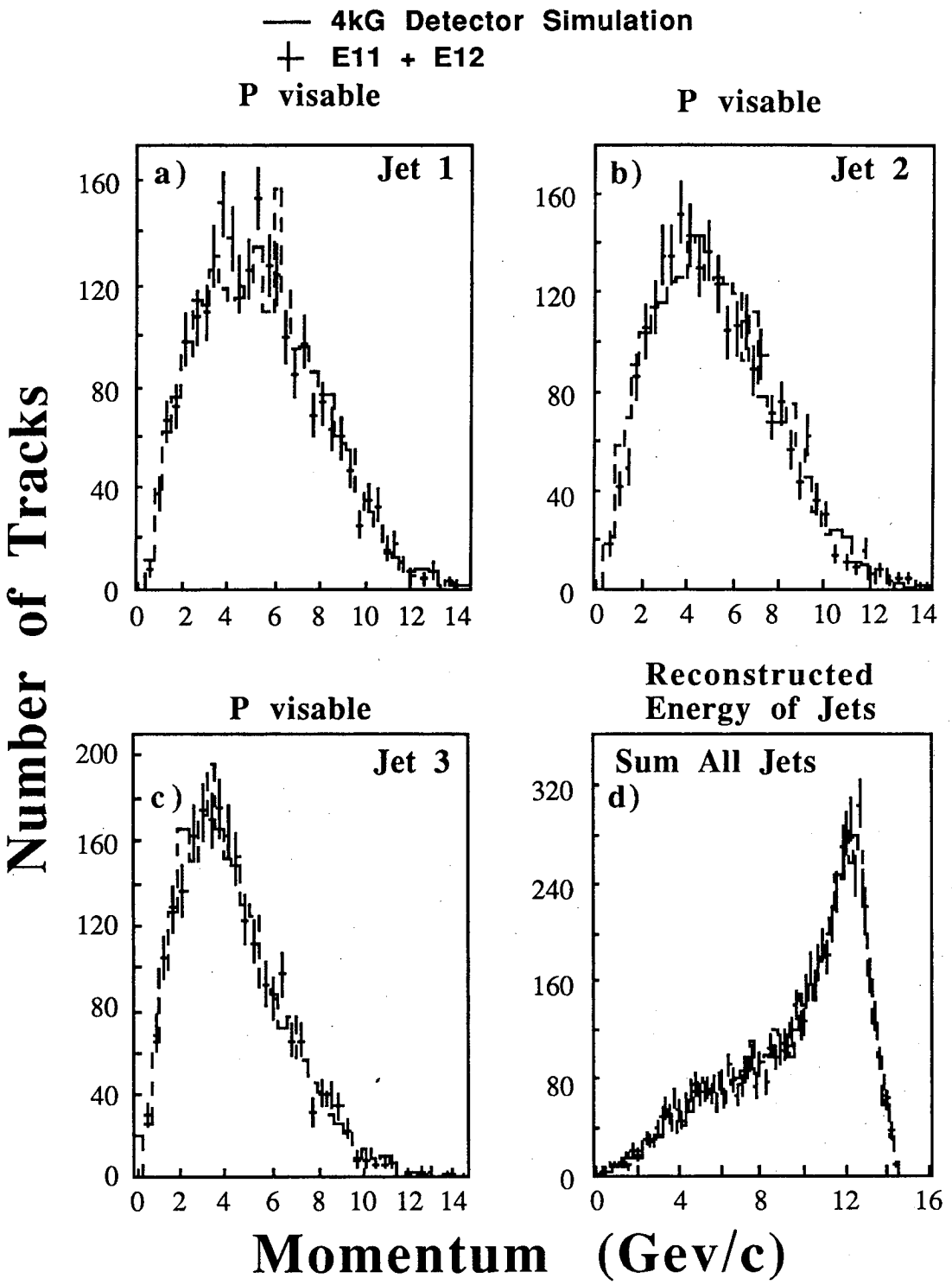

Figure 5.10: Comparisons between the Data and the Monte Carlo visible energy in each jet of a 3 jet events. a) Most energetic jet, b) next most energetic jet and c) least energetic jet. Figure d) shows the distribution of reconstructed parton energies for all jets by method explained explained in section **5.4**.

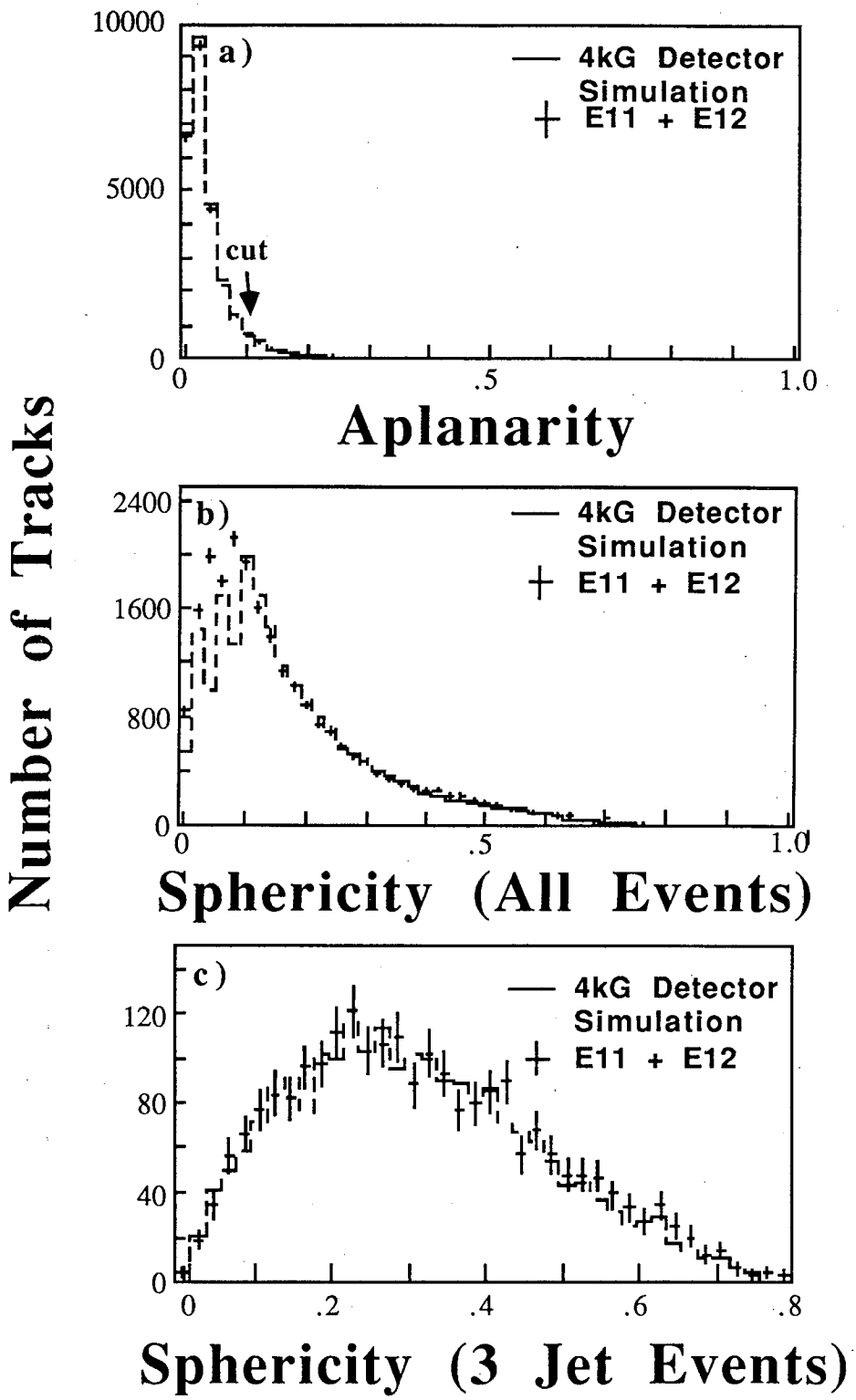

Figure 5.11: Comparison of sphericity and aplanarity in three jet events. a) Aplanarity, b) Sphericity for all events and c) Sphericity for 3 jet events.

between the sphericity observed for three jet events in both the Data and the Monte Carlo. Figure 5.11b shows the distribution of aplanarities for accepted events (aplanarity less than 0.1) in both the Monte Carlo and the Data[2]

The comparisons show that the difference between the Monte Carlo and the Data is not large. This gives us confidence that using TPCLUND will give us reasonable values for detector acceptances.

5.4 3 Jet Event Selection

We saw in chapter two that one possible outcome of an e^+e^- annihilation event is the production of three collimated jets. These events signal the production of a hard p_t gluon. Unfortunately confinement prevents us from observing the primary partons directly. Instead our detector views the debris of fragmentation of the primary partons.

Hadronization produces a cone of particles which travel in the same direction as the initiating parton. The opening angle of the cone is about 20° at our energy[73]. The object of any jet–finding algorithm must be to determine the final state particles which are most likely associated to the hadronization of a quark (anti–quark) or gluon. But no matter how clever we are we will be unable to distinguish between the hadronization of any two primary partons if the two partons are at an angle with respect to each other of smaller than $\sim 20°$. Even worse, the rate of emission of gluons from quarks is proportional to $1/\sin\theta$ where θ is the angle between the quark (or anti–quark) and the emitted gluon. Hence most three parton events are observed as two jet events.

The direction of the primary parton is partially preserved by hadronization. Hadrons fragmenting from a primary parton do not carry much momentum transverse (p_t) to the direction of the primary parton. These hadrons acquire p_t only

[2]cf. References [17,22,39] for the definition of aplanarity and sphericity.

by soft gluon emission or Fermi motion by the quarks which form the hadron. Typically the p_t of a hadron is about 250 to 350 MeV/c. Primary quarks, for example have energies of $\sim$ 10 GeV/c in hard three parton events at PEP. Hence the component of momentum transverse to the direction of the primary parton is relatively small.

5.4.1 Jet Finding Algorithms

Jet finding algorithms can be characterized as attempts to find clusters of particles which together are probably associated with a single parton where the parton could be a quark, anti–quark or a gluon. Each algorithm has criteria for what is a cluster, and for when two separate clusters should be merged into a single cluster. If we cannot merge any more clusters together, the clusters found at this point are called "jets" and the algorithm stops.

Beyond these broad brushstrokes of similar philosophy in every jet finding algorithm, there are very different techniques for the implementation of cluster finding. The irony is that most cluster finding algorithms get about the same result: they find the same number of jets in any particular event. For this study, we choose to use "similarity" clustering described by K. Lanius[74].

We assign a measure to the angle between two tracks in the similarity clustering method. We form a similarity matrix, S_m, whose components are given by

$$D_{ij} = \frac{1}{2}(1 + \cos\theta_{ij}) \tag{5.20}$$

where θ_{ij} is the angle between the i^{th} and j^{th} tracks. We calculate the generalized **multicity**[75] for k clusters as

$$T_k = \frac{\sum_{m=1}^{k} |\sum_{j \in S_m} \vec{p}_j|}{\sum_{j=1}^{n} |\vec{p}_j|} \tag{5.21}$$

where p_j is the momentum of the j^{th} particle, S_m is the set of particles which form the m^{th} cluster and n is the total number of particles in the event. This

quantity is the generalization of thrust and triplicity as described by S. Brandt and H. D. Dahmen. The sum

$$\vec{P}_m = \sum_{j \in S_m} \vec{p}_j$$

is the momentum for the m^{th} cluster.

The quantity T_k is less than or equal to one and $T_k \leq T_{k+1}$. Note that only if every particle is a separate cluster does T_k equal one. If we have guessed too many clusters, eliminating one cluster will not change T_k by very much. But once we go to too few clusters T_k will drop precipitously. Let us assume that we have assigned particles to the correct parton. If we now eliminate a cluster which actually corresponds to a parton, we would assign the particles in this cluster to a different jet. This will give a momentum which is the vector sum of the momenta of the two primary partons. Hence T_k is reduced by the triangle inequality.

The situation is similar if we assign the wrong particles to a cluster. We can use this fact as a basis for a different type of cluster finding algorithm. We can maximize the T_k in equation 5.21 over all possible partitions of n particles. We then must use some criteria which cuts the procedure off. This forms the basis of the method called **normicity** of A. Bäcker[73]. The difference between similarity and normicity is the different algorithm for deciding what particles belong to which clusters.

Similarity works because the partition which maximizes T_k is for the most part the same that maximizes D_{ij}. Similarity and normicity will yield the same results if we use only the fastest particles. The only difference will come in assigning low momentum particles. But we must limit the number of possible partitions to maximize T_k if we use the normicity method. For instance, the number of possible classes to partition N particles into three jets is given by the

equation[75]

$$S_N^{(3)} = \frac{1}{2}(3^{N-1}+1) - 2^{N-1} \,. \tag{5.22}$$

This number grows rather rapidly with N. As an example consider $N = 10$ and $N = 12$. Then the number of classes is given by $S_{10}^{(3)} = 9330$, and $S_{12}^{(3)} = 86526$. Hence we must confine the number of particles considered in order to maximize T_k. Typically one only takes the fastest F (an integer constant) particles and maximizes T_k in normicity. We lose very little information by considering the fastest particles because the fastest particles carry most of the information about the primary parton. As long as F is chosen to be somewhat larger than the maximum number of primary partons possible in an event, we will find all possible jets. The typical value of F is eight.

The procedure for actually assigning particles to clusters with the similarity method begins by considering only F particles in equation 5.21. We then consider each of the particles as a jet and compute the multicity for $k = F$ jets. We then compute a similarity matrix S_D with entries given by D_{ij}. We search this similarity matrix for the maximum entry $D_{ij}^{\max}$. We merge the i^{th} and j^{th} clusters. The merged clusters now define a new cluster, o. We form a new similarity matrix, $S_D^{(1)}$. The similarity of the new cluster o to a cluster l is defined as

$$D_{lo}^{(1)} = \text{Min}\,(D_{li}, D_{lj}) \tag{5.23}$$

where $l \neq i$ and $l \neq j$. The rest of the entries in the new similarity matrix are unchanged from the unreduced matrix,

$$D_{lm}^{(1)} = D_{lm} \quad l, m \neq i \text{ or } j \,.$$

The multicity T_{k-1} is now computed. We define D_k as

$$D_k = T_k - T_{k-1} \,. \tag{5.24}$$

Recalling that $T_{k-1} \leq T_k$ because of the triangle inequality, we see that $D_k \geq 0$. We continue to merge the closest two clusters in similarity until

$$T_k \geq T_k^{\min} \text{ and } D_k \geq D_k^{\min}$$

where $T_k^{\min}$ and $D_k^{\min}$ are constants.

The rest of the particles not used in jet finding, are assigned to clusters by an iterative procedure described by A. Bäcker[73]. A slow particle is first assigned to the closest jet. This determines a new direction for each of the jets. We now recalculate the angle between each of the slow particles and every jet. If the angle between this slow particle and the various jets was not minimum for the jet the particle had been assigned, we reassign the particle to the jet which did have the minimum angle and repeat the procedure. We continue until all of the slow particles are at a minimum angle to the jet to which they were assigned.

Monte Carlo simulations showed that setting F to eight gave reasonable results. Next we assume that we will never see greater than five jets. We set the constants $T_k^{\min}$ to 0.999 and $D_k^{\min}$ to 0.1 for $k = 6, 7$ and 8 to turn off finding greater than five jets. We plot the number of jets found versus the number of primary partons produced by the LUND Monte Carlo with the detector–simulated by TPCLUND for a variety of $T_k^{\min}$ and $D_k^{\min}$. We then optimize the remaining constants $T_k^{\min}$ and $D_k^{\min}$ by maximizing our efficiency and minimizing the confusion of finding each of $k \leq 5$ jets which originated from k partons.

We also required the aplanarity of an event to be less than 0.1. Momentum conservation dictates that the three primary partons should lie in a plane. Aplanarity measures how much an event deviates from planarity . Finally, if the visible energy of the cluster

$$\sum_{j \in S_m} |\vec{p}_j|$$

is less than 500 MeV/c, we redistributed the particles in this cluster to other clusters by the same procedure used to assign slow particles to clusters.

Table 5.2 shows in detail the number of jets found as a function of different numbers of primary partons. We used the LUND Monte Carlo generator as tuned by J. W. Gary[39] and used TPCLUND to simulate the detector. Photons were also used in the jet finding algorithm.

Number Jets Found	Number Partons Generated 2	3	4	*Total*
$P_{vis} > 500$ MeV/c				
1	273	878	40	1191
2	5741	28521	2581	36848
3	212	5047	1136	6395
4	63	833	290	1186
5	6	93	30	129
$P_{vis} > 1.5$ GeV/c				
1	771	3180	227	4178
2	5409	28425	2758	36952
3	64	3699	989	4752
4	9	129	111	249
5	0	3	2	5

Table 5.2: Number of Jets found as a function of Number of Partons Generated . We used the LUND Monte Carlo event generator and particles were tracked thru the detector with the TPCLUND detector simulator. Out of 80000 hadronic events generated with LUND, 52140 events passed thru the hadronic event cuts.

Table 5.2 shows that most of the events had three initial partons. This is because most events have a quark, anti–quark and a soft gluon. However, most of the three jet events found by the similarity cluster method originated from events with three initial partons. Our signal for three jet events with three initial partons to noise of three jet events with two, four or more initial partons is

$$\text{Signal to Noise} = \begin{cases} 5047/1348 = 3.74 & 500 \text{ MeV/c cut} \\ 3699/1053 = 3.51 & 1.5 \text{ GeV/c cut} \end{cases}$$

This is very similar to the results reported by K. Lanius[74]. We list in Table 5.3

the results of running the jet finder on experimental data.

Experiment	Hadronic Candidates	Number of Jets Found 0	1	2	3	4	5
$P_{vis} > 500$ MeV/c							
E11	11006	1	192	7874	1200	234	34
E12	15056	2	345	10436	1649	344	34
E11 + 12	26062	3	537	18310	2849	578	68
$\frac{1}{2}$E62	26076	6	596	18424	3198	593	65
$P_{vis} > 1.5$ GeV/c							
E11	11006	25	678	7897	965	92	2
E12	15056	80	1175	10465	1311	117	7
E11 + 12	26062	105	1853	18362	2276	209	9
$\frac{1}{2}$E62	26076	158	2089	18476	2376	125	3

Table 5.3: List of number of Jet candidates for experiments 11 and 12. The "0" column is the number of unclassified events. We use only one half of the Monte Carlo data available for this comparison since the entire Monte Carlo data set has about twice the number of hadronic events. Note that the Monte Carlo agrees with the Data to better than 10%.

Finally, figures 5.12a, b and c show the angular resolution for determining the direction of the primary partons in three jet events. This plot was made using the LUND generator with the detector–simulated by the TPCLUND Monte Carlo. We used only events where the number of jets found was the same as the number of primary partons in the event (in this case 3). We then computed the jet energies under the assumption that each quark is massless and the annihilation occurs in a center of mass frame at rest with respect to the detector. The Energy of the i^{th} jet is given by the expression

$$E_i = E_{\text{cm}}\alpha_i/(\alpha_1 + \alpha_2 + \alpha_3) \tag{5.25}$$

where E_{cm} is the center of mass energy of the interaction,

$$\alpha_1 \;=\; \sin(\phi^{(3)} - \phi^{(2)})\,,$$

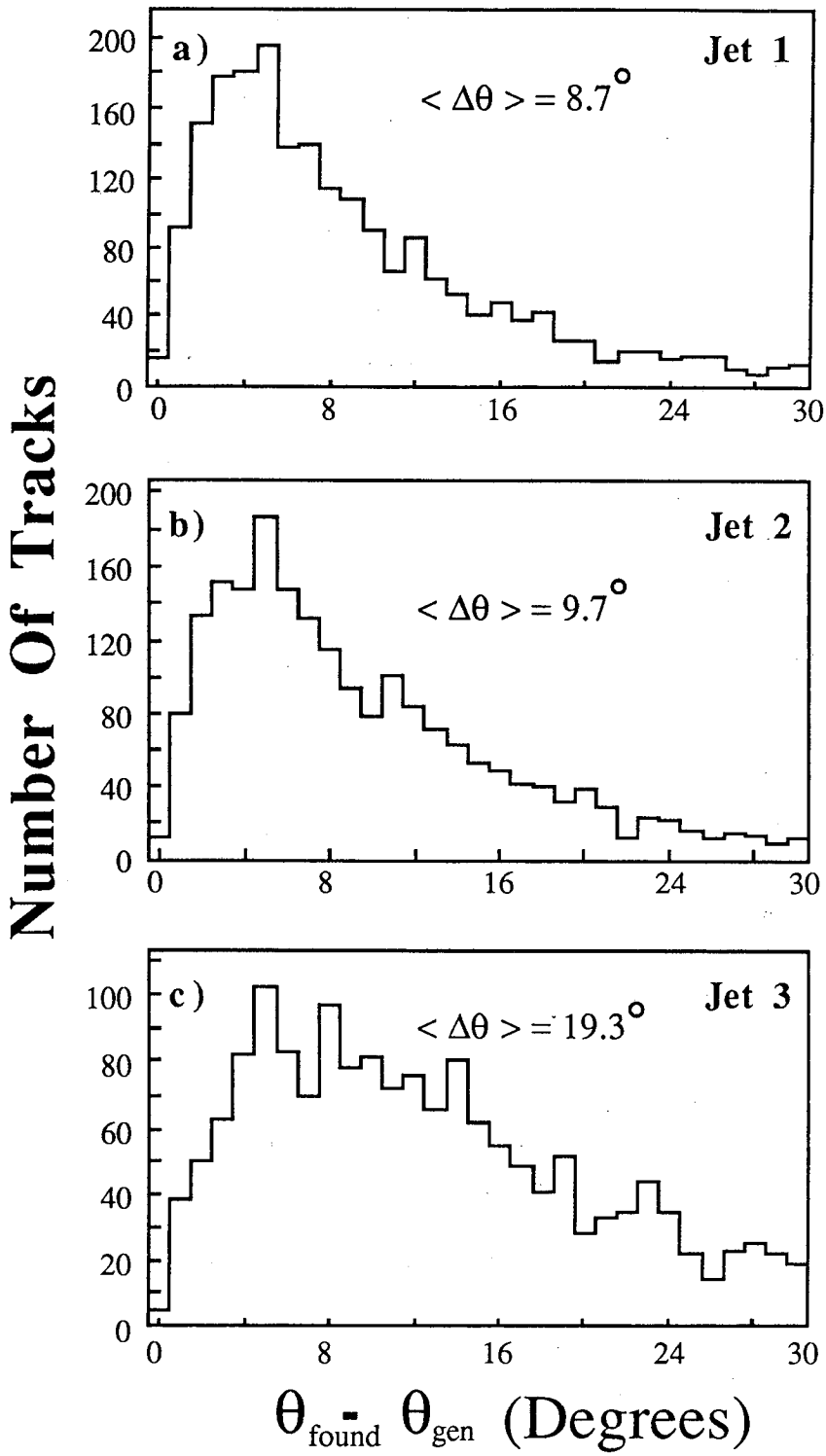

Figure 5.12: Angular resolution for each of the jets found in a 3 jet event. Figure a, is the highest energy jet 1, b is for jet 2 and c is for the lowest energy jet 3.

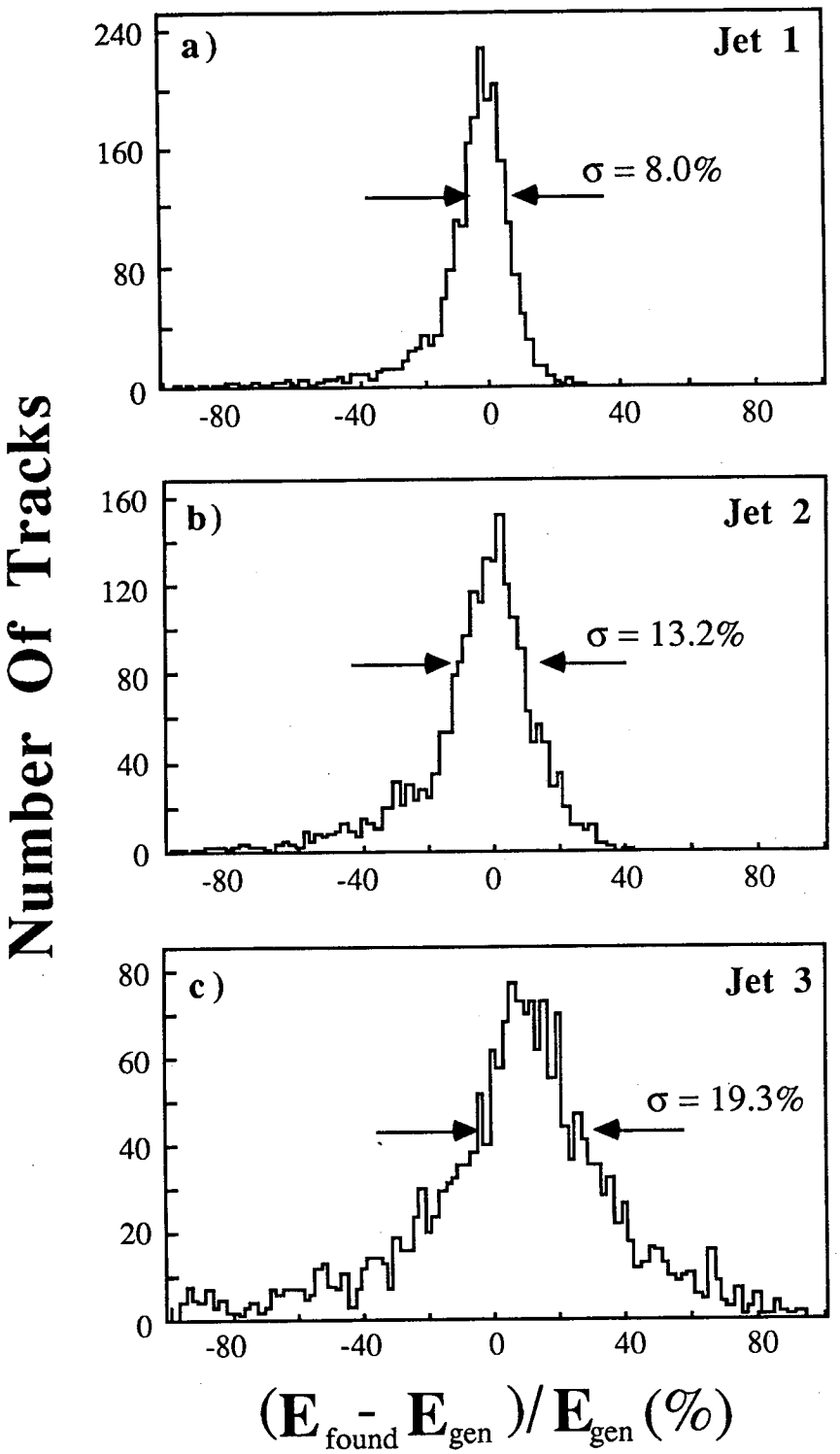

Figure 5.13: Energy resolution for each of the jets found in a 3 jet event. Figure a, is the highest energy jet 1, b is for jet 2 and c is for the lowest energy jet 3.

$$\alpha_2 = \sin(\phi^{(1)} - \phi^{(3)}) ,$$
$$\alpha_3 = \sin(\phi^{(2)} - \phi^{(1)}) ,$$

and $\phi^{(i)}$ is angle of the jet i in the event plane. Note that since we take the difference of the angles between the jets, the axis in the event plane by which we define the angle can be chosen arbitrarily. The jets are then ordered by their energy, i.e. $E_3 < E_2 < E_1$. Figure 5.12a is the angular resolution of jet 1, b jet 2 and c jet 3.

The corresponding energy resolution plots can be found in figures 5.13a, b and c. We can see that the resolution is not symmetric about zero resolution. There is a bias towards events whose generated parton energy was less than the energy determined by equation 5.25. This is because of initial state radiation, i.e. the electron and/or the positron can radiate a photon before the electron and positron annihilate. This lowers the center of mass energy of this particular annihilation so the partons are produced with less energy. Also the assumption that the center of mass system is at rest in the laboratory reference frame of the detector is no longer true. Hence equation 5.25 is no longer valid. Happily this is a small effect and we can correct for it by use of the Monte Carlo. We use the prescription of Berends and Kleiss[76] to generate events with initial state radiation in the LUND and TPCLUND Monte Carlos. This prescription is in fact what generated the bias we observe in these energy resolution plots.

Table 5.4 lists the angular and energy resolutions for each of the three jets. The table was constructed by using events where the number of jets found equalled the number of initial partons (in this case 3). The resolution only quotes the gaussian central region of each plot and cuts out the initial state radiation tail. Notice that the lowest energy jet has a factor of two worse angular and energy resolution than the highest energy jet.

The table also lists the resolutions for both the LUND event generator and the LUND event generator with the detector simulation TPCLUND. We notice that a "perfect" detector would improve the energy resolutions but not bring those resolutions to zero uncertainty. This is because we cannot always correctly assign each track to a jet. This problem is almost entirely caused by low ($<\sim$ 1 GeV) particles.

Monte Carlo	Jet	Angular Resolution	Energy Resolution
LUND + TPCLUND	1	$8.68° \pm 0.25°$	$6.83 \pm 0.18\%$
	2	$9.65° \pm 0.29°$	$6.73 \pm 0.20\%$
	3	$21.91° \pm 0.83°$	$19.29 \pm 0.69\%$
LUND only	1	$4.73° \pm 0.13°$	$4.35 \pm 0.12\%$
	2	$6.14° \pm 0.17°$	$7.46 \pm 0.21\%$
	3	$16.49° \pm 0.61°$	$12.28 \pm 0.35\%$

Table 5.4: List of Angular and Energy resolutions of 3 jet events. LUND only table was constructed by using all the tracks generated by the LUND event generator, +TPCLUND used only particles which the simulation of the detector found as tracks. See text for further information.

Chapter 6

Unfolding the TPC - The Analysis Method

As described in previous chapters, the TPC is an excellent detector for measuring momentum and energy loss simultaneously. As we see in figure 5.7 the dE/dx vs $\ln p$ curve shows rather narrow bands corresponding to charged electrons, muons, pions, kaons and protons $e^{\pm}$, $\mu^{\pm}$, $\pi^{\pm}$, $K^{\pm}$ and $p, \overline{p}$. We will try to use these excellent separations to solve the following problem:

> Given the underlying spectra (Number of particles vs $\ln p$) for the different charged particle species, what are we most likely to observe in the TPC?

We can invert this question:

> Given the observed dE/dx vs $\ln p$ scatter plot observed in the TPC, what are the most likely underlying spectra for $e^{\pm}$, $\mu^{\pm}$, $\pi^{\pm}$, $K^{\pm}$ and $p, \overline{p}$?

6.1 The Mathematical formulation of the problem

Let us assume the underlying spectrum is given by $N_k(p)$ where k is e, μ, π, K and protons, and p is the momentum. Then the most likely number of particles observed in the TPC at energy loss d' and momentum p' is given by

$$E_{\mathrm{TPC}}(d', p') = \sum_{k, N_{pr}} N_{pr} \int_{p} P_N(N_{pr}, N_k(p))\ Prob_k(p \rightarrow d', p')$$

$$= \sum_k \int_p Prob_k\,(p \rightarrow d', p') \times \sum_{N_{pr}} N_{pr}\, P_N(N_{pr}, N_k(p)) \tag{6.1}$$

where $P_N(N_{pr}, N_k(p))$ is the probability of producing N_{pr} particles where we expect $N_k(p)$, $Prob_k\,(p \rightarrow d', p')$ is the probability of a particle of momentum p being measured at momentum p' and truncated mean energy loss d'. We account for fluctuations in the number of particles produced at at each momentum by including the term $P_N(N_{pr}, N_k(p))$[77]. However

$$\sum_{N_{pr}} N_{pr}\, P_N(N_{pr}, N_k(p))$$

is just the expectation value of N_{pr}, which is $N_k(p)$. The equation then becomes:

$$E_{\mathrm{TPC}}\,(d', p') = \sum_k \int_p N_k(p) Prob_k\,(p \rightarrow d', p')\,. \tag{6.2}$$

Clearly the heart of the problem lies in determining this probability. For instance, if the measurement errors were gaussianly distributed and the average truncated mean as a function of momentum is given by the function $Tr(p/mass_k)$ then $Prob_k\,(p \rightarrow d', p')$ would be:

$$Prob_k\,(p \rightarrow d', p') = \frac{1}{\sqrt{2\pi\sigma_p^2}} \exp^{-(p-p')^2/2\sigma_p^2} \times \frac{1}{\sqrt{2\pi\sigma_d^2}} \exp^{-(Tr(p/mass_k)-d')^2/2\sigma_d^2} \tag{6.3}$$

where σ_p is the momentum measurement width and σ_d is the truncated mean measurement width.

Additionally, we must consider the problem of binning of the scatter plot. We need to know the probability of a particle of generated momentum bin i being measured in momentum bin i' and truncated mean bin j'. This probability is given by

$$Prob_k\,(i \to i'j') = \int_{p\in \mathrm{Bin}\,i} dp\, \frac{1}{\sqrt{2\pi\sigma_p^2}} \frac{1}{\sqrt{2\pi\sigma_d^2}} \int_{\mathrm{Bin}\,i'} \int_{\mathrm{Bin}\,j'} \exp^{-(p-p'_{i'})^2/2\sigma_p^2} \times \exp^{-(Tr(p/mass_k)-d'_{j'})^2/2\sigma_d^2}\, dp'_{i'}\, dd'_{j'} \Big/ \int_{p\in \mathrm{Bin}\,i} dp\,. \tag{6.4}$$

The next step is to determine the actual spectrum $N_k(p)$. Let $E_{\mathrm{TPC}}(j',i')$ be the most likely contents of scatter plot bin j', i' where j' is the energy loss bin and i' is the bin for the measured momentum of the particle. We must compare this estimated contents to the actual observed contents $O_{\mathrm{TPC}}(j',i')$. We note that Poisson statistics would give $Poisson(N,\mu) = \mu^N e^{-\mu}/N!$ as the probability to observe N particles when we expect μ particles. Therefore, we define the likelihood for the TPC observation to be[78]

$$\mathcal{L}' = \prod_{\mathrm{Bins}\ j',i'} Poisson(O_{\mathrm{TPC}}(j',i'), E_{\mathrm{TPC}}(j',i')). \tag{6.5}$$

The log likelihood then becomes

$$\begin{aligned} \ln \mathcal{L}' &= \sum_{\mathrm{Bins}\ j',i'} \ln Poisson(O_{\mathrm{TPC}}(j',i'), E_{\mathrm{TPC}}(j',i')) \\ &= \sum_{\mathrm{Bins}\ j',i'} (O_{\mathrm{TPC}}(j',i') \ln E_{\mathrm{TPC}}(j',i') - E_{\mathrm{TPC}}(j',i')) \\ &\quad - \sum_{\mathrm{Bins}\ j',i'} \ln O_{\mathrm{TPC}}(j',i')!\,. \end{aligned} \tag{6.6}$$

We now maximize the likelihood by varying $N_k(p)$ which changes $E_{\mathrm{TPC}}(j',i')$. Notice however that $\sum_{\mathrm{Bins}j',i'} \ln O_{\mathrm{TPC}}(j',i')!$ is a constant given a particular observation. Therefore we can define a new likelihood function

$$\ln \mathcal{L} = \sum_{\mathrm{Bins}\ j',i'} (O_{\mathrm{TPC}}(j',i') \ln E_{\mathrm{TPC}}(j',i') - E_{\mathrm{TPC}}(j',i'))\,. \tag{6.7}$$

The result of maximizing this function will be no different from the result of maximizing $\ln \mathcal{L}'$.

Finally, to connect the value of $\ln\mathcal{L}$ to χ^2, assume the bin contents were *gaussianly* distributed about the most likely contents of bin j', i' . Then the probability of observing $O_{\rm TPC}(j', i')$ for a particular bin j', i' is given by

$$Prob(O_{\rm TPC}(j', i'), E_{\rm TPC}(j', i')) = \exp^{-(O_{\rm TPC}(j',i') - E_{\rm TPC}(j',i'))^2/2\sigma^2_{j',i'}} \times constant. \tag{6.8}$$

Defining the log likelihood as we did above and dropping the irrelevant constants, we obtain [79]

$$\begin{aligned} \ln\mathcal{L} &= \sum_{\text{Bins } j',i'} \left(\frac{-(O_{\rm TPC}(j', i') - E_{\rm TPC}(j', i'))^2}{2\sigma^2_{j',i'}} \right) \\ &= -\frac{\chi^2}{2}. \end{aligned} \tag{6.9}$$

Since this relation is only true for gaussian statistics, it is the definition for pseudo χ^2. Nevertheless, we shall use this relation to get a feeling for how good a fit we have.

6.2 Testing Unfolding

These are several problems in unfolding TPC data:

1. The measurement errors in momentum and dE/dx are not constant. The measurement error in momentum, σ_p, varies as

$$\frac{\sigma_p(\sigma_{cou}, \sigma_{vtx})}{p} = \sqrt{(\sigma_{vtx}\ p)^2 + (\sigma_{cou}/\beta)^2} \tag{6.10}$$

and the measurement error in dE/dx, σ_d, is given by the formula

$$\sigma_d = \sigma_{min} \times \frac{dE}{dx} \Big/ (dE/dx)_{min} \tag{6.11}$$

where σ_{vtx} is the vertex momentum measurement error, σ_{cou} is the multiple scattering error and σ_{min} is the error in measuring dE/dx at minimum ionization. Note that the dimension of σ_{vtx} is 1/ GeV/c and σ_{cou} is *dimensionless*.

2. There are regions of the dE/dx vs $\ln p$ scatter plot where the particles are ambiguously identified. These regions are called *cross over* regions.

3. $Tr(\eta)$ is a complicated function of $\eta = p/mass$. In the region of the Energy loss curve that falls as $1/\beta^2$, this function is a very steeply falling curve. Once the curve reaches minimum ionization it rises slowly to the relativistic plateau. This implies we need a way of dividing the curve into these two different regions.

We conclude that it would be useful to explore what are the limitations on unfolding TPC data. We do this in a two step process.

The first step is to create a **toy model**. This rather simple model is used to understand the basic manner in which unfolding works and to derive some information on systematic errors. The next step is to use the LUND fragmentation model. The generated events are then run thru a detector simulation (TPCLUND) which produces an expected dE/dx vs $\ln p$ scatter plot. We then fit this plot and compare our answer to the actual spectra of particles LUND generated. This determines our systematic error in using this method to analyze data.

Finally, we analyze data observed in the TPC and determine the best parameterization possible.

6.2.1 Toy Model for Unfolding the TPC

To explore how good an analytic model we need to represent TPC data, let us eliminate some of the complications we will observe in the real data. First, let us have only one charged particle. Second, let us make the truncated mean as a function of x a linear function

$$y = Tr(x) = A(x - x_0) + B \ .$$

Finally, let the spectrum $N_{toy}(x)$ be a linear function:

$$N_{toy}(x) = \begin{cases} \mathbf{L}\,(C(x-x_0)+D) & x > x_0 \\ 0 & x < x_0 \end{cases} \tag{6.12}$$

where $\mathbf{L}$, C and D are all non–negative constants. We now introduce the dimensionless variable $p* = p/(1.0\ \mathrm{GeV/c} + cp)$. This variable has the following nice property:

$$\begin{aligned} \sigma_{p*} = \delta \ln p* &= \frac{\delta p}{p}\frac{1}{1.0\ \mathrm{GeV/c} + cp} \\ &= \sigma_{cou}\sqrt{(\frac{\sigma_{vtx}}{\sigma_{cou}}p)^2 + \frac{1}{\beta^2}}\Big/(1.0\ \mathrm{GeV/c} + cp) \end{aligned} \tag{6.13}$$

If we set $c = \sigma_{vtx}/\sigma_{cou}$, then in the limit of large p,

$$\delta \ln p* \approx \sigma_{cou}\frac{cp}{cp} = \sigma_{cou}. \tag{6.14}$$

This means at high momentum, $\ln p*$ has an approximately constant measurement error[80]. Hence, we set $x = \ln p*$ and $y = dE/dx$. The measurement error in y will be given by equation 6.11.

The following exercise was performed:

- Let

$$R = \int_{-\infty}^{x} N_{toy}(t)dt \Big/ \int_{-\infty}^{max} N_{toy}(t)dt$$

  where R is a random number and max is the maximum in lnp^* that we will generate. Since $N_{toy}(t)$ is a simple linear function, $R = F(x)$ can be inverted : $x = F^{-1}(R)$. Figure 6.1 shows what was generated for 10 experiments where

$$N_{toy}(x) = 20\,\mathbf{L}\,(x + 1.4)$$

  where $\mathbf{L} = 15.0$, and $max = 0.4$. The histogram fits a line,

$$N_{toy}^{fit}(x) = \mathbf{L}\,(C_f(x + 1.4) + D_f)$$

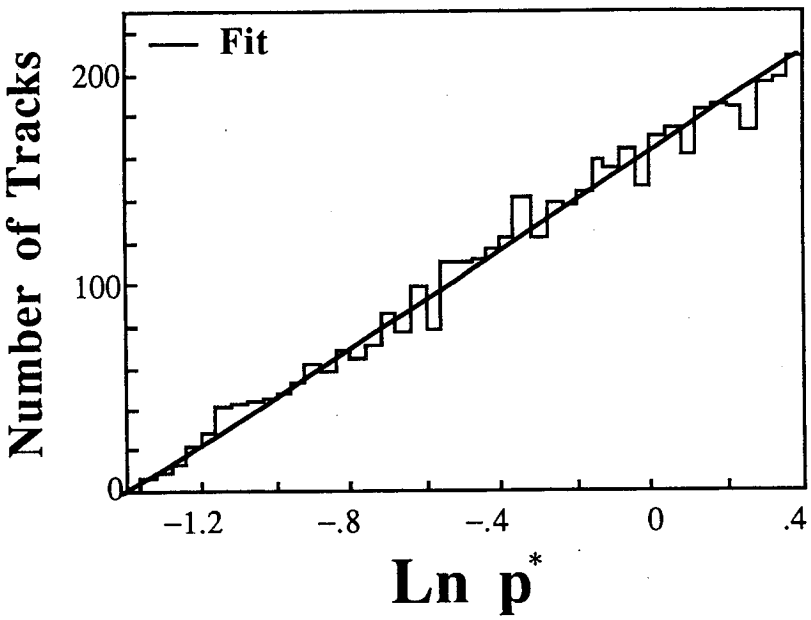

Figure 6.1: $N_{toy}(x)$ generated

where $C_f = 19.28 \pm 0.40$ and $D_f = 0.07 \pm 0.70$. The χ^2 per degree of freedom (χ^2/DOF) is 24.3/43 if we compare $N_{toy}(x)$ with the fit of the line. This χ^2/DOF indicates that what we actually generate is consistent with the line we *wish* to generate. If there were problems with the random number generator, this would not be the case.

- We choose a measured momentum and dE/dx. One can do this by generating two random numbers between 0 and 1, R_1 and R_2. Let $R = -2\ln(1 - R_1)$ and $\phi = 2\pi R_2$. Then we can generate two gaussianly distributed random numbers:

$$\begin{aligned} (\ln p*)_m &= (\ln p*)_g + \sigma_{p*} R\cos\phi \\ (dE/dx)_m &= Tr((\ln p*)_g) + \sigma_d R\sin\phi\ . \end{aligned} \tag{6.15}$$

where the subscripts m and g refer to "measured" and generated quantities respectively. "Measured" in this case is what we generate to simulate gaussian measurement errors.

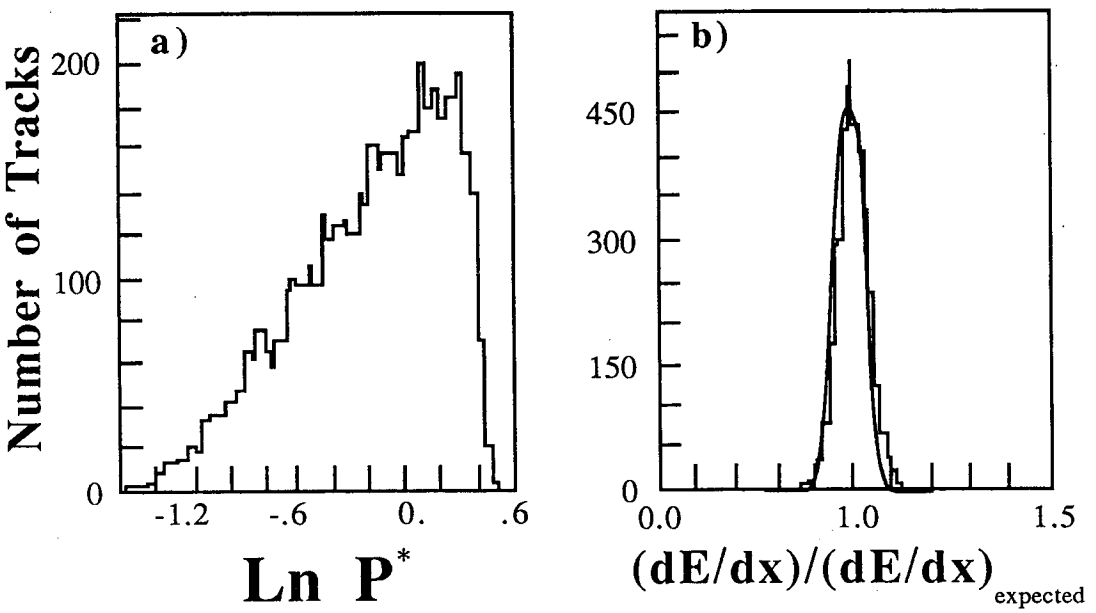

Figure 6.2: Projections of the generated "measured" quantities

Figure 6.2 shows two projections. Figure 6.2a shows the projection onto the y axis of

$$(dE/dx)_R \equiv (dE/dx)_{measured}/(dE/dx)_{expected} \text{ vs } \ln p* \ .$$

where $(dE/dx)_{expected} = Tr((\ln p*)_m)$. If one generates the quantities correctly, then one would expect $\langle (dE/dx)_R \rangle$ to be 1.0 and $\sigma_{(dE/dx)_R}$ to be $\sigma_{min} = 0.039$. The gaussian fit shown is

$$\begin{aligned} \langle (dE/dx)_R \rangle &= 1.0002 \pm 0.0006 \\ \sigma_{(dE/dx)_R} &= 0.03855 \pm 0.00040 \ . \end{aligned}$$

To construct a model for this generated data, we begin with equation 5.4. Notice that this equation for $Prob_k\,(i \rightarrow i'j')$decomposes into $Prob(P)_k(i \rightarrow i') \times Prob(E)_k(i \rightarrow j')$ *if and only if* $Tr(\eta)$ is a constant or varies slowly over the momentum bin i. We will assume that this latter condition is met and set $Tr(\eta)$ to the value corresponding to η at the middle of momentum bin i. We store into two arrays, $\mathbf{Smear_P}(i,i')$ and $\mathbf{Smear_E}(i,j')$, the decomposed probabilities so

$$Prob_k\,(i \rightarrow i'j') = \mathbf{Smear_P}(i,i')\,\mathbf{Smear_E}(i,j') \ . \qquad (6.16)$$

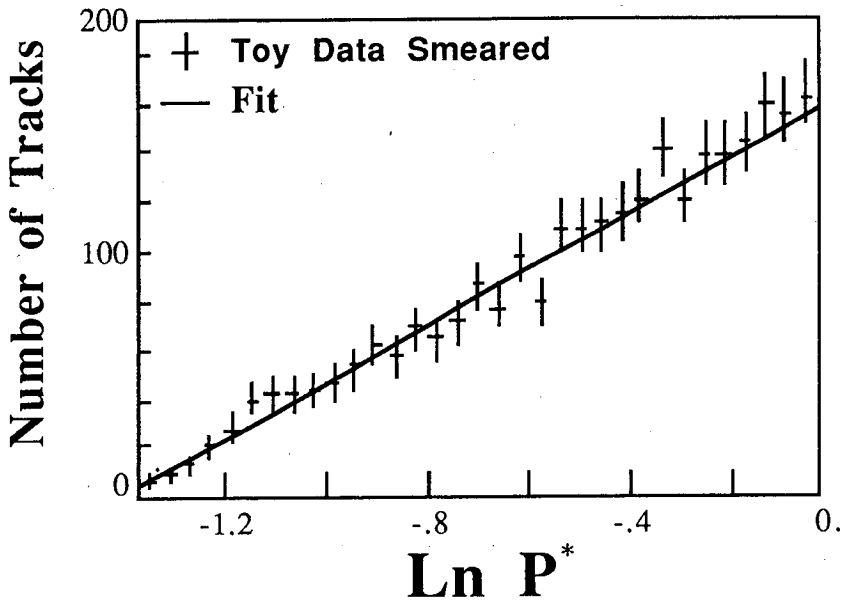

Figure 6.3: $N_{toy}(x)$ generated, $-1.36 \leq x \leq -0.04$.

The final ingredient in the model is defining which bins in dE/dx vs $\ln p*$ space are used in determining the pseudo χ^2. First of all, we cannot get too close to the edges. Notice that in the projection onto the $\ln p*$ axis of the generated data in figure 6.2a there is a drop off near $\ln p* = max = 0.4$. This is because we don't generate data for $\ln p* > 0.4$. If we did generate data beyond max, then "particles" generated above max would feed down into lower momentum bins because of measurement error and hence would fill in this drop off. However, we cannot make an infinite grid in order to compute $Prob_k\,(i \rightarrow i'j')$ and so we must put bounds on x and y over which we compute the smearing. In order to be able to use the maximum amount of data, one should set the high x bound to max and only use bins for χ^2 where $x <\sim 0.2$. Next we notice that over the 10 experiments the fitted C parameter to figure 6.1 is a bit over a standard deviation low. If however we only fit to $x \leq -0.04$, then the fitted value for $C = 19.77 \pm .55$, well within errors of 20.0 (see figure 6.3). Finally when we get too far from the $Tr(\eta)$ vs $\ln p*$ curve, there is no reason to compute smearing to

it. Hence only for bins where

$$Prob_k\,(i \rightarrow i'j') > smear\_min$$

do we smear or use the bin in the pseudo χ^2 calculation. *Smear_min* is a just small constant on the order of 0.1% to 1%.

Table 6.1 summarizes the maximum likelihood fit of the **toy model** in for 10 different generated "experiments" using this model[1]. The χ^2_{comp} columns are not the pseudo χ^2's as defined by equations 6.6 and 6.9; rather it is a direct comparison between $N^{fit}_{toy}(\ln p*)$ and $N_{toy}(\ln p*)$. It was defined as

$$\chi^2_{comp} = \sum_{bins} \left[\frac{N^{fit}_{toy}(x_i) - N_{toy}(x_i)}{\Delta N^{fit}_{toy}(x_i)} \right]^2 \tag{6.17}$$

where x_i refers to the value of x in the middle of the i^{th} bin and $\Delta N^{fit}_{toy}(x_i)$ was determined using the full covariance matrix V[78]:

$$\Delta N^{fit}_{toy}(x_i) = \sum_{m,n=1,2} \int_{Bin\,i} \frac{\partial N^{fit}_{toy}(t)dt}{\partial P_m} V_{mn} \int_{Bin\,i} \frac{\partial N^{fit}_{toy}(t)dt}{\partial P_n} \Bigg|_{P_k = P^{fit}_k,\, k=1,2} \Delta P_m \Delta P_n \tag{6.18}$$

where V_{mn} is the m^{th}, n^{th} entry of covariance matrix V, $P_1 \equiv C$ and $P_2 \equiv D$ (see 6.12). Also $\chi^2_{comp>1}$ is the same as χ^2_{comp} except that only bins where $N_{toy}(x) > 1.$ are used.

As shown in table 6.1, the average of χ^2_{comp}'s is respectable. Also the average of the C_{fit} and D_{fit} are well within errors of the generation coefficients $C = 20$ and $D = 0$. The likelihood fit is also reasonably unbiased. This can be seen from the fact that $\int N^{generated}_{toy}$ and $\int N^{fit}_{toy}$ are $\sim -0.1\%$ different in each experiment (see the following table).

We also observe that the systematic error (σ_{sys}) is much smaller that the statistical error. When $x = -1.15$, the number of particles in an x bin is 2.4.

[1]Experiment number 4 seems to be a statistical aberration. If one throws out experiments 8 and 4, the best and worst comparisons to N_{toy} respectively, the average of the remaining χ^2/DOF drops from 1.80 to 1.29.

test	C_{fit}	D_{fit}	χ^2_{comp}	$\chi^2_{comp>1}$	$\chi^{2\ init}_{pseudo}$	$\chi^{2\ fit}_{pseudo}$
1	20.4 ± 2.0	0.3 ± 1.1	19.8	18.3	413.11	412.55
2	18.1 ± 1.9	0.9 ± 1.1	26.8	16.9	382.14	381.12
3	20.5 ± 2.0	-1.0 ± 1.1	67.3	59.5	400.04	398.75
4	16.1 ± 1.8	2.5 ± 1.1	242.4	160.0	401.57	395.39
5	22.5 ± 2.0	-1.2 ± 1.1	37.1	28.9	371.48	369.88
6	21.1 ± 2.0	-0.1 ± 1.1	13.5	13.5	405.79	405.09
7	21.6 ± 2.0	-1.5 ± 1.1	91.4	81.0	431.82	429.98
8	19.7 ± 1.9	0.3 ± 1.1	3.8	2.9	381.48	381.41
9	22.1 ± 2.0	-0.9 ± 1.1	22.9	17.2	412.86	411.71
10	22.5 ± 2.0	-1.4 ± 1.1	51.8	41.9	403.45	401.68
Ave	20.5 ± 2.8	-0.2 ± 1.6	57.7	44.0	400.37	398.76
Ave_5	19.5 ± 2.9	0.3 ± 1.8	78.7	56.7	393.67	391.54

Table 6.1: Table of 10 experiments with $\sigma_{cou} = 0.06, \sigma_d = 0.039$. Ave_5 is the average of the first 5 experiments.

test	$\int$ Gen	$\int$ Fit
1	288	287.8
2	267	266.8
3	265	264.5
4	272	271.7
5	288	287.7
6	291	290.2
7	270	269.7
8	278	277.6
9	288	287.8
10	285	284.7
Ave	279.2 ± 10.0	278.9 ± 9.9
Ave_5	276.0 ± 10.1	275.7 ± 10.1

Table 6.2: Number of particles generated and the total number of particles fit for 10 experiments with $\sigma_{cou} = 0.06, \sigma_d = 0.039$. This shows that the fit is reasonably unbiased.

This means the statistical error (σ_{stat}) is

$$\sigma_{stat} \geq \frac{1}{\sqrt{2.4}} = 58\%$$

for $x \leq -1.15$. At $x = 0$, the number of particles in an x bin is 16.8. This implies that

$$\sigma_{stat} \geq \frac{1}{\sqrt{16.8}} = 24\%$$

for $-1.15 \leq x \leq 0$.. We plot in figure 6.4a,b the projection of $\Delta S_{toy} \equiv (N_{toy}^{fit} - N_{toy})/N_{toy}$ vs x scatter plot onto the ΔS_{toy} axis. Figure 6.4a is the projection onto the S_{toy} axis for $x \leq -1.15$ and figure 6.4b is the projection onto the S_{toy} axis for $x \geq -1.15$. We equate the systematic error for the **toy model** to the standard deviation of S_{toy} in each of the two projections. We find

$$\sigma_{sys} = \begin{cases} 35 \pm 11\% & x \leq -1.15 \\ 6.0 \pm 0.3\% & x \geq -1.15 \end{cases}$$

Hence for $x \leq -1.15$, $\sigma_{sys} \sim \sigma_{stat}$ and for $-1.15 \leq x \leq 0$, σ_{stat} is a factor of four larger than the σ_{sys}. When we double the statistics for the generated experiment, we expect the statistical error to decrease by the square root of 2. But we see in table 6.3 that the systematic error also drops by the same factor. This means we could expect in real data this technique will yield reasonable systematic errors. These results merely show the **toy model** is self consistent. What happens if our model parameters (σ_{cou}, σ_d, $y = A(x - x_0) + B$, etc) are incorrect? We begin by regenerating the first five experiments. But then we determine $Prob(P)(i \rightarrow i')$ and $Prob(E)(i \rightarrow j')$ with incorrect values of σ_{cou} and σ_{min}. Table 6.3 shows the average $\chi^{2\,init}_{pseudo}$, $\chi^{2\,fit}_{pseudo}$ and σ_{sys} over the five experiments for various values of σ_{cou} and σ_{min}.

Near the best values in parameter space, χ^2_{pseudo} equals

$$(P_1 - P_1^0)^2/\sigma_{P_1}^2 \tag{6.19}$$

in the limit of χ^2_{pseudo} being a function only of P_1. If we fit the different χ^2's as a function of σ_{cou} and σ_{min} we estimate $\sigma_{cou} = 0.065 \pm 0.011$ and $\sigma_{min} =$

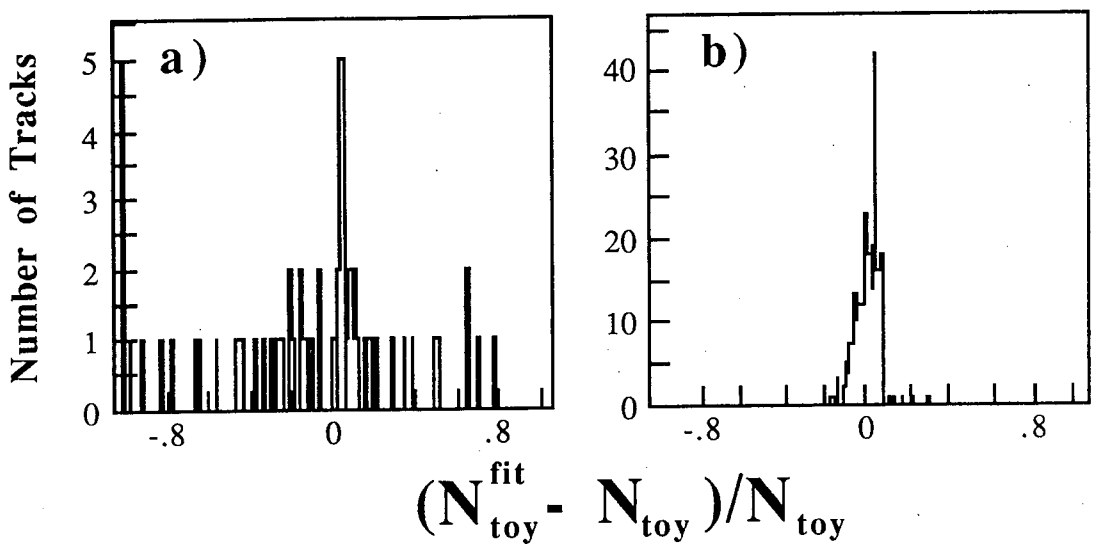

Figure 6.4: Figure a) is the projection onto ΔS_{toy} axis for $x \leq -1.15$ and b) is the projection onto ΔS_{toy} axis for $x \geq -1.15$

Par	Value	$\chi^{2\,init}_{pseudo}$	$\chi^{2\,fit}_{pseudo}$	$\sigma_{sys}(\%)$ $\ln p \leq -1.15$	$\sigma_{sys}(\%)$ $\ln p \geq -1.15$
	0.050	395.42 ± 15.89	393.27 ± 15.70	47.5 ± 5.9	6.4 ± 0.4
	0.055	394.35 ± 17.21	392.22 ± 17.03	48.0 ± 6.0	6.5 ± 0.4
	0.060	393.67 ± 16.63	391.54 ± 16.50	43.3 ± 3.8	6.0 ± 0.3
σ_{cou}	0.065	393.42 ± 16.02	391.29 ± 15.89	45.9 ± 5.8	6.7 ± 0.4
	0.070	393.61 ± 15.38	391.47 ± 15.28	46.3 ± 5.9	6.8 ± 0.4
	0.075	394.26 ± 13.17	392.11 ± 13.12	46.6 ± 5.9	6.9 ± 0.4
	0.080	395.37 ± 12.58	393.21 ± 12.56	47.1 ± 6.0	6.9 ± 0.4
	0.035	401.70 ± 19.51	399.47 ± 18.99	46.9 ± 6.0	6.7 ± 0.4
	0.037	396.47 ± 17.00	394.36 ± 16.65	46.0 ± 5.8	6.6 ± 0.4
	0.039	393.67 ± 16.63	391.54 ± 16.50	43.3 ± 3.8	6.0 ± 0.3
σ_{min}	0.041	392.77 ± 13.12	390.67 ± 13.20	45.0 ± 5.7	6.6 ± 0.4
	0.043	393.52 ± 11.71	391.45 ± 12.03	44.8 ± 5.7	6.6 ± 0.4
	0.045	395.67 ± 10.60	393.62 ± 11.71	44.6 ± 5.7	6.6 ± 0.4
	0.047	399.02 ± 9.80	396.96 ± 10.62	44.7 ± 5.7	6.7 ± 0.4
Double Statistics		488.45 ± 13.51	487.02 ± 13.61	37.2 ± 4.6	4.2 ± 0.3

Table 6.3: Average of first 5 experiments, vary σ_{cou} and σ_{min}. Double Statistics is $\mathbf{L} = 30$, $\sigma_{cou} = 0.06$ and $\sigma_{min} = 0.039$

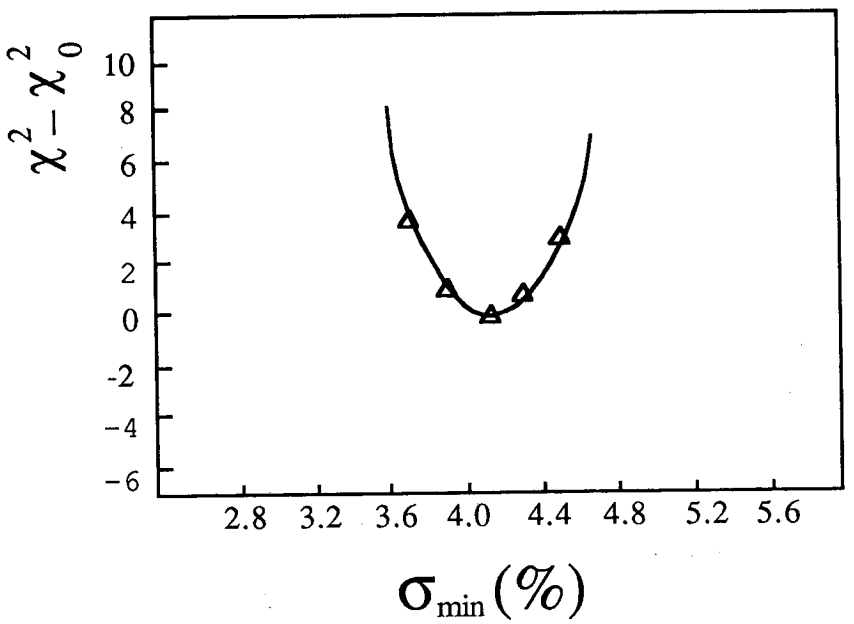

Figure 6.5: Fit of $\chi^{2\,init}_{pseudo}$ vs σ_{min}.

0.0412±0.0022. Table 6.4 summarizes fitting χ^2_{pseudo} by this method and figure 6.5 gives an example of one of the fits. Notice we get the same fitted parameters if we use $\chi^{2\,init}_{pseudo}$ from our initial spectrum or we use the minimum $\chi^{2\,fit}_{pseudo}$ found by fitting the best spectrum. Recall that we generated our distributions with $\sigma_{cou} = 0.06$ $\sigma_{min} = 0.039$. Hence our determinations of these parameters using equation 6.19 are systematically high. In fact our determination of σ_{min} is about 1σ high.

From	Fitted Parameters	
	σ_{cou}	σ_{min}
$\chi^{2\,init}_{pseudo}$	0.065 ± 0.011	0.0412 ± 0.0022
$\chi^{2\,fit}_{pseudo}$	0.065 ± 0.011	0.0412 ± 0.0022

Table 6.4: Fitting χ^2_{pseudo} as a function of σ_{cou} and σ_{min}. Initial χ^2_{pseudo} is computed by setting N^{fit}_{toy} to N_{toy} generated. Fit χ^2_{pseudo} was the minimum χ^2 found using the CERN program MINUIT.

To understand this systematic difference, we must consider the assumption under which we constructed the smearing probabilities. It was assumed that $Tr(\eta)$ varies slowly over the $\ln p*$ bin and hence one can decompose the probability for smearing into a product of a momentum smear and a dE/dx smear. But over a momentum bin dE/dx changes by

$$\Delta(dE/dx) = A\Delta(\ln p*) = -4.33 \times 0.04 = -0.16 .$$

This means that percentage change in dE/dx is $-0.16/(\sim 15)$ or about 1% in a typical x bin for the **toy model.**

We can generate experiments with dE/dx = constant to check this effect. If dE/dx = constant, then one can strictly decompose the smearing probability as in equation 5.16. Unfortunately, we cannot tell anything about the smearing along the $\ln p*$ (x) axis if $dE/dx(y)$ = constant. Also we don't expect any difference in the fit for different σ_d's because the only important variable is the measurement error along the x axis. Nevertheless, the pseudo χ^2 should be minimum for $\sigma_d = 0.039$, the generated measurement error along the y axis.

We can see in table 6.5 that this is indeed the case. We plot χ^2_{pseudo} vs σ_d in figure 6.6. We estimate that $\sigma_d = 0.0399 \pm 0.0017$ using equation 6.19. This means that the systematic error dropped by a factor of two by moving to a more correct analytic model.

We surmise from this exercise that there is a systematic error due to inability to make a perfect analytic model. Conversely, we have to do the best job we can in constructing this analytic model.

6.2.2 Determining parameters for analytic method

In general, how can we determine the resolution parameters of our analytic model? We can measure quantities like the multiple scattering error (σ_{cou}), the vertex momentum error (σ_{vtx}) and the dE/dx measurement error (σ_{min}) etc by

σ_{min}	$\chi^{2\ init}_{pseudo}$	$\chi^{2\ fit}_{pseudo}$	$\sigma_{sys}(\%)$ $\ln p \leq -1.15$	$\sigma_{sys}(\%)$ $\ln p \geq 1.15$
0.035	350.4 ± 39.1	348.2 ± 37.8	31.1 ± 4.0	6.9 ± 0.4
0.037	344.4 ± 35.1	342.2 ± 33.7	31.1 ± 4.0	6.9 ± 0.4
0.039	341.9 ± 35.6	339.6 ± 33.9	31.1 ± 4.0	6.9 ± 0.4
0.041	342.2 ± 29.0	340.0 ± 27.5	31.1 ± 4.0	6.9 ± 0.4
0.043	344.8 ± 26.7	342.5 ± 25.1	31.1 ± 4.0	6.9 ± 0.4
0.045	349.1 ± 24.8	346.9 ± 23.1	31.1 ± 4.0	6.9 ± 0.4
0.047	354.9 ± 23.2	352.6 ± 21.5	31.1 ± 4.0	6.9 ± 0.4

Table 6.5: Average of first five experiments with $dE/dx = 15$ and varying σ_{min}

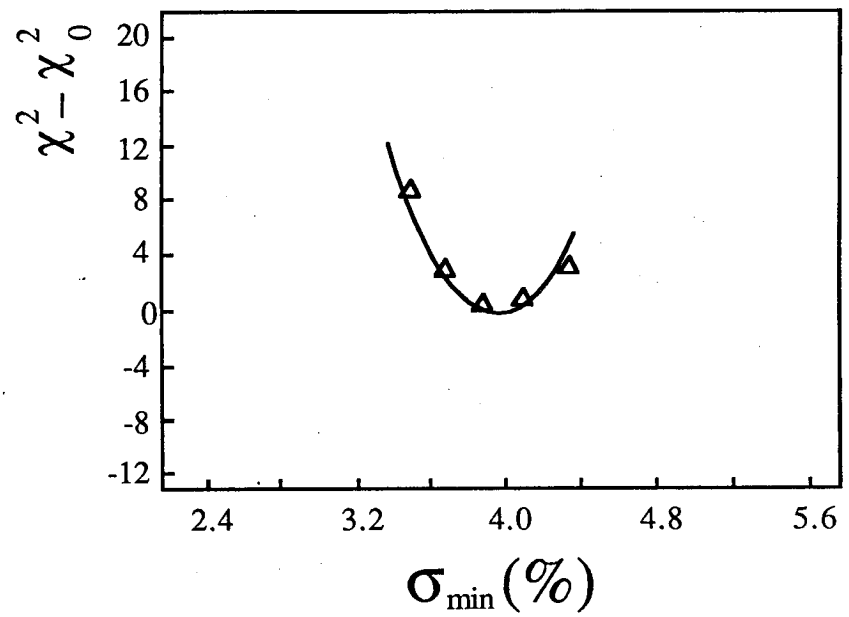

Figure 6.6: Plot of χ^2_{pseudo} vs σ_d for $dE/dx = 15$

other methods (See section 5.3). But all of these methods use representations of the data which differ from this 2–dimensional analytic representation. In fact the way we measure the value of σ_{cou} depends slightly on the values of σ_{vtx} and σ_{min} and *vice versa*. We cannot determine these parameters simultaneously.

Also, the various measurements contain different systematic errors. For instance, σ_{vtx} is determined by Bhabha scattering ($e^+ e^- \rightarrow e^+ e^-$) and so does not contain any systematics due to the multi-track environment of hadronic events. Hence it is useful to determine the best values of the parameters of the analytic model using the analytic model itself if possible.

One possible method would be to create the equivalent histograms to the histograms one forms from the data which measure the quantities experimentally. For example, consider σ_{cou}. As the reader will see in section 6.3, we determine σ_{cou} by plotting $\ln(p_{measured}/p_{expected})$ vs $(dE/dx)_{measured}$ where $p_{expected} = Tr^{-1}((dE/dx)_{measured})$. $Tr^{-1}(dE/dx)$ is the inverse of the function $Tr(p)$, ie. Tr^{-1} determines the expected momentum for a given energy loss. If one measures the width in momentum in the $1/\beta^2$ region of the plot, one measures the momentum measurement error and hence principally σ_{cou} (See figure 6.11).

But we can form the same plot in the analytic model because we predict the weight of each entry in the dE/dx vs $\ln p$ plot (see figure 5.7). This plot can obviously serve as a check but there is a far more powerful method which can also determine the best global parameters simultaneously.

Let us fix $N_k(p)$ and vary the parameters of the analytic model. Near the best values for the parameters of the model[78,79],

$$\chi^2(P_1^M, \ldots, P_n^M) = \sum_{i=1}^{n} \frac{(P_i^M - P_i^0)^2}{\Delta^2 P_i} + 2 \sum_{i<j} C_{ij} \frac{(P_i^M - P_i^0)(P_j^M - P_j^0)}{\Delta P_i \Delta P_j} + \chi_0^2 \quad (6.20)$$

where P_i is the i^{th} parameter, P_i^0 is the value of this parameter which minimizes χ^2, P_i^M is the M^{th} set of parameters, $\chi^2(P_1^M, \ldots, P_n^M)$ is the value of χ^2 which

corresponds to this set of parameters, and C_{ij} is the correlation between the i^{th} and j^{th} parameters.

Given different sets of parameters and χ^2, one could determine the $n+\frac{n(n+1)}{2}+1$ different unknowns in equation 6.20 or one could fit the best curve in parameter space which best describes the set of χ^2. We choose the later method because the χ^2's are only parabolic near the minimum in χ^2 space and hence any determination of the parameters by inversion is likely to be faulty. Also fitting circumvents the problem of extracting the P_i^0's. If one inverts, one must determine the coefficients of

$$\begin{aligned} Y &= A_1P_1^2+\cdots+A_nP_1^2+B_{12}P_1P_2+\cdots+B_{n-1\,n}P_{n-1}P_n \\ &\quad +C_1P_1+\cdots+C_nP_n+D\,. \end{aligned} \tag{6.21}$$

As one can see, in order to determine the P_i^0's, one must complete the square of this equation.

We do pay a price for fitting. We must attach an error to each data point in order to fit a hyperparabolic curve to a set of points. But attaching an error to a χ^2 is an unsatisfactory if not a meaningless operation. However we operationally handled this problem by attaching a small error (1.0) to each χ^2 and fitting a hyperparabolic curve. We then reattached a smaller error (0.1) to each χ^2 and refitted this set of points. If the fits didn't differ by much, the solution was called *stable* and we used the values found by the fit for the parameters.

If the solution was not stable, we examined the set of χ^2's. Usually a non–stable solution meant that near some P_i^0, the χ^2 were not very parabolic. We eliminated any trouble points and refit.

6.3 Resolution

It is possible to determine the resolution parameters from the data by other means beside the 2-dimensional analytic representation. The important parameters which must be determined are the truncated mean measurement error σ_d, multiple scattering error σ_{cou}, and the vertex momentum measurement error σ_{vtx}. The following table shows the method by which each of these quantities was measured.

σ_d	Pions at minimum ionization
σ_{cou}	Pions, Kaons and Protons in the $1/\beta^2$ region of dE/dx vs $\ln p$.
σ_{vtx}	Bhabha sample

6.3.1 Energy loss measurement error

We use a momentum band which straddles pions at minimum ionization in the TPC in order to determine σ_d, the energy loss measurement error. It is $-0.8 \leq \ln p \leq -0.6$. In figure 5.7, we can see 2 bands which correspond to pions and electrons. The beginning of electron, kaon crossover also begins in this momentum slice. We see there is a clear separation between the pions and the electrons plus kaons.

Figure 6.7 shows the projection onto the y axis of $\mathcal{R}$ vs $\ln p$ where

$$\mathcal{R}_M = \frac{(dE/dx)_{measured}}{(dE/dx)^{\pi}_{expected}} \equiv \frac{(dE/dx)_M}{(dE/dx)^{\pi}_E} \tag{6.22}$$

and $(dE/dx)^{\pi}_E$ is the expected dE/dx for a pion with momentum p. We define the energy loss resolution function as

$$R_g(\mathcal{R}_k(p_m), \mathcal{R}_M, \sigma_{\mathcal{R}}) = \frac{1}{\sqrt{2\pi}\sigma_{\mathcal{R}}} e^{\frac{-(\mathcal{R}_k(p_m)-\mathcal{R}_M)^2}{2\sigma_{\mathcal{R}}{}^2}} \tag{6.23}$$

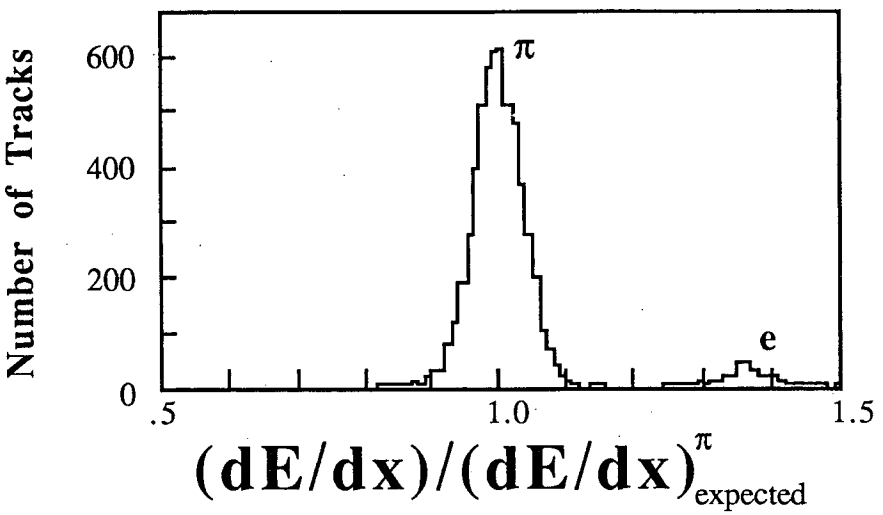

Figure 6.7: Projection of dE/dx vs $\ln p$ onto the dE/dx axis for $-0.8 \leq \ln p \leq -0.6$.

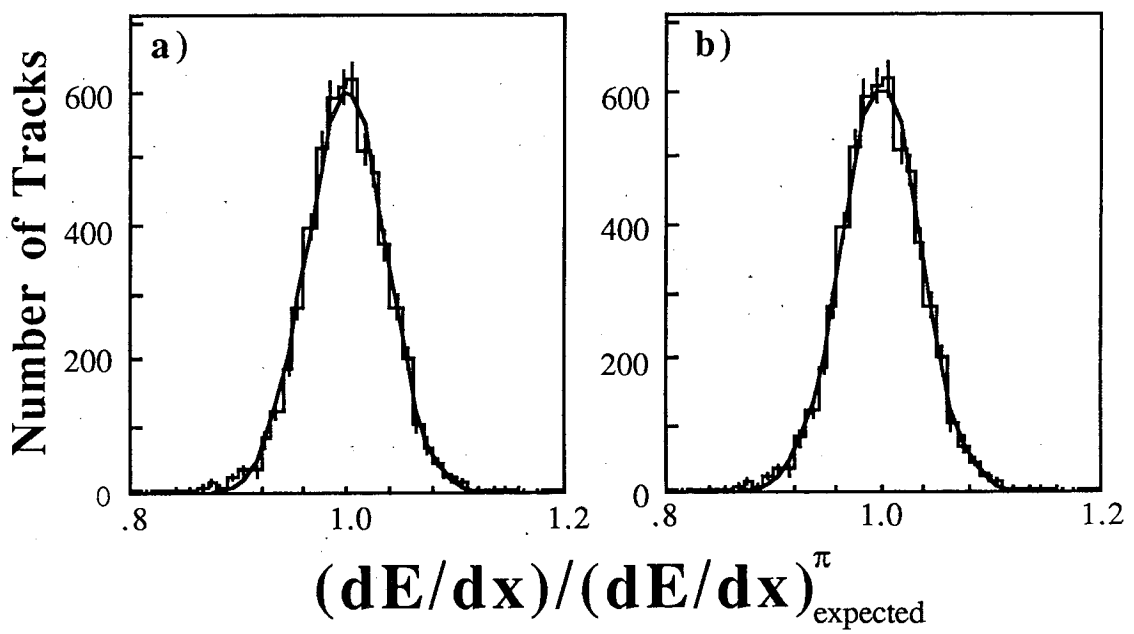

Figure 6.8: Fit of $\mathcal{R}$ for pions at minimum ionization. Figure a uses the resolution function R. Figure b uses the weighted sum over wires, the resolution function R'.

where k is $e^{\pm}$, $\mu^{\pm}$, $\pi^{\pm}$, $K^{\pm}$ and $p, \bar{p}$ $\mathcal{R}_k(p_m)$ is the expected $\mathcal{R}_M$ for a particle with measured momentum p_m and $\sigma_{\mathcal{R}}$ is the energy loss measurement error for $\mathcal{R}$. In Figure 6.8a we isolate a pion sample by requiring $0.8 \leq R \leq 1.1$. Overplotted onto this plot is a gaussian fit to the above resolution function. The best fit values for the average of $\mathcal{R}$ and the measurement error of this quantity were

$$\begin{aligned} \langle \mathcal{R} \rangle &= 0.99922 \pm 0.00050 \\ \sigma_{\mathcal{R}} &= 0.03730 \pm 0.00041 \end{aligned}$$

for experiment 11 (all relevant information about the different experiments are shown in table 5.3). The measurement error $\sigma_{\mathcal{R}}$ is made up of several components.

$$\sigma_d \equiv \sigma_{\mathcal{R}} = \sqrt{\sigma_{\mathcal{R}}^{min\,2} \frac{dE/dx(p)}{(dE/dx)_E^{\pi}} \frac{(dE/dx)_{min}}{(dE/dx)_E^{\pi}} + \frac{\Delta^2 \mathcal{R}}{12} + \sigma_p^2 \frac{\Delta^2 \mathcal{R}}{\Delta^2 p}} \qquad (6.24)$$

where $\sigma_{\mathcal{R}}^{min}$ is the measurement error of $\mathcal{R}$ at minimum ionization, σ_p is the momentum resolution, $\Delta\mathcal{R}$ is the variation of $\mathcal{R}$ over the momentum range $-0.8 \leq \ln p \leq -0.6$ and Δp is the momentum width of the of the momentum range. The term

$$\frac{\Delta^2 \mathcal{R}}{12}$$

represents the contribution to the width due to the fact that the particles are measured at a range of $\mathcal{R}$'s. If one assumes the particles are equally distributed over the $\mathcal{R}$ range, one can estimate this width by the standard deviation of a square over the range. The term

$$\sigma_p^2 \frac{\Delta^2 \mathcal{R}}{\Delta^2 p}$$

represents the contribution to the width because dE/dx varies over the momentum bin.

The most important term,

$$\sigma_{\mathcal{R}}^{min\,2} \frac{dE/dx(p)}{(dE/dx)_E^{\pi}} \frac{(dE/dx)_{min}}{(dE/dx)_E^{\pi}}$$

was derived by assuming the measurement error in dE/dx, scales according to the square root of dE/dx[53]. To first order, the dE/dx resolution $\sim 1/\sqrt{N_{el}}$ where N_{el} is the number of electrons detected in the TPC. The scaling law holds since $dE/dx \propto N_{el}$. Table 6.6 summarizes $\sigma_{\mathcal{R}}^{min}$ for all experiments and Monte Carlos that we used.

Experiment	Centroid - 1	$\sigma_{\mathcal{R}}^{min}$	Tail $\equiv T$	χ^2/DOF
E11	$-8.5 \pm 5.0 \times 10^{-4}$	$3.726 \pm 0.041 \times 10^{-2}$	1.0	2.73
	$-1.13 \pm 0.52 \times 10^{-3}$	$3.864 \pm 0.050 \times 10^{-2}$	1.482 ± 0.060	1.99
E12	$-9.1 \pm 6.0 \times 10^{-4}$	$3.608 \pm 0.049 \times 10^{-2}$	1.0	1.43
	$-1.02 \pm 0.61 \times 10^{-3}$	$3.704 \pm 0.057 \times 10^{-2}$	1.447 ± 0.073	0.94
E11+	$-1.09 \pm 0.32 \times 10^{-3}$	$3.722 \pm 0.027 \times 10^{-2}$	1.0	4.85
E12	$-1.28 \pm 0.33 \times 10^{-3}$	$3.884 \pm 0.033 \times 10^{-2}$	1.541 ± 0.036	1.96
E62	$3.9 \pm 3.4 \times 10^{-4}$	$3.759 \pm 0.028 \times 10^{-2}$	1.0	4.28
	$3.4 \pm 3.4 \times 10^{-4}$	$3.955 \pm 0.035 \times 10^{-2}$	1.569 ± 0.038	1.57
		Cut at 0.5%		
E11	$-7.5 \pm 5.0 \times 10^{-4}$	$3.715 \pm 0.040 \times 10^{-2}$	1.0	2.34
	$-1.13 \pm 0.52 \times 10^{-3}$	$3.813 \pm 0.048 \times 10^{-2}$	1.417 ± 0.060	1.75
E12	$-9.4 \pm 4.5 \times 10^{-4}$	$3.580 \pm 0.049 \times 10^{-2}$	1.0	1.15
	$-1.06 \pm 0.61 \times 10^{-3}$	$3.655 \pm 0.062 \times 10^{-2}$	1.369 ± 0.062	0.87
E11+	$-1.08 \pm 0.33 \times 10^{-3}$	$3.710 \pm 0.027 \times 10^{-2}$	1.0	3.35
E12	$-1.21 \pm 0.33 \times 10^{-3}$	$3.808 \pm 0.031 \times 10^{-2}$	1.443 ± 0.039	1.11
E62	$3.8 \pm 3.4 \times 10^{-4}$	$3.730 \pm 0.027 \times 10^{-2}$	1.0	2.64
	$3.4 \pm 3.4 \times 10^{-4}$	$3.840 \pm 0.037 \times 10^{-2}$	1.421 ± 0.047	1.17

Table 6.6: Summary of dE/dx resolution for all experiments and Monte Carlos. Please see text for explanation of results. Number of wires hit ≥ 80, $\lambda \leq 60°$.

Also we expect the dE/dx resolution to scale with the number of wires used in determining the truncated mean. Figure 6.9 is a plot of the $\sigma_{\mathcal{R}}$ vs N_{wires} where N_{wires} was the number of wires used in the truncated mean for pions at minimum ionization. The function which was overplotted was

$$\sigma_{\mathcal{R}}^{min}(N_{wires}) = \sqrt{\frac{\sigma_{183}^2}{N_{wires}} 183 + c^2}\,. \tag{6.25}$$

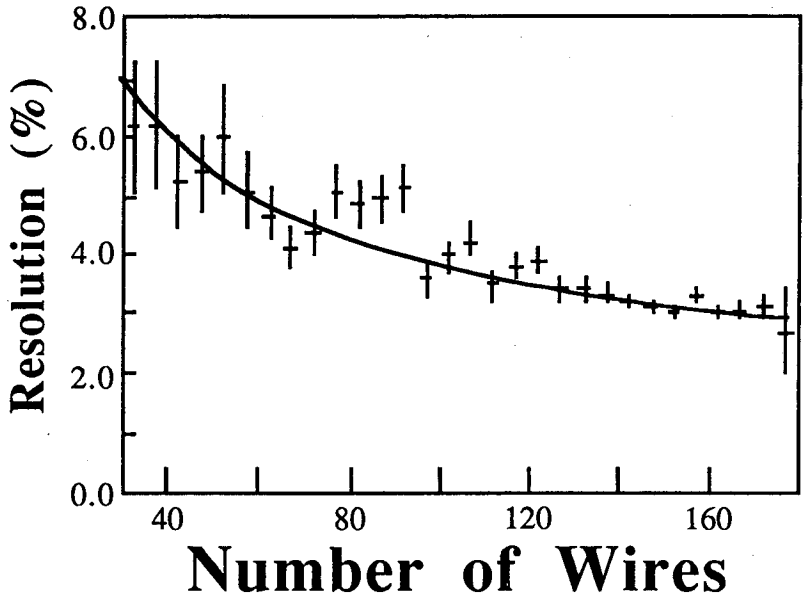

Figure 6.9: Variation of dE/dx resolution with N_{wires} in Experiment 11.

Experiment	$\sigma_{\mathcal{R}}^{183}$	c
E11	$3.009 \pm 0.031 \times 10^{-2}$	$0.0 \pm 4.4 \times 10^{-3}$
E12	$2.964 \pm 0.087 \times 10^{-2}$	$8.8 \pm 4.2 \times 10^{-3}$
E11+E12	$2.611 \pm 0.070 \times 10^{-2}$	$1.72 \pm 0.15 \times 10^{-2}$
E62	$2.903 \pm 0.091 \times 10^{-2}$	$1.28 \pm 0.29 \times 10^{-2}$

Table 6.7: Summary of dE/dx resolution for all experiments and Monte Carlos. This table lists the fitted variation in the dE/dx resolution vs Number of wires hit. Number of wires hit ≥ 30, $\lambda \leq 60°$.

Table 6.7 summarizes the fits for this variation for all relevant experiments.

We can then define a new resolution function which is simply the weighted sum over the number of wires used in the determination of the truncated mean times the resolution function for that number of wires:

$$R'_g(\mathcal{R}_k(p_m), \mathcal{R}_M, S_f) = \sum_{N_{wires}} W(N_{wires}) R_g(\mathcal{R}_k(p_m), \mathcal{R}_M, S_f \times \sigma_{\mathcal{R}}^{min}(N_{wires})) \; . \tag{6.26}$$

The fit using this resolution function is shown in figure 6.8b. We maintained the shape of $\sigma_{\mathcal{R}}^{min}$ but allowed for an arbitrary scale factor S_f. This factor was fit to be ~ 1.05 to 1.10. Table 6.8 gives the fits using this resolution function.

Experiment	Centroid - 1	S_f	Tail $\equiv T$	χ^2/DOF
E11	$-8.5 \pm 5.0 \times 10^{-4}$	1.048 ± 0.011	1.0	2.40
	$-1.13 \pm 0.52 \times 10^{-3}$	1.079 ± 0.014	1.427 ± 0.065	1.98
E12	$-1.28 \pm 0.43 \times 10^{-3}$	1.024 ± 0.010	1.0	1.92
	$-1.29 \pm 0.43 \times 10^{-3}$	1.054 ± 0.011	1.474 ± 0.051	0.91
E11+E12	$-1.10 \pm 0.33 \times 10^{-3}$	1.0515 ± 0.0076	1.0	4.29
	$-1.27 \pm 0.33 \times 10^{-3}$	1.0924 ± 0.0091	1.519 ± 0.038	2.08
E62	$3.9 \pm 3.4 \times 10^{-4}$	1.0315 ± 0.0077	1.0	3.60
	$3.4 \pm 3.4 \times 10^{-4}$	1.0779 ± 0.0096	1.528 ± 0.040	1.56
		Cut at .5%		
E11	$-8.4 \pm 5.0 \times 10^{-4}$	1.041 ± 0.011	1.0	1.69
	$-9.8 \pm 5.1 \times 10^{-4}$	1.056 ± 0.013	1.299 ± 0.072	1.51
E12	$-1.28 \pm 0.43 \times 10^{-3}$	1.0203 ± 0.0096	1.0	1.45
	$-1.29 \pm 0.43 \times 10^{-3}$	1.041 ± 0.011	1.399 ± 0.055	0.62
E11+E12	$-1.11 \pm 0.33 \times 10^{-3}$	1.0268 ± 0.0074	1.0	2.44
	$-1.21 \pm 0.33 \times 10^{-3}$	1.0490 ± 0.0087	1.392 ± 0.043	1.11
E62	$3.8 \pm 3.4 \times 10^{-4}$	1.0263 ± 0.0075	1.0	2.70
	$3.4 \pm 3.4 \times 10^{-4}$	1.0564 ± 0.0099	1.423 ± 0.046	1.33

Table 6.8: Summary of dE/dx resolution for all experiments and Monte Carlos using the variation of $\sigma_{\mathcal{R}}^{min}$ with number of wires hit. Note that in general using the sum over wires improves the representation of the data. Number of wires hit ≥ 80, $\lambda \leq 60°$.

If one examines the χ^2's, we notice that resolution function R'_g gives a better

representation of the data than R_g. However it could be argued that neither representation is particularly good. If we cut data where

$$\begin{array}{lcll} \int_{-\infty}^{x} R_g(\mathcal{R}_k(p_m), \mathcal{R}_M, \sigma_{\mathcal{R}}^{min}) & < & 0.5\% & , \quad x < 0 \\ \int_{x}^{\infty} R_g(\mathcal{R}_k(p_m), \mathcal{R}_M, \sigma_{\mathcal{R}}^{min}) & < & 0.5\% & , \quad x > 0 \quad \forall k = 1 \ldots 5 \end{array}$$

(or replace R_g with R'_g) we find the χ^2/DOF drops from around ~ 2 to ~ 1 (see figure 6.10a for R_g, figure 6.10c for R'_g and table 6.6 for the fits and summary of this result). We conclude that while weighting a sum over the number of wires produces an excellent representation of pions at minimum, there are still problems at the order of one percent.

We can improve the representation by adding a slight non–gaussian tail to the resolution function. If we define

$$R(\overline{x}, x, \sigma, T) = \frac{1}{\sqrt{2\pi}} \frac{T\sigma}{T^2 - 1} \frac{e^{-(x-\overline{x})^2/2(T\sigma)^2} - e^{-(x-\overline{x})^2/2(\sigma/T)^2}}{(x - \overline{x})^2} \tag{6.27}$$

(and R') where T is a constant to be fit, we can include some of the behavior of the tails. If T equals 1 then $R \equiv R_g$. The results of fitting with this resolution function are also found in table 6.6 and the plot for R can be found in figure 6.10b and for R', figure 6.10d. The different fitted T parameters are listed in the column labeled Tail. We notice that the χ^2/DOF drop by about a factor of two by including the "Tail". Also, part of the "Tail" in R is due to a different number of wires being hit all with different sigma's.

6.3.2 Multiple Scattering Error

We can use a similar procedure to the one we used to determine the energy loss measurement error, to determine the multiple scattering error, σ_{cou}. This is because in the $1/\beta^2$ region of the dE/dx vs $\ln p$ plot, over small ranges in dE/dx, there is a small variation in $\ln p$.

In analogy with equation 6.22, we define $\mathcal{P}$ as

$$\mathcal{P} = \ln p_m / T r_\pi^{-1}((dE/dx)_M) \, . \tag{6.28}$$

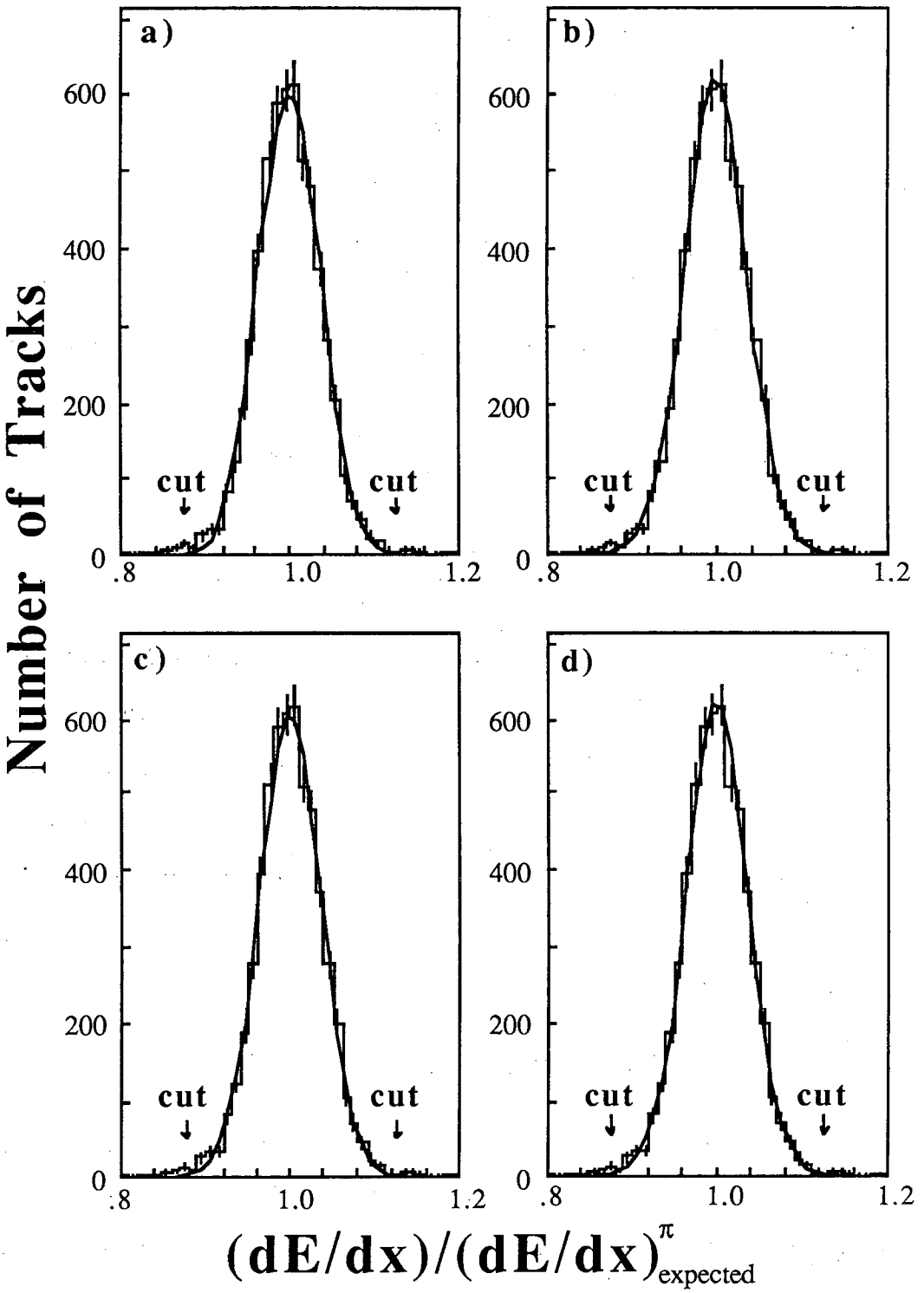

Figure 6.10: Fit of $\mathcal{R}$ for pions at minimum ionization. Figures a and b use the resolution function R. We add the slightly non–gaussian tail in figure b. Figures c and d use the weighted sum over wires , resolution function R'. In figure d we add the slight non–gaussian tail to R'.

where $Tr_\pi^{-1}((dE/dx)_M)$ is the expected momentum for a pion of measured energy loss $(dE/dx)_M$[81]. We use the logarithm because

$$\delta p_m = p_m \sqrt{(p_m \sigma_{vtx})^2 + \sigma_{cou}^2/\beta^2}$$

by equation 6.10. In the limit of small measured momentum p_m

$$\frac{\sigma_p}{p_m} = \sigma_{cou}/\beta$$

Hence $\Delta\mathcal{P}$ will approximately be the same in the $1/\beta^2$ region of the dE/dx plot for different particles at the same dE/dx (same β) [2].

The width $\sigma_\mathcal{P}$ is in analogy with equation 6.24

$$\sigma_\mathcal{P} = \sqrt{\sigma_\mathcal{P}^{A^2} + \frac{\Delta^2\mathcal{P}}{12} + \sigma_d^2 \frac{\Delta^2\mathcal{P}}{\Delta^2 dE/dx}} \tag{6.29}$$

where

$$\frac{\Delta^2\mathcal{P}}{12}$$

represents the addition to the width due to the finite bin width in $\mathcal{P}$ and

$$\sigma_d^2 \frac{\Delta^2\mathcal{P}}{\Delta^2 dE/dx}$$

represents the contribution of the changing momenta over the dE/dx bin.

One should also notice that since dE/dx is solely a function of $\eta = p_m/m$, that the average of $\mathcal{P}$ over a dE/dx range should be m/m_π. This follows directly from

$$Tr_\pi^{-1} = \eta \times m_\pi \, .$$

But at the same energy loss, η is the same for all particle species. Hence the centroid of the $\mathcal{P}$ distribution should be the same η multiplied by the mass of the particle in question.

[2] Actually, this approximation begins to break down for momenta appropriate for the $1/\beta^2$ of protons because $p_m \times \sigma_{vtx}$ becomes large

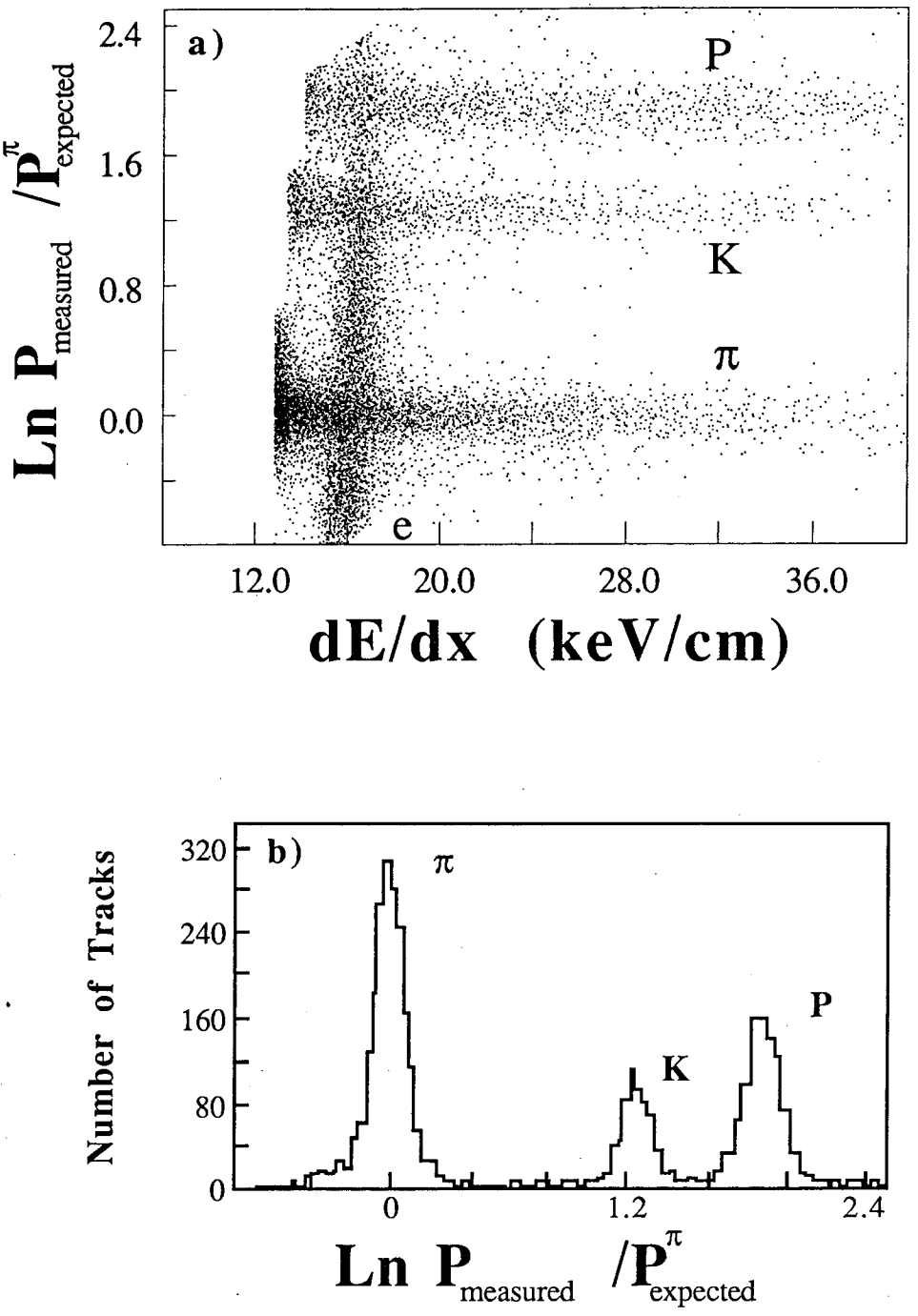

Figure 6.11: Plot of $\mathcal{P}$ vs dE/dx. a) The scatter plot for experiment 11; b) the projection of a onto the $\mathcal{P}$ axis

dE/dx KeV/cm	$\overline{dE/dx}$ KeV/cm	$Tr_\pi^{-1}(\overline{dE/dx})$ GeV
18.3 – 19.0	18.65	0.1544
19.0 – 20.0	19.50	0.1469
20.0 – 22.0	21.00	0.1363
22.0 – 24.0	23.00	0.1253
24.0 – 27.0	25.50	0.1147
27.0 – 30.0	28.50	0.1050

Table 6.9: List of dE/dx slices used for fitting $\sigma_{\mathcal{P}}^A$

Figure 6.11a shows the scatter plot of $\mathcal{P}$ vs dE/dx for experiment 11. We see the bands for $\pi^\pm$, $K^\pm$, $p,\bar{p}$ along with a vertical band for $e^\pm$. We only consider $dE/dx \geq 18.3$, which effectively cuts away from the electron band. We take slices in dE/dx according to the following table. We then compute $\sigma_{\mathcal{P}}^A$ for each slice and fit the set of them to the assumed variation of σ with momentum. When fitting the best $\sigma_{\mathcal{P}}^A$ for each dE/dx slice, one must also allow the centroid to be different from m/m_π. Since the number of particles produced varies over the momentum range corresponding to the dE/dx slice, the average dE/dx is not the average of the low and high edges of the slice. This means the average momentum expected for the pion will not be

$$Tr^{-1}\left(\overline{(dE/dx)}\right)$$

because we have calculated $\overline{(dE/dx)}$ by averaging the low and high edges of the slice. We correct for this effect by allowing the centroid to be multiplied by a factor close to 1.0. Typically this factor was in the range of .99 to 1.01. Another reason why the centroid is not where we expected is that there is a systematic error $\sim 0.1\%$ in inverting dE/dx.

As an example, table 6.10 is a compilation of the best fits for $\sigma_{\mathcal{P}}^A$ in experiment 11. We plot the function $\sigma_{\mathcal{P}}^A$ vs $Tr^{-1}(\overline{dE/dx})$ in figures 6.12a, b and c. Figure a is for pions, b for kaons and c for protons. Overplotted onto the kaon and proton

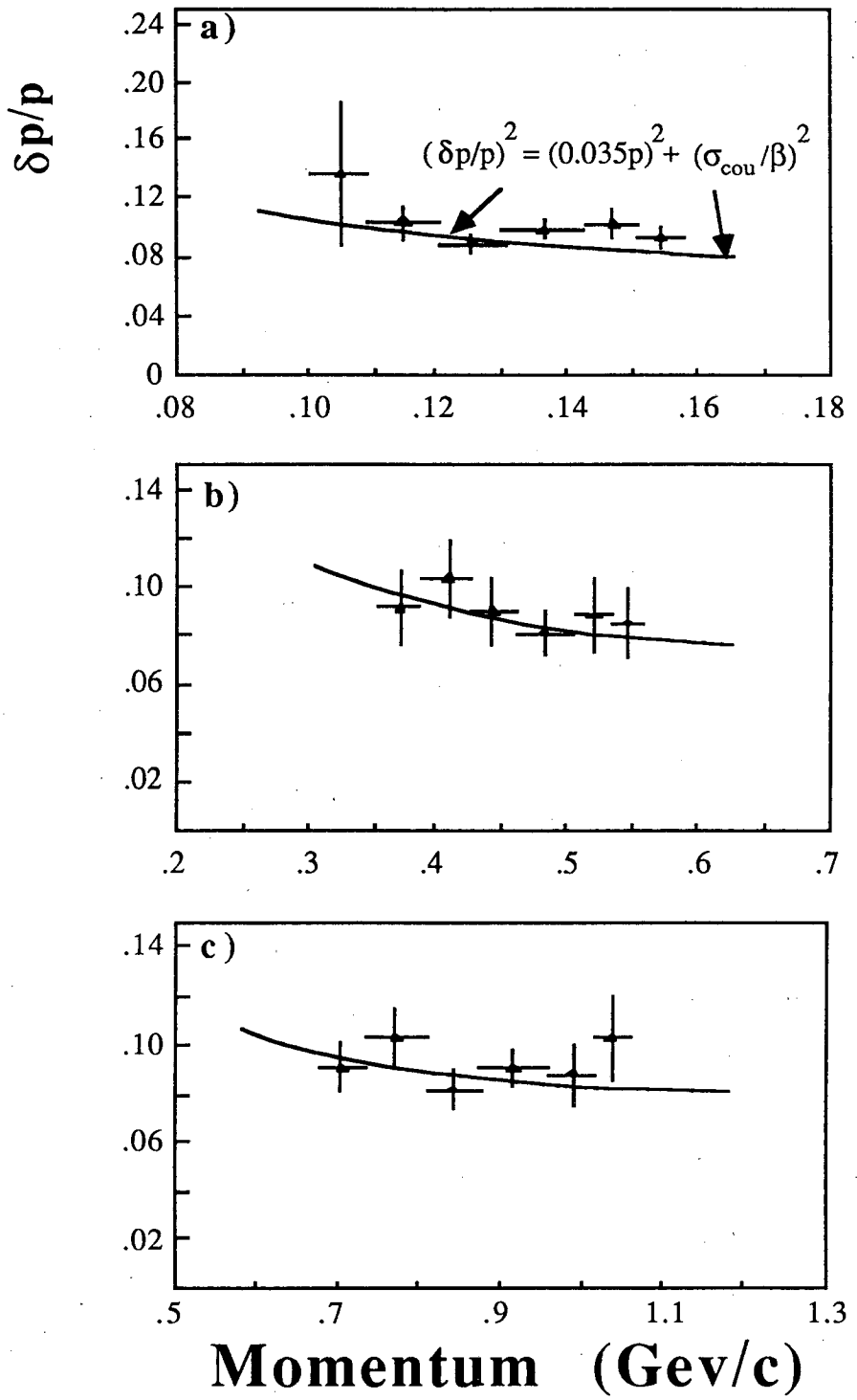

Figure 6.12: σ_p^A vs p experiment 11. a) pions, b) kaons, and c) protons.

dE/dx Range	$\sigma_p^A \times 10^2$ π	K	P
18.3 – 19.0	9.27 ± 0.65	8.5 ± 1.2	10.3 ± 1.7
19.0 – 20.0	10.31 ± 0.87	8.8 ± 1.5	8.8 ± 1.2
20.0 – 22.0	9.87 ± 0.65	8.12 ± 0.88	9.06 ± 0.74
22.0 – 24.0	8.98 ± 0.65	9.0 ± 1.3	8.14 ± 0.77
24.0 – 27.0	10.4 ± 1.2	10.3 ± 1.6	10.3 ± 1.1
27.0 – 30.0	13.7 ± 4.5	9.1 ± 1.5	9.08 ± 0.94

Table 6.10: Compilation of σ_p^A in experiment 11.

Experiment	σ_{vtx}	$\sigma_{cou} \times 10^2$	χ^2/DOF
E11	0.035	5.72 ± 0.22	0.47
E12	0.035	5.57 ± 0.14	2.18
E11+E12	0.035	5.533 ± 0.093	1.49
E62	0.025	4.431 ± 0.070	1.98

Table 6.11: Table of multiple scattering errors for all Experiments and Monte Carlos. Number of wires hit ≥ 80 and $\lambda \leq 60°$.

plot is the best fit using kaon and proton data together. Pions were not included because at these low momenta, there is appreciable $\pi \rightarrow \mu$ decay contamination. Monte Carlo studies indicate that the effect on σ_p^A is between 7 and 14% of sigma itself. We fixed σ_{vtx} because we don't quite have enough lever arm and statistics to fit this parameter using this restricted range of momenta. There is a summary of this fit for all relevant experiments in table 6.11.

If we examine the fit to σ_p^A in figure 6.13 for the Monte Carlo, we notice that the form of σ_p is not correct. We correct σ_p to be the same form as the Monte Carlo when we are analyzing Monte Carlo data. We made this correction by plotting

$$\Delta p_G = (p_m(TPC) - p_G(TPC))/p_G(TPC)$$

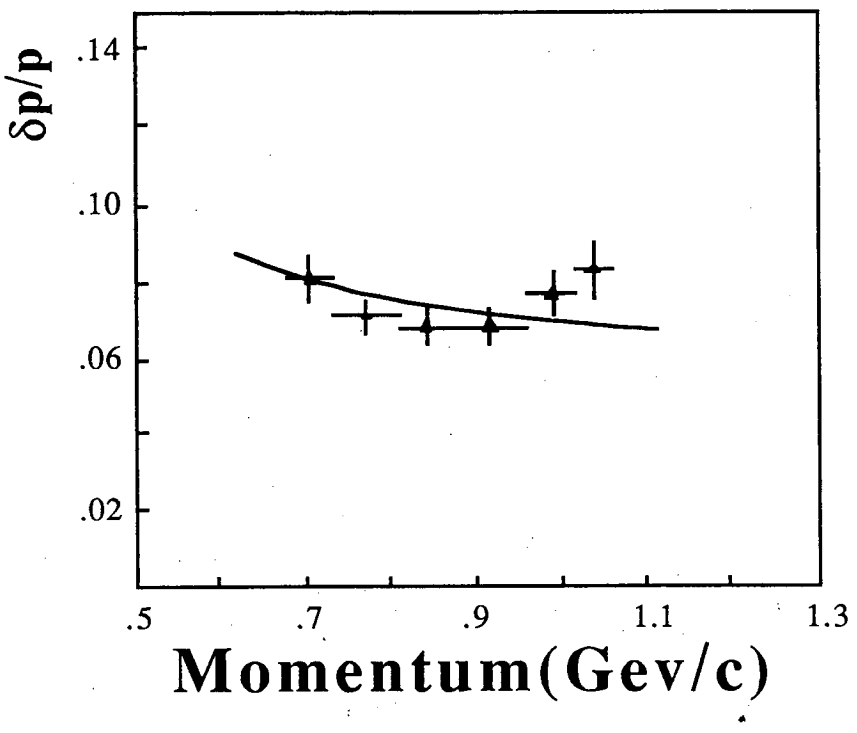

Figure 6.13: σ_p^A vs $\ln p$ for Experiment 62 (TPCLUND Monte Carlo)

vs $p_G(TPC)$ where

$$p_G(TPC) = p_G(MC) - P_{loss}(p_G(MC), m_k)$$

and $p_G(MC)$ is the Monte Carlo generated momentum and $P_{loss}(p_G(MC), m_k)$ is the expected momentum loss of a particle of mass m going thru the material in front of the TPC (see section 6.4.2 for a discussion of P_{loss}). The sigma of this distribution is $\sigma_p/p = \delta \ln p$.

We fit the best σ^f_{cou} and σ^f_{vtx} using the form for σ_p given in equation 6.10. Then we define a correction

$$\mathrm{Cor}_p^k(P) = \left(1 - \frac{(\delta \ln p)^k_M}{\sigma_p(\sigma^f_{cou}, \sigma^f_{vtx})/p}\right) \tag{6.30}$$

Finally, we fit a polynomial, $\mathrm{Polycor}_p^k$, to the set of data points defined above for each $k \in e, \mu, \pi, K,$ protons. An example of a fit is in figure 6.14. When we

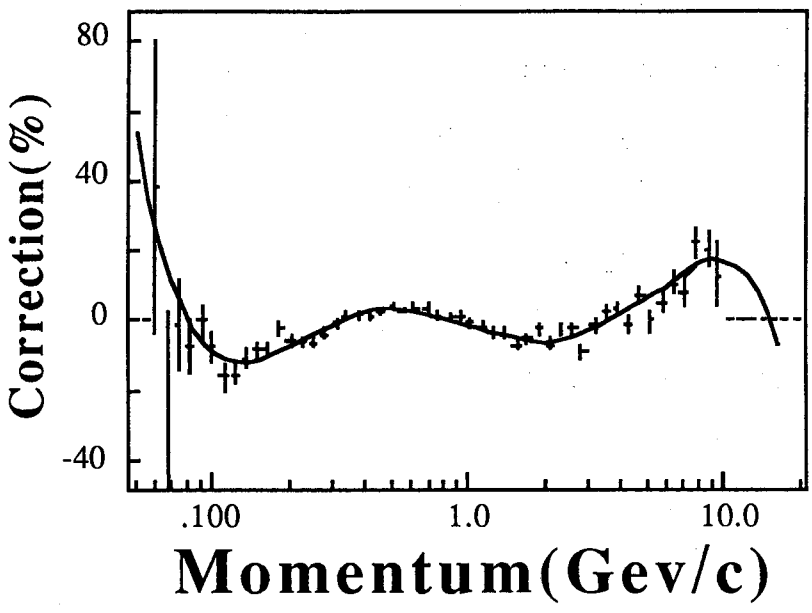

Figure 6.14: Fit of Polycor_p^π for 4 kG.

use the analytic method,

$$\Delta^k \ln p = (1 - \text{Polycor}_p^k) \times \frac{\sigma_p(\sigma_{cou}, \sigma_{vtx})}{p} \tag{6.31}$$

where σ_{cou} and σ_{vtx} are parameters which are fit using the method of section 6.2.2 for Monte Carlo experiments.

6.3.3 Vertex Momentum Measurement Error

The last resolution parameter to be determined from the data is the vertex momentum measurement error, σ_{vtx}. This parameter was measured by using Bhabhas in the data. However, the Monte Carlo allows us to generate a single particle at a particular momentum for which the tracking of the detector can be simulated.

σ_{vtx} in the Data

Bhabhas were selected by requiring

- Two well measured showers consistent with having been initiated by electrons or photons. Details on what cuts a shower must pass to be considered having been initiated by electromagnetic energy can be found elsewhere[46]. Note, however, that showers produced within 60mrad are merged together. This is because of interactions of electrons or photons with the Outer Drift Chamber(ODC) or the magnet coil. On average these interactions spread out an electromagnetic shower by about this much.

- We required the electrons to be back to back.

$$\begin{aligned} \Delta\lambda &< 3 \text{ milliradians(mr)} \\ \Delta\phi &< 6 \text{ mr} \\ \lambda &\leq 45^\circ \end{aligned}$$

  The first two cuts eliminate background from electrons which bremsstrahlunged. The cut on the dip angle insures that the electrons were in the Hexagonal Calorimeter (HEX).

The results of this selection are seen in figure 6.15. We plot

$$\text{Sign of electron charge} \times 1/\text{Momentum}$$

in this plot for tracks selected by these criteria. We use 1/Momentum because the measured curvature of a track is the quantity which has gaussian errors and is always defined. The quantity 1/Momentum is proportional to curvature.

The non–gaussian tails in figure 6.15[82] are from electrons which bremsstrahlunged. We only use the shaded region in our fit of the peaks to avoid biasing the fit with this background. The following table shows the result of this fit for experiment 11.

Experiment	$\Delta p/p^2\overline{\sin\theta}$
11	$\leq 3.2\%/\text{GeV}$

Using Bhabha events is not the optimal way to determine the vertex momentum resolution for multi–hadron events. This is because we will have more

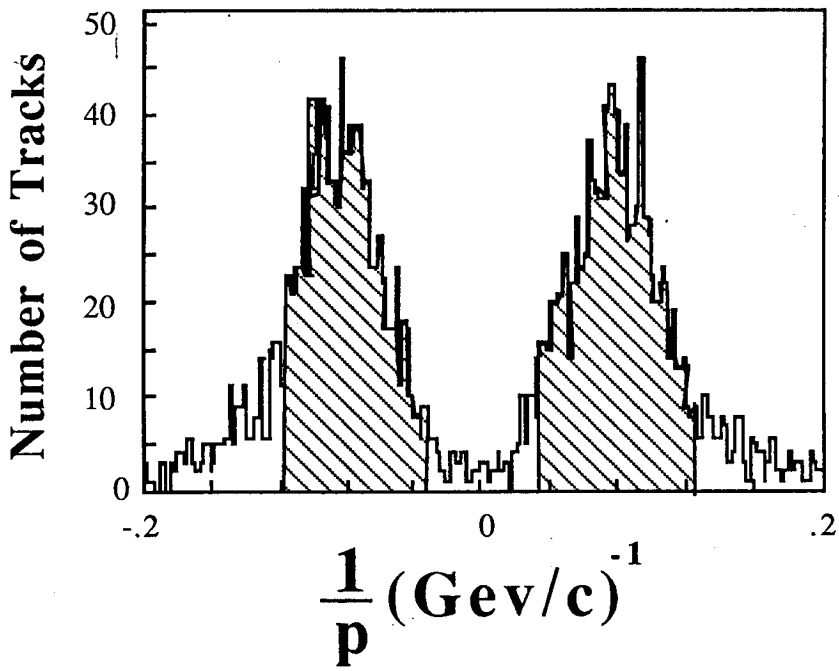

Figure 6.15: $(\frac{q}{e}$/Momentum for Bhabhas found for runs 594 to 900 in experiment 11. The sign of the electron's charge is $\frac{q}{e}$.

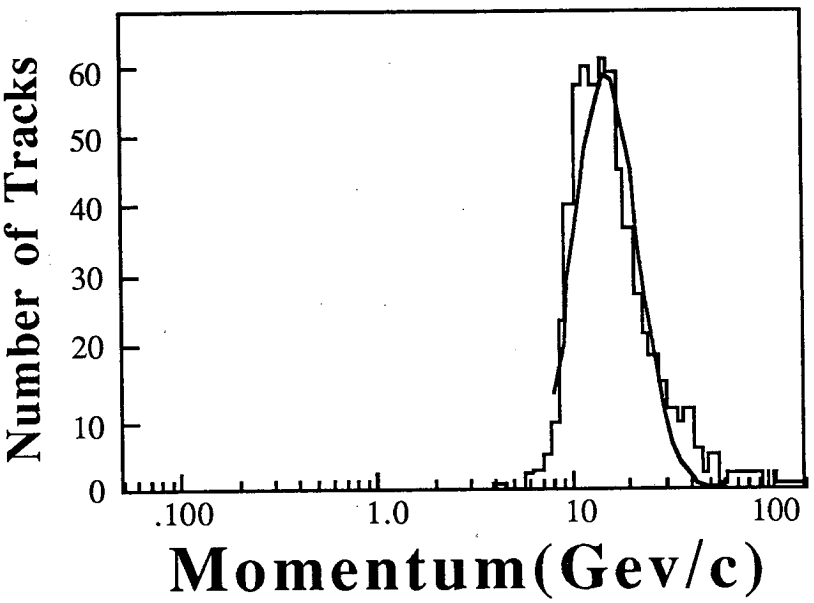

Figure 6.16: $\ln p$ measured for 1000 kaons generated at 14.5 GeV and tracked using 4 kG TPCLUND

tracks to match an event vertex in $q\bar{q}$ events and the TPC has a slight degradation tracking multi–track events. To get a more realistic idea of the momentum resolution, we examine all tracks found for a series of runs. The details of the method can be found in references [83] and [84]. The following table summarizes the results for experiments 11 and 12.

Experiment	Bias	σ_{vtx}
11 + 12	$(-0.5 \pm 0.2)\%$	$(3.6 \pm 0.2)\%$ GeV/c

σ_{vtx} in the Monte Carlo

The LUND Monte Carlo generator allow us to generate a single particle between two chosen momenta. If one makes the difference in the momenta very much smaller than the average momentum, this will effectively generate a monoenergetic beam of particles.

We generated 1000 kaons at 4.49, 5.48, 6.06, 7.04, 10.00 and 14.50 GeV.

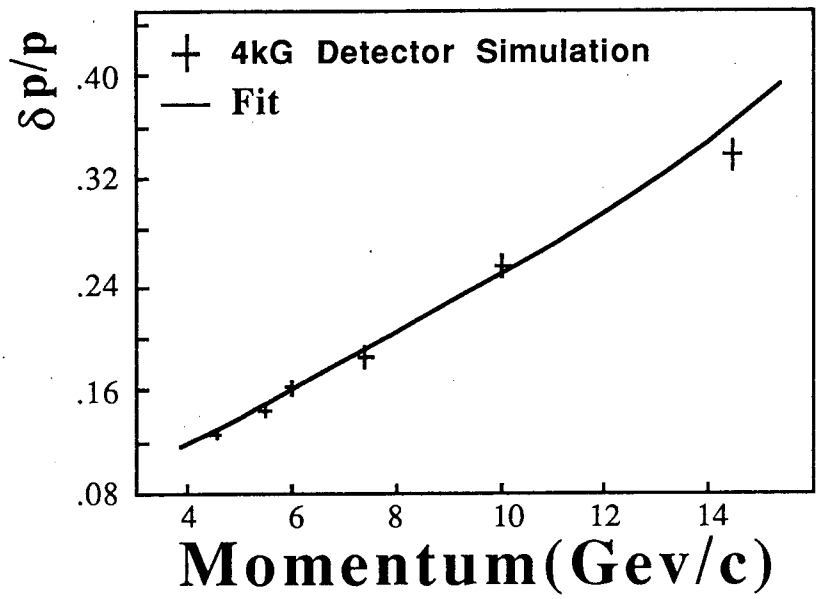

Figure 6.17: Fit of $\delta \ln p$ using 4 kG detector simulation for momenta greater than 4 GeV.

We tracked these kaon samples using the detector simulation TPCLUND. A track was accepted if it passed the track selection criteria detailed in section 5.2. Figure 6.16 shows the measured $\ln p$ for kaons generated in the 14.50 GeV run and tracked in a 4 kG magnetic field with TPCLUND. Using equation 6.10 and setting $\sigma_{cou} = 0.045$ we can determine σ_{vtx} by fitting the variation of the width of $\ln p_m$ to the form in equation 6.10. Figure 6.17 shows the 4 kG fit.

Magnetic Field	σ_{cou}	σ_{vtx} Fit	σ_{vtx} $p = 14.5$ GeV/c only
4 kG	0.045	0.0253 ± 0.0003	0.0234 ± 0.001

Table 6.12: List of vertex momenta found in 4 kG Monte Carlo simulation.

6.4 Analysis of dE/dx vs $\ln p$ plot

We must improve our **toy model** in several important areas in order to be able to analyze the TPC data produced in the experiment or simulated by TPCLUND.

1. Remove the approximation that we can decompose the probability into the product of two independent integrals as in equation 6.16.

2. Add detector and physics effects. This includes acceptance, $\pi \rightarrow \mu$ decay and energy loss in the material in front of the TPC.

3. Determine the Resolution constants for the 2–dimensional representation.

The remainder of this chapter is devoted to discussing these issues.

6.4.1 Accurate analytic probability calculation

The problem of making an accurate analytic model of the TPC is not only a physics issue but also one of computer science. To put it simply, what is the most efficient way to integrate over a fine two dimensional grid?

We want the bin sizes along the x and y axes to be on the order of sigma along the axis. This implies that the bin size along the dE/dx axis should be on the order of 0.44 KeV/cm. We actually used a bin size along this axis of half this, 0.256 KeV/cm. We have a much harder problem along the x axis. The error in measuring $\ln p$ at low momentum is on the order of $\sigma_{cou} = 0.06$ in the 4 kG running and 0.02 in the 13 kG running. However at high momentum the measurement error in $\ln p$ is $\sigma_{vtx} \times p$. This corresponds to a $\frac{dp}{p}$ of 0.3 in the 4 kG running and about 0.04 in the 13 kG running at a momentum of 8.0 GeV. We chose the bin size along the $\ln p$ axis to be 0.1 which is a reasonable compromise with space requirements.

We are interested in the range of momenta between $\ln p = -2.5$ and $\ln p = 2.5$ and the range of dE/dx between 10.0 KeV/cm and 32.0 KeV/cm. This implies

that we need about fifty momentum bins and about one hundred dE/dx bins. Actually we need more bins because of the edge problem discussed in section 6.2.1. We must smear from more bins than we are interested in because we have to put a finite limit on the grid. No particles are produced in the analytic model above and below the grid limits. The high momentum limit is not unreasonable because we must conserve the momentum and energy of the initial interaction, but the lower limit is artificial. We chose to expand the grid to sixty momentum bins and one hundred twenty five dE/dx bins.

Next we must consider how to do the integration of equation 6.4. Our first approximation is to consider the dE/dx in a momentum bin to be the value for dE/dx of a particular particle species at the center of a bin in $\ln p$. Unfortunately, at low momentum, in one $\ln p$ bin of 0.1, the dE/dx vs η curve drops thru **many** dE/dx bins. We will get horrible results if we approximate the dE/dx of a bin as above. The solution to this problem is to introduce what we call a *mini* bin. A *mini* bin is contained in a momentum bin **but** the dE/dx for that particle only travels thru one dE/dx bin. Pions, for example, need about 300 *mini* bins over the grid we have constructed but protons in contrast only need 125 *mini* bins.

In figure 6.18 we show the projection onto the dE/dx axis of TPCLUND data and our prediction. In figure 6.18a we don't use *mini* bins. One observes bumps which have the width of the dE/dx resolution. Clearly this is due to assuming the dE/dx in a bin is the dE/dx for a particle at the middle of a $\ln p$ bin. Figure 6.18 b includes *mini* bins.

If we assume the number of *mini* bins is 200 for each charged particle, then smearing must be computed to $125 \times 60 = 7500$ bins for each of $200 \times 5 = 1000$ *mini* bins. This rather daunting number of 7.5 million smears need to be computed each iteration used in computing the minimum in χ^2_{pseudo} space. In computing the minimum, it takes on the order of 1500 iterations to minimize the

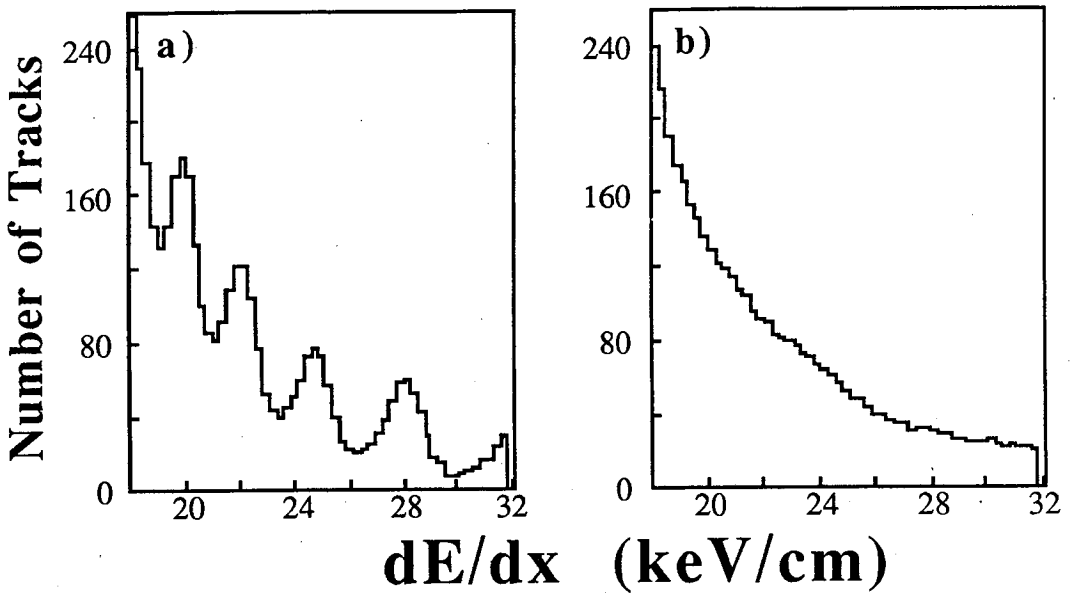

Figure 6.18: Projection onto dE/dx axis of predicted dE/dx vs $\ln p$ plot for the $1/\beta^2$ region. a) no *mini* bins b) with *mini* bins. Experiment 62 TPCLUND data where $\sigma_{cou} = .045$.

χ^2 in the CERN MINUIT program. Obviously, without some simplification, this would be a extremely time consuming operation even with a *super computer*.

The first assumption, is to approximate a *uniform* distribution of particles in a *mini* bin. This approximation allows us to compute the smearing from each *mini* bin to the rest of the grid only once. If one examines equation 6.2, one sees that without this approximation, we must recompute the smearing grid each time. But with this approximation, $E^k_{\rm TPC}(i',j')$ can be decomposed into

$$\begin{aligned} E^k_{\rm TPC}(i',j') &= \sum_{i \in mini\ \text{bins}} \int_{p\in i} N_k(p)dp \times Prob_k(i \rightarrow i'j') \\ &= \sum_{i \in mini\ \text{bins}} Prob_k(i \rightarrow i'j') \int_{p\in i} N_k(p)dp \end{aligned} \tag{6.32}$$

where k refers to each particle species. Since only $N_k(p)$ varies on each iteration of MINUIT, the smearing probability $Prob_k$, need only be computed once.

Now we need to reduce the number of points to which we smear. Most of this grid is empty as can be seen in figure 5.7. One obvious way to remove the

unwanted grid points is to require more than a minimum amount of smearing to a grid point before we use that point. We assume there is one particle per *mini* bin. Only if

$$E^k_{\rm TPC}(i',j') = \sum_{i \in mini\ \rm bins} Prob_k(i \rightarrow i'j') > smear\_bin \qquad (6.33)$$

where *smear_bin* is a constant, do we smear this particle to the $i'j'$ grid point. This approximation reduces the number of total smears by a factor of 50.

Finally, we don't want bins where we will predict a negligible number of particles, to be used in the calculation of χ^2_{pseudo}. We follow the same idea as the above smearing cut except we sum over all particles k. Then if this sum is greater than some small constant χ^2_{min}, we use this grid point in the calculation of χ^2_{pseudo}.

One might ask, why not have MINUIT determine the best values of the resolution parameters? The program MINUIT hunts for minimums in χ^2 space by taking the gradient of equation 6.20[85]. It gets more accurate results because it has a better algorithm to determine the correlations between terms. However there is a catch. First, MINUIT takes a number of iterations proportional to the number of terms in equation 6.20. The number of terms equals

$$\text{Number of Terms} = n + \frac{n(n+1)}{2} + 1$$

where n is the number of parameters we need to fit for the spectrum. Hence if we add k resolution parameters to fit by MINUIT, the number of iterations to obtain the spectrum will increase proportional to

$$\approx \frac{(n+k)^2}{n^2}\ .$$

Hence our method of taking a restricted number of points and constructing a small grid while less accurate, will require far fewer iterations to obtain our resolution parameters and our spectrum.

On top of this effect, it takes about fifteen minutes of CPU time to compute the smearing probabilities $Prob_k$ on the VAX 11/780 (about three minutes on a VAX 8600 series computer). By comparison, it takes only three seconds to compute $E^k_{\rm TPC}(i',j')$ for a fixed smearing grid. Hence by determining the resolution parameters in a crude way, the amount of computer time required for the entire problem will drop by an order of magnitude or so.

6.4.2 Detector considerations

To make an accurate representation of the data, we must correct for detector and physics effects.

Acceptance

The most serious detector effect is the inability to detect all the particles produced in an e^+e^- interaction. We correct for the acceptance of our detector by use of the LUND generator and the TPCLUND detector simulator. The acceptance of the detector for particle species k is defined as

$$Acc^k(p) = \frac{\text{Number of } k \text{ Detected in TPCLUND}}{\text{Number of } k \text{ Generated in LUND at momentum } p} . \qquad (6.34)$$

The reason why we defined the acceptance of the detector at the vertex momentum p is because there is a considerable amount of material in front of the TPC (please see section 3.1). Hence the momentum we detect in the TPC is less than the momentum the particle was created with at the vertex. Notice this definition of acceptance includes Monte Carlo estimates for

- geometrical acceptance,
- losses of particles (primarily pions) due to interactions with the material in front of the TPC,
- production of particles (primarily protons) by nuclear interactions,

- decays in flight of pions and kaons and
- decays of higher mass resonances into pions, kaons and protons.

Energy Loss in Material in front of the TPC

We know by the theory of energy loss as detailed in section 4, that the energy lost in a given material by particles of the same plus or minus charge should be a function of only the velocity β of the particle. We can translate this dependence on β to a sole dependence on the more convenient $\eta = p/m$ since

$$\eta = \beta/\sqrt{1-\beta^2}\,.$$

We calculated the effect of the material in front of the TPC by plotting the energy measured in the TPC minus the energy a particle was generated with in the TPCLUND Monte Carlo vs $\ln\eta$ for all the different charged particles. It should be noted that the energy lost by pions is consistent with the energy lost by kaons in the detector simulation. However low η protons and kaons have inconsistent energy losses in the beam pipe in the same simulation.

The reason for the inconsistency between the low η kaons and protons is that a large number of low momentum protons are produced in inelastic interactions between pions and the material in front of the TPC. Hence, the protons produced in this manner on average traverse less material than hadrons produced in the primary interaction. Therefore we expect that the energy lost by protons is slightly less than pions and kaons because these particles are not produced copiously in beam pipe interactions. The TPCLUND Monte Carlo simulates this effect and therefore the lower energy loss experienced by protons in the detector simulation merely reflects this.

We group the $\pi^{\pm}$ and $K^{\pm}$ data together to fit the energy lost by pions and kaons in front of the TPC. We make a separate fit for protons and as a practical

matter use this fit for anti–protons too. For all particles, the range in $\ln\eta$ was divided into two parts: A low η region where $\eta < \eta_{min}$ where η_{min} is the value of η at minimum ionization ($\eta_{min} = 3.71$) and a high η region. There is no relativistic rise in the Monte Carlo and therefore the energy lost by particles whose $\eta > \eta_{min}$ was fit to a constant. In this region we estimate the energy lost by particles detected by the TPC to be on the order of 8.9 MeV.

The approximation that there is no relativistic rise is not bad because at the energies where $\eta > \eta_{min}$, the error in determining the energy by this approximation is

$$\frac{\delta E_{lost}}{E} \sim \frac{0.005}{E} < \frac{0.005}{\eta m} < \frac{1.5 \times 10^{-3}}{m} .$$

Even this is an overestimate because the largest deviations of the energy lost by particles passing thru material in front of the TPC would occur at momenta much larger than the momentum at minimum ionization in the material.

$\pi \rightarrow \mu$ decay

We must rely on the LUND Monte Carlo and the detector simulation TPCLUND to calculate the effect of $\pi \rightarrow \mu$ decay. There will be several effects of $\pi \rightarrow \mu$ decay:

1. a momentum shift,

2. worse momentum resolution, and

3. a small shift in the average energy loss in the TPC from what we would have expected for a muon.

We expect that in the rest frame of the pion

$$P^{\mu} - P^{\pi} = 0.21(E_{\pi}\cos\theta^{*} - P^{\pi}) \qquad (6.35)$$

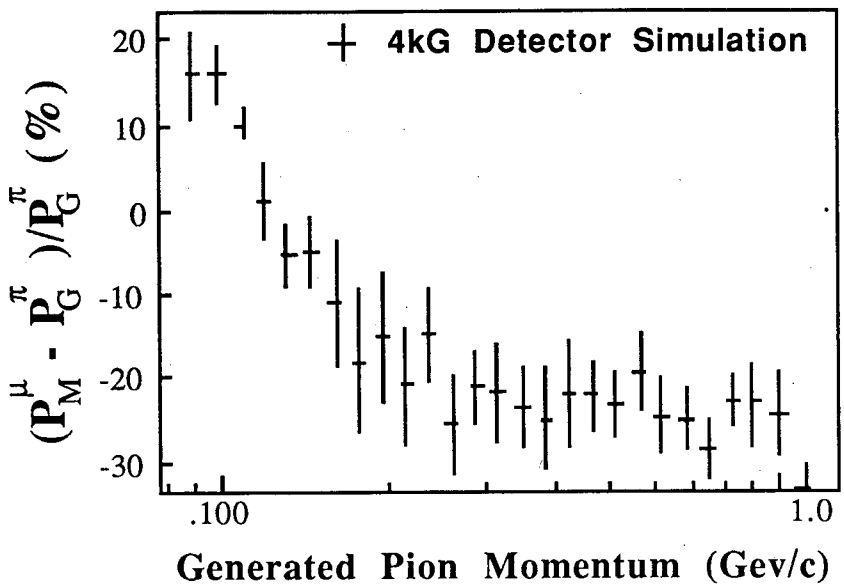

Figure 6.19: The momentum shift of the detected muon in $\pi \rightarrow \mu$ decay.

where E_π is the energy of the pion and $\cos\theta^*$ is the angle between the line of flight of the pion in the *lab* frame and the direction of the muon in the *rest* frame of the pion. If we average the above quantity over all angles, $\langle\cos\theta^*\rangle \approx 0$ [3]. Hence we expect

$$\langle P^\mu - P^\pi \rangle = -0.21 \langle P^\pi \rangle \ .$$

We plot $(P_M^\mu - P_G^\pi)/P_G^\pi$ vs $\ln P_G^\pi$ in figure 6.19 where P_M^μ is the momentum of the muon measured in the TPCLUND detector simulator and P_G^π is the pion momentum generated in the LUND Monte Carlo. We find for momenta such that $\ln P_G^\pi \geq\sim -2.0$,

$$\langle \frac{P_M^\mu - P_G^\pi}{P_G^\pi} \rangle = \begin{cases} -0.229 \ \pm \ 0.011 & \ln P_G^\pi \geq -2.0 \quad 4\,\mathrm{kG} \\ -0.207 \ \pm \ 0.0087 & \ln P_G^\pi \geq -1.8 \quad 13\,\mathrm{kG} \end{cases}$$

just as expected by equation 6.35. However this relation seems to be violated at momenta less than $\ln P_G^\pi <\sim -2.0$. This effect is an acceptance effect. At $P_G^\pi = 135$ MeV, we expect to lose about 25 MeV in the material in front of the

[3] It is not exactly zero because of acceptance holes

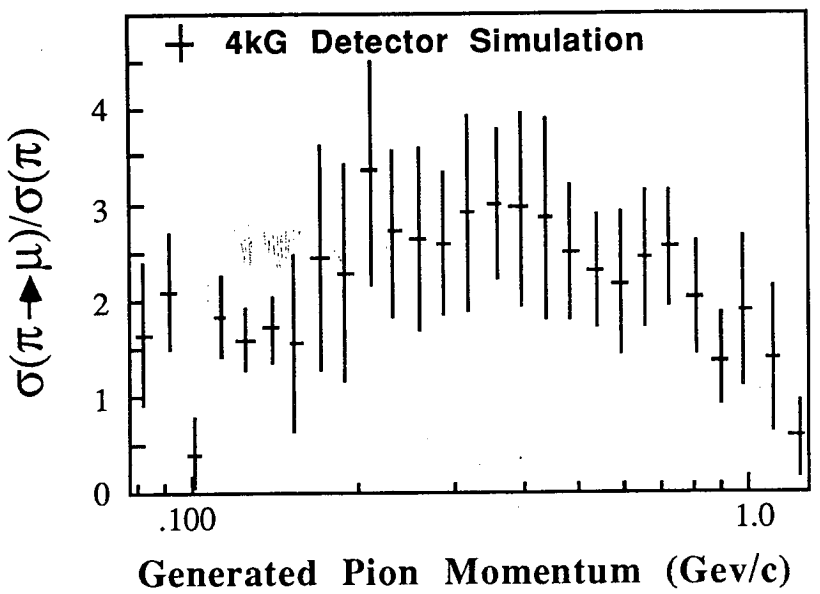

Figure 6.20: The broadening of the momentum resolution in $\pi \rightarrow \mu$ decay.

TPC. The muon loses another 29 MeV in the decay itself of $\pi \rightarrow \mu$. Hence if a 135 MeV pion is created in the interaction, on average we expect to measure a 85 MeV muon in the TPC. Particles of this momentum rarely make it into the TPC. Therefore only muons from the decay of 135 MeV pions statistically biased toward higher momenta will be seen in the detector.

Also the muon from $\pi \rightarrow \mu$ decay will not be measured as well as we would expect. When we find a set of tracks in the detector, we constrain all of these tracks to come from a single point in space (the primary interaction point). The exception to this rule is when we are looking for secondaries. However in $\pi \rightarrow \mu$ decay, we cannot look for "V's" because we don't detect the neutrino. But since pions decay some distance from the primary interaction ($c\tau$ for the pion is 780 cm), constraining the muon detected in the TPC to the vertex will result in an error. This error leads to a broadening of the momentum resolution for the detected track.

To calculate this effect, we plot $(P_M^\mu - P_G^\pi)/\sigma_p(P_{EXP}^\pi)$ vs $\ln P_G^\pi$ in figure 6.20 where P_{EXP}^π is the expected pion momentum in the TPC:

$$P_{EXP}^\pi = P_G^\pi - P_{loss}(P_G^\pi, m_\pi)$$

where $P_{loss}(P_G^\pi, m_\pi)$ is the expected momentum which would be lost in the material in front of the TPC. It is calculated from the Energy lost in the obvious way

$$P_{loss}(p,m) = p - \sqrt{(\sqrt{p^2+m^2} - E_{lost}(p,m))^2 - m^2}\,. \tag{6.36}$$

Basically we see that the momentum resolution of the muon is about twice as bad as we would have expected for a pion that would not have decayed to a muon.

Finally, the pion may decay to a muon inside the TPC. Since there is so little Q in the interaction, the muon will travel in nearly the same direction as the pion. Our tracking algorithm will assume that all the points belong to the same track with perhaps a little larger than usual scatter at the decay point. When we go to "hang" wires onto the track, some of the wires will have an dE/dx consistent with a pion and some will have a dE/dx consistent with a muon with 29 MeV less energy. This implies that the overall dE/dx of the track will be slightly higher than we would expect for a muon traversing the TPC. Hence, on average the muon dE/dx will be slightly shifted to a higher value. We can allow for this effect by allowing the "mass" of muons from π decay to be corrected by some small amount.

We show this effect in figure 6.21 in the detector simulation. Plotted in this figure are $\ln P_M^\mu / Tr_\pi^{-1}((dE/dx)_M)$ vs $(dE/dx)_M$. We explained in section 6.3.2 that the centroid of this distribution should be $\ln m_\mu/m_\pi$. If we fit figure 6.21 to a constant we find

$$\ln(m_{\pi\to\mu}/m_\pi) = \begin{cases} -0.2239 \pm 0.0070 & 4\,\mathrm{kG} \\ -0.2952 \pm 0.0050 & 13\,\mathrm{kG} \end{cases}$$

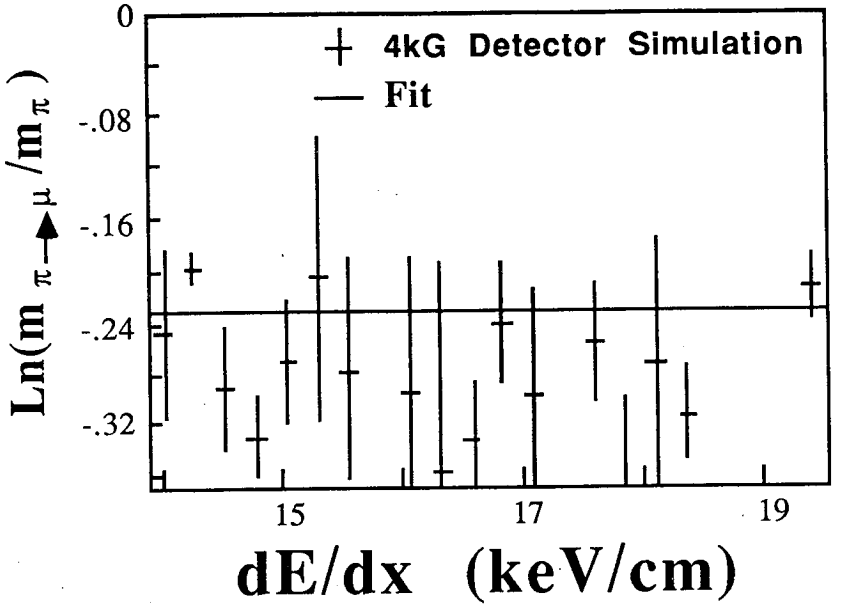

Figure 6.21: The dE/dx of muons from $\pi \rightarrow \mu$ decay.

which corresponds to a $\pi \rightarrow \mu$ "mass" of

$$m_{\pi\rightarrow\mu} = \begin{cases} 111.1 \pm 3.5 & 4\,\mathrm{kG} \\ 103.5 \pm 1.8 & 13\,\mathrm{kG} \end{cases}$$

in the detector simulation.

Momentum Bias

It is possible that the detector will have a systematic shift between the measured momentum and what the momentum actually was in the detector. We allow for this possibility by including a momentum bias. All measured momenta will be shifted by this correction.

Corrections

We chose to maintain the shape determined by the detector simulation of all corrections. However, we allowed a multiplicative constant to change the scale

of all corrections. Symbolically, our corrections usually have the form

$$Cor_k = (1 - s\, f(p_{vtx}, m_k)) \tag{6.37}$$

where f is the shape of the correction as determined by the Monte Carlo detector simulation and s is a scale factor. There are two exceptions: The energy lost by particles in the material in front of the TPC was just multiplied by a scale factor

$$E_{lost} = s\, E^{MC}_{lost}(p_{vtx}, m_k)$$

The momentum bias and the mass correction for $\pi \rightarrow \mu$ have no scale factors s (or $s = 1$). The following table gives the corrections and the order of each polynomial. We fix the factor s by using the method outlined in section 6.2.2.

Correction	Degree	Scale
$p = p(1 - \text{Bias})$	0	N
$p_{\pi\rightarrow\mu} = p(1 - s f_{p_\pi\rightarrow\mu})$	4	Y
$\sigma_p(\pi \rightarrow \mu) = s\sigma_p\,(p_{vtx} - P_{lost}(p_{vtx}, m_\pi))$	0	Y
$m_{\pi\rightarrow\mu} = m_\mu\,(1 - f_{\pi\rightarrow\mu})$	0	N
$E_{lost} = s\, f_{E_{lost}}$	4	Y

Putting it all together

The number of particles we expect in a grid bin $i'j'$ must be modified by the corrections we have mentioned in this section.

$$N(i'j') = \sum_{k=1}^{6} \sum_{i,l} \int_{p\in l} N_k(p)\, dp\, Acc^k(l) Prob^k_{loss}(i,l)\, Prob_k(i \rightarrow i'j') \tag{6.38}$$

where N is the number of particles expected to be found in grid bin $i'j'$, i and l refer to the *mini* momentum bins, $Prob^k_{loss}(i,l)$ is the probability for particle k to lose momentum $p_i - p_l$, Acc and $Prob_k$ were described earlier. Particle 6 is defined as $\pi \rightarrow \mu$ decay. $Prob^k_{loss}(i,l)$ is given by

$$Prob^k_{loss}(i,l) = \begin{cases} 1 & p_i - p_l = P_{loss}(p_i, m_k) \\ 0 & p_i - p_l \neq P_{loss}(P_i, m_k) \end{cases}$$

where P_{loss} is given by equation 6.36. We need to modify $Prob_k$ in trivial ways because of $\pi \rightarrow \mu$ decay and the momentum bias. Finally, particle $\pi \rightarrow \mu$, is defined in terms of the spectrum of pions. So the spectrum N_6 is defined as

$$N_6(p) = N_\pi(p)$$

and the acceptance of $\pi \rightarrow \mu$ decay is

$$Acc(6) = \frac{\text{Number of } \pi \rightarrow \mu \text{ decay detected in TPCLUND}}{\text{Number of } \pi \text{ generated in LUND}} .$$

6.4.3 Determining Resolution Parameters

The determination of the probability of measuring a particle at a particular energy loss dE/dx and momentum p' for a particle traveling thru the TPC at momentum p is the most crucial aspect of the two dimensional method. This presents less of a problem for the detector–simulated data. We know everything about simulated data. Hence, we can know precisely the resolution inside the Monte Carlo. Experimental data presents us with more unknowns.

We use the χ^2 method presented in section 6.2.2 in order to determine the resolution parameters for both the detector–simulated data and the experimental data. We of course move from the toy model to the more complete description of TPC data given in equation 6.38. However the multiple scattering error, σ_{cou}, the vertex momentum error, σ_{vtx}, the dE/dx resolution, σ_d, the "Tail" parameter, the momentum bias, and the scale factors for the energy loss and $\pi \rightarrow \mu$ decay were all fixed by the χ^2 method.

Our procedure is to form a grid of five points for each parameter. The pseudo χ^2 is formed at each point and written to disk. If P_0 is the value of the parameter and ΔP_0 is the statistical error on the value of the parameter, the five points used are:

$$P_0 \pm 2\Delta P_0,\ P_0 \pm \Delta P_0 \text{ and } P_0 .$$

Afterwards, a global fit using equation 6.20 is made which results in a new set of resolution parameters. These new resolution parameters and their errors are then used as a starting point for another iteration. The reason we need more than one iteration is that the parabolic form is merely an approximation for how the χ^2 varies near the best values of the resolution parameters. Additionally every new set of resolution parameters slightly changes the bins accepted for use in the comparison of the data to the fit for a given spectrum. We continue iterating the resolution parameters until the χ^2/DOF reaches a minimum value. At this point, the set of resolution parameters is taken as the best values and used in the fitting.

One of the major uncertainties in using the χ^2 method to determine the resolution parameters is the value of the underlying spectrum, $N_k(p)$. Our object is to find this spectrum in the case of the experimental data . One worry is that after determining a set of resolution parameters with an initial spectrum, we find that our spectrum fitted with those resolution parameters would give a different set of resolution parameters.

The detector–simulated data presents no problem because we know the underlying generating distributions of particles. Needless to say that is not true in the case of the experimental data. We solved the problem by the method of *relaxation*. That is, we set the initial set of resolution parameters for the experimental data using the LUND as the initial spectrum. We then fit the experimental data using this initial set of resolution parameters. We then used the fitted spectrum to redetermine the resolution parameters. We then repeated the entire procedure until all resolution parameters determined in two successive iterations were consistent with one another (i.e. within statistical errors of one another).

We remark that only two iterations were required before the consistency con-

dition was met. The resolution parameters found using LUND as the underlying spectrum are reasonably close to the final parameter values. Table 6.14 lists the initial and final values of the resolution parameters for experiments 11 and 12. Table 6.13 lists the values of resolution parameters found for the detector–simulated data. The column labeled "systematic error" is an estimate of the systematic error in using the χ^2 method to determine the resolution parameters and the actual parameter. It is merely the difference between the values of the resolution parameters found for detector–simulated data by the χ^2 technique and using other methods as shown in section 6.3. We note that the systematic error in determining the resolution parameter is generally larger than the statistical error in each of the resolution parameters.

Finally, the systematic errors for determining the $\pi \rightarrow \mu$ parameters are large. The pion spectrum under $\sim$ 200 MeV/c is predominantly $\pi \rightarrow \mu$ decay. Therefore, we do not report the pion spectrum for momenta under 200 MeV/c.

Parameter	Best Value	Expected	Systematic Error
σ_{cou}	$4.504 \pm 0.071 \times 10^{-2}$	4.431×10^{-2}	0.073×10^{-2}
σ_{vtx}	$3.17 \pm 0.27 \times 10^{-2}$	2.53×10^{-2}	0.64×10^{-2}
σ_d	$4.081 \pm 0.014 \times 10^{-2}$	3.730×10^{-2}	0.351×10^{-2}
Tail	1.656 ± 0.014	1.421	0.235
Eloss	1.020 ± 0.007	1.00	0.02

Table 6.13: Resolution Parameters found in the Detector–Simulated Data

Parameter	Initial	Final
	E11	
σ_{cou}	$5.56 \pm 0.17 \times 10^{-2}$	$5.94 \pm 0.20 \times 10^{-2}$
σ_{vtx}	$4.24 \pm 0.23 \times 10^{-2}$	$4.06 \pm 0.23 \times 10^{-2}$
σ_d	$3.904 \pm 0.024 \times 10^{-2}$	$3.8961 \pm 0.0047 \times 10^{-2}$
Tail	1.510 ± 0.031	1.544 ± 0.013
Eloss	0.882 ± 0.051	0.6760 ± 0.017
	E12	
σ_{cou}	$5.88 \pm 0.10 \times 10^{-2}$	$6.01 \pm 0.16 \times 10^{-2}$
σ_{vtx}	$4.01 \pm 0.18 \times 10^{-2}$	$3.67 \pm 0.23 \times 10^{-2}$
σ_d	$3.9061 \pm 0.0071 \times 10^{-2}$	$3.9211 \pm 0.0079 \times 10^{-2}$
Tail	1.4918 ± 0.0094	1.515 ± 0.012
Eloss	0.8773 ± 0.0039	0.8765 ± 0.0029

Table 6.14: List of Resolution Parameters found for the experiments

Chapter 7

Results and Conclusion

We are now prepared to analyze data and present results on the cross section of charged hadrons in 3–jet events. The chapter is organized as follows: first we will present the testing of the method, then will present the inclusive cross section of charged hadrons in the entire experimental data sample. We will then present the testing and results for 3–jet events.

7.1 Testing the method

The only way to check the method is to generate detector–simulated data via TPCLUND. Recall that TPCLUND produces a set of measured tracks for a given generated e^+e^- annihilation event. We can then use the dE/dx vs $\ln p$ plot as the "Data" to analyze using the two dimensional method. We then compare the fitted spectrum to the generated spectrum used for the detector simulator. We choose LUND as the generator for the simulated data although we could use other fragmentation models as the generators. However, LUND–generated data using TPCLUND as the detector simulator has been tuned to match our data[39].

We use the resolution parameters determined for the detector–simulated data (see the previous section). We first check how well the Monte Carlo generated event sample can be fit. We select hadronic events in the detector– simulated

data using the same cuts as in the real data. Out of 40,000 LUND–generated e^+e^- annihilation multi–hadronic events, 26,000 events pass the event selection cuts (please see chapter 5). We then must chose a functional form to represent the differential cross section, $d\sigma/dE$ where E is the energy of the particle.

We will now make the assumption that scaling holds true and so we expect

$$f(A,n) = \left(\frac{d\sigma}{dE_h}\right)_0 = A\beta\frac{(1-z)^n}{z} \tag{7.1}$$

as detailed in chapter 2. This equation holds true for each hadronic particle species, so A and n are parameters which need to be fit for each charged hadron separately. In equation 7.1, $z = E_h/E_q$ where E_h is the energy of the hadron and E_q is the energy of the initiating parton. Also β equals the usual p_h/E_h where p_h is the hadron's momentum.

Obviously, the fitted spectrum should not depend on the function chosen. However there are some functions which must be excluded. Recall that TPC data has regions of ambiguity between charged particles called crossover regions. Functions which rapidly change in this region cannot be used. That is

$$\frac{\partial f(p_1, p_2, \ldots)}{\partial p_i}$$

should not be large in the crossover region for any parameters used in the fit of the cross section. Otherwise the parameters for the particles involved in the cross over region can fluctuate wildly.

In the cross over regions only the sum of the two particle species is constrained. For instance, we used the sum of exponentials as the functional form for the cross section for each of the hadrons. When we fit the detector– simulated data from the Monte Carlo, we got too many kaons and too few protons in the kaon–proton cross–over region.

The determination of the differential cross section in the crossover region is subject to the following very restrictive assumption:

> The differential cross section in the crossover region is a smooth function connected to the regions outside of the momentum (or energy) interval of the crossover region.

In other words, the cross section outside of crossover region determines the value of the cross section inside the crossover region. Since the crossover regions are small, this should not be much of a problem. However,

- the values of the cross section inside the crossover region could conceivably be very far off, but
- The sum of the cross sections of the two particle species in the crossover region should be correct in the crossover region.

The two particle species most affected by the crossover regions are the kaons and the protons. The crossover region for the kaon and proton occurs at momentum ~ 3 GeV. But our measurement error on the momentum at this point is rather substantial

$$\frac{\delta p}{p} \approx 12\% \ .$$

This means the kaon proton (KP) crossover region will be extended. Additionally, kaons and protons are produced far less prodigiously than pions. Therefore, we not only display the spectrum for kaons and protons separately but also the sum of kaons and protons.

Finally, it is necessary to add some additional terms to the differential cross section when we fit the entire data sample. There are two reasons for this. First, many of the final state hadrons are the results of decays of higher mass hadrons. For instance the LUND Monte Carlo predicts that 80% of the final state pions are actually the result of decays. Second, the entire event sample contains partons at many parton energies. Most hadronic events have two very energetic partons

recoiling against each other at one half the center of mass energy. We implicitly assume mono-energetic partons by using the form in equation 7.1.

We added one term to the kaon and proton cross sections:

$$\frac{d\sigma}{dE} = \left(\frac{d\sigma}{dE}\right)_0 + C/E^2 \tag{7.2}$$

where C is a parameter to be fit and E is the energy of the hadron and $(d\sigma/dE)_0$ is from equation 7.1. Notice that the correction to the cross section, C/E^2, goes as $1/E^2$ and is therefore only prominent at low energies.

We needed to add an additional term for the pions

$$\frac{d\sigma}{dE} = \left(\frac{d\sigma}{dE}\right)_0 + C/E^2 + D\exp\left(-\eta E\right) \tag{7.3}$$

where D and η are parameters to be fit. The new term dies exponentially in E. Therefore the high energy behavior of the scaling cross section is approximately preserved by this functional form for all charged hadron cross sections. Additionally, the correction terms do not vary appreciably in the crossover regions.

Electrons and muons are not fit in this way. Electrons are mostly the result of conversions of photons in the material in front of the TPC. High momentum muons are from the decays of heavy quarks but they are so swamped by the number of pions they can be ignored. To fit the lepton species we use the expected momentum spectrum of each lepton species from the Monte Carlo (LUND generator with the TPCLUND detector simulator). We scale the spectra by the ratio between the number of hadronic events in the Monte Carlo and the number in the experiment. We then allow the scale of the electrons to be fit by the two dimensional method. The scale of the muons is fixed to one. When we fit detector-simulated data we expect the scale of the electrons to be consistent with one. Of course, fitting the actual experimental data may not give us a number consistent with one because the Monte Carlo is only good to 10% to 20%.

Before we list the comparison between the generated data and two dimensional fit to the detector simulation of this data, we will discuss the concept of **hadronic fractions**. The fraction of a particular hadron (pion, kaon or proton) at a particular momentum is defined as

$$f_h(p) = \frac{N_h(p)}{\sum_{h=\pi,K,p} N_h(p)} \tag{7.4}$$

where $N_h(p)$ is the number of hadrons h at momentum p. The advantage of this quantity over the actual spectrum is that the acceptance appears in both the numerator and the denominator of this expression. Since the acceptance for all charged hadrons is about the same, to first order there will be a no systematic error in this quantity from the uncertainty in the acceptance. Low energy protons are the only exception. A large number of protons (not anti–protons) with energies less than $\sim$ 1.0 GeV are produced by pion interactions with the aluminum beam pipe. Hence, there is a larger uncertainty in the number of low energy protons due to the systematic uncertainty in the acceptance than in the number of low energy kaons and pions. We will discuss this further in section 7.2.1.

Table 7.1 then gives the results of using the detector–simulated data to test the two dimensional method. The "LUND" column is the fit of the LUND–generated data itself. The "2-D fit" column is the result of using the two dimensional method to fit the parameters using detector–simulated data. Notice that equation 6.38 includes the acceptance correction. Therefore this fit is the most likely underlying generating spectrum for each of the hadrons. The systematic error column lists the difference between the fitted spectrum and the actual LUND–generated spectrum in percent. Finally, the systematic error in the fractions column gives the error between the hadronic fraction measured and the actual hadronic fractions generated. Since fractions themselves are equivalent to percentages, the "Error Fractions" column gives the absolute error, not the percentage error.

Parameter	LUND	2D–Fit	Systematic Error Spectrum(%)	Fraction
		π		
A	0.250	0.219 ± 0.008		
n	3.318	2.973 ± 0.078		
C	-3.964×10^{-3}	$-2.956 \pm 0.088 \times 10^{-2}$	3.5	0.005
D	0.722	0.777 ± 0.021		
η	1.807	1.634 ± 0.023		
		K		
A	7.46×10^{-2}	$7.38 \pm 0.29 \times 10^{-2}$		
n	2.69	2.60 ± 0.10	3.7	0.004
C	-3.8×10^{-3}	$-3.5 \pm 1.6 \times 10^{-3}$		
		P		
A	3.58×10^{-2}	$2.35 \pm 0.44 \times 10^{-2}$		
n	2.97	2.83 ± 0.32	2.0	0.005
C	2.45×10^{-2}	$2.72 \pm 0.34 \times 10^{-3}$		

Table 7.1: Comparison between the generated data and two dimensional fit to the detector–simulated data (E62).

7.2 Inclusive Cross Sections in the Entire Data Sample

Once we have determined the resolution parameters in the data, we can use the method to fit the inclusive cross sections of charged hadrons in the experimental data. Figure 7.1a shows the 90% Confidence Level (CL) limits on the inclusive scaling cross section

$$\frac{1}{\beta\sigma_{\rm had}^{\rm tot}}\frac{d\sigma_h}{dx}$$

where $\sigma_{\rm had}^{\rm tot}$ is the total hadronic cross section, σ_h is the cross section for charged pions, kaons or protons, x is defined as the energy of the hadron E_h divided by twice the beam energy $E_{\rm beam}$, ie. $x = E_h/2E_{\rm beam}$. Figure 7.1b shows the 90% CL limit on the hadronic fractions. We add together the experiments 11 and 12 for the purposes of these figures.

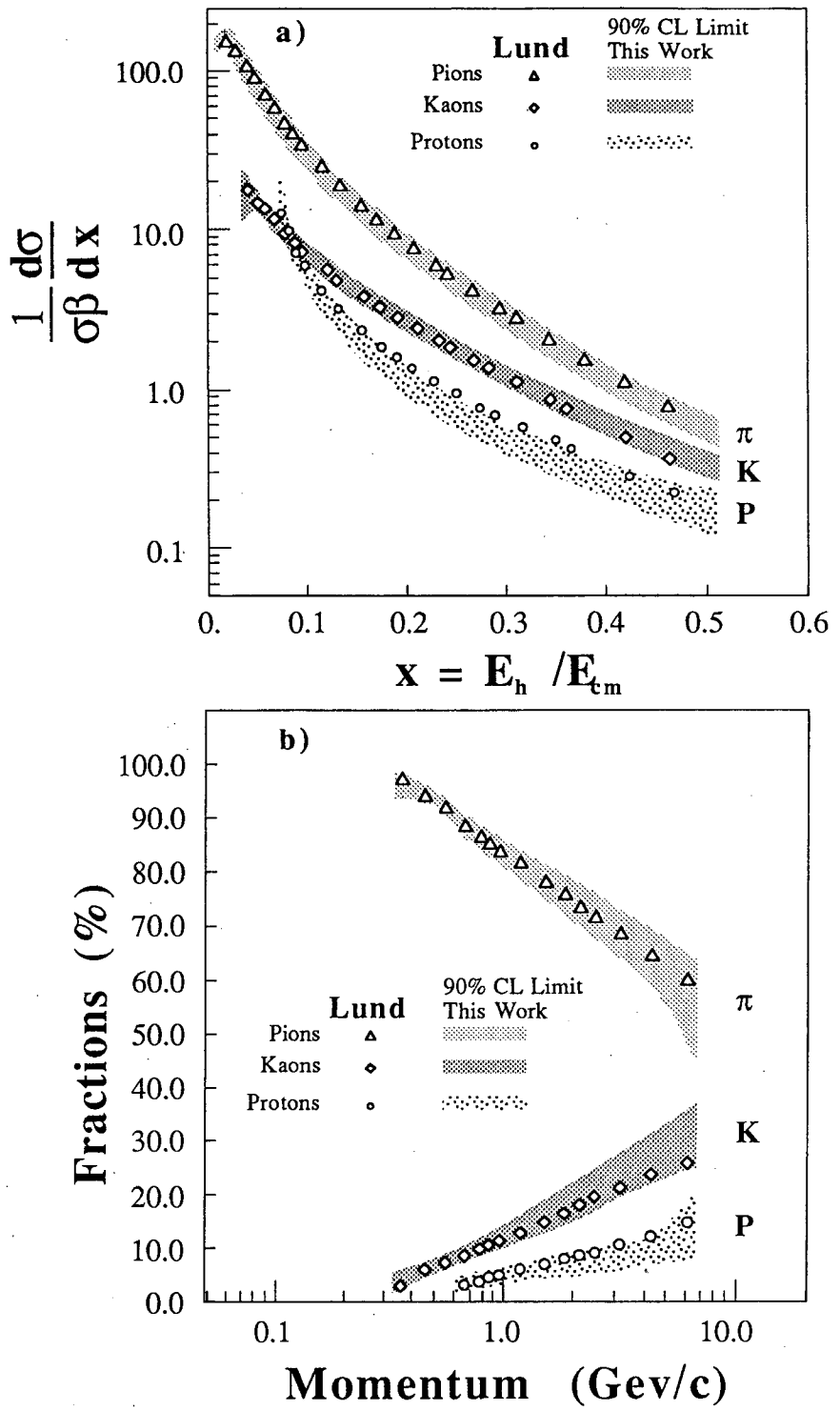

Figure 7.1: Results of E11+12. a) Scaling cross sections in x, b) Hadronic fractions in momentum. The Shaded area represents the 90% CL limits from this measurement.

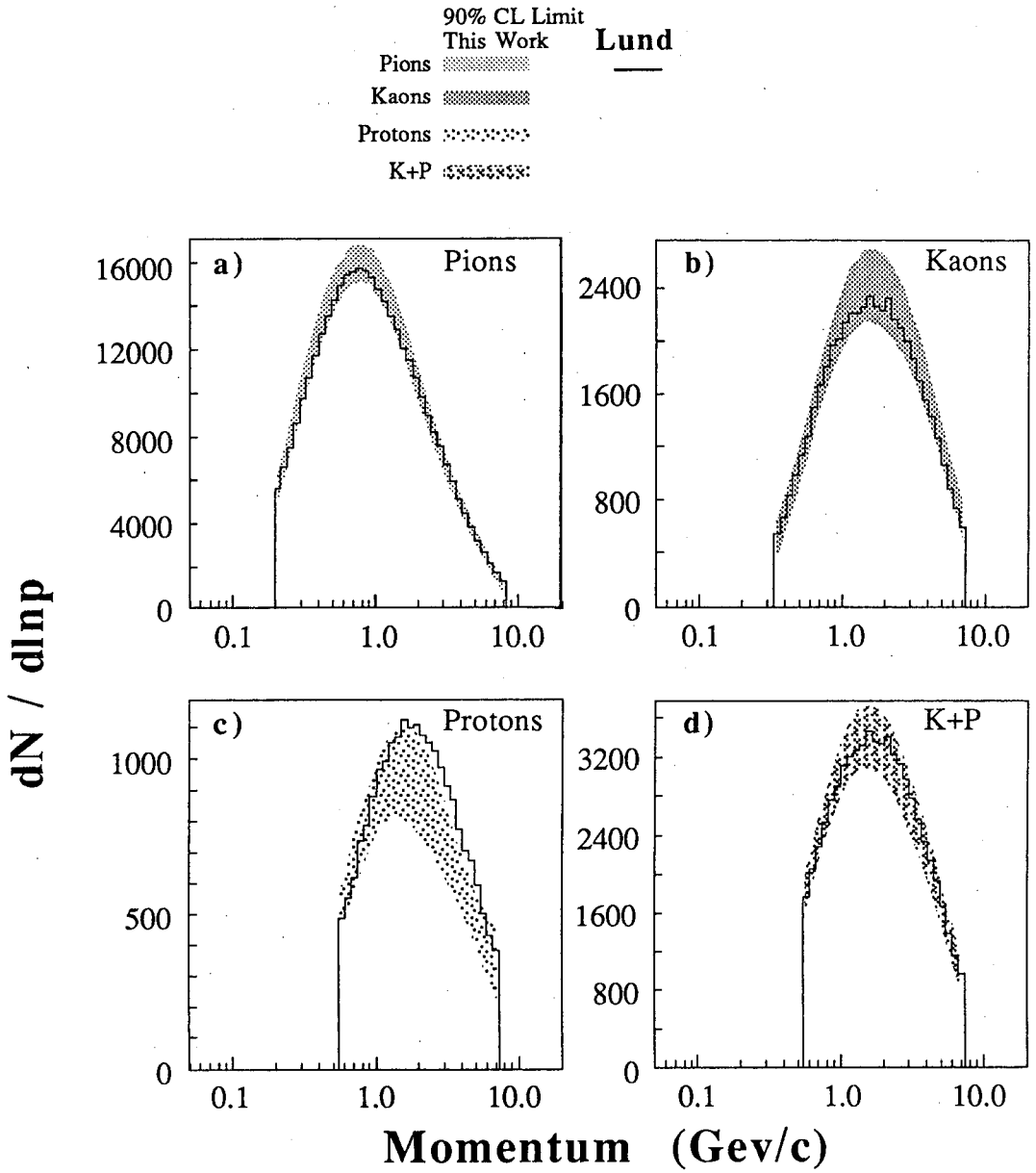

Figure 7.2: Spectrum in Momentum of the Hadrons. a) Pions, b) Kaons, c) Protons and d) Kaons plus Protons. The Shaded area represents the 90% CL limits from this measurement.

We compare our limits to the prediction of LUND for pions, kaons and protons. We used 100,000 simulated hadronic events for the LUND prediction. Notice that the LUND predictions and the measurements are in good agreement for both the pions and the kaons, but that the proton measurement is systematically lower than the LUND prediction at high x (high momentum). The disagreement while small is certainly appreciable as table 7.3 shows.

Figure 7.2 shows the 90% CL limits on $dN/d\ln p$ for pions, kaons, protons and kaons plus protons. Note that while protons have the same slight disagreement with LUND as reflected in the scaling cross section and the fractions, kaons plus protons is consistent with LUND. This must mute our conclusion that LUND is inconsistent with the data. Kaons and protons are not well separated in dE/dx. Since the KP crossover region is at relatively high momentum, this separation is extended in momentum. Therefore kaons plus protons is better measured than protons separately. However since there are a factor of two fewer protons than kaons the kaon plus proton measurement may be consistent with LUND and still have protons separately inconsistent. Additionally, our simulations do not indicate that protons will be badly measured. Our estimate of the systematic error in the proton measurement is included in the overall systematic error (see table 7.1).

Table 7.2 gives the list of fitted parameters for E11 and E12 separately along with the weighted sum of the two experiments[78]. The fitted parameters for pions and kaons are consistent in experiments 11 and 12 but the fitted parameters for protons are not. The fitted proton spectra for the two experiments are consistent. This is because we do not detect enough protons to fix the high energy behavior of the proton cross section. This allows the form C/E^2 to accommodate the entire spectrum albeit at large errors. Notice that even in experiment 12 where we fit a a value for A and n in $(d\sigma/dz)_0$, we find the data is consistent

with $A = 0$.

Table 7.3 lists χ^2's comparisons between LUND and the measured scaling cross sections, $dN_h(p)/dp$ and the fractions. We take the error on each momentum (or x) bin as the sum (in quadrature) of the statistical and systematic error on the fitted value. Table 7.4 lists the bins in x and momenta used for the comparisons[71]. The binning in x was chosen to reflect the decrease in numbers of particles with rising x. Also, the error in the momentum increases at large p so the bin sizes used in the fraction comparison increase at large momentum. Some of the momentum bins are chosen to isolate the cross over regions[71]. As an example, the momentum bin from 1.0 GeV/c to 1.35 GeV/c ($0.0 \leq \ln p \leq 0.3$) isolates the pion, kaon crossover region.

We also compare this result to previous measurements by TASSO[32] at three different center of mass energies. Figure 7.3 shows the comparison of this measurement with the TASSO pion cross section, figure 7.4 the comparison to the TASSO kaon cross section and figure 7.5 the comparison to the TASSO proton cross section. We notice that there is reasonable agreement between TASSO and our limits. However, TASSO measures a more copious production of low momentum kaons than this measurement would allow. Also the scaling cross section for protons seems to be different at different energies. The proton scaling cross section measured by TASSO at 34 GeV is consistent with this measurement. However there is a mild disagreement between the TASSO proton cross sections measured at 14 GeV, 22 GeV and 34 GeV. Part of the problem could be statistics. The 14 GeV and the 22 GeV measurements used only $\sim$ 2500 hadronic events. The 34 GeV measurements used $\sim$ 20000 hadronic events. Additionally, the hadronic multiplicity rises logarithmically with Energy. Therefore, the lower energy measurements contain a factor of $\sim$ 20 fewer protons than the 34 GeV measurement.

Parameter	E11	E12
	Electron	
S_e	$1.054 \pm 0.015 \pm 0.093$	$1.016 \pm 0.013 \pm 0.064$
	Pion	
A	$0.1803 \pm 0.0092 \pm 0.015$	$0.1505 \pm 0.0057 \pm 0.021$
n	$3.76 \pm 0.12 \pm 0.32$	$3.399 \pm 0.090 \pm 0.35$
C	$-0.0251 \pm 0.0011 \pm 0.0024$	$-0.02126 \pm 0.00082 \pm 0.0021$
D	$0.423 \pm 0.025 \pm 0.074$	$0.468 \pm 0.018 \pm 0.062$
η	$1.852 \pm 0.060 \pm 0.12$	$1.745 \pm 0.036 \pm 0.11$
	Kaon	
A	$0.049 \pm 0.025 \pm 0.0098$	$0.0485 \pm 0.0021 \pm 0.010$
n	$2.63 \pm 0.15 \pm 0.35$	$2.79 \pm 0.12 \pm 0.30$
C	$-0.0051 \pm 0.0014 \pm 0.0051$	$-0.0049 \pm 0.0011 \pm 0.0055$
	Proton	
A	$0.00042 \pm 0.00059 \pm 0.0012$	$0.0087 \pm 0.0026 \pm 0.014$
n	0.0	$2.95 \pm 0.58 \pm 1.8$
C	$0.026 \pm 0.0011 \pm 0.0041$	$0.018 \pm 0.0020 \pm 0.0087$

E11+E12	
	Electron
S_e	$1.0325 \pm 0.0098 \pm 0.11$
	Pion
A	$0.1587 \pm 0.0048 \pm 0.026$
n	$3.53 \pm 0.072 \pm 0.47$
C	$-0.02261 \pm 0.00066 \pm 0.0032$
D	$0.452 \pm 0.015 \pm 0.096$
η	$1.772 \pm 0.031 \pm 0.17$
	Kaon
A	$0.0485 \pm 0.0021 \pm 0.014$
n	$2.72 \pm 0.092 \pm 0.46$
C	$-0.0050 \pm 0.00088 \pm 0.0075$

Table 7.2: List of fitted parameters for E11, E12 and the weighted sum (E11+E12).

Experiment	π	K	P	K+P
		$1/(\sigma\beta)d\sigma/dx$		
E11	42.0/37	10.9/31	80.3/26	4.3/26
E12	18.3/37	3.1/31	20.6/26	2.2/26
E11+E12	10.4/37	7.5/31	51.9/26	2.6/26
		$dN/d\ln p$		
E11	44.5/31	11.0/27	80.6/22	4.3/18
E12	18.7/31	3.1/27	20.6/22	2.2/18
E11+E12	2.1/31	10.1/27	61.4/22	3.8/18
		Fractions		
E11	4.8/15	11.2/15	25.4/12	—
E12	0.5/15	11.4/15	3.9/12	—
E11+E12	3.0/15	6.5/15	8.8/12	—

Table 7.3: The χ^2/DOF comparisons between LUND and this result.

Binning		
	$1/(\sigma\beta)d\sigma/dx$	
$0.00 \le x \le 0.01$	$0.10 \le x \le 0.12$	$0.30 \le x \le 0.33$
$0.01 \le x \le 0.02$	$0.12 \le x \le 0.14$	$0.33 \le x \le 0.36$
$\vdots$	$\vdots$	$0.36 \le x \le 0.39$
$0.08 \le x \le 0.09$	$0.26 \le x \le 0.28$	$0.39 \le x \le 0.44$
$0.09 \le x \le 0.10$	$0.28 \le x \le 0.30$	$0.44 \le x \le 0.49$
	Fractions	
$-1.6 \le \ln p \le -1.4$	$-0.3 \le \ln p \le -0.2$	$0.7 \le \ln p \le 0.8$
$-1.4 \le \ln p \le -1.2$	$-0.2 \le \ln p \le -0.1$	$0.8 \le \ln p \le 1.0$
$-1.2 \le \ln p \le -0.9$	$-0.1 \le \ln p \le 0.0$	$1.0 \le \ln p \le 1.3$
$-0.9 \le \ln p \le -0.7$	$0.0 \le \ln p \le 0.3$	$1.3 \le \ln p \le 1.6$
$-0.7 \le \ln p \le -0.5$	$0.3 \le \ln p \le 0.5$	$1.6 \le \ln p \le 2.0$
$-0.5 \le \ln p \le -0.3$	$0.5 \le \ln p \le 0.7$	
	$dN(\ln p)/d\ln p$	
	$-1.6 \le \ln p \le 2.0,\ \Delta \ln p = .1$	

Table 7.4: List of bins used for χ^2 comparisons of LUND to this measurement.

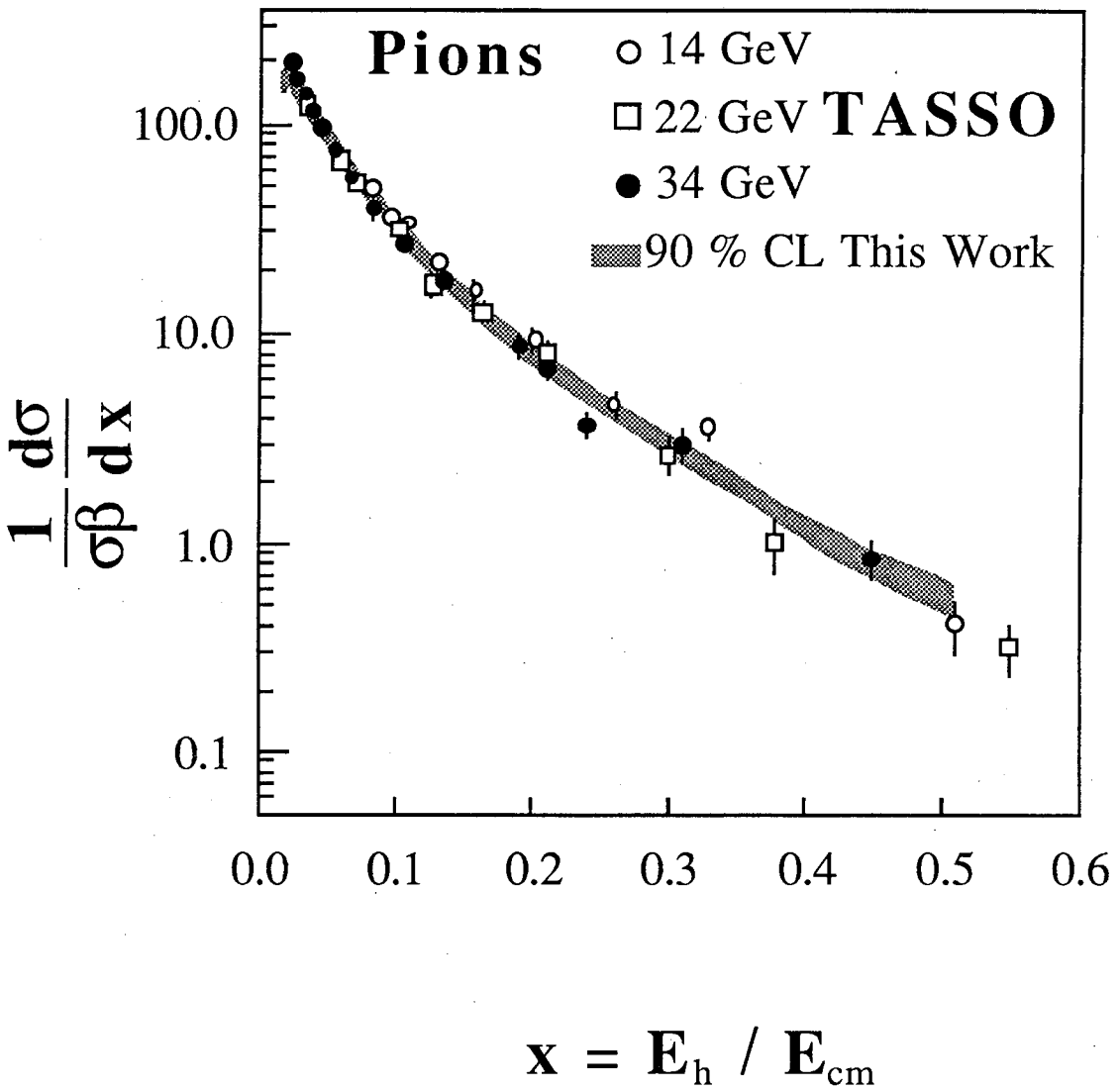

Figure 7.3: Comparison of this measurement to TASSO $\pi^+ + \pi^-$ scaling cross section. See text.

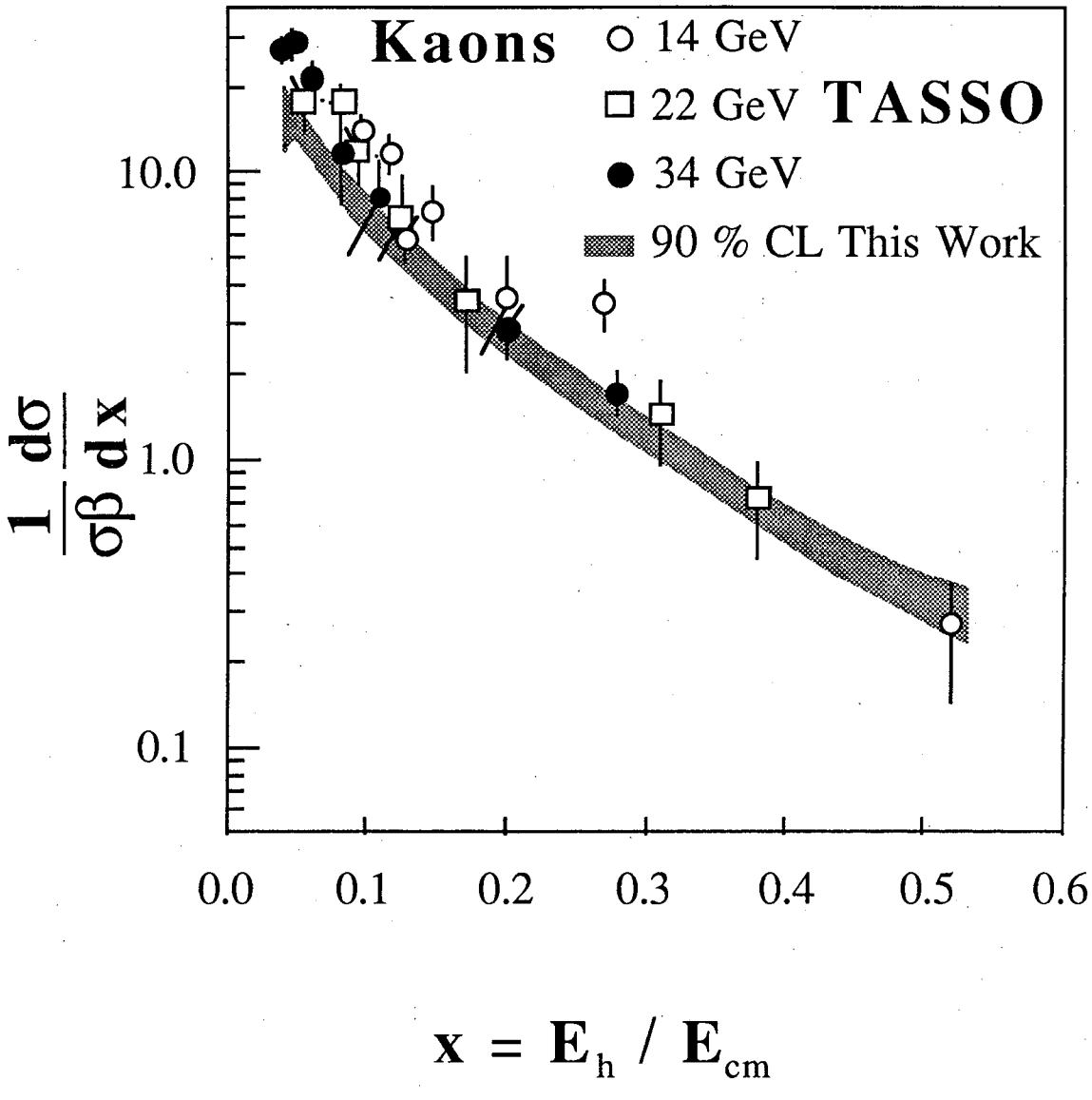

Figure 7.4: Comparison of this measurement to TASSO $K^+ + K^-$ scaling cross section. See text.

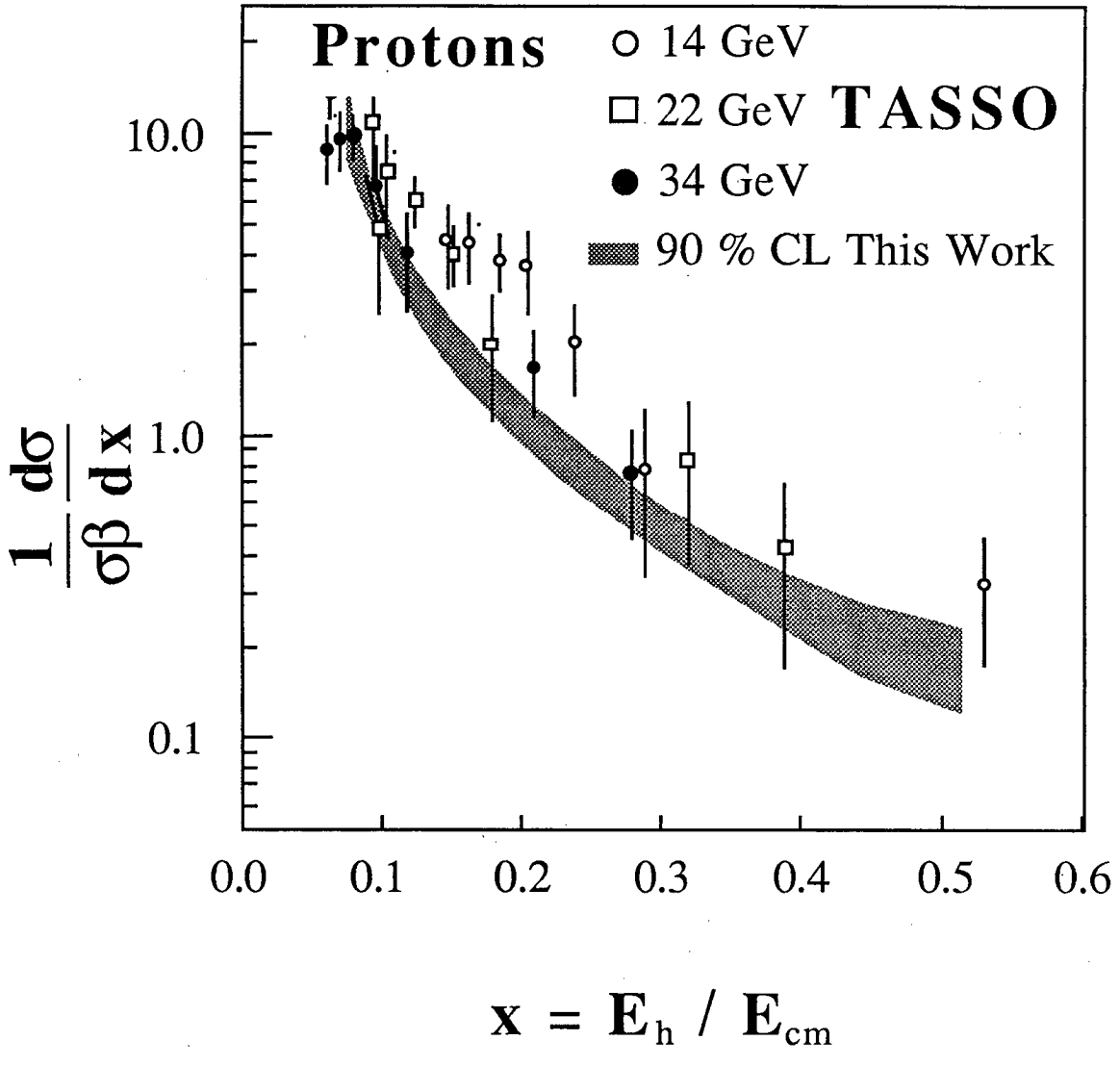

Figure 7.5: Comparison of this measurement to TASSO P + $\overline{\text{P}}$ scaling cross section. See text.

The limits also include systematic errors from this measurement. We shall now discuss the elements of the systematic error determination.

7.2.1 Systematic Error Determination in Data

There are several sources of systematic error in the determination of the inclusive cross section: the resolution function, the acceptance, analysis cuts and the method itself. We simply varied the relevant quantities over the maximum range in order to determine the systematic error caused by each. The systematic error of the method itself was the difference between the fit of LUND using the "2-D" method and what was generated by LUND itself. See table 7.1 for the values we use for the systematic error.

The Resolution Function

The χ^2 method of determining the parameters also gives the statistical error and the correlation between the various resolution parameters. Recall that χ^2 space in the vicinity of the best values of the resolution parameters can be described by the following equation

$$\chi^2 = \chi_0^2 + (p_1 - p_1^0, p_2 - p_2^0, \ldots) V \begin{pmatrix} p_1 - p_1^0 \\ p_2 - p_2^0 \\ \vdots \end{pmatrix} \tag{7.5}$$

where p_i is the value of the parameter, p_i^0 is the fitted best value of the parameter and V is the correlation matrix for the parameters [78]. Recall also that this equation can also be used to describe any function of the parameters near the best fitted parameters (cf. reference [78,79], equation 6.18).

Symbolically, we can write function f at $p_1, p_2, \ldots$ near the best fitted values of the parameters as

$$f = f(p_1^0, p_2^0, \ldots) + (\frac{\partial f}{\partial p_1}\Delta p_1, \frac{\partial f}{\partial p_2}\Delta p_2, \ldots) V \begin{pmatrix} \Delta p_1 \partial f/\partial p_1 \\ \Delta p_2 \partial f/\partial p_2 \\ \vdots \end{pmatrix} \Bigg|_{p_k = p_k^0,\, k=1,2,\ldots} \tag{7.6}$$

In particular, this expression applies to the number of particles in every momentum (or x) bin. The only parameters which were allowed to vary during the fit were those describing the spectra. Hence, the statistical error only reflects the uncertainty in a spectrum due to the uncertainty in the parameters pertaining to all charged particles. There are other parameters on which the answer depends which are not allowed to vary during the fit. In particular the resolution parameters, the acceptance and the analysis cuts are not allowed to change during the fit.

We determine the systematic error in the spectrum by using equation 7.6. To determine $\partial N/\partial p_k$, we refit the spectra with different values of p_k. We used $p_k \pm \Delta p_k$ as the different parameter values where Δp_k is the one sigma error on parameter p_k including the systematic error on that parameter. The resolution parameters fit in this way are the multiple scattering error, σ_{cou}, the vertex momentum measurement error, σ_{vtx}, the dE/dx resolution, σ_d, and the dE/dx resolution function "Tail" parameter.

The energy loss and momentum bias were handled slightly differently. We simply set the multiplicative energy loss factor to one and the momentum bias to zero for the systematic error due to the uncertainty in measuring these two parameters. This overestimates the systematic error due to the uncertainty in the energy loss and momentum bias parameters.

dE/dx

The expected energy loss curve for a particle at a given $\beta\gamma$ is only known to 0.5%[53]. Knowledge of this curve is crucial because Kaon–Proton separation in dE/dx is not as large as πK or πP dE/dx separation. Compounding the problem is the relatively small number of kaons and protons produced in an e^+e^- annihilation event. Therefore we must see how the answer varies with

changes in the dE/dx curve as a function of η.

The systematic error due to uncertainty in the dE/dx curve was fixed by multiplying the curve by $\pm 0.5\%$. That is, we maintained the shape of the curve but increased and decreased its value by 0.5%. This is an overestimate of the error due to this uncertainty because only the high $\beta\gamma$ part of the curve is uncertain by this amount. The rest of the curve is known to better than one half percent.

Acceptance

We used $40K$ LUND–generated hadronic events in order to determine the acceptance. We allowed the acceptances to vary by $\pm 1.3\sigma$ bin by bin in order to determine the 90% confidence level error. All particles should have about the same acceptance because acceptance is predominately determined by *geometry*. Hence the acceptances as calculated by the Monte Carlo for each of the hadrons are about the same. Therefore, all hadronic acceptances were increased and decreased simultaneously when we computed the systematic error.

The acceptances rise rapidly from zero, leveling out at about 0.33. The rapid rise from zero of the acceptance begins at the highest value of energy loss (dE/dx) that we use in the analysis. The acceptances at higher momenta are not as well known as at the lower momenta because there are not as many high momentum as low energy hadrons generated due to phase space.

The only exception is low momentum protons. We have frequently mentioned that low momentum protons are produced by interactions of pions with the the aluminum beam pipe. We determine the systematic error due to our inability to determine the interaction cross section by calculating the cross sections for negative particles only and multiplying them by two.

Additionally, the Monte Carlo with the detector simulator produces about a 10% deficit in the total number of particles produced between 200 MeV and

410 MeV. We cannot determine if the uncertainty is due to the LUND generator or the TPCLUND detector simulator. Therefore an additional 10% uncertainty is added for the pion acceptance in this region. We reason that pions and electrons are the only particles detected in this momentum range. The worse possible case for the determination of the pion cross section is that the entire uncertainty is due to the pions only.

Table 7.5 shows the contribution of all sources of systematic error to the uncertainty in the fractions. The table shows the average contribution to the systematic error in the fractions due to each of its components. It should be used as a guide to the sensitivity of our result to uncertainties in resolution, the energy loss curve, acceptance and energy loss by particles in the beam pipe. This table should only be used as a guide because each momentum bin is affected by the systematic error sources differently. In general, the highest momentum bin has the largest systematic error (See figure 7.1b for instance). This is because the momentum resolution, $\delta p/p$, in this momentum bin is on the order of 30%. This is far and away the momentum bin with the worst momentum resolution used in this measurement.

	Systematic Error Source			
Particle	Res	Eloss/Bias	dE/dx	Acc
π	0.0059	0.0006	0.0140	0.0115
K	0.0051	0.0006	0.0134	0.0089
P	0.0027	0.0004	0.0056	0.0105

Table 7.5: Average uncertainty of Fraction due to systematic error source, E11+E12.

Analysis cuts

We use only two analysis cuts in our data. These cuts are used to remove $\sim 1\%$ tails of our resolution function. The cuts were

1. the value at which to stop calculating our momentum and energy loss resolution, and

2. the minimum number of particles expected in a dE/dx vs $\ln p$ bin if the momentum spectrum for e, μ, π, K and protons were flat and were equal to one particle per momentum bin.

We nominally set the first cut to 0.5% and the later cut to 0.5%. The systematic error was determined by changing both of the cuts to 1.0%.

The fitted parameters change by a far smaller value than the systematic errors due to resolution or the acceptance when we change these two analysis cuts.

7.3 3–Jet Events

The stage is now set for the presentation of the main results of this thesis: the inclusive cross sections of charged hadrons in three jet events.

The previous sections laid out the procedure we used to determine the inclusive cross sections for the entire data sample. We apply the same procedure to the three jet event sample. However there are several additional systematic effects we must take into consideration when we analyze the three jet event sample.

Fit used for 3–jet sample

The ideal way to analyze the three jet event sample would be to fit the underlying z spectra for the various charged particle species. We have seen in chapter 2 and the results from TASSO reproduced earlier in this chapter that the most important characteristic of the inclusive cross sections is scaling. Unfortunately, we face two problems:

1. Experimentally, we can only reconstruct the jet energies and measure a particle's momentum and energy loss. Hence, when we fit a cross section,

we can use the jet energy to form a prediction that can be compared to the momentum and energy loss spectra. If we were fitting a scaling cross section, for instance, we can predict the number of particles at a certain momentum by convoluting the jet energy spectrum with the scaling cross section. We could change the parameters of the cross section until we found the best match between the fitted momentum spectrum and the measured spectrum. Yet, as we have stated several times in this thesis, most pions and many kaons and protons detected by the TPC are the result of decays. There is no simple relationship which can describe the connection between the initial parton energy and the final state hadron momenta if decays are involved. Therefore the convolution mentioned above will not provide a good description of the data and certainly will not yield the underlying z spectrum of the primary hadrons produced during fragmentation.

2. The jet energies are known only to 10% at best. Therefore any convolution involving jet energies will only be good to 10% too.

We are reduced to measuring the momentum spectra of the hadrons for each jet individually. This will not allow us to compare the quark and gluon jets directly. We will only be able to make comparisons indirectly thru models of fragmentation. Fragmentation models (we focus on LUND here) predict hadronic momentum spectra for given z fragmentation functions.

Form of the Fitting Function

We use the same form for the hadronic momentum spectra for each of the jets in the three jet sample as we used when we fit the entire hadronic event sample (equations 7.1, 7.2 and 7.3). However we no longer have monoenergetic partons initiating each of the jets.

First, let us recall the definition of jet #1, #2 and #3 from section 5.4: $E_1 > E_2 > E_3$ where E_i is the reconstructed energy of jet $\#i$. We wish to place each of the jets on an equal footing. One possibility is to set E_q to the average energy of the partons for each of the jets, $E_{\rm AVE}$. This has the drawback that approximately one half of the initiating partons actually have an energy larger than $E_{\rm AVE}$. Since $(d\sigma/dE)_0$ goes to zero as z goes to one, $(d\sigma/dE)_0$ will not describe the particles of momentum greater than $E_{\rm AVE}$ in a jet. Therefore we choose to set E_q to E_c where E_c is defined to be the energy at which only 10% of the initiating partons have an energy greater than this value. To determine E_c, We simply determine the energy at which

$$\int_0^{E_c} N(E_j)\, dE_j / N_{\rm TOTAL} = \text{VALUE}$$

where $N(E_j)$ is the jet energy distribution, $N_{\rm TOTAL}$ is the total number of events and VALUE is an arbitrarily chosen number between zero and one.

We should emphasize that the particular choice of E_c is not critical. The fitted $(d\sigma/dE)_0$ will not be the fundamental fragmentation function since we are not properly taking into consideration the different energy partons within a jet.

We modified the functional form of the pion inclusive cross section. We changed $(d\sigma/dE)_0$ to

$$\left(\frac{d\sigma}{dE_\pi}\right)_0 = A\beta\frac{(1-z)^n}{z}(1+B(1-z))$$

where B is a constant to be fit[86]. This additional term somewhat accounts for the softening of the pion spectrum due to decays of heavier resonances.

Another difference between the functional forms used in fitting the three jet sample and the entire hadronic event sample is that we fixed D to zero for jet #3 (see equation 7.3). When we left D for jet #3 free, the fit put contributions from the term $D\exp(-\eta E_h)$ to zero by driving η and D to a very large numbers,

$\sim 10^{10}$ with very large errors. This precluded the fit from determining reasonable errors on the other parameters.

To save computer time we did not fit the hadronic spectra for all three jets. Instead we only fit the momentum spectra of jets #1 and #3. We used the Monte Carlo to determine the proportion of quarks and gluons as the initiating parton in each of the jets. That is

$$Jet_i = \sum_{k = Q,\, G} P(i,k) \times Frag(k)$$

where $P(i,k)$ is the probability that jet i has k as the initiating partons, k being either quark or gluon. Since $P(i,Q) + P(i,G) = 1$ and there are three jets, we can invert the equation and set one jet as the linear combination of the other two.

According to the LUND Monte Carlo, jet #1 is initiated by a quark about 90% of the time, jet #2 is initiated by a quark about 80% of the time. Jet #3 is initiated by a gluon about 70% of the time. Since jet #2 is usually initiated by a quark, we chose to fit jets #1 and #3. Jet #2 is then approximately 80% jet #1 and 20% jet #3.

Finally, we did not use the same momentum range to fit the momentum spectrum as we did with the entire event sample. This is because pions were not represented very well by this form in the Monte Carlo. If we set

$$z = \frac{\sqrt{E_h^2 + m_i^{i\,2}}}{E_q}$$

where E_h is the hadron's energy and m_i^i is a parameter to be fit for each jet we could fit the pion spectra from 80 MeV/c to 7.4 GeV/c in the Monte Carlo well. The fit for the parameter m_i^i was on the order of 300 MeV in the Monte Carlo. The results when we fit the data are shown in table 7.6. We do not quote an error on this parameter because the fit was unreliable with m_t free.

	m_t(MeV)	
Jet	LUND	E11+12
#1	312	404
#2	257	348
#3	206	191

Table 7.6: Fitted values for m_t in LUND and Experiments 11 plus 12.

The only spectrum affected by the inclusion of m_t is the pion spectrum. The reason m_t is required for the pion spectrum is probably decays. The energy threshold at which we observe a pion is not the mass of the pion in a decay. It is increased because of the minimum momentum transferred to the pion by the decay of the higher mass resonance. This is effectively accounted for by adding m_t to the definition of z. Kaons and protons are not affected because fewer kaons and protons are produced as a result of decays and the masses of the kaons and protons are, in general, much higher than the minimum energy transferred to these particles in a decay.

We circumvent this problem by fitting only particles at momenta higher than 500 MeV/c. We chose 500 MeV/c because m_t is fit to be this order of magnitude. Thus, by fitting particles of momenta larger than 500 MeV/c, we can fix m_t to zero. The average difference between the spectrum with m_t free and m_t set to zero for momenta larger than 500 MeV/c was less than 2.0% in all cases and less than 1.0% in the case of pions and kaons.

Additional Systematic effects

We used the same method as outlined in section 7.2.1 to determine the systematic error on the measurement of the three jet inclusive cross sections. Additionally, there are several different systematic errors we must account for.

1. We assumed the second jet can be described as a linear combination of jets #1 and #3. We allowed the coefficient of jet #1 to increase to 90% and decrease to 70% when we determined the systematic effect of using this assumption. On average, the momentum spectrum changed by less than the statistical error on the spectrum when we changed the linear combination which forms jet #2.

2. We used a cut of 500 MeV on the momentum visible in the jet when we determined the jet structure of the events. We determined the effect of this cut by requiring the visible momentum in a jet to be 1.5 GeV. We redetermined the acceptances and refit. Please see table 5.3 for the differences between using 500 MeV and 1.5 GeV as the visible energy cut. We then determined the systematic error due to the momentum visible cut by scaling the 1.5 GeV answer. The scale is set to the ratio of the number of three jet events using the 500 MeV/c momentum visible cut to the number of three jet events using the 1.5 GeV/c momentum visible cut. We then can compare the *shapes* of the hadronic spectra using the two cuts. The shape of the momentum spectrum of the kaons and protons changed only within statistical errors when this cut was varied. The shape of the low momentum spectrum of the pions in the three jets changed slightly more than the statistical error. This is not unexpected because we throw out more low momentum particles than high momentum particles if we raise this cut. Moreover, all hadronic fractions changed by less than the statistical error when we changed the visible energy cut.

3. The effect of the production of low momentum protons in the beam pipe was determined by a different procedure. We lose one half of the statistics when we use only negative particles. Therefore, the determination of the cross sections for pions and kaons also suffers. For each particular species, the

number of negative particles resulting from an e^+e^- annihilation should be the same as the number of corresponding positive particles by iso–spin invariance; baryon number, strangeness and charge conservation in the strong interaction. Therefore, the fraction of anti–protons determined by solely using the negative particle sample should be the same as the fraction of protons plus anti–protons in the total sample. However, because the material in front of the detector is made of atoms (not an anti–atom to be found), inelastic interactions of particles emanating from the annihilation event with the material primarily results in protons or electrons. Rarely will an anti–proton be produced. Hence the difference between two times the cross section for anti–protons and the cross section for protons plus anti–protons for momenta less than 1.0 GeV/c is a measure of the systematic error due to uncertainties in the cross section for the production of protons in the beam pipe. The difference between the proton fraction and the proton plus anti–proton fraction averages 0.005 for momenta less than 1.0 GeV/c.

4. The effect on the momentum spectrum due to the choice of E_c must be considered. Obviously increasing E_c decreases z and should therefore increase the value of n in $(d\sigma/dE)_0$. But the fitted momentum spectrum should not change. We set E_c to several different values. We also used two different jet energy spectra to determine the average parton energy. First, we can use the jet energy spectrum as determined from the data. Second, initial state radiation changes the center of mass of the e^+e^- interaction. We can account for this effect by using the Monte–Carlo generated parton energy distribution instead of the jet energy spectrum from the data.

   The effect of using different E_c's proved to be negligible. The momentum spectrum changed by less than one percent for each of the different E_c's

shown in table 7.7.

JET	E_{AVE}	SIGMA	E_c(GeV) 85%	90%	95%
Use Generated Parton Energy from LUND Monte Carlo					
#1	12.5	1.2	13.8	13.9	14.1
#2	10.5	1.7	12.3	12.7	13.3
#3	5.1	2.1	7.5	7.9	8.3
Use Jet Energies Determined in Experimental Data					
#1	12.0	2.4	—	13.6	—
#2	11.2	1.5	—	13.2	—
#3	5.4	2.2	—	8.3	—

Table 7.7: List of E_c's for different values of the percentage of total jets with energy less than E_c.

7.3.1 3–Jet Results and Discussion

We now present the results for the fit of the three jet spectra. Figures 7.6, 7.7 and 7.8 show the limits on the hadronic fractions of the three jets from this work. Figures 7.9, 7.10 show the limits on the momenta spectra for the hadrons in jets #1 and #3

Table 7.9 shows the values of the fitted parameters for jets #1 and #3 along with the systematic error on each of the parameters. Table 7.8 shows the χ^2/DOF for the momentum spectra and the fractions. Table 7.10 shows the estimate and breakdown of the systematic errors. The "Res" column is the contribution of the uncertainty in the resolution parameters to the systematic error in the spectra. The "Dedx" column is the contribution of the uncertainty in the Energy loss function to the systematic error, "Acc" refers to acceptance, "Qper" is the contribution of the 10% error in the quark percentage in each of the three jets,

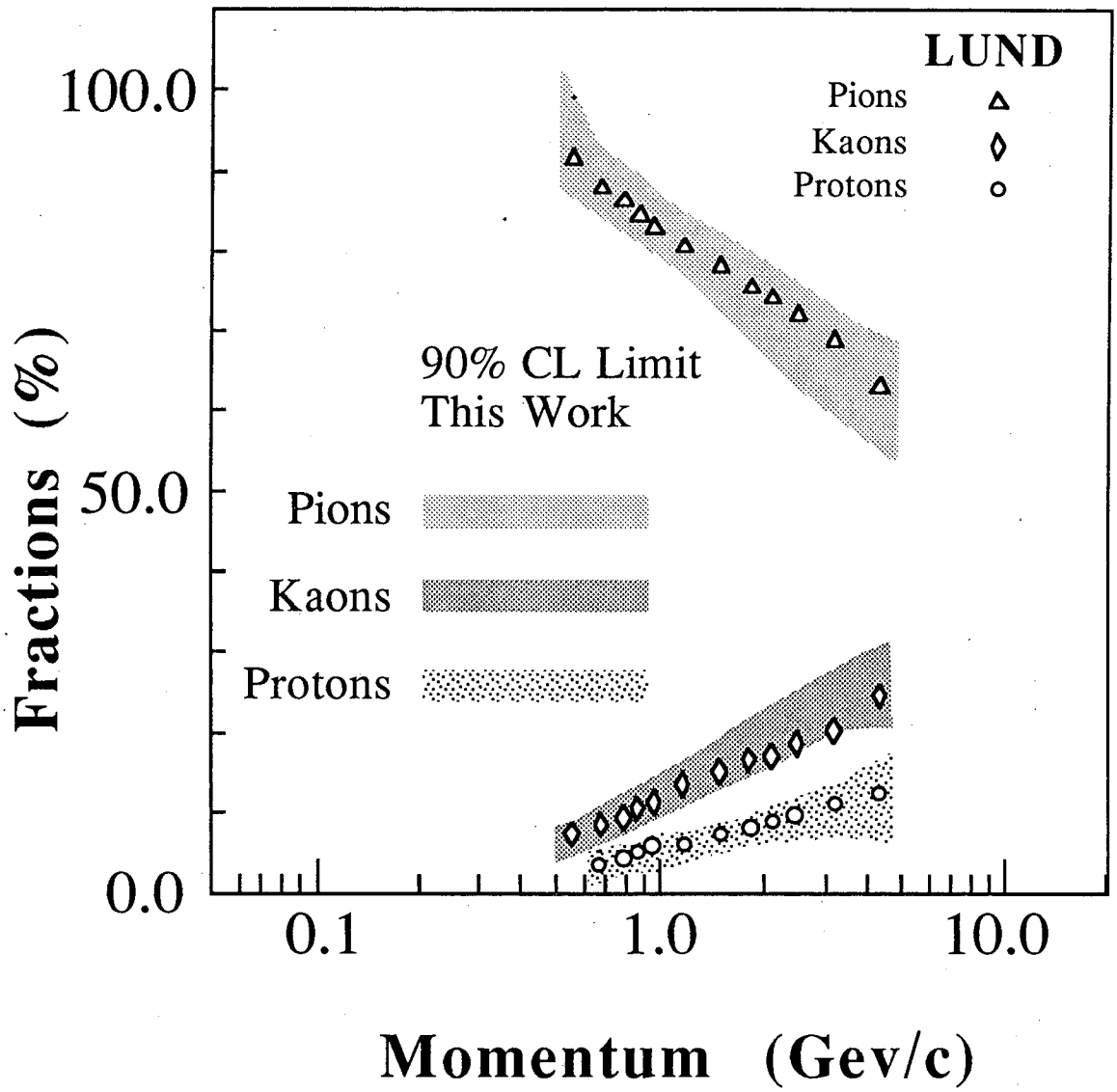

Figure 7.6: The Charged hadronic fractions in Jet #1. The shaded regions are the 90% CL limits from this work.

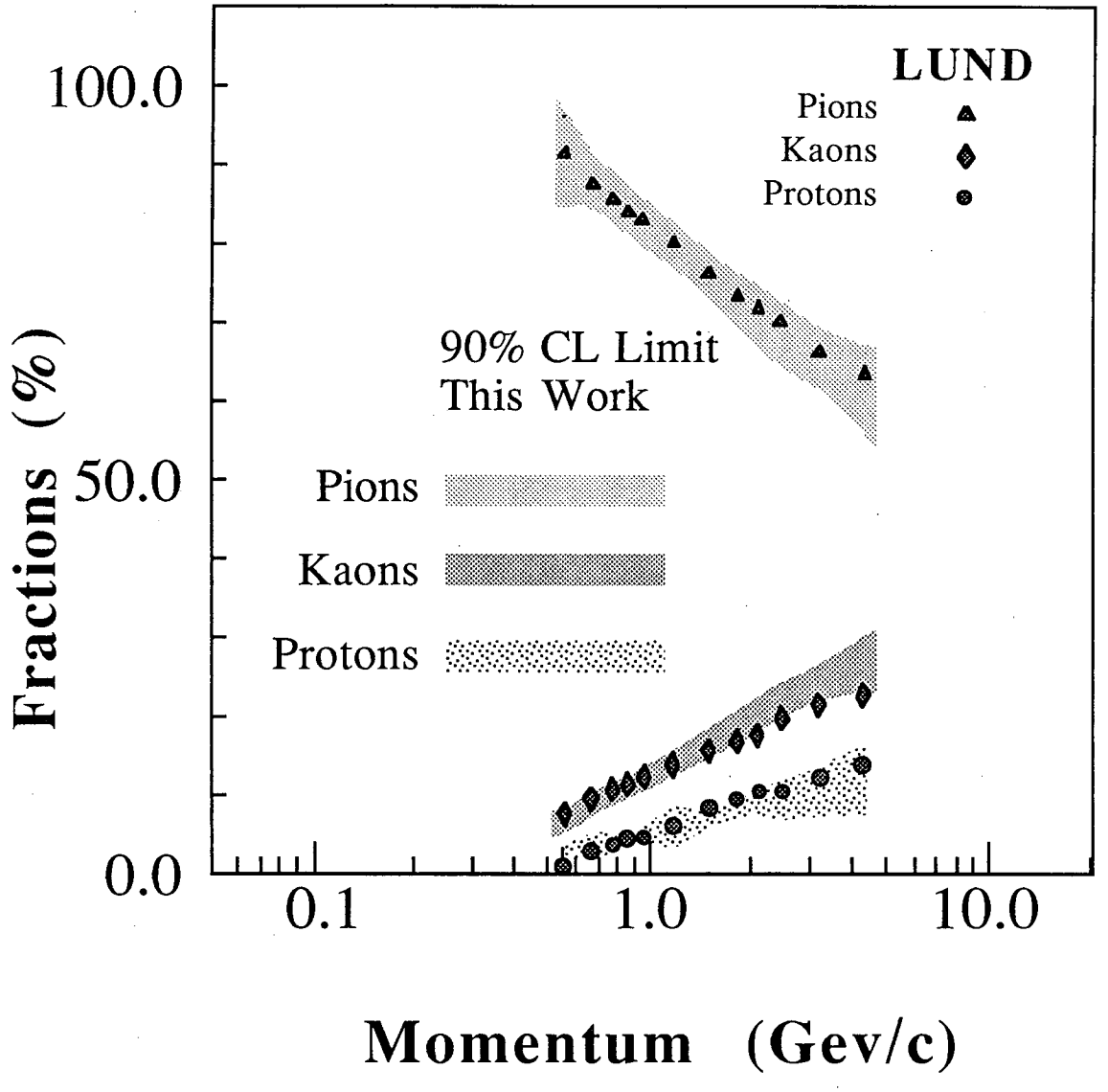

Figure 7.7: The Charged hadronic fractions in Jet #2. The shaded regions are the 90% CL limits from this work.

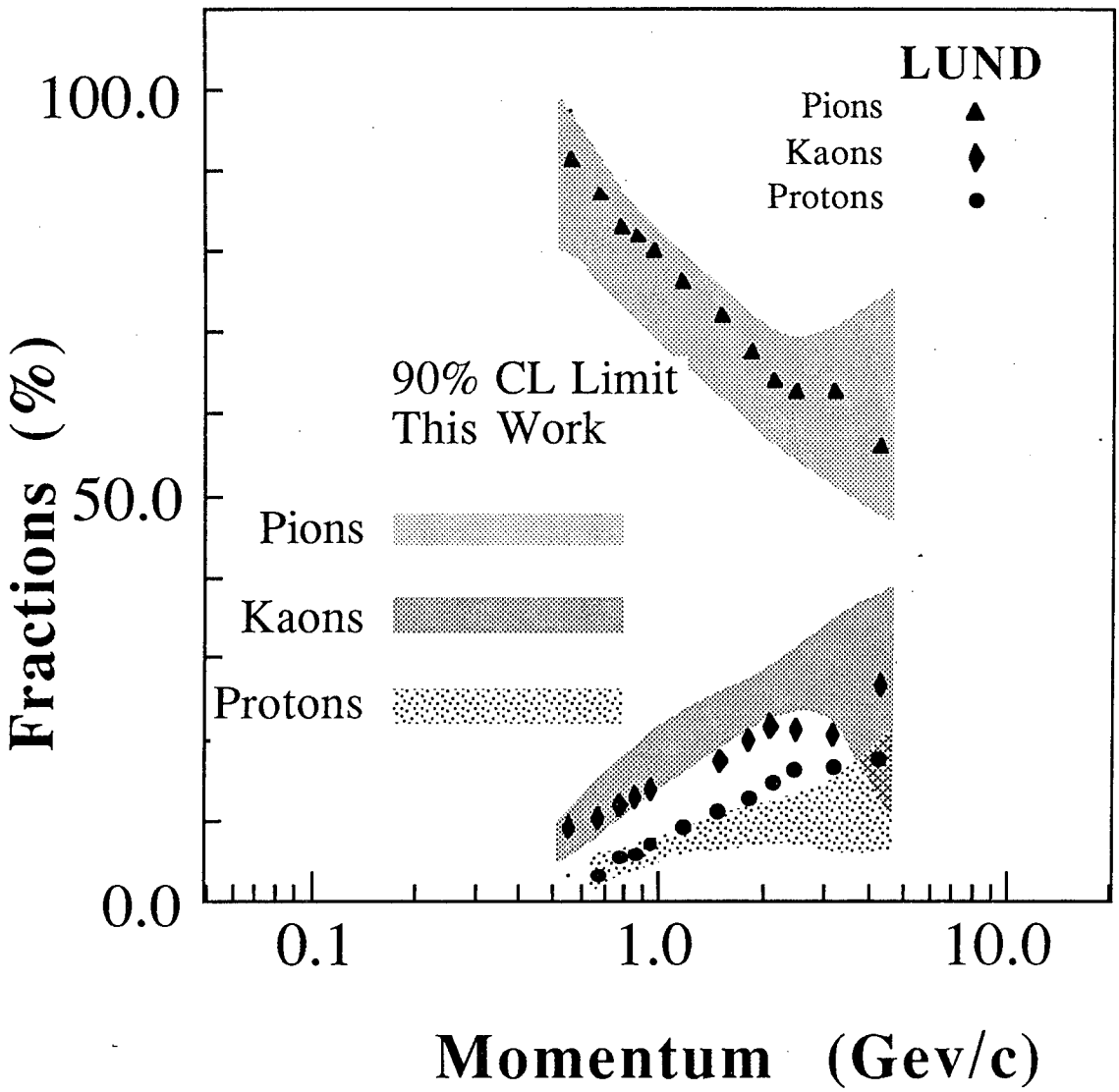

Figure 7.8: The Charged hadronic fractions in Jet #3. The shaded regions are the 90% CL limits from this work.

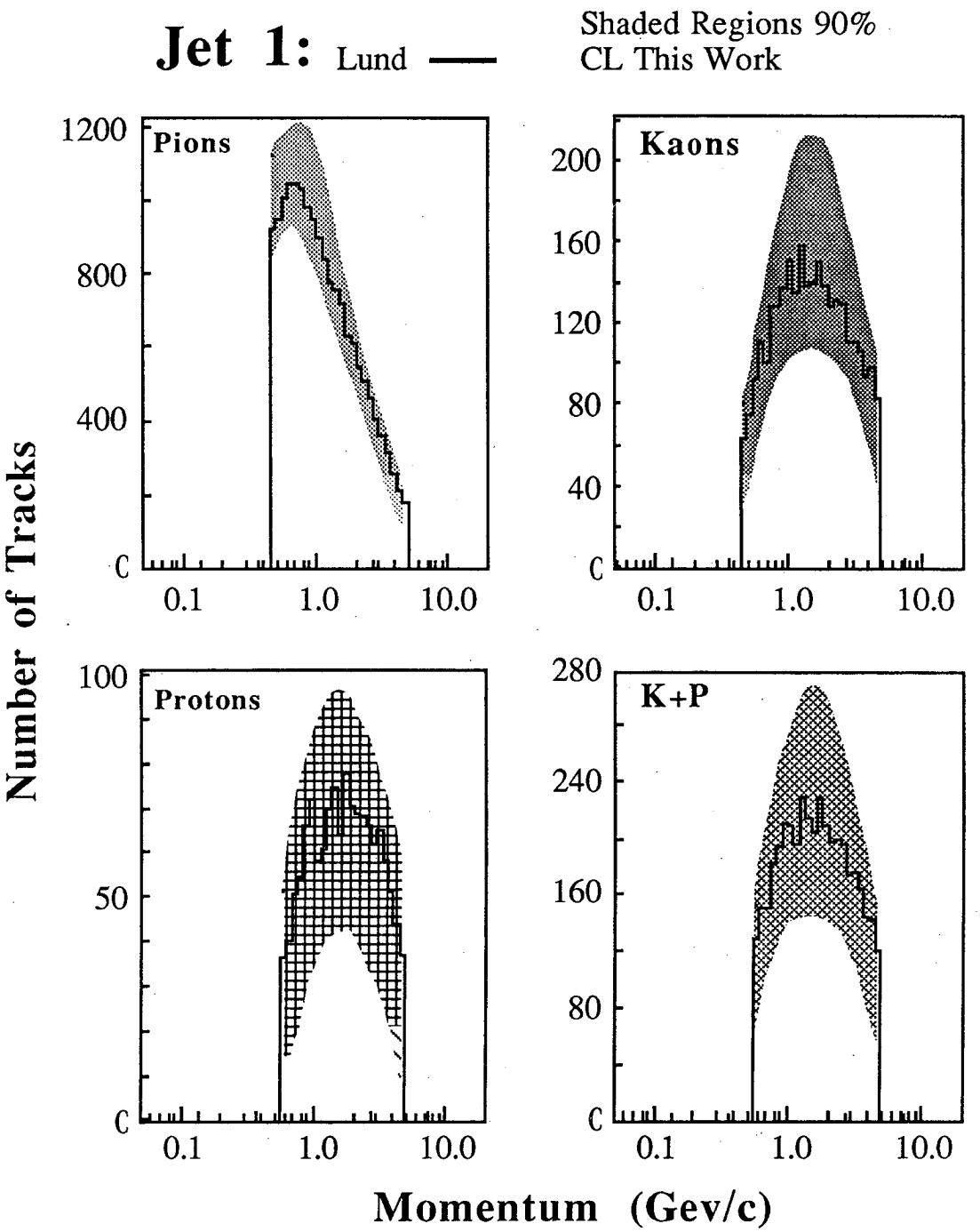

Figure 7.9: The Charged hadronic momenta spectra for Jet #1. The solid histogram is the LUND prediction. The shaded regions are the 90% CL limits from this work.

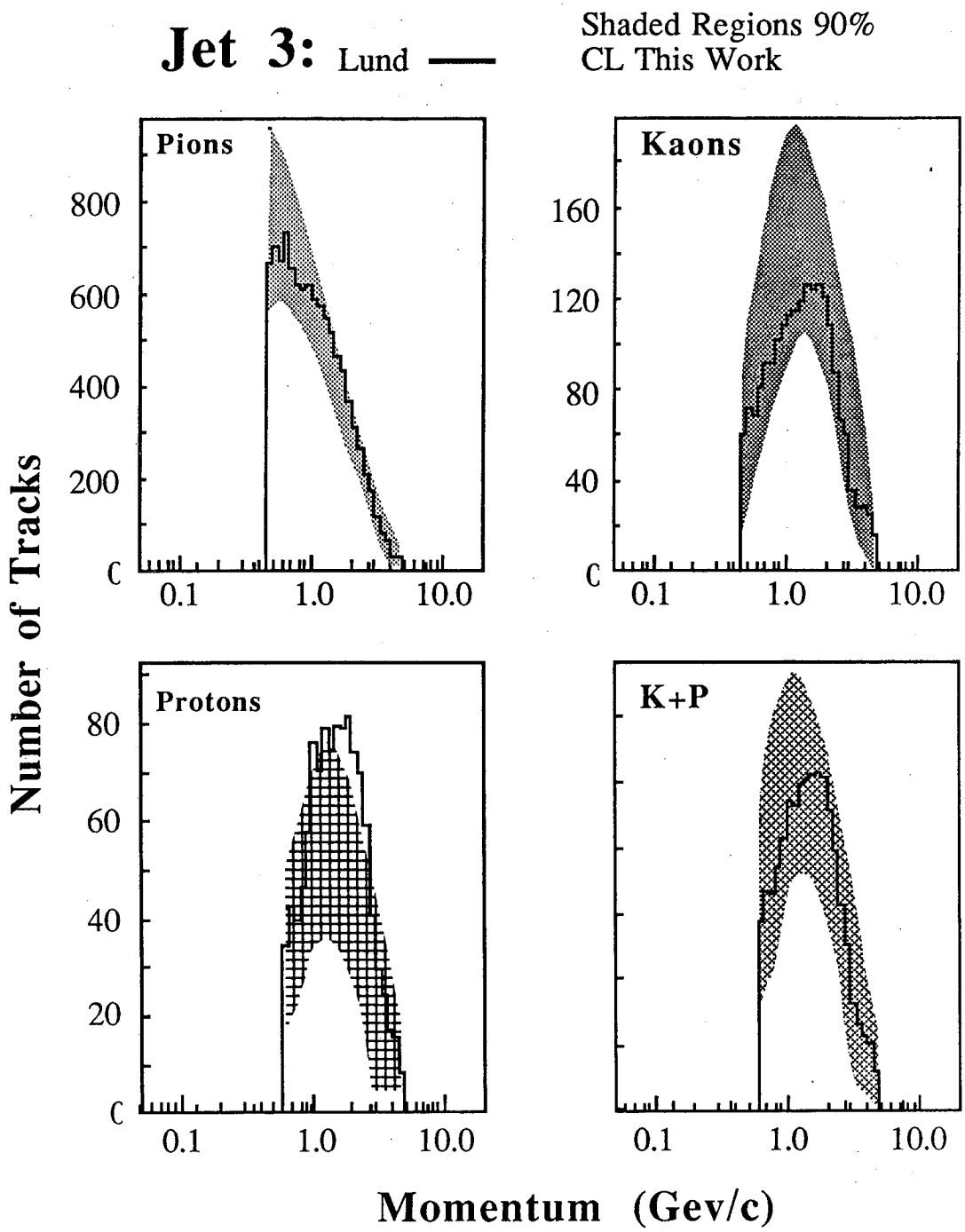

Figure 7.10: The Charged hadronic momenta spectra for Jet #3. The solid histogram is the LUND prediction. The shaded regions are the 90% CL limits from this work.

"Ech15" represents changing the visible momentum in a jet cut to 1.5 GeV, "Nob" refers to fixing B to zero and "Stat" is the statistical error. We note that nearly all of the systematic errors are less than the statistical error.

Jet	π	K	P	K+P
		$dN/d\ln p$		
#1	3.9/10	3.4/18	3.0/16	2.1/10
#2	2.0/10	3.6/18	5.9/16	0.6/10
#3	6.6/10	6.4/18	21.5/15	2.1/9
		Fractions		
#1	1.3/12	4.4/12	1.6/11	—
#2	0.6/12	15.4/12	33.5/12	—
#3	3.0/15	28.7/12	28.0/11	—

Table 7.8: The χ^2/DOF comparisons between LUND and this result.

We see that the proton fraction in jet #3 is overestimated by LUND. The χ^2/DOF for the proton fraction in the third jet is a high 28.0/11. This is also reflected in the increased χ^2/DOF of the proton momentum spectrum in the third jet of 21.5/15. We also notice that even in jet #1, LUND is systematically higher than this measurement, but the statistical and systematic errors are so large that LUND is still consistent with the number of protons we measure in jet #1.

Recall that LUND also slightly overestimates the proton cross section for the entire event sample. The easiest explanation for both discrepancies is that the high x fragmentation of protons in LUND is incorrect.

Most hadronic events are formed from the fragmentation of two partons recoiling apart from one another at 14.5 GeV/c each. In this case, $x \sim 0.4$ corresponds to 6.0 GeV/c. But our momentum resolution is very much degraded at this momentum. Therefore, there are relatively large systematic errors on the

Par	Jet #1	Jet #3
	Electron	
S_e	$0.722 \pm 0.064 \pm 0.084$	$0.516 \pm 0.073 \pm 0.048$
	Pion	
A	$5.544 \pm 0.057 \pm 1.14$	$3.396 \pm 0.041 \pm 0.45$
n	$3.247 \pm 0.068 \pm 0.27$	$3.658 \pm 0.076 \pm 0.27$
B	$2.6877 \pm 0.0032 \pm 0.57$	$2.59 \pm 1.95 \pm 0.15$
C	$-0.18 \pm 0.20 \pm 0.40$	$0.047 \pm 0.022 \pm 0.065$
D	$3.7 \pm 1.7 \pm 3.6$	—
η	$1.84 \pm 0.30 \pm 0.48$	—
	Kaon	
A	$6.30 \pm 0.84 \pm 1.2$	$4.73 \pm 0.80 \pm 0.69$
n	$3.32 \pm 0.30 \pm 0.40$	$3.07 \pm 0.26 \pm 0.29$
C	$-0.078 \pm 0.036 \pm 0.039$	$-0.117 \pm 0.049 \pm 0.046$
	Proton	
A	$1.6 \pm 1.4 \pm 1.8$	$3.0 \pm 1.0 \pm 0.6$
n	$4.2 \pm 2.1 \pm 2.9$	$5.4 \pm 1.6 \pm 0.6$
C	$0.128 \pm 0.067 \pm 0.096$	$0.039 \pm 0.020 \pm 0.047$

Table 7.9: List of fitted parameters for Jets #1 and #3.

Systematic error source (%)							
Particle	Res	Dedx	Acc	Qper	Ech15	Nob	Stat
			Jet #1				
π	1.3	0.9	8.5	3.2	6.5	0.3	2.4
K	3.7	4.5	19.4	1.9	3.0	0.1	6.8
P	4.3	1.9	23.9	2.6	7.2	0.5	11.1
			Jet #2				
π	1.4	0.8	8.7	3.3	7.3	0.4	2.2
K	3.4	4.3	19.9	1.9	4.0	0.1	5.9
P	3.9	1.9	24.0	2.1	6.6	0.5	9.8
			Jet #3				
π	1.1	1.3	12.8	0.3	8.1	1.3	6.1
K	3.5	5.4	28.6	1.6	11.0	1.4	13.4
P	4.2	2.0	31.2	2.6	8.5	0.8	17.3

Table 7.10: The average percentage error on the fitted spectrum due to the above systematic error sources.

measured proton fraction for momenta greater than $\sim 3-4$ GeV/c. Without the degradation of the momentum resolution at large momenta, the disagreement between LUND and the 90% CL limit established by this measurement of the proton fraction would be worse.

The third jet in a three jet event does not suffer this problem. Since the initiating parton is of lower energy ($E_{\rm AVE} \sim 5.0$ GeV), x on the order of 0.4 corresponds to a momentum of about $2.0-3.0$ GeV/c. The momentum error on this range of momenta is relatively small and hence the systematic effects are reduced. This is why the disagreement between LUND and the measured proton fractions in the third jet is more definitive than in the case of the overall data sample.

More speculatively, we consider the behaviour of the charged hadron cross section at high z. We first note that the high z behaviour of all hadrons can be

approximately be described as

$$\lim_{z \to 1} \frac{d\sigma}{dz} \approx (1-z)^3$$

in both the three jet sample and the overall hadronic event sample. However, we do not correctly account for the different energy partons which make up the jets in the three jet sample. Instead we fix an arbitrary constant, E_c, define z as E_h/E_c and then fit the momentum spectra. As we stated in the previous section, the fitted momentum spectra do not change with E_c. But, the parameters of the cross section do change. The power n (of the term $(1-z)^n$) must increase with increasing E_c in order that the measured momenta spectra remain constant. One can see in Table 7.11 that value of n in fact does increase as E_c is set to larger values. We see that jets 1 and 3 are consistent with one another. However,

	$\int_0^{E_c} N(E_j)dE_j/N_{\text{TOTAL}}$		
	85%	90%	95%
	π		
Jet #1	3.04	3.14	3.28
Jet #3	3.37	3.65	3.94
Δn	0.33	0.51	0.66
	K		
Jet #1	3.21	3.30	3.42
Jet #3	2.85	3.09	3.33
Δn	−0.36	−0.21	−0.11
	P		
Jet #1	4.08	4.15	4.28
Jet #3	5.09	5.46	5.82
Δn	1.01	1.31	1.54

Table 7.11: List of n's for Jet 1 and Jet 3. Statistical and Systematic errors on each n should be about the same as listed in table of parameters.

over the range of E_c's, the difference between the proton n's for jets 1 and 3 is

over one. This hints that the quark and gluon jets may have a different proton inclusive cross section. This is in agreement with the theoretical expectation that the gluon jet should be softer than the quark jet by a factor of $(1-z)$[27]. Such an effect would be more visible in the proton than in the pi and K meson inclusive cross sections. This is because of the smaller amount of momentum transferred to the protons from the decay of heavier baryons than would be transferred to the pi and K mesons from the decay of a higher mass resonance. Hence, the z of the final state proton is close to that of the initiating baryon thereby preserving any fragmentation effects.

However, we simply do not have the statistics to reach a conclusive answer on this topic. The high z behaviour of the jets 1 and 3 is statistically consistent.

7.4 Conclusions

We have measured the inclusive cross sections of charged hadrons in all hadronic events and in three jet events. We found that the high z behavior of $d\sigma/dz$ is approximately

$$\frac{(1-z)^{\sim 3}}{z}$$

for all charged hadrons where $z = E_h/E_q$, E_h being the hadronic energy and E_q is the parton energy. We also see that the high z behavior of kaons and pions in jets one and three are consistent. There is a hint that protons have different behaviours in jets one and three.

Finally, LUND slightly overestimates the number of protons in the overall hadronic data sample and clearly overestimates the number of protons in jet three. This result is tempered by the problem of separating kaons and protons. The number of kaons plus protons is better measured than the protons. The LUND prediction for kaons plus protons is consistent with this measurement.

Bibliography

[1] cf. J. J. Sakurai. *Advanced Quantum Mechanics.* Addison–Wesley Publishing Company, Reading Massachusetts, 1977.

[2] Murray Gell–Mann and Yuval Ne'eman. *The Eightfold Way.* W. A. Benjamin, INC., New York, 1964.

[3] cf. D. Flamm and F. Schöberl. *Introduction to the Quark Model of Elementary Particles, Volume 1.* Gordon and Breach Science Publishers, New York, London, Paris, 1982.

[4] M. Gell-Mann. *Phys. Lett.* **8**, 214 (1964).

[5] G. Zwieg. *CERN Report* **8419/TH412**, 1 (1964).

[6] cf. W.M. Gibson and B.R. Pollard. *Symmetry Principles in Elementary Particle Physics.* Cambridge University Press, Cambridge, 1976.

[7] Morton Hamermesh. *Group Theory and its Application to Physical Problems.* Addison–Wesley Publishing Company, Reading, Massacusetts, 1964.

[8] J.D. Bjorken and E.A. Paschos. *Phys. Rev.* **185**(5), 1975 (1969).

[9] Francis Halzen and Alan D. Martin. *Quarks and Leptons.* John Wiley and Sons, New York, 1984.

[10] R. Brandelik *et al*, The TASSO Collaboration. *Phys. Lett.* **83B**(2), 261 (1979).

[11] Ch. Berger *et al*, The PLUTO Collaboration. *Phys. Lett.* **86B**(3, 4), 413 (1979).

[12] James D. Bjorken and Sidney D. Drell. *Relativistic Quantum Fields, Vols. I, II.* McGraw–Hill Book Company, New York, 1965.

[13] Albert Messiah. *Quantum Mechanics, Vols. I, II.* John Wiley and Sons, INC., New York, 1958.

[14] John David Jackson. *Classical Electrodynamics.* John Wiley and Sons, INC., New York, 1975.

[15] Eugene D. Commins and Philip H. Bucksbaum. *Weak Interactions of Leptons and Quarks.* Cambridge University Press, Cambridge, 1983. This book show how Yang–Mills theory is used to describe the weak interaction.

[16] Ch. Berger *et al*, The PLUTO Collaboration. *Phys. Lett.* **97B**(3,4), 459 (1980).

[17] R. Brandelik *et al*, The TASSO Collaboration. *Phys. Lett.* **94B**(3), 437 (1980).

[18] G. Wolf. *DESY* **81-086**, 64–74 (1981).

[19] John Ellis, Mary K. Gaillard, and Graham G. Ross. *Nucl. Phys.* **B111**, 253 (1976).

[20] R.K. Ellis, D.A. Ross, and A.E. Terrano. *Phys. Rev. Lett.* **45**(15), 1226 (1980).

[21] R.K. Ellis, D.A. Ross, and A.E. Terrano. *Nucl. Phys.* **B178**, 421 (1981).

[22] W. Bartel *et al*, The JADE Collaboration. *Phys. Lett.* **91B**(1), 142 (1980).

[23] Ch. Berger *et al*, The PLUTO Collaboration. *Phys. Lett.* **86B**(3,4), 418 (1979).

[24] R. Brandelik *et al*, The TASSO Collaboration. *Phys. Lett.* **97B**(3, 4), 453 (1980).

[25] R.D. Field and R.P. Feynman. *Nucl. Phys.* **B136**, 1 (1978).

[26] A. Casher, H. Neuberger, and S. Nussinov. *Phys. Rev.* **D20**, 179 (1979).

[27] Werner Hofmann. *Jets of Hadrons*, page 1. Volume 90 of *Springer Tracts in Modern Physics*, Springer–Verlag, Berlin, 1981.

[28] G. Altarelli and G. Parisi. *Nucl. Phys.* **B126**, 298 (1977).

[29] Martin L. Perl. *High Energy Hadron Physics.* John Wiley and Sons, New York, 1974.

[30] Sidney D. Drell, Donald J. Levy, and Tung–Mow Yan. *Phys. Rev.* **187**(5), 2159 (1969).

[31] R. Brandelik *et al*, The DASP Collaboration. *Nucl. Phys.* **B148**, 18 (1960).

[32] R. Brandelik *et al*, The TASSO Collaboration. *Z. Phys. C* **17**, 5 (1983).

[33] Bo Andersson, Gösta Gustafson, and Torbjörn Sjöstrand. *Z. Phys. C* **6**, 235 (1980).

[34] Julian Schwinger. *Phys. Rev.* **128**, 2425 (1962).

[35] P. Hoyer *et. al. Nucl. Phys.* **B161**, 349 (1979).

[36] A. Ali et al. *Phys. Lett.* **B93**, 155 (1980).

[37] B. Andersson, G. Gustafson, and C. Peterson. *Z. Phys. C* **1**, 105 (1979).

[38] Michael E. Peskin. Aspects of the dynamics of heavy–quark systems. In Patricia M. McDonough, editor, 11^{th} *SLAC Summer Institute on Particle Physics*, page 151, Stanford Linear Accelerator Center, Stanford University, Stanford, California, 1983.

[39] J.W. Gary. *Tests of Models for Parton Fragmentation in e^+e^- Annihilation.* PhD thesis, University of California, Berkeley, November 1985. LBL–20638.

[40] H. Aihara, et al., the TPC collaboration. *Phys. Rev. Lett.* **57**(25), 3140 (1986).

[41] T.D. Gottschalk. *Nucl. Phys.* **B214**, 201 (1983).

[42] D. Amati and G. Veneziano. *Phys. Lett.* **83B**(1), 87 (1979).

[43] A. R. Clark et al. *Proposal for a PEP Facility based on the Time Projection Chamber.* Technical Report, Lawrence Berkeley Laboratory, 1976.

[44] William W. Moses. *Measurement of the Inclusive Branching Fraction $\tau^- \rightarrow \nu_\tau \pi^- \pi^\circ$ + neutral meson(s).* PhD thesis, University of California, Berkeley, November 1986. LBL–22579.

[45] H. Aihara et al., The TPC collaboration. *IEEE Trans. on Nucl. Sci.* **NS-30**(1), 153 (1983).

[46] H. Aihara et al., The TPC collaboration. *Nucl. Instr. and Meth.* **217**, 259 (1983).

[47] D.H. Badtke et al. *Nucl. Instr. and Meth.* **188**, 497 (1981).

[48] H. Aihara et al., The TPC collaboration. *IEEE Trans. on Nucl. Sci.* **NS-30**(1), 67 (1983).

[49] W.W.M. Allison et al. *The Identification of Secondary Particles by Ionisation Sampling (ISIS).* Technical Report, Nuclear Physics Laboratory, Oxford, 1974.

[50] Jay N. Marx. Particle Identification by Energy Loss Measurement and Long Drift Imaging Chambers. In Anne Mosher, editor, *Summer Institute on Particle Physics, July 28 - August 8, 1980*, page 215, Stanford Linear Accelerator Center, Stanford University, Stanford, California, 1981.

[51] cf. F. Reif. *Fundamentals of Statistical and Thermal Physics.* McGraw-Hill Book Company, New York, 1965.

[52] H. Aihara et al., The TPC collaboration. *IEEE Trans. on Nucl. Sci.* **NS-30**(1), 76 (1983).

[53] Marjorie D. Shapiro. *Inclusive Hadron Production and Two Particle Correlations in e^+e^- Annihilation at 29 GeV Center-of-Mass Energy.* PhD thesis, University of California, Berkeley, December 1985. LBL–18820.

[54] H. Aihara et al., The TPC collaboration. *IEEE Trans. on Nucl. Sci.* **NS-30**(1), 162 (1983).

[55] P. Oddone and P. Nemethy. *TPC note* **TPC-LBL-78-63**, 1 (1978).

[56] H. Aihara et al., The TPC collaboration. *IEEE Trans. on Nucl. Sci.* **NS-29**(1), 427 (1982).

[57] Nicholas John Hadley. *Charged Hadron Production in e^+e^- at PEP with the TPC.* PhD thesis, University of California, Berkeley, May 1985. LBL–16116.

[58] Gerald Lynch. *TPC note* **TPC-LBL-81-6**, 1 (1981).

[59] W.W.M. Allison and J.H. Cobb. *Ann. Rev. Nucl. Part. Sci.* **30**, 253 (1980).

[60] D. Ritson. Instrumentation. In Anne Mosher, editor, *Summer Institute on Particle Physics, July 28 - August 8, 1980*, page 177, Stanford Linear Accelerator Center, Stanford University, Stanford, California, 1981.

[61] F. Lapique and F. Piuz. *CERN Report* **CERN/EF 79/4**, 1 (1979).

[62] Glen Cowen, private communication. The 14 kG data energy loss curve was measured and is shown to agree with the theoretical expectation.

[63] Gerald Lynch. *TPC note* **TPC-LBL-78-17**, 1 (1978).

[64] G. Lynch. *TPC note* **TPC-LBL-82-3**, 1 (1982).

[65] N. Hadley and G. Lynch. *TPC note* **TPC-LBL-82-7**, 1 (1982).

[66] English and Hanna. *Canad. J. Res.* **31**, 768 (1953).

[67] B. Jean-Marie, V. Lepeltier, and D. L'Hote. *Nucl. Instr. and Meth.* **159**, 213 (1979).

[68] Gerald Lynch. *TPC note* **TPC-LBL-83-6**, 1 (1983).

[69] N. Hadley, P. Robrish, and D. Pollard. *TPC note* **TPC-LBL-77-42**, 1 (1977).

[70] Forest Rouse, Peter Robrish, Nick Hadley, and Ray Fuzesy. Results of the materials test chamber 11/15/82-3/14/83. March 1983. This note describes the systematics involved in making a measurement with the Materials Test Chamber.

[71] H. Aihara *et al*, The TPC Collaboration. *Phys. Rev. Lett.* **52**, 577 (1984).

[72] H. Yamamoto and N. Toge. *TPC note* **TPC-UT-84-2**, 1 (1984).

[73] Andreas Backer. *Z. Phys. C* **12**, 161 (1982).

[74] K. Lanius, H.E. Roloff, and H. Schiller. *Z. Phys. C* **8**, 251 (1981).

[75] S. Brandt and H. D. Dahmen. *Z. Phys. C* **1**, 61 (1979).

[76] F.A. Berends and R. Kleiss. *Nucl. Phys.* **B178**, 141 (1981).

[77] Gerald Lynch, private communication. If one uses the binomial theorm, the correct partitioning and sums over all possible configurations one can prove that this is correct.

[78] Philip R. Bevington. *Data Reduction and Error Analysis for the Physical Sciences.* McGraw-Hill Book Company, New York, 1969.

[79] G.P. Yost. *Lectures on Probability and Statistics.* Technical Report 16993 Rev., LBL, June 1985. Presented as a course on Statistics, Imperial College, London, U.K., January–April 1983.

[80] Gerald Lynch. Momentum bias corrections. A short note about possible momentum variables whose errors have a gaussian distribution.

[81] Gerald Lynch, private communication.

[82] Ronald J. Madaras, private communication. Plot courtesy of Ron Madaras.

[83] Ronald J. Madaras. Tuning distortion corrections to improve tpc momentum resolution. May 1983. Transparances of lecture given at TPC group meeting on May 27, 1983.

[84] Ronald J. Madaras. Distortion corrections and momentum resolution in the pep-4 tpc. July 1985. Transparances of lecture given at TPC group meeting on July 12, 1985.

[85] F. James and M. Roos. *Computer Physics Communications* **10**, 343 (1975).

LAWRENCE BERKELEY LABORATORY
TECHNICAL INFORMATION DEPARTMENT
UNIVERSITY OF CALIFORNIA
BERKELEY, CALIFORNIA 94720